Annual Report 2018

Physik-Department

Lehrstuhl für Funktionelle Materialien

mit dem

Fachgebiet Physik Weicher Materie

Technische Universität München

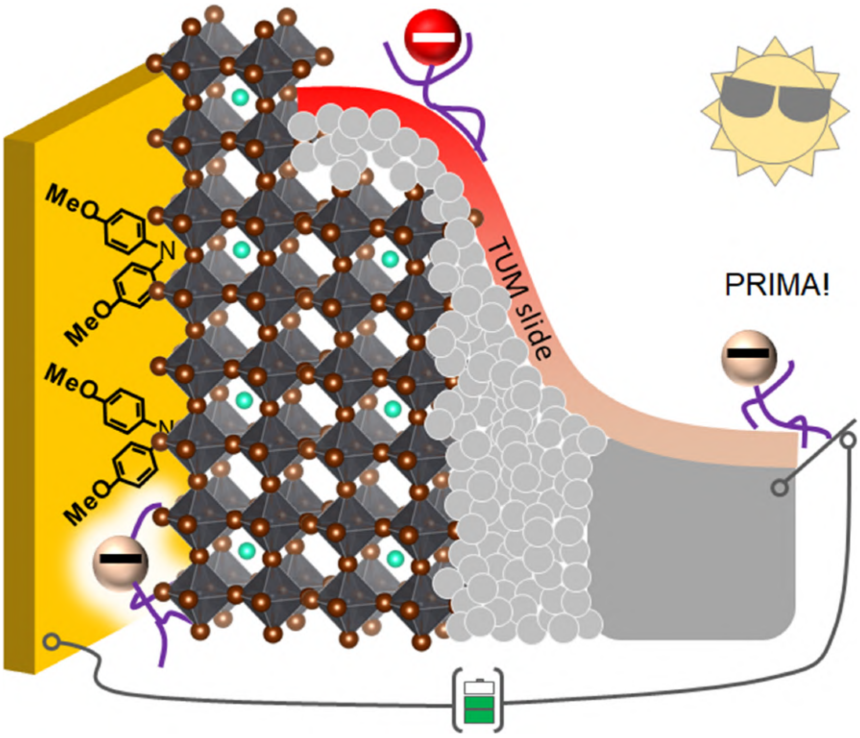

Prof. Dr. Peter Müller-Buschbaum
Chair of Functional Materials

Prof. Dr. Christine M. Papadakis
Soft Matter Physics Group

Physik-Department
Technische Universität München
James-Franck-Straße 1
85748 Garching

Secretaries: Marion Waletzki
Carola Kappauf

Tel.: +49(0)89 289 12452
Fax: +49(0)89 289 12473

Email: muellerb@ph.tum.de
papadakis@tum.de
marion.waletzki@ph.tum.de
carola.kappauf@ph.tum.de

www.functmat.ph.tum.de
www.polymer.ph.tum.de
www.softmatter.ph.tum.de

Editors: Dr. Volker Körstgens, Florian Jung

Cover-page picture:

Architecture diagram of a planar perovskite solar cell and the inner motions of electrons during device operation.

Preface

It is a great pleasure to present the annual report for the year 2018 in the name of the staff of the Chair of Functional Materials and the Soft Matter Physics Group. It provides an overview of our teaching, research, and development activities. Our research activities are focused on functional materials and cover a broad range from soft matter physics to developments of methods and instrumentation. We examine the fundamental physics of material properties using mainly scattering methods (neutron, x-ray and light scattering). The general goal of our research is to explain the functional characteristics of soft condensed matter from the knowledge of the molecular dynamics and nanostructure as well as their kinetics.

In the year of 2018, we witnessed several important changes: On 1st April 2018, Prof. Peter Müller-Buschbaum succeeded Prof. Winfried Petry as Scientific Director at the research neutron source Heinz Maier-Leibnitz (FRM II) and as the Director of the Heinz Maier-Leibnitz Zentrum as well as in heading the Chair of Functional Materials. About 300 guests joined the official farewell ceremony for Prof. Petry on 25th October 2018. Winfried Petry will continue his engagement at TU Munich, since he was awarded with the honorary title of Emeritus of Excellence of the Technical University of Munich.

In 2018, the chair activities covered the specific areas of responsive polymers, thin polymer films, polymer films for application in photovoltaics and polymer-hybrid systems as well as real-time characterization, instrumentation and new materials. The activities in the fields of polymer films for application in photovoltaics and polymer-hybrid systems have been successfully continued. With *"TUM.solar"*, the keylab in the network of the Bavarian Collaborative Research Project *"Solar Technologies go Hybrid"* (SolTec) headed by Prof. Müller-Buschbaum is running in its seventh year of funding. Research activities cover a broad area of next generation solar cells, such as organic solar cells, dye sensitized solar cells, hybrid solar cells and organometal halide perovskite solar cells. Also thermoelectric materials and energy storage materials with focus on lithium ion battery technology are actively researched. Moreover, we investigated polymers with complex architecture, novel responsive polymers (also under high pressure), self-assembling polymers in solution, multiresponsive and orthogonally switchable polymers as well as polymers for medical applications. Special focus was on the pathways of structural changes upon application of a change of environment. A major review on solvent vapor annealing of nanostructured block copolymer thin films was published.

The in-house experiments available in the laboratories of the chair were supplemented by the lively activities at numerous large scale facilities, comprising synchrotron radiation and neutron scattering experiments, also at the FRM II. In particular, the in-house x-ray scattering experiments were operated with full time schedule. The imaging ellipsometer was further upgraded towards liquid environments to allow for more elaborate measurements. In collaboration with our guest, Prof. Alfons Schulte, the sample environment for high-pressure research was substantially improved, now allowing for investigations of both the dynamics and the kinetics.

In 2018, the Chair of Functional Materials comprised 7 fellows, 48 PhD students, 23 master students, 22 bachelor students, 7 student assistants and 7 administrative and technical staff members. 9 PhD theses were accomplished; moreover, 7 master theses as well as 21 bachelor theses were finished. As in the years before, we had the pleasure to host numerous guests from abroad, which stimulated a lively and inspiring scientific atmosphere. Prof Alfons

Schulte, University of Central Florida, was awarded with an August-Wilhelm Scheer Visiting Professorhip, which allowed him to visit the Soft Matter Physics Group and to continue the high-pressure research. At the same time, he was appointed member of the TUM Institute of Advanced Study.

In general, all members of the chair were very active at conferences and workshops, participating with both, talks and posters. We organized a summer school for the chair in Obertauern, Austria, during which the group members presented talks on fundamental aspects of soft matter physics and had extensive group discussions. Moreover, important conferences were organized by members of the chair: Prof. Peter Müller-Buschbaum co-organized the MLZ Conference *"Neutrons for Culture and Arts"*, the 8th MSE Colloquium *"Advances in Energy Transition"* and the *"German Conference for Research with Synchrotron Radiation, Neutrons and Ion Beams at Large Facilities 2018 (SNI2018)"*. Again, two Edgar-Lüscher seminars were organized by Prof. Peter Müller-Buschbaum, this year on the subjects *"Große Instrumente für große Fragestellungen"* and *"Physik der Ozeane und Atmosphäre"*.

Regarding teaching activities of the chair, we offered lectures in general physics for the TUM elite engineers in the Munich School of Engineering (MSE) (Müller-Buschbaum) and lectures in advanced physics for future teachers in vocational schools (Papadakis). Specialized lectures comprised *"Polymer physics"* (Papadakis) and *"Nanostructured soft materials"* (Müller-Buschbaum). Prof. Papadakis acted again as a deputy women's representative of the Physics Department. Moreover, Prof. Müller-Buschbaum heads the activities in the *"Network Renewable Energies (NRG)"* in the MSE.

As a service to the community, Prof. Papadakis acted as one of the Editors-in-Chief of *"Colloid and Polymer Science"* and Prof. Müller-Buschbaum served as Associate Editor at *"ACS Applied Materials & Interfaces"*.

This annual report comprises a selection of the different research topics and projects carried out in the individual groups of the chair. It highlights the dedicated and successful research activities and collaborations with other groups and large scale facilities. We wish all chair members a fruitful continuation and a very successful year 2019.

Peter Müller-Buschbaum and Christine M. Papadakis March 2019

Contents

1 Responsive polymers

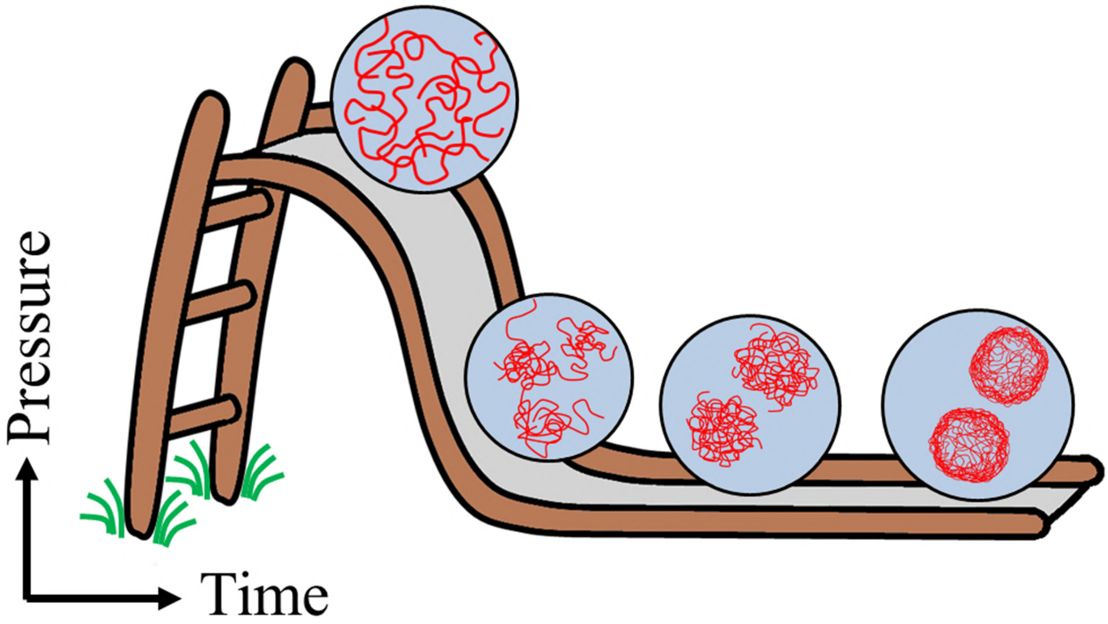

1.1 The structural, thermal and dynamic behavior of the thermoresponsive polymer poly(*N*-isopropylmethacrylamide)

C.-H. Ko, K.-L. Claude, D. Schanzenbach[1], B.-J. Niebuur, F. Jung, J.-J Kang, H. Frielinghaus[2], L. Barnsley[2], V. Pipich[2], B. Wu[2], A. Schulte[3], P. Müller-Buschbaum, A. Laschewsky[1,4], C. M. Papadakis

[1] Universität Potsdam, Potsdam-Golm, Germany
[2] MLZ, Garching, Germany
[3] University of Central Florida, Orlando, U.S.A
[4] Fraunhofer IAP, Potsdam-Golm, Germany

Poly(*N*-isopropylmethacrylamide) (PNIPMAM) is a thermoresponsive polymer exhibiting lower critical solution temperature (LCST) behavior in aqueous solution. Compared to the well-investigated poly(*N*-isopropylacrylamide) (PNIPAM), which has similar chemical structure, PNIPMAM has a higher transition temperature (43 ^{o}C [1] instead of 32^{o}C). This may be due to the presence of the additional methyl groups on the vinyl backbone, which cause steric hindrance and weaken the intramolecular interactions [2]. The coil-to-globule transition of PNIPMAM chains makes it a potential candidate for applications such as drug encapsulation, tissue engineering, and in microfluidics, and the higher transition temperature may in some cases be convenient. The higher LCST enables us to design materials within suitable temperature range. To elucidate the influence of the additional methyl group on the structural changes at the phase transition, we investigate the temperature- and concentration-dependent phase behavior of PNIPMAM in D_2O using turbidimetry to reveal the cloud point, T_{CP}, differential scanning calorimetry (DSC) to determine the dehydration temperature, Raman spectroscopy to characterize the hydration state, and (very) small-angle neutron scattering (VSANS and SANS) at instruments KWS-3 and -1 at the Heinz Maier-Leibnitz-Zentrum to investigate the solution structures. PNIPMAM with molar mass 17000 g/mol was dissolved in D_2O at concentrations of 5 mg/ml to 150 mg/ml.

The turbidimetry measurements revealed that T_{CP} lies in the range 42-45 ^{o}C, depending on concentration (Fig. 1.1a). DSC revealed an endothermic peak at 45-47 ^{o}C, reflecting the dehydration at the phase transition. Thus, the polymer solutions first undergo a macroscopic phase separation, and the polymer chains dehydrate only 2-3 ^{o}C above T_{CP}.

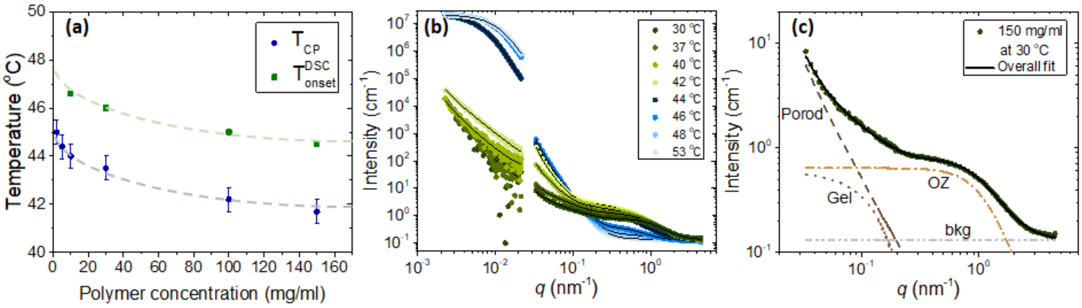

Figure 1.1:
a) Phase diagram determined by turbidimetry and DSC, b) SANS and VSANS scattering curves of 150 mg/ml in D_2O, and c) fitting model for the SANS data.

Raman spectroscopy revealed that a sharp red-shift of the CH stretching bands occurs at T_{CP}, indicating that the hydrophobic substituents of PNIPMAM undergo a strong dehydration and that hydrophobic interactions dominate above T_{CP}. Comparing the peak frequencies to the ones of PNIPAM, it is seen that PNIPMAM is more hydrated than PNIPAM, whereas the dehydrated state above T_{CP} are similar.

SANS measurements confirmed the formation of large aggregates above T_{CP} and showed scattering due to local concentration fluctuations as well (Figure 1.2). To analyze the SANS data, an additional term was needed to describe scattering from physical crosslinks due to the hydrophobic moieties, giving rise to scattering at intermediated momentum transfers. We find that, in the one-phase state, the physical crosslinks have an effect on the chain conformation and that loosely packed large inhomogeneities are present. At T_{CP}, the polymer chains collapse and form large aggregates. Their size decreases upon heating, which is attributed to the release of water. The density of physical crosslinks increases drastically upon heating.

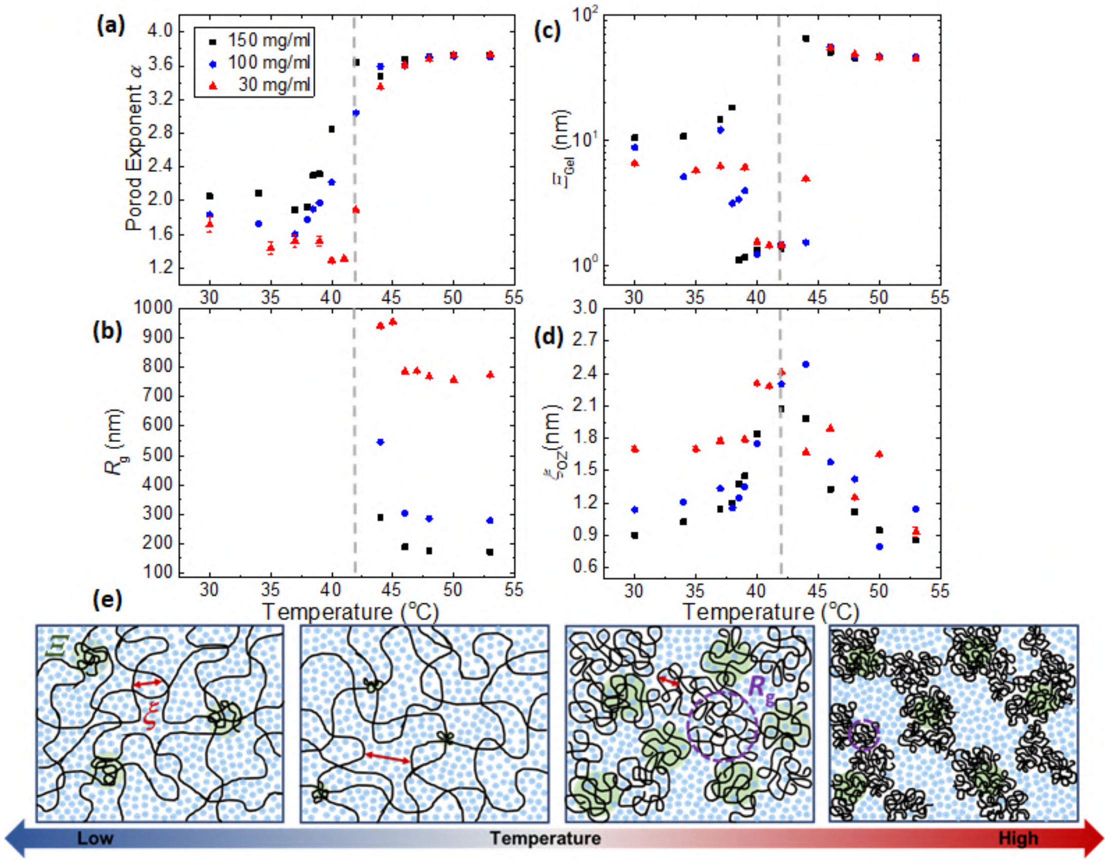

Figure 1.2:
a) Porod exponent, b) radius of gyration, c) correlation length of physical crosslinks, d) OZ correlation length of the 150, 100, and 30 mg/ml polymer solutions, e) and schematic structures in dependence on temperature. (Grey dashed lines indicate the T_{CP} of 150 mg/ml polymer solutions.)

The phase transition mechanism of PNIPMAM in D_2O is summarized in Fig. 1.2e. In the one-phase region, loosely packed large inhomogeneities and physical crosslinks caused by hydrophobic moieties exist. In the two-phase region, the chains are collapsed, as expected for thermoresponsive polymers, and aggregates form which shrink with increasing temperature. In the one-phase state, the hydrophobic groups of PNIPMAM are more hydrated than PNIPAM. The additional methyl groups in PNIPMAM thus result in significant differences regarding the hydration behavior and the structural behavior around the phase transition.
The project is funded by Deutsche Forschungsgemeinschaft (DFG).

[1] K. Kunota, et al., *Polym. J.* **22**, 1051, (1990)

[2] J. Pang, et al., *J. Theor. Comput. Chem.* **10**, 359, (2011)

1.2 Formation and growth of mesoglobules in aqueous poly(N-isopropylacrylamide) solutions revealed with kinetic small-angle neutron scattering and fast pressure jumps

B.-J. Niebuur, L. Chiappisi[1], X. Zhang, F. Jung, A. Schulte[2], C. M. Papadakis

[1] ILL, Grenoble, France

[2] University of Central Florida, Orlando, U.S.A.

The understanding of the mechanisms of growth in aggregating systems and the origin of the stability of the resulting aggregates is of great importance in a wide variety of research areas, ranging from the study on proteins to the design of smart materials. To study the kinetics of aggregate formation, temperature jumps to induce the phase transition in combination with time-resolved scattering methods have been applied. However, due to slow heating and temperature gradients, the early stages of mesoglobule formation could not be resolved. An alternative method of inducing phase transitions is a change in pressure. With pressure jumps, the phase separation can be induced much more rapidly than with temperature jumps.

In the present work, we investigate the pathway of aggregation of a 3 wt% solution of the thermoresponsive polymer poly(N-isopropylacrylamide) in D_2O [1], which, at atmospheric pressure, exhibits lower critical solution temperature (LCST) behavior with a cloud point temperature $T_{cp} \approx 32$°C. Above T_{cp}, PNIPAM forms stable mesoglobules with sizes of $\sim$100 nm, which do not lead to the expected macroscopic phase separation [2]. We combine kinetic small-angle neutron scattering (SANS) and pressure jumps to follow the early stages of mesoglobule formation, their growth and long-term behavior with a time resolution of 0.05 s. The measurements were performed at the instrument D11 at the ILL. Using a neutron wavelength of λ = 6 Å and sample-detector distances of 1.5, 8 and 34 m, a q range of 0.02 - 3 nm^{-1} was covered. The sample was mounted in a copper beryllium pressure cell, capable of withstanding pressures up to 350 MPa, with a sample thickness of 2 mm.

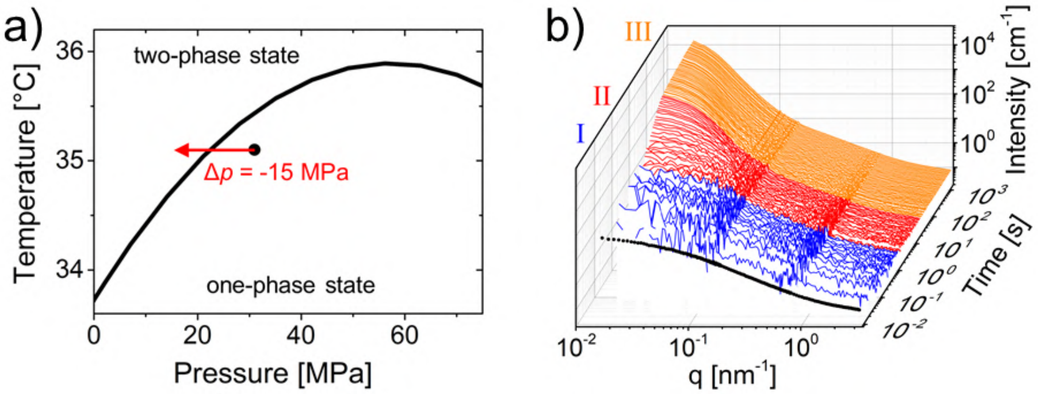

Figure 1.3:
(a) Phase diagram of the 3wt% PNIPAM solution in D_2O as measured by turbidimetry [1]. The arrow depicts the start and end pressure of the jump. (b) SANS data obtained after the pressure jump in regime I (blue curves), regime II (red curves), and regime III (orange curves). Black symbols: pre-release measurement.

In Fig. 1.3a, the phase diagram of PNIPAM in the temperature-pressure frame determined using turbidimetry [1] is presented. A pressure jump with a magnitude of -15 MPa is performed from the one-phase state at 31 MPa and 35.1°C to the two-phase state at 16 MPa, depicted by the arrow. The SANS data obtained before and after the pressure jump is presented in Fig. 1.3b. In the one-phase state (before the pressure jump), a shoulder above $\sim$ 0.06 nm^{-1} is observed, which shows the presence of correlation fluctuations. It can be modeled with the Ornstein-Zernike structure factor, which gives a correlation length, ξ_{OZ}. Directly after the jump (regime I), the shoulder increases slightly in intensity, but can still be modeled with the Ornstein-Zernike structure factor. After 1.4 s (regime II), a second shoulder below $\sim$ 0.1 nm^{-1} arises, which increases strongly in intensity and shifts strongly to lower q values. This contribution can be attributed to scattering from growing mesoglobules, and is modeled with the Guinier-Porod form factor. It includes the radius of gyration of the mesoglobules, R_g, and the Porod exponent, m, indicative of the surface structure. After $\sim$30 s (regime III), the growth of the mesoglobules slows down strongly.

The characteristic parameters from the fits are presented in Fig. 1.4a. In regime I, ξ_{OZ} increases from $\sim$16 to $\sim$30 nm, indicating the formation of small clusters by nucleation and growth. In regime II, R_g continues the trend of ξ_{OZ}. It increases according to $R_g \propto t^{1/3}$, which shows that the growth is diffusion-limited. In regime III, R_g increases weakly and follows logarithmic growth. From a fit [1], the energy barrier for coalescence is found to be 6.2 k_BT, i.e., significantly larger than the thermal energy. m increases from $\sim$2 to $\sim$5 in regime II, followed by a weak decrease in regime III. The value $m > 4$ is due to a concentration gradient at the surface of the particles. In this case, water at the surface of the mesoglobules rapidly diffuses out in regime II, leading to a dense polymeric shell. The viscoelastic effect thus stabilizes the mesoglobules: If the chain entanglement time is much longer than the contact time of two mesoglobules, the probability of coalescence is low, preventing rapid growth of the mesoglobules [3].

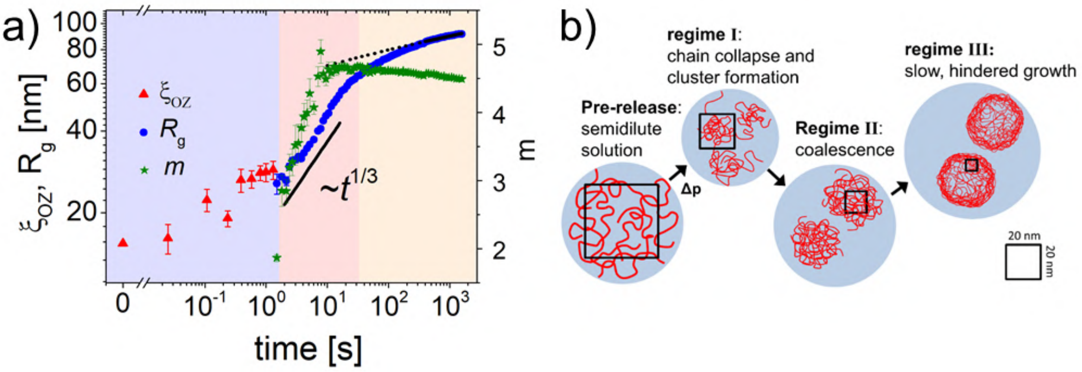

Figure 1.4:
(a) Time-dependence of ξ_{OZ} (red triangles), R_g (blue dots) and m (green stars), obtained from fits of the SANS data, and a fit of logarithmic growth model to R_g (black solid line). (b) Schematic representation of the mesoglobule formation and growth. The black squares indicate similar length scales in each illustration.

In summary, we showed that, using pressure jumps in combination with kinetic SANS, the different stages of mesoglobule formation and growth can be elucidated (Fig. 1.4b). This opens up opportunities for studies of more complex systems.

[1] B.-J. Niebuur, L. Chiappisi, X. Zhang, F. Jung, A. Schulte, C. M. Papadakis, *ACS Macro Lett.* **7**, 1155-1160 (2018)

[2] B.-J. Niebuur, K.-L. Claude, S. Pinzek, C. Cariker, K. N. Raftopoulos, V. Pipich, M.-S. Appavou, A. Schulte, C. M. Papadakis, *ACS Macro Lett.* **6**, 1180-1185 (2017)

[3] H. Tanaka, *Phys. Rev. Lett.* **71**, 3158-3161 (1993)

1.3 Morphology of thermoresponsive molecular brushes with copolymer side arms in aqueous solution

J.-J. Kang, J. Zhao[1], H. Frielinghaus[2], L. Barnsley[2], F. Kohler[3], H. Dietz[3], S. Pispas[1], C.M. Papadakis

[1] National Hellenic Research Foundation, Athens, Greece
[2] JCNS at MLZ, Garching, Germany
[3] TU München, Physik-Department, Chair of Biomolecular Nano-Technology, Garching, Germany

Poly (ethylene oxide) (PEO) and poly (propylene oxide) (PPO) are known to be thermoresponsive polymers, both exhibiting lower critical solution temperature (LCST) behavior. Their cloud points are very different because PEO is significantly more hydrophilic than PPO. In the present work, the LCST behavior of molecular brushes based on PEO and PPO is investigated. They feature side arms from PEO-PPO copolymers which are densely grafted on a poly(*p*-hydroxystyrene) (PHOS) backbone. The side arms are random (P*r*E) or diblock copolymers (P*b*E) [1,2]. In both cases, the weight fraction of PPO is 59.2 wt%. Degrees of polymerization of the backbone and of the side arms range between 90-140 and 160-250, respectively.

2 wt% solutions of P*r*E and P*b*E in D_2O were investigated. To characterize the structural variations with temperature, dynamic light scattering (DLS) as well as small angle neutron scattering (SANS) measurements at KWS-1 at Heinz Maier-Leibnitz-Zentrum were performed. Temperatures were chosen to range from room temperature, RT, up to 64 °C. Besides, real-space images of the samples were obtained by cryo transmission electron microscopy (cryo-TEM) of very dilute solutions in H_2O (0.01 wt%).

DLS reveals that both P*r*E and P*b*E have hydrodynamic radii of 15-16 nm at low temperatures and form large aggregates above 38 °C and 60 °C, respectively (Fig. 1.5). These temperatures are vastly different, despite the weight fraction of PPO in the side arms being the same. The much higher aggregation temperature, T_{agg}, of the P*b*E solution may be attributed to a hydrophilic shell formed by the completely water-soluble PEO, which shields the PPO blocks from contact with water. In contrast, in P*r*E, the randomly distributed PPO segments are exposed to water, resulting in a collapse at lower temperature.

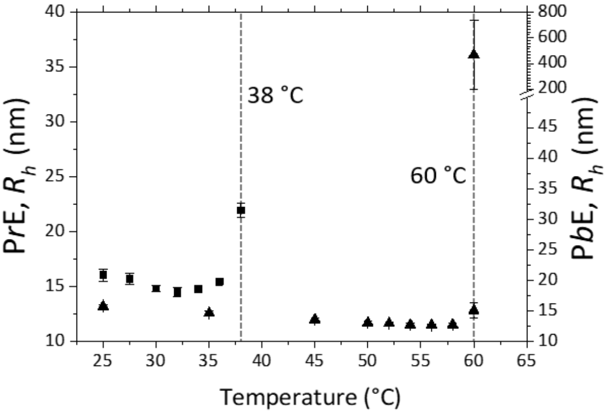

Figure 1.5:
Temperature-dependent hydrodynamic radii, R_h, of P*r*E (squares, left axis) and P*b*E (triangles, right axis) in aqueous solution (2 wt% in D_2O). The vertical dotted lines mark the respective aggregation temperatures, T_{agg}.

The SANS data confirm the formation of aggregates at RT by the strong increase of scattering intensity at low momentum transfers (Fig. 1.6). The distinct peaks indicate a strong correlation between the closely packed brushes forming the aggregates. Furthermore, model fitting reveals that both, P*r*E and P*b*E, are flat ellipsoidal particles having a polymer-rich core and a water-rich shell. At RT, the shell contains 52 % water for P*r*E and 66 % for P*b*E. As the temperature approaches T_{agg}, water is completely repelled out of P*r*E. In contrast, P*b*E still contains 60 % of water in its shell, which is formed by the hydrophilic PEO. At temperatures above T_{agg}, P*r*E tends to form medium-sized aggregates being correlated with each other, whereas P*b*E forms randomly distributed large aggregates.

Fig. 1.7 shows the images of single molecules obtained by cryo-TEM on P*r*E. Due to the high grafting density of the side arms, the backbones can be clearly recognized, revealing the "bottlebrush" shape. Considering the flat ellipsoids found in SANS experiments as well as the good water solubility of P*r*E at RT, we conclude that, at high concentration, the molecular brushes coil up to increase the contact between the side arms and water, as sketched in the inset of Fig. 1.7.

To summarize, molecular brushes with PEO-*r*-PPO and PEO-*b*-PPO copolymer side arms undergo different dehydration processes and interact differently with each other above the phase transition temperature. Moreover, concentration has an effect on the degree of coiling of the backbone, due to maximization of polymer-water contact. Thus, the densely grafted architecture leads to materials with new and complex properties.

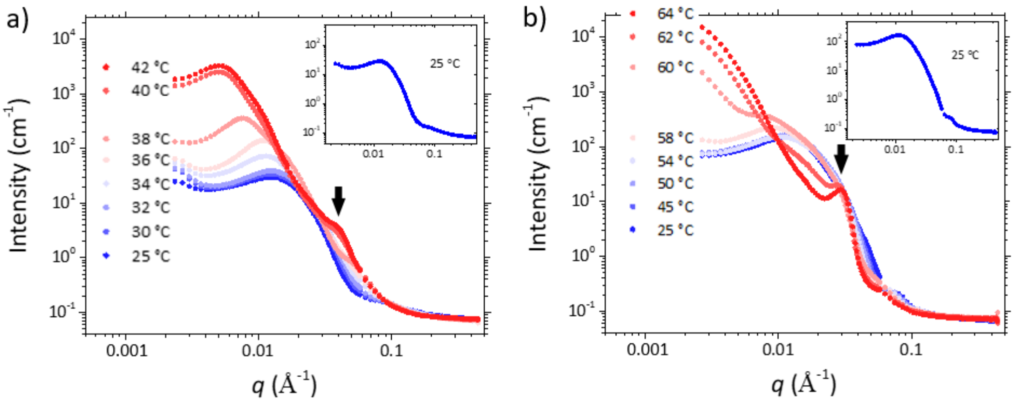

Figure 1.6:
SANS data at selected temperatures for 2 wt% solutions of (a) P*r*E and (b) P*b*E in D_2O. RT data are shown in the insets. The black arrows mark the peaks emerging above T_{agg}.

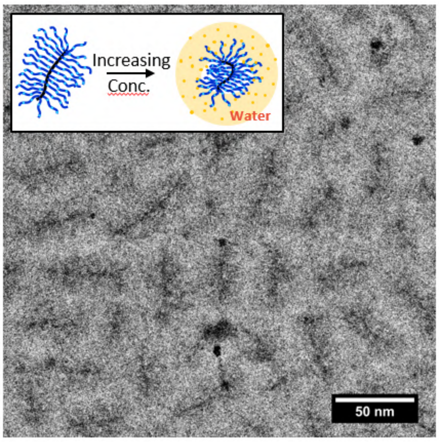

Figure 1.7:
Cryo-TEM image of a very dilute P*r*E solution. The inset shows the change of the chain conformation in dependence on polymer concentration.

[1] J. Zhao, G. Mountrichas, G. Zhang, S. Pispas, *Macromolecules* **43**, 1771-1777 (2010)

[2] J. Zhao, G. Zhang, S. Pispas, *J. Polym. Sci. A* **48**, 232-23280 (2010)

1.4 Thermoresponsive behavior of poly(2-oxazoline)-based molecular brushes

K. Shehu, J.-J. Kang, C. Sachse[1], H. Frielinghaus[2], L. Barnsley[2], R. Jordan[1], C.M. Papadakis

[1] Technische Universität Dresden, Dresden, Germany
[2] JCNS at MLZ, Garching, Germany

Poly(2-alkyl-2-oxazoline)s (POx) are known for their tunable thermoresponsive properties, which, together with their biocompatibility makes them potential materials for biomedical applications. When the alkyl substituent is chosen to be an ethyl group, the polymer exhibits lower critical solution temperature (LCST) behavior in aqueous solution with the cloud point, T_{cp}, being around 67 °C. In the present work, a POx-based molecular brush PiPOx$_{100}$-*g*-PEtOx$_{17}$ is investigated, which is composed of a hydrophobic poly(2-isopropenyl-2-oxazoline) (PiPOx) backbone and poly(2-ethyl-2-oxazoline) (PEtOx) side arms, which have hydrophobic tert-butyloxycarbonyl end groups [1]. The aim of the work is to characterize the influence of the densely-grafted architecture on the LCST behavior of the PEtOx side arms.

We carried out turbidimetry measurements to determine T_{cp} and dynamic light scattering (DLS) to characterize the behavior of the hydrodynamic radius R_h of the molecular brushes around T_{cp}. Small-angle neutron scattering (SANS) at KWS-1 (Heinz Maier-Leibnitz-Zentrum) was carried out to determine the shape and size, inner structure and correlation of the molecular brushes. The polymer concentration in H_2O (for turbidimetry) or D_2O (for DLS and SANS) was chosen at 3 wt%.

Using turbidimetry, T_{cp} was found at 41 °C with a hysteresis of 1 °C (Fig. 1.8a). DLS shows that R_h increases from 6.7 ± 0.5 nm to 8.3 ± 0.9 nm as the temperature approaches T_{cp} (Fig. 1.8b), which may be due to a change of shape.

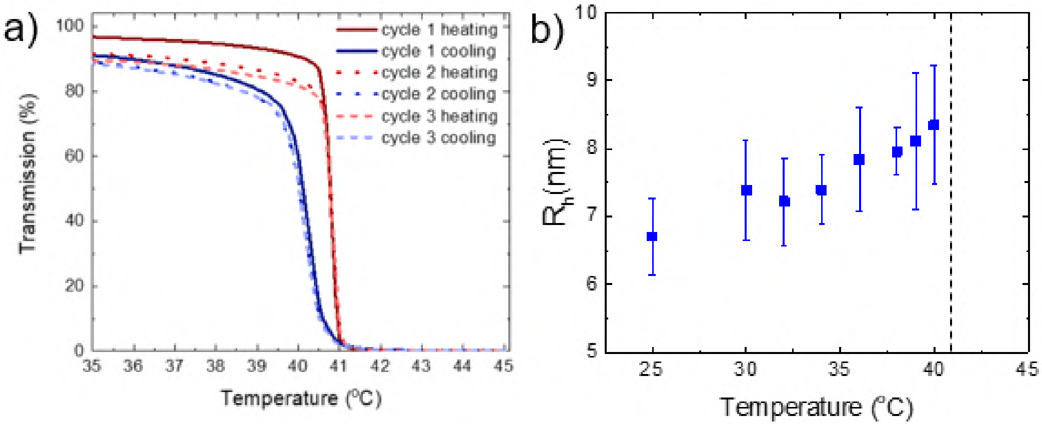

Figure 1.8:
(a) Turbidity measurements on a 3 wt% solution of PiPOx$_{100}$-*g*-PEtOx$_{17}$ in H_2O. Heating and cooling runs. (b) Temperature dependence of the hydrodynamic radius, R_h, from DLS (in D_2O). The vertical dotted line marks T_{cp}.

The SANS data could be analyzed by a cylinder model (Fig. 1.9a), implying elongated molecules, and the Percus-Yevick hard-sphere structure factor was used to describe the interaction between the molecular brushes. It is found that the cylinder length increases with temperature, as T_{cp} is approached, while the cylinder radius stays constant (Fig. 1.9b), resulting in an overall growth of the molecular size, which confirms the DLS result. It is supposed that the molecules undergo dehydration as temperature increases, leading to a straightening of the molecular brush. Above T_{cp}, both the cylinder length and radius decrease, i.e. the molecular brushes collapse. Aggregate scattering is present at low momentum transfers q at all temperatures. Its slope suddenly increases at T_{cp}, i.e. the aggregates are loose below and become compact above.

In summary, T_{cp} of the molecular brush is suppressed from 67 °C to 41-42 °C, i.e. by 27 °C with respect to PEtOx homopolymers, which is attributed to the densely-grafted structure of the molecular brush and the hydrophobic end groups. Figure 1.10 shows the temperature-dependent conformational changes of the molecular brushes. From room temperature to T_{cp}, the molecular brushes stretch out due to dehydration; whereas the collapse in a wide temperature range above T_{cp}. Loose aggregates exist below T_{cp}, which become compact above.

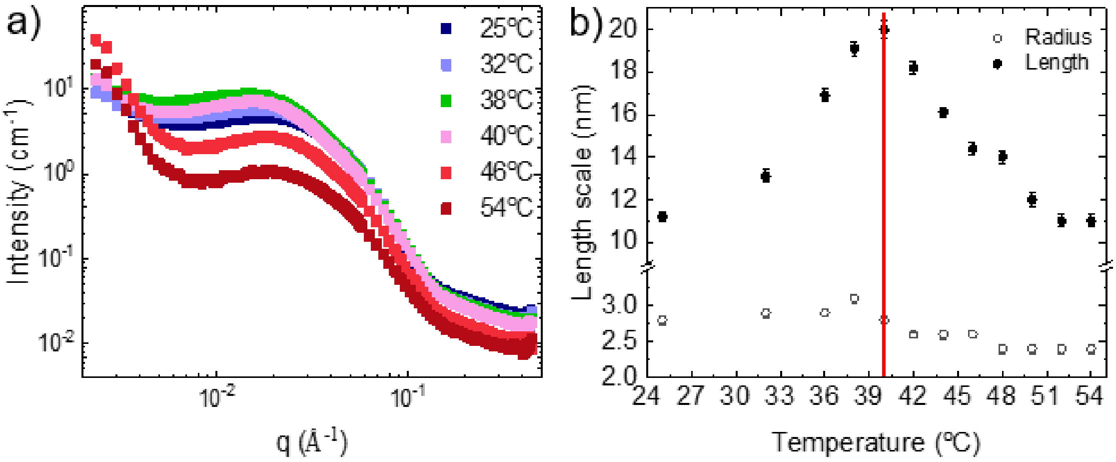

Figure 1.9:
(a) SANS data at selected temperatures. (b) Resulting cylinder radius and length.

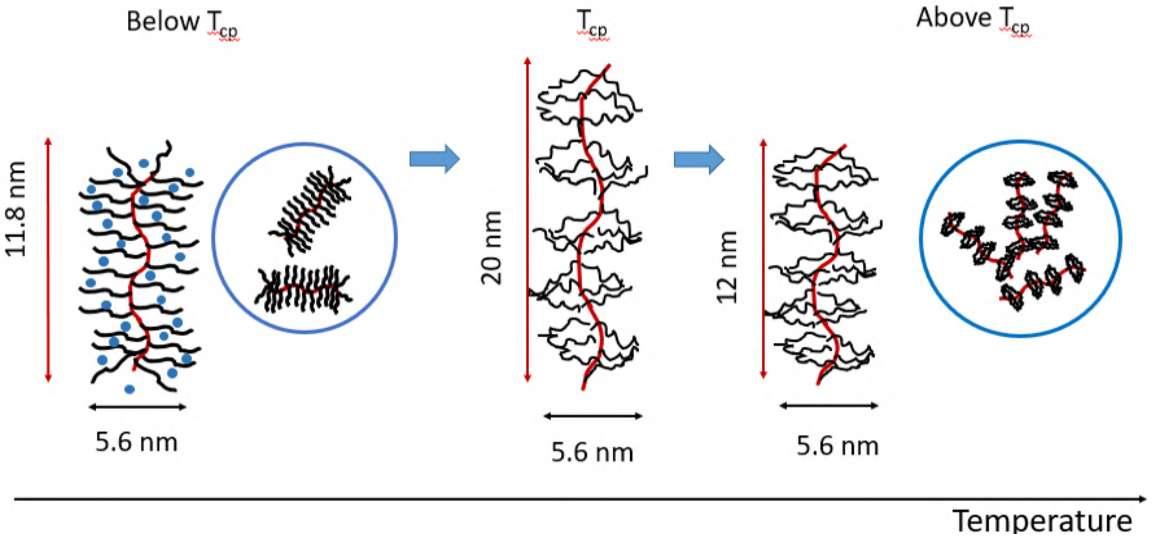

Figure 1.10:
Schematics of the temperature-dependent structural variation.

[1] N. Zhang, S. Huber, A. Schulz, R. Luxenhofer, R. Jordan, *Macromolecules* **42**, 2215-2221 (2009)

1.5 pH dependent microphase separation in thin films from a multiresponsive pentablock terpolymer investigated with GISAXS

F. Jung, M. Schart, E. Meidinger, J.-J. Khang, S. Ariaee[1], D. Posselt[1], H. Amenitsch[2], C. Tsitsilianis[3], C. M. Papadakis

[1] Roskilde University, IMFUFA, Denmark
[2] Graz University of Technology, Austria
[3] University of Patras, Greece

Responsive block copolymer thin films are of interest for many applications, e.g. as fast sensors or switchable membranes [1]. Many of these systems are based on physical hydrogels, where a stimuli-responsive midblock is end-capped by hydrophobic end blocks. In aqueous solution, the end blocks associate and act as crosslinks which are bridged by the midblocks. In non-aqueous solutions, phase separation may occur due to incompatibility between blocks and may lead to morphologies different from the one formed in aqueous environment. Using weak polyelectrolytes (PE) as blocks allows to further tune the segregation behavior. In the case of a cationic PE, the side groups are protonated/ionized at pH values below the dissociation constant, pK_b, and neutral above. The degree of ionization, α, affects the polymers' chain conformation: Large values of α lead to chain stretching due to electrostatic repulsion and to an increased swelling capacity in polar solvents. Moreover, the segregation strength between nonionic blocks and the PE blocks increases with α [2]. This leads to a strong dependence of the microphase separation on the pH value.

In this work, we investigate thin films from the pentablock terpolymer $PMMA_{85}$-*b*-$PDMAEMA_{184}$-*b*-$P2VP_{209}$-*b*-$PDMAEMA_{184}$-*b*-$PMMA_{85}$ (MMA stands for methyl methacrylate, DMAEMA for 2-(dimethylamino)ethyl methacrylate and 2VP for 2-vinylpyridine). Their morphology was studied as a function of the pH value during film preparation using grazing-incidence small-angle X-ray scattering (GISAXS). The volume fractions of the blocks are $\phi_{PMMA} = 0.15$, $\phi_{PDMAEMA} = 0.63$ and $\phi_{P2VP} = 0.23$, which are expected to result in a cylinder morphology [3]. PDMAEMA and P2VP are both cationic PEs with different pK_b values, as shown in Fig. 1.11. At pH values < 5, both blocks are protonated and highly soluble in water. At pH > 5, P2VP becomes non-ionized and hydrophobic, while PDMAEMA becomes non-ionized at pH > 7.8, but remains hydrophilic.

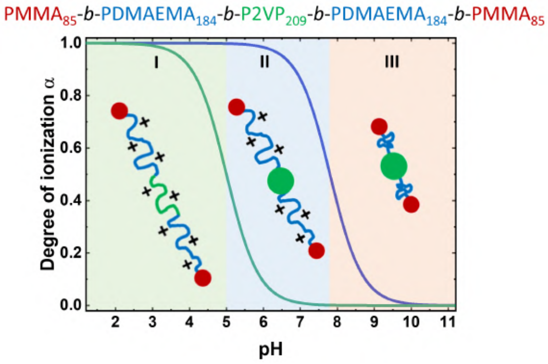

Figure 1.11:
Degree of ionization of P2VP (green line, $pK_b \approx 5.0$) and PDMAEMA (blue line, $pK_b \approx 7.8$) as a function of pH. Three regimes are indicated: regime I: pH < 5; regime II: $5 <$ pH < 7.8; regime III: pH > 7.8. The expected chain conformations in aqueous solution in each regime are shown as well. Red: PMMA, blue: PDMAEMA and green: P2VP.

Films were prepared by spin coating from 3 wt% aqueous solutions of pH 2.1 and pH 4.0 (regime I in Fig. 1.11), pH 5.4 (regime II), and from 2 wt% solutions in methanol (MeOH). MeOH was chosen to obtain the nonionized state (regime III). Film thicknesses of as-prepared films were between 73 nm and 147 nm. Since the preparation parameters, e.g. spin frequency and duration, were kept the same for all films, the differences in film thickness may be due to electrostatic repulsion at large α hindering the deposition of polymers during spinning.

GISAXS measurements were performed at the SAXS beamline at ELETTRA. In Fig. 1.12a, the 2D scattering maps for the different preparation conditions are shown. For pH 2.1, only diffuse scattering around the specular peak is observed, indicating that the film is disordered and not microphase-separated. For pH 4.0, weak scattering peaks appear at small q_y values, which hint at large inhomogeneities in the film. For pH 5.4 and MeOH, Bragg peaks are observed along q_y along with Bragg rods which extend parallel to q_z. The presence of Bragg rods indicates that the cylinders are primarily oriented normal to the substrate. Thus, the films are microphase-separated, and the scattering pattern is attributed to a morphology of hexagonally packed, standing cylinders.

To confirm this initial analysis of the 2D maps and to obtain more quantitative information, horizontal linecuts were made at the specular peak position (Fig. 1.12b). Fits to the scattering curves were performed by a sum of a power law function and a constant background to account for background scattering and a Lorentzian to model the scattering peaks. The curve for pH 2.1 could be fitted without a Lorentzian because it is disordered. For the remaining curves, reasonable fits were obtained, and it was found that the domain spacing is slightly larger in films prepared from MeOH compared to the film prepared from pH 5.4, and that inhomogeneities at pH 4.0 are much larger than the microphase-separated domains.

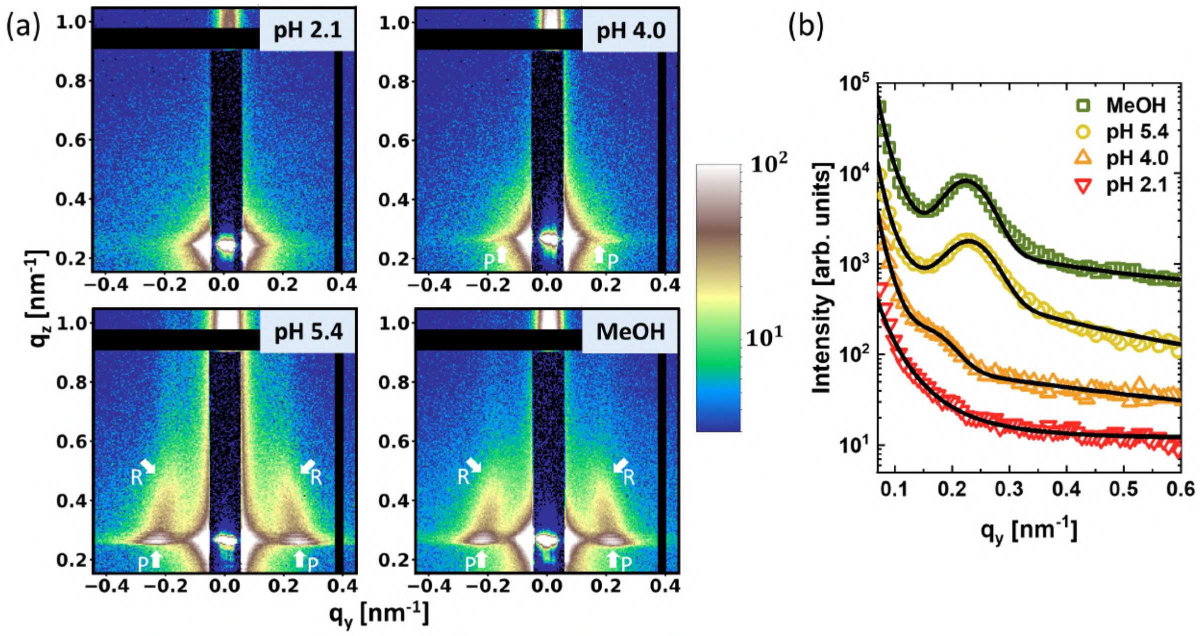

Figure 1.12:
(a) 2D GISAXS maps of films prepared from aqeuous solutions at the pH values indicated and from MeOH. Bragg peaks (P) and Bragg rods (R) are indicated with white arrows.
(b) Horizontal linecuts at the specular peak position (open symbols). Black lines indicate model fits.

The project is funded by Deutsche Forschungsgemeinschaft (DFG).

[1] I. Tokarev, S. Minko, *Soft Matter* **5**, 511-524 (2009)

[2] C. R. Stewart-Sloan, B. D. Olsen, *ACS Macro Lett.* **3**, 410-414 (2014)

[3] H. Liu, C. Huang, A. Shi, *Macromolecules* **48**, 6214-6223 (2015)

1.6 Smart nano-sensors made of stimuli-responsive polymers in thin films

N. Aldosari, L. Kreuzer, J. Pantle, V. Hildebrand[1], A. Laschewsky[1], C. M. Papadakis,
P. Müller-Buschbaum

[1] Universität Potsdam, Potsdam-Golm, Germany

Stimuli-responsive polymers offer a versatile tunable system that can be effectively used in sensor applications. These polymers are able to change their physical or chemical properties in response to an external stimuli such as pH, pressure, magnetic fields and salt concentration [1]. A special subclass of these polymers is thermoresponsive polymers. In solution they can switch from a polymer-polymer favorable interactions regime to a polymer-solvent favorable interactions regime, where they absorb and release large amounts of water upon temperature change. While the swelling behavior of these polymers in solution was previously studied and is reasonably well understood, their behavior in thin films is not completely discerned yet [2]. As we are dealing with thin films, the effects of the substrate and the film's confinement are not negligible and must be taken into consideration when studying such systems. In previous studies it was found that these effects were more pronounced for thin films and are weaker for thicker ones [3].

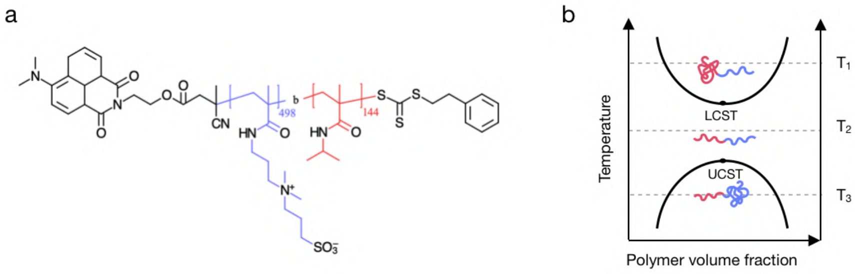

Figure 1.13:
a) Chemical structure of $P(SPP)_{498}$-b-$P(NIPMAM)_{144}$. The PSPP block is colored in blue whereas the PNIPMAM block is colored in red. b) Corresponding phase diagram of $P(SPP)_{498}$-b-$P(NIPMAM)_{144}$ in D_2O.

In our present work, we investigate the cyclic water storage in responsive polymer thin film consisting of a nonionic poly(N-isopropylmethacryylamide) block and a zwitterionic poly(sulfobetaine) block. Its chemical structure is shown in Fig. 1.13. This composition provided a system with both upper critical solution temperature (UCST) stemming from the P(SPP) block and lower critical solution temperature (LCST) behavior coming from the P(NIPMAM) block. For an UCST type behavior, the polymer becomes hydrophilic above this temperature and hydrophobic below it. The opposite is true for a LCST type polymer and this enables the film to swell and collapse as the temperature changes. In the case of our polymer the LCST is higher than its UCST creating an intermediate regime where both polymers can swell. In this work, we study their swelling behavior in thin films using two techniques: Spectral reflectance (SR) and Fourier Transform Infrared spectroscopy (FTIR). Two sets of polymer films on silicon substrates were prepared by two methods: spin coating and drop casting. In addition, the spin coated samples were treated with solvent vapor annealing. This resulted in smooth films with extraordinary homogeneity ideal for observing the swelling behavior using SR. Three temperatures were selected: T_1 above the LCST, T_2 between the LCST and UCST and T_3 below the UCST marked in Fig. 1.13 on the phase diagram. This phase diagram is representative for the polymer in aqueous solution and does not necessarily apply for the polymer in thin film morphology. The swelling behavior in D_2O atmosphere was monitored with SR repeatedly for overall three cycles. The thickness values obtained were fitted to a relative humidity sensitive model developed by Li et al. [3] and modified by Jaczewska [4]. The fit is represented by the red line shown in Fig. 1.14a. The results show high values of swelling ratio for temperatures below the UCST. This deviates from results obtained for the same polymer in solution where the highest swelling ratio was reached at a temperature between the UCST and LCST where both polymers are in the hydrophilic regime [2]. The results also demonstrate the repeatability of the swelling of the invistigated film which is promising for nano-sensor applications.

With FTIR, the changes in the molecular structure of the polymer are studied as the films swells in D_2O atmosphere. For FTIR, we used drop cast samples which produced thicker inhomogeneous films. These films are ideal for FTIR measurements where they maximize the signal (via their increasing thickness) and minimize the interference effects of the film (via their heterogeneity). With this technique the molecular changes of the polymer are measured as D_2O molecules diffuse in the film. A custom-made humidity cell was used where the D_2O reservoir is connected to the sample cell by a narrow tube causing the relative humidity is the sample cell to rise slowly resulting in a total measurement time of almost 7 days. This allowed for an in-situ tracking of the swelling behavior of the block copolymer film. The data prove a repeatable behavior of the D_2O uptake of the film. The deuteration of the polymer film, however, shows an unrepeatable trend. Moreover, it is found that heavy water is rapidly absorbed at the SO_3^- group where it reached roughly its maximum value by the second day whereas changes in other structures are slower and extend over the course of the 7 days of measurement which agrees with previous results.

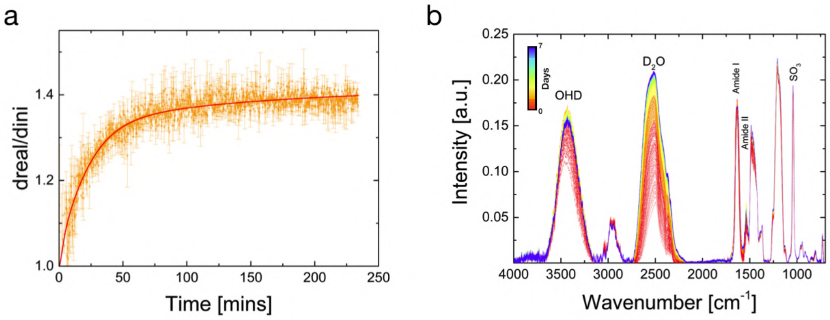

Figure 1.14:
a) Swelling ratio d_{real}/d_{ini} of P(SPP)$_{498}$-b-P(NIPMAM)$_{144}$ as a function of time at temperature T_3 (orange points). The data is fitted with a theoretical model (red line). b) FTIR spectra of P(SPP)$_{498}$-b-P(NIPMAM)$_{144}$ at temperature T_3

In conclusion, using two techniques SR and FTIR, the repeatability of our polymer film swelling behavior is observed. With FTIR, detailed insights about the swelling mechanism on a molecular scale is obtained. These results show that thin polymer films are a very promising candidate for nano-sensor applications.

[1] M. Wei, Y. Gao, X. Li, and M. J. Serpe, *Polymer Chemistry*. **8**, 127 (2017).

[2] N. S. Vishnevetskaya, V. Hildebrand, B.-J. Niebuur, I. Grillo, S. K. Filippov, A. Laschewsky, P. Müller-Buschbaum, and C. M. Papadakis, *Macromolecules*. **50**, 3985–3999 (2017).

[3] Y. Li and T. Tanaka, *The Journal of Chemical Physics*. **92**, 1365 (1990).

[4] J. Jaczewska, I. Raptis, A. Budkowski, D. Goustouridis, J. Raczkowska, M. Sanopoulou, E. Pamuła, A. Bernasik, and J. Rysz, *Synthetic Metals*. **157**, 726 (2007).

2 Thin films

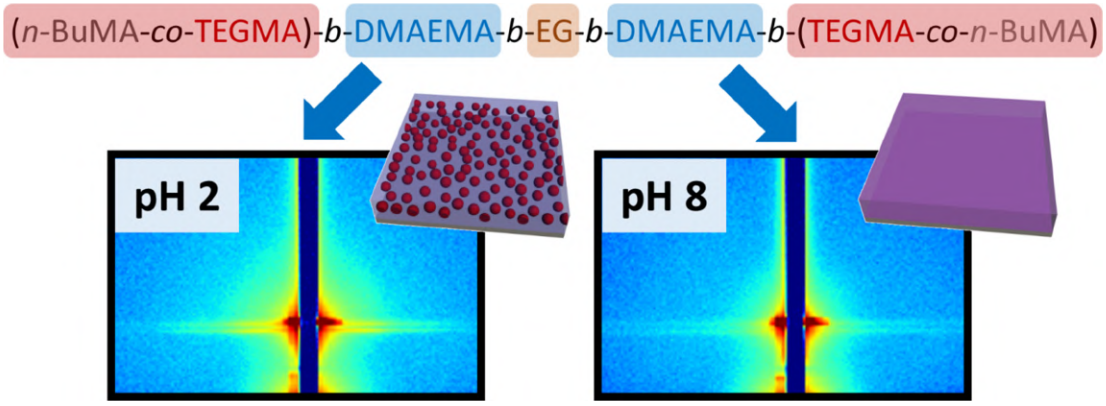

2.1 Self-assembly of large iron oxide nanoparticles in ultrahigh molecular weight linear diblock copolymer films

W. Cao, S. Xia, X. Jiang, M. Appold[1], M. Opel[2], M. Gallei[1], M. Schwartzkopf[3],
S. V. Rot[3,4], P. Müller-Buschbaum

[1] TUD, Darmstadt, Germany
[2] WMI, Garching, Germany
[3] DESY, Hamburg, Germany
[4] KTH, Stockholm, Sweden

Iron oxide nanoparticles (NPs) with diameters (D) of a few to tens of nanometers have attracted much attention in the field of data storage, sensors, catalysis, and biomedicine, because of their intriguing size-dependent magnetic properties [1, 2]. In general, iron oxide NPs become superparamagnetic at room temperature when the size of iron oxide NPs is below about 20 nm. While for large sized iron oxide NPs, the larger the size of the NPs, the higher is throughput and accuracy in bioscreening [1]. Moreover, precise control over their organization is central to improve the performance of next-generation magnetic devices.

Block copolymers (BCPs), which are considered as promising templates for the self-assembly of functional NPs, have gained increasing attention because of their tunability in various periodic nanostructures, such as spheres, cylinders, lamellae, and many other complex assemblies. So far, most studies focused on the self-assembly of magnetic NPs with diameters of no more than 10 nm [2, 3]. In the present work, this limitation is addressed using ultrahigh molecular weight (UHMW) diblock copolymers as templates for the self-assembly of periodic hybrid materials containing large iron oxide NPs ($D = 27.0 \pm 0.6$ nm).

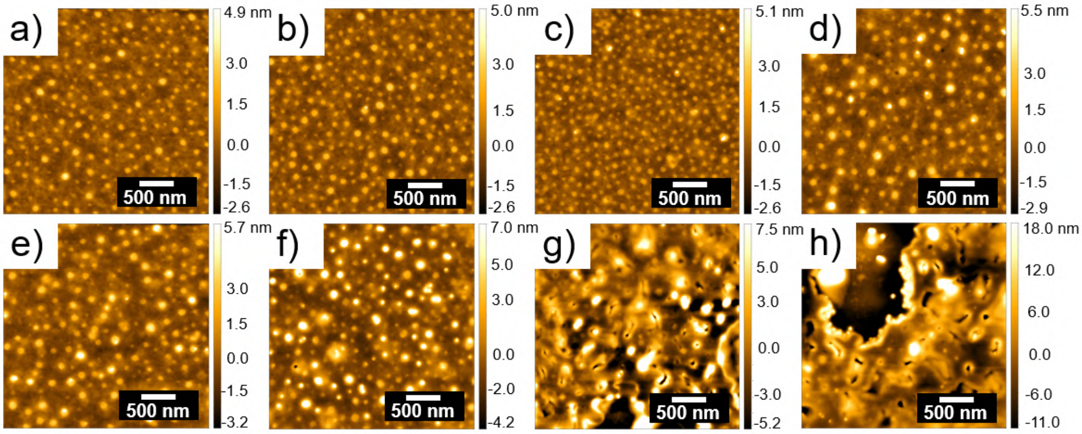

Figure 2.1:
AFM images of hybrid films with increasing iron oxide NP concentrations of a) 0, b) 0.1, c) 0.5, d) 1.0, e) 2.0, f) 5.0, g) 10.0, and h) 20.0 wt%.

To study the film surface morphology on a local scale, all films are investigated by AFM. In Fig. 2.1, the bright domains, dark matrix and white dots are the PMMA, PS and iron oxide NPs, respectively. The NPs are selectively incorporated inside the PMMA cylinders due to the hydrogen bonding between the carboxylic acid groups on iron oxide and the PMMA side chains. Fig. 2.1a presents a relatively ordered cylindrical morphology of a NP-free PS-b-PMMA film, which is obtained from microphase separation during solvent vapor annealing. With NPs added at low concentration (0.1 and 0.5 wt%), the order of the cylindrical structure is improved, especially at the concentration of 0.5 wt% (Fig. 2.1c). However, the PMMA domain size decreases, instead of growth for accommodating NPs. This can be explained by the location of the NPs. As see in Fig. 2.1b and c, they prefer to locate at the interface of PS and PMMA, which leads to the decrease of the PMMA chain sizes to obtain a minimum energy for the hybrid system. As the NP concentration increases from 0.5 to 5.0 wt%, more and more NPs are located in the PMMA domains, which leads to the increase of the PMMA domain size (Fig. 2.1c-f). Most interestingly, when the NP concentration increases to 10 wt%, a chain-like network appears inside the hybrid film (Fig. 2.1g). However, higher NP loading leads to the formation of a discontinuous film (Fig. 2.1h).

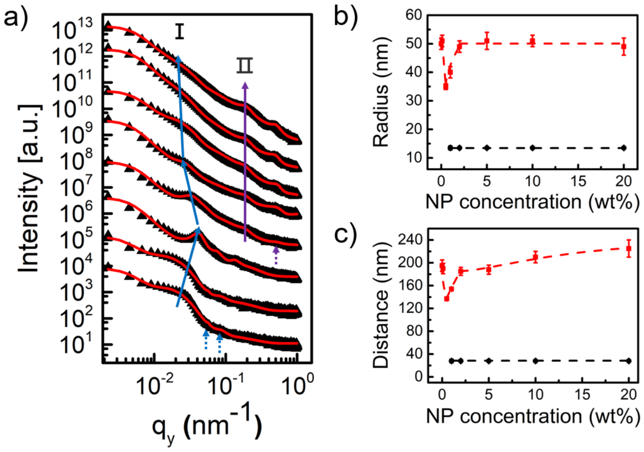

Figure 2.2:
a) Horizontal line cuts obtained from the 2D GISAXS data for hybrid films with different NP concentrations (0, 0.1, 0.5, 1.0, 2.0, 5.0, 10.0 and 20.0 wt% from bottom to top). The solid red lines represent the fits to the data (black dots). Feature structures extracted from the fits are b) the radius and c) the inter-domain distance of the nanostructures. The dashed lines in b)and c) are guides to the eye.

For a quantitative analysis, horizontal line cuts at the Yoneda peak position are performed from the 2D GISAXS data and plotted together with the corresponding fits as shown in Fig. 2.2a. In Fig. 2.2a, two main characteristic structures are observed. They are marked with I and II and correspond to the structure of the PMMA cylinders and iron oxide NPs.
For the NP-free PS-b-PMMA sample, various intensity peaks at relative q positions of 1, $\sqrt{3}$ and 3 times of the main peak (q_y = 0.027 nm^{-1}, denoted as peak I, shown as a solid blue arrow) are observed, which are the characteristic peaks of the hexagonally packed PMMA cylinders in the PS matrix. This peak becomes more prominent, and it moves to higher q_y values with increasing NP concentration until 0.5 wt%, which indicates the formation of higher ordered hexagonal nanostructures with smaller center-to-center distances. With increasing NP concentration from 0 to 0.5 wt%, the domain radius and inter-domain distance, extracted from the peak I, decrease from 50 nm to 35 nm (Fig. 2.2b) and from 195 nm to 137 nm (Fig. 2.2c), respectively. However, as NP concentration further increases, the peak I shifts to lower q_y values and gets less prominent (Fig. 2.2a). The corresponding domain radius and inter-domain distance increase from 35 nm to 50 nm and from 137 nm to 185 nm, respectively. These changes can be explained by the incorporation of NPs inside the PMMA domains, which result in the expansion of the domain size and inter-domain distance. In addition, another broad scattering feature (peak II, shown as a solid purple arrow) with a second-order peak (marked by a dashed purple arrow) is seen in the smaller q_y region at NP concentration $\geq$ 1.0 wt%, which represents the center-to-center distance of the NPs. The corresponding NP radius and distance keep constant at 13.5 nm and 28.0 nm, respectively.

[1] K. Nishio, M. Ikeda, N. Gokon, S. Tsubouchi, H. Narimatsu, Y. Mochizuki, S. Sakamoto, A. Sandhu, M. Abe, H. Handa, *J. Magn. Magn. Mater.* **310**, 2408-2410 (2007)

[2] Y. Yao, E. Metwalli, M. Opel, M. Haese, J. F. Moulin, K. Rodewald, B. Rieger, P. Müller-Buschbaum, *Adv. Mater. Interfaces* **3**, 1500712 (2016)

[3] S. Xia, L. Song, V. Körstgens, M. Opel, M. Schwartzkopf, S. V. Rot, P. Müller-Buschbaum, *Nanoscale* **10**, 11930 (2018)

2.2 Co-nonsolvency-induced constrained swelling of PMMA-*b*-PNIPAM thin films in mixed vapor atmospheres

C. Geiger, C. Henschel[1], L. P. Kreuzer, T. Widmann, A. Laschewsky[1], C. M. Papadakis, P. Müller-Buschbaum

[1] Universität Potsdam, Potsdam-Golm, Germany

Upon heating, the thermo-responsive polymers PNIPAM (poly(N-isopropylacrylamide)) and PNIPMAM (poly(N-isopropylmethacrylamide)) undergo a typical coil-to-globule phase transition in aqueous solution at their specific lower critical solution temperatures (LCSTs) [1]. Looking at the molecular scale, the transition is accompanied by a structural disruption and reordering of solvent molecules around the polymer chain. While water and a variety of different organic compounds individually act as good solvents for PNIPAM and PNIPMAM, when mixed together as solvent and cosolvent, the polymers will precipitate for a certain composition range, which is called co-nonsolvency [2]. The addition of the cosolvent shifts the LCST to lower temperatures.

We investigate the co-nonsolvency behavior of thin films of diblock copolymers comprised of a hydrophobic PMMA (poly(methyl methacrylate)) and a thermo-responsive block in mixed atmospheres of water and volatile organic compounds such as ethanol and acetone. To ensure a consistent quality of films, they are thermally annealed after spin-coating and examined via optical microscopy. Out of a number of different choices, 1,4-dioxane proved to be the best spin-coating agent by far. Rows of profilometric measurements showed an excellent batch film thickness variance of less than $4\,\mathrm{nm}$ at a total film thickness up to several hundred nanometers.

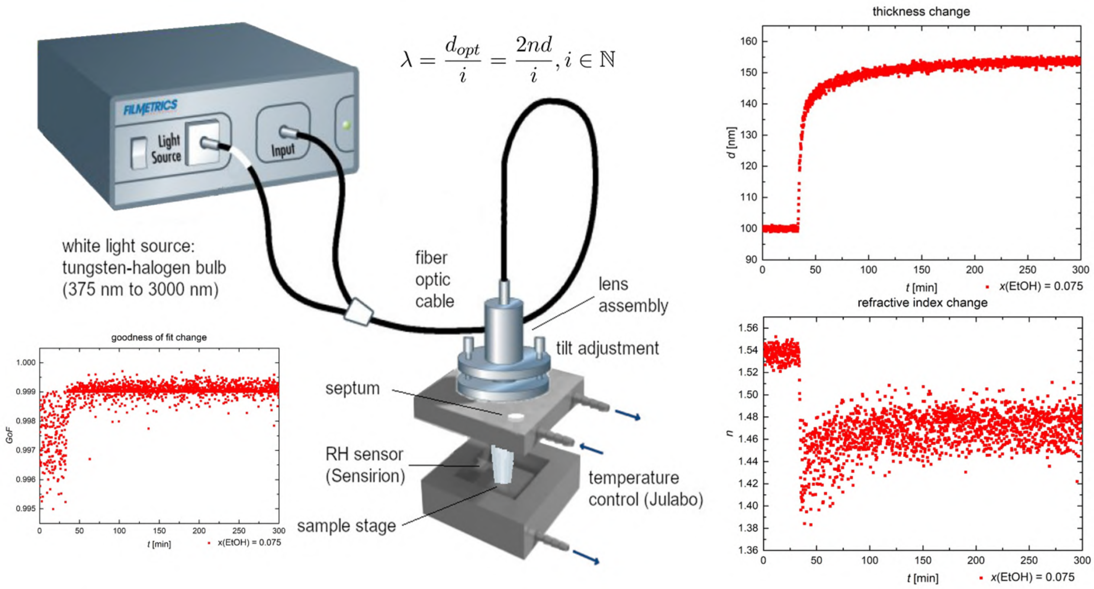

Figure 2.3:
Spectroscopic reflectometry setup. Light is focused onto the thin film (spot size $\varnothing \approx 2\,\mathrm{mm}$, wavelength range $375\,\mathrm{nm} \leq \lambda \leq 3000\,\mathrm{nm}$). The reflected interference signal is recorded. Its characteristic intensity oscillations are used to obtain the optical thickness d_{opt} and fit the films' refractive index n and thickness d.

Fig. 2.3 displays the spectroscopic reflectometry setup used to monitor the films' evolution of thickness d and refractive index n during swelling experiments [3]. Automated measurements allow time resolved data as the mixed vapor atmosphere builds up to an equilibrium from a liquid reservoir around a levelled sample stage in a custom-made chamber. With the diffusion of

solvent and cosolvent into the films, the thickness first rapidly increases, then proceeds to slowly build up or stagnate dependent on the vapor composition. The refractive index coherently drops to smaller values at the incorporation of solvent molecules.
To decouple d and n from the observable d_{opt}, all of the automatically fitted spectra of time-resolved measurements need to consistently exhibit a $GOF \geq 0.995$. The fitting constraints are set to constant values for all measurement rows inside an experiment in order to achieve a comparable standard.

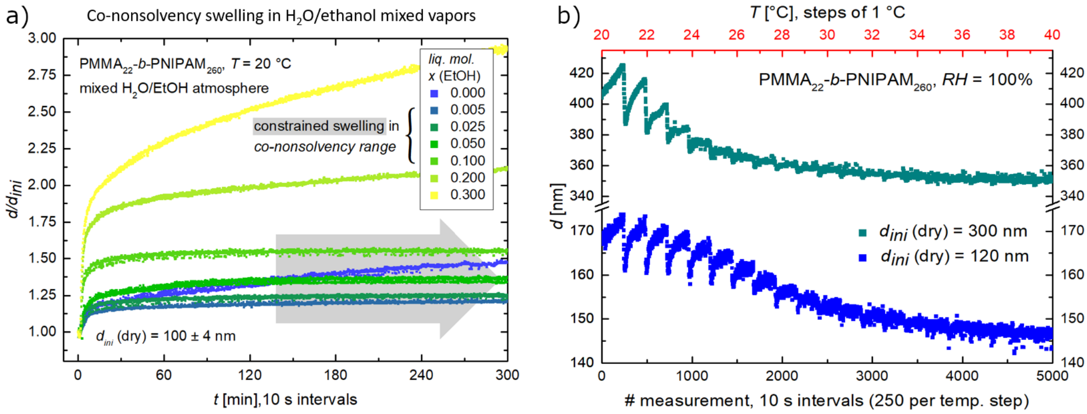

Figure 2.4:
a) H_2O/ethanol mixtures of different molar ratios causing different swelling behaviors of dry films in and outside of the co-nonsolvency range (drying achieved after 2 h exposure to N_2 flow). b) Thermo-response of ready-swollen films (after 2 h in saturated H_2O vapor).

Results from swelling experiments with thin films from PMMA$_{22}$-*b*-PNIPAM$_{260}$ (DP_n according to ^{1}H-NMR) are shown in fig. 2.4. Graphs a) and b) respectively demonstrate a vapor-induced co-nonsolvency behavior and a thickness-dependent thermo-response of this particular block copolymer thin film system.
The co-nonsolvency effect is observed as constrained swelling. The relevant vapor compositions derived from the liquid molar ratios are in accordance with the co-nonsolvency-relevant molar ratio range of mixed solvent/cosolvent polymer solutions. It is worth mentioning that the vapor composition cannot be directly measured due to the cross sensitivity of commercial sensors. However, it can be calculated via the liquid-vapor equilibrium ratio using the Antoine equation and the NRTL (non-random two liquid) empirical model for non-ideal binary mixtures. [4]
To examine their thermo-response, already swollen films are heated in steps of 1 °C every 40 min. Switch-like contraction and water expulsion followed by temperature-dependent re-swelling happen at each step. Throughout the duration of the entire experiment, contraction kinetics always happen at a significantly faster timescale than the swelling kinetics. The envelope shape function of the overall thin film contraction strongly depends on the initial film thickness d_{ini} in the dried state. To collect more information about inner morphology changes, selectivity to solvent and cosolvent, diffusion speeds and concentration gradients, the films will be characterized by neutron reflectometry.

[1] Y. Okada, F. Tanaka, *Macromolecules* **38**, 4465-4471 (2010)

[2] F. Tanaka, T. Koga, I. Kaneda, F. M. Winnik, *J. Phys.: Condens. Matter* **23**, 284105 (2011)

[3] D. Magerl, M. Philipp, X.-P. Qiu, F. M. Winnik, P. Müller-Buschbaum, *Macromolecules* **48**, 3104-3111 (2015)

[4] B. Hadrich, N. Kechaou, *J. C. C. E.* **31**, 46-48 (2010)

2.3 Swelling behavior and structural properties of a pH and temperature responsive telechelic pentablock copolymer in thin films

F. Jung, P. A. Panteli[1], D. Posselt[2], D.-M. Smilgies[3], C. Tsitsilianis[4], C. S. Patrickios[1], C. M. Papadakis

[1] University of Cyprus, Nicosia, Cyprus
[2] Roskilde University, IMFUFA, Denmark
[3] Cornell University, Ithaca, NY, USA
[4] University of Patras, Patras, Greece

Stimuli responsive block copolymers strongly change their properties upon a change of the environment and may be used for tissue engineering or for drug delivery [1]. In thin films, they find use as fast sensors or switchable membranes. Many of these systems are based on physical hydrogels, where a stimuli-responsive midblock is end-capped by hydrophobic end groups. In aqueous solution, the end blocks associate and act as crosslinks which are bridged by the midblocks. The dynamics of the gel can be tuned by using temperature-responsive polymers as end blocks [2]. In thin films, a responsive midblock, e.g. a polyelectrolyte which is pH-responsive, may be used to tune the self-assembly process, while a temperature change may be used to immobilize the end blocks and to freeze the so created nanostructure. The latter feature is especially interesting for solvent vapor annealing (SVA), which is a versatile technique to improve long-range order in polymer thin films and alter its morphology, but with the drawback that non-equilibrium morphologies are often difficult to preserve during solvent removal [3].

In the present work, thin films from the telechelic pentablock terpolymer P(n-BuMA$_8$-*co*-TEGMA$_8$)-*b*-PDMAEMA$_{50}$-*b*-PEG$_{46}$-*b*-PDMAEMA$_{50}$-*b*-P(n-BuMA$_8$-*co*-TEGMA$_8$) were investigated in-situ during SVA using grazing-incidence small-angle X-ray scattering (GISAXS). The endblocks are statistical copolymers of the thermoresponsive TEGMA (triethylene glycol methyl ether methacrylate) and the hydrophobic n-BuMA (n-butyl methacrylate). Increasing the temperature increases their hydrophobicity and thus leads to a reduced mobility. The intermediate PDMAEMA poly(2-(dimethylamino)ethyl methacrylate) block is a weak cationic polyelectrolyte, which becomes ionized at low pH values. PEG stands for poly(ethylene glycol) and is hydrophilic. Films were prepared via spin coating from aqueous solutions of different pH values, which led to film thicknesses between 50-60 nm, measured with a spectral reflectance device. Fig. 2.5a shows the swelling behavior of films prepared at pH 1.9 (PDMAEMA is fully ionized) and pH 8.1 (PDMAEMA is weakly ionized) during SVA using both water and toluene vapor. Water is a polar solvent and expected to dissolve PDMAEMA and PEG, while toluene is nonpolar and expected to dissolve the endblocks and the non-ionized PDMAEMA. This leads to a strong dependence of the swelling ratio on the pH value, as can be seen in Fig. 2.5b: Films prepared at low pH swell significantly in water, but poorly in toluene, since the latter does not dissolve the ionized PDMAEMA. Increasing the pH reduces the water uptake and strongly increases the swelling capability in toluene.

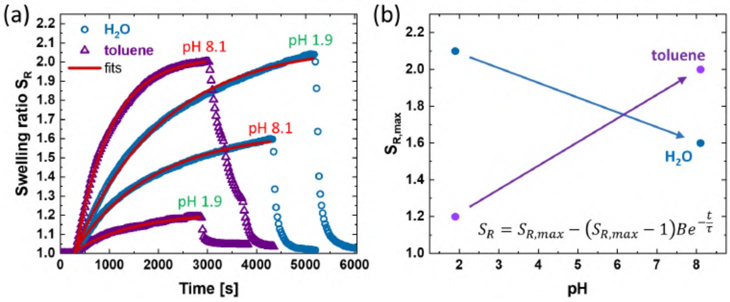

$$S_R = S_{R,max} - (S_{R,max} - 1)Be^{-\frac{t}{\tau}}$$

Figure 2.5:
(a) Swelling ratio, S_R, of films prepared at pH 1.9 and pH 8.1 during SVA in water (blue circles) and toluene (purple triangles). Red lines are fits of exponentials. (b) Maximum swelling ratio, $S_{R,max}$, obtained from the fits shown in (a). Arrows are guides to the eye.

In situ GISAXS investigations during SVA were performed at beamline D1 at CHESS, and an overview of the results is shown in Fig. 2.6. To extract morphological information, horizontal linecuts along the Yoneda peak were fitted assuming a morphology of spherical objects distributed on a radial paracrystal. Fits were performed in the framework of the DWBA using the Born Again software package. Films prepared at pH 1.9 feature spheres with radii between 7.6-7.9 nm (Fig. 2.6a,b). During swelling in water vapor, R_{sphere} increases, and the film becomes disordered at high swelling ratios. After drying, spheres are reformed and R_{sphere} is slightly larger than before SVA. Swelling in toluene slightly reduces R_{sphere} but does not lead to significant morphological changes. Films prepared at pH 8.1 are initially disordered, which indicates that a certain degree of ionization of PDMAEMA is necessary in order for microphase separation to occur (Fig. 2.6c,d). During swelling in water vapor, the film remains disordered throughout the complete annealing cycle, in agreement with the results from lower pH (Fig. 2.6a). Films swollen in toluene feature small spheres with R_{sphere} of 5.4 nm, which is unstable during drying, where the film becomes disordered again. Therefore, assuming that both PDMAEMA at pH 8.1 and the copolymer endblocks are soluble in toluene, while PEG is insoluble in toluene, it may be concluded that at pH 1.9 spheres are formed by the copolymer endblocks and microphase separation is driven by their incompatibility with the ionized PDMAEMA matrix, while at pH 8.1, spheres are formed by PEG during swelling in toluene due to its incompatibility with the solvent.

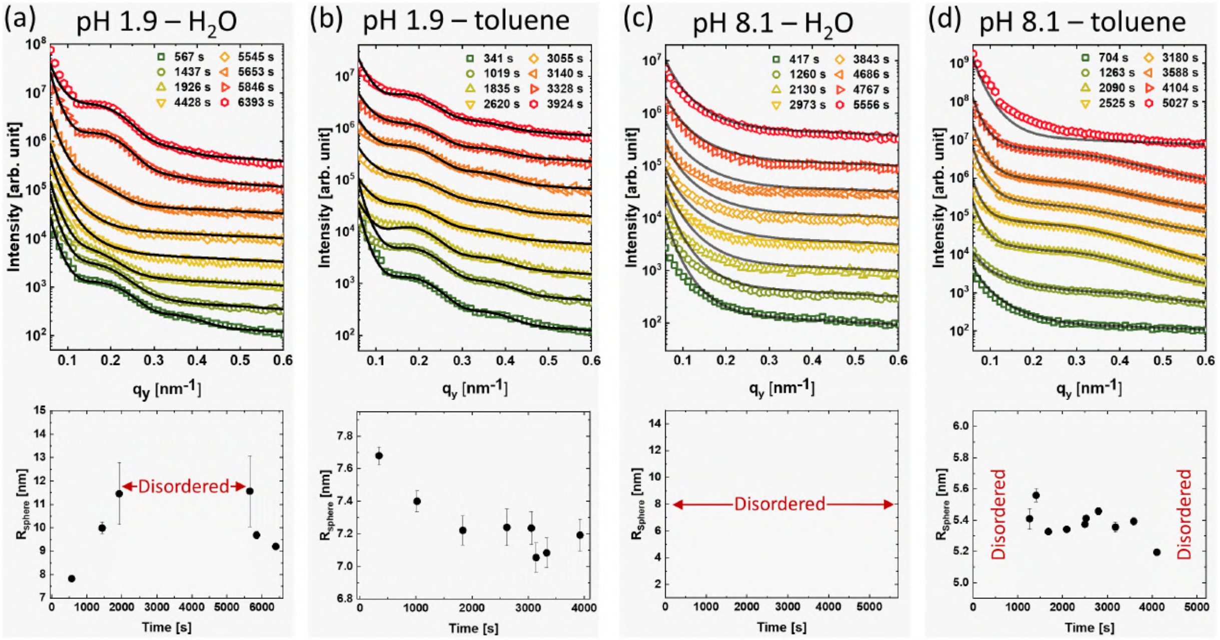

Figure 2.6:
Overview of in situ GISAXS experiments: (a) pH 1.9 swollen in H_2O; (b) pH 1.9 swollen in toluene; (c) pH 8.1 swollen in H_2O; (d) pH 8.1 swollen in toluene. Top row: horizontal linecuts along the Yoneda peak (open symbols) at specific times corresponding to Fig. 2.5a. Black lines indicate best fits to the data assuming a morphology of spherical objects distributed on a radial paracrystal. Bottom row: sphere radius obtained from the fits.

The project is funded by Deutsche Forschungsgemeinschaft (DFG).

[1] C. Tsitsilianis, *Soft Matter* **6**, 2372-2388 (2010)

[2] C. Tsitsilianis, C. Ko, F. Jung, C. S. Patrickios, C. Papadakis, et al. *Macromolecules* **51**, 2169-2179 (2018)

[3] A. V. Berezkin, F. Jung, D. Posselt, D.-M. Smilgies, C. M. Papadakis, *Adv. Funct. Mater.* **28**, 1706226 (2018)

2.4 Facile optimization of thermoelectric properties in PEDOT:PSS thin films through acido-base and redox dedoping using readily available salts

N. Saxena, J. Keilhofer, A. K. Maurya, G. Fortunato[1], J. Overbeck[2], P. Müller-Buschbaum

[1] Empa, St. Gallen, Switzerland

[2] Swiss Nanoscience Institute, Basel, Switzerland

Waste heat occurs in all processes found in daily life, such as in the human body, car engines, power plants, etc. This heat is usually emitted into the environment and thus is rendered useless for all intents and purposes. Since a large amount of energy is lost in this fashion, one can think about methods which allow for making it usable again. Using thermoelectricity, which allows for the transformation of a temperature gradient along a thermoelectric material into electrical power, will allow this.

The Seebeck effect describes the flow of charge carriers in a material along a temperature gradient due to diffusion. This leads to an accumulation of charges at the cold end and to a deficiency of charges at the hot end, ultimately resulting in an electrical potential. This potential in turn forces part of the charges in the direction opposite to the temperature gradient due to drift. The resulting effective potential is commonly termed thermovoltage, since its magnitude depends on the magnitude of the temperature gradient. Other quantities that determine the efficiency of a thermoelectric material are on the one hand the electrical conductivity, which describes the ability of charges to travel through the material, and the thermal conductivity which describes the ease of maintaining a temperature gradient. Only if a temperature gradient is present, electrical power can be harvested.

Common thermoelectric materials mostly comprise heavy elements such as bismuth, tellurium, lead, etc. While these compounds often show promising thermoelectric conversion efficiencies, the often found toxicity, rarity, high cost and difficulty in processing of these elements has impeded a large-scale implementation of thermoelectric devices for energy generation in daily life. In an alternative approach, we make use of conducting polymers as promising candidates for thermoelectric materials. Some of the advantages include the environmentally friendly materials, which are mostly carbon-based, and due to the dispersability in solvents, also the possibility for economic and easy large-scale processing through methods such as printing or spray-coating. Among the many different conductive polymers, poly(ethylene dioxythiophene):poly(styrene sulfonate) (PEDOT:PSS) has attracted great attention in the research community to its promising properties regarding optical semi-transparency, environmental aspects, since water can be used as a solvent and potentially high electrical conductivity. Especially the high electrical conductivity, which approaches that of inorganic semiconductors, renders this material interesting for thermoelectric application.

This, however, poses some problems with respect to the thermoelectric capabilities of PEDOT:PSS. The high electrical conductivity is a result of its intrinsic electronic properties. For the PH1000 formulation of PEDOT:PSS, a ratio of 1:2.5 is given by the manufacturer, which is such that the charge carrier concentration on conducting PEDOT chains is very high. While this allows for the high electrical conductivities, observed after appropriate treatments of thin films, it is also responsible for low Seebeck coefficients. The counteracting dependency of Seebeck coefficient and electrical conductivity on the charge carrier concentration is already known from inorganic thermoelectrics, and in this case limits the applicability of PEDOT:PSS for thermoelectric applications.

Herein, easily available inorganic salts with acido-basic or redox properties are used to reduce the charge carrier concentration in PEDOT:PSS, in order to achieve an optimization of the thermoelectric power output. Among these are sodium hydrogencarbonate, sodium sulfite and

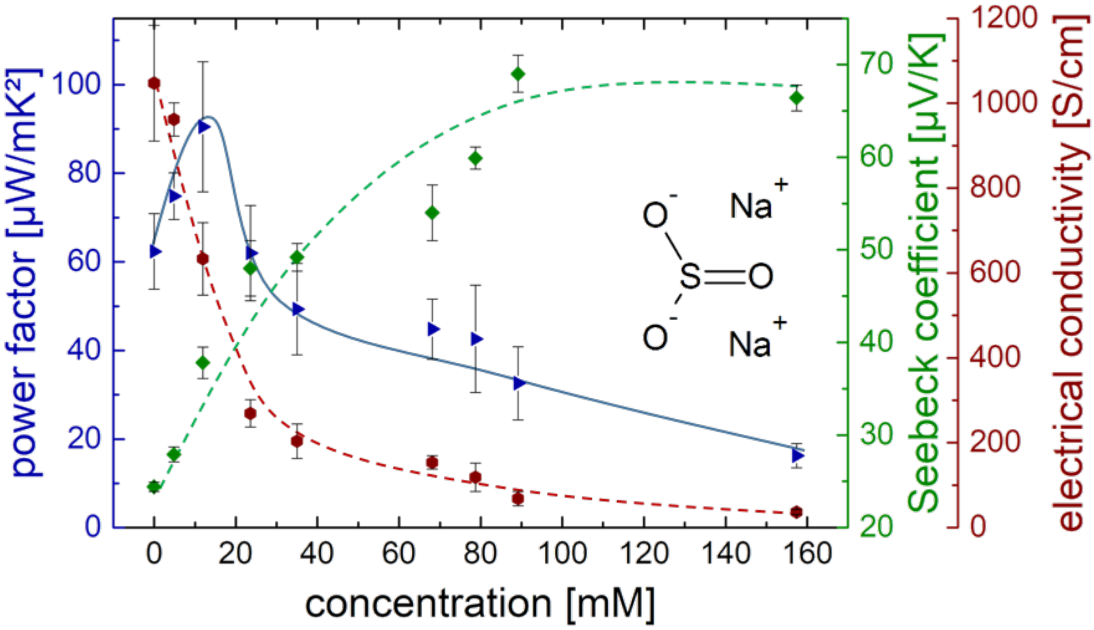

Figure 2.7:
Thermoelectric parameters of PEDOT:PSS thin films dedoped with different concentrations of sodium sulfite. Seebeck coefficients are shown in green, electrical conductivities in brown and power factors in blue. Dashed lines serve as guides to the eye.

sodium borohydride, out of which the results of the dedoping with sodium sulfite are exemplarily shown in Fig. 2.7. Dedoping is achieved by preparation of aqueous solutions of sodium sulfite and mixing different amounts directly with the PEDOT:PSS solution prior to film fabrication using spin-coating. The films are then post- treated with ethylene glycol, in order to cause rearrangement of the structure and lead to high electrical conductivities.
Indeed, treatment with the salt leads to a release of electrons and a subsequent increase of the Seebeck coefficient due to loss of charge carriers, which levels off for high concentrations of dedopant. Consequently, the electrical conductivity drops due to the same effect. However, this effectively leads to a maximum in the power factor, yielding values up to $95\ \mathrm{W\,K^{-2}m^{-1}}$. Similar effects are also seen for the other used salts.
UV-Vis spectroscopy reveals the mechanism to be the transition of bipolaronic states, which are present in pristine PEDOT:PSS, to polaronic and neutral states, being in conjunction with the observed loss in electrical conductivity. X-ray photoelectron spectroscopy (XPS) is used to get an indication of the average oxidation level of the sulfur in PEDOT, which is reduced after dedoping with the redox-active sodium sulfite and sodium borohydride. In Raman spectroscopy, a transition from the quinoid state of PEDOT, in which the chains possess an extended-coil or linear conformation, to the benzoid state, in which the chains possess a more coil-like conformation. All these effects support the notion of loss of charge carrier concentration being responsible for the enhancement of thermoelectric power output. Thus, this study opens a new window of tunability in PEDOT:PSS,

[1] N. Saxena, J. Keilhofer, A. K. Maurya, G. Fortunato, J. Overbeck, P. Müller-Buschbaum, *ACS Appl. Energy Mater.* **1**, 336 – 342 (2018)

2.5 Post-treatment of thermoelectric polymer thin films with ionic liquids

A.-L. Oechsle, N. Saxena, P. Müller-Buschbaum

In times of increasing energy consumption, climate change and shortage of resources, it is of immense importance for our future to find alternative ways to produce energy. Renewable energy sources are already commonly used as in solar and wind power. However, beneath these techniques it is also important to reduce the waste of energy.

Nearly all processes in our daily life generate heat as a byproduct that dissipates into the environment and therefore cannot be further used as energy. In every engine, electronic device, bad insulated building or even the human body a significant amount of energy is lost as so called waste heat. Thermoelectric generators provide a very promising way to convert this waste heat back into useable energy.

In thermoelectric materials a temperature gradient leads to the diffusion of charge carriers from the hot side to the cold side, resulting in a deficit respectively accumulation of charges, and therefore an electrical potential. This conversion of a temperature gradient directly into electrical power is described by the Seebeck effect.

So far, typically used thermoelectric materials contain heavy elements for example bismuth, tellurium and lead. These inorganic materials normally provide good efficiencies, but are rare, toxic, expensive and difficult to process. Therefore, our research is focused on organic conductive polymers as thermoelectric materials. These own some advantages like low or no toxicity, lightweight, flexibility, low cost and solution based processability, which would allow a large-scale implementation. However, up to now they cannot compete with the thermoelectric efficiencies of inorganic materials.

An often used parameter to gauge the thermoelectric properties of a material is the so called power factor $PF = S^2\sigma$, which depends on the Seebeck coefficient (S) and the electronic conductivity (σ). Hence, to improve the thermoelectric efficiencies of a conductive polymer these two values have to be increased by enhancing its electronic and morphological features. In general, there are two ways to do so, namely primary and secondary doping.

Primary doping describes the change of the oxidation state and therefore the variation of the number of charge carriers. It can be achieved for example by acido-based or redox doping with inorganic salts [1]. An increasing charge carrier amount in the polymer, increases the conductivity, but decreases the Seebeck coefficient. This inverse relation is due to the rise of the electric field with increasing σ that causes a drift current converse to the diffusion current from the hot to the cold side.

Secondary doping however relates to a permanent change of the morphological structure within the polymer and can be achieved for example by polar solvents [2]. Structural changes within the conductive polymer mainly influence the electrical conductivity but have nearly no effect on the Seebeck coefficient.

Consequently with these methods only one of the two parameters σ or S can be enhanced, while the other stays constant or even decreases.

In this work, we use the conductive polymer PEDOT:PSS (poly(ethylene dioxythiophene):poly(styrene sulfonate)) to fabricate thin thermoelectric films. In order to enhance its thermoelectric properties we followed the approach to post-treat the films with ionic liquids. Ionic liquids have been seen to possess both, primary and secondary doping effects and therefore are able to improve S as well as σ [3]. In our case the PEDOT:PSS thin films were post-treated with different concentrated solutions of the ionic liquid EMIM-DCA (1-ethyl-3-methylimidazolium dicyanamide) in THF (tetraydrofuran).

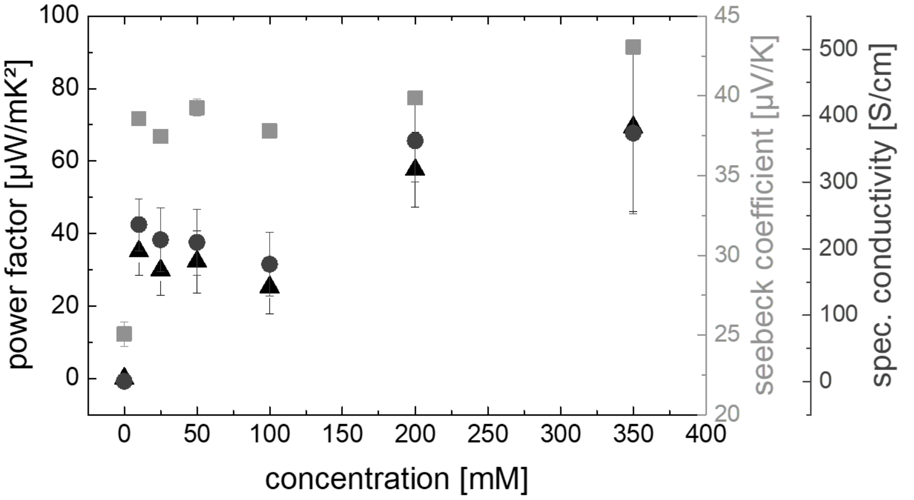

Figure 2.8: Seebeck coefficient (■), specific conductivity (•) and calculated power factor (▲) of PEDOT:PSS thin films post-treated with different concentrations of EMIM-DCA in THF.

After a washing step with THF to remove excess of ionic liquid, the Seebeck coefficient, electrical conductivity, T-dependent resistance and UV-Vis spectra of the films were measured. Fig. 2.8 shows, that upon post-treatment with EMIM-DCA the Seebeck coefficient and the conductivity increase, and therefore the calculated power factor also increases.

These results indicate that EMIM-DCA has a primary and secondary doping effect on PEDOT:PSS. In the UV-Vis spectra, shown in Fig. 2.9 a) it can be observe that neutral (N) and polaronic (P) states are formed with increasing EMIM-DCA concentration. Hereby the reduction of PEDOT by the DCA anions is revealed and therefore its influence on the electronic state (primary doping). Furthermore, the T-dependent resistance behavior changes upon post-treatment with EMIM-DCA, see Fig. 2.9 b). PEDOT:PSS without ionic liquid treatment shows a resistance decrease with increasing T, which indicates a conductivity primary due to T-activated hopping of charge carriers between the PEDOT domains. After post-treatment with EMIM-DCA the samples show a more metallic conductivity behavior. This can be related to the interaction of the EMIM cation with the PSS and therefore a structural change (secondary doping).

In conclusion, the thermoelectric properties of PEDOT:PSS were successfully improved by post-treatment with the ionic liquid EMIM-DCA, due to primary and secondary doping.

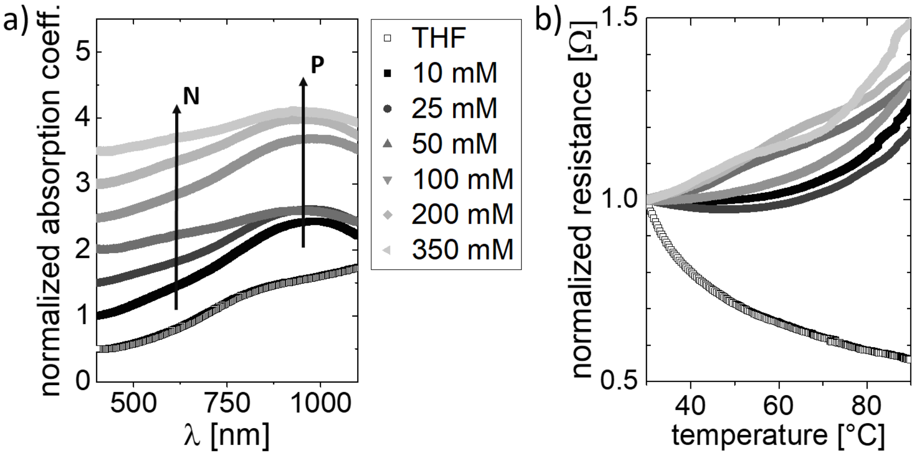

Figure 2.9: a) Normalized UV-Vis spectra and b) temperature dependent resistance of PEDOT:PSS thin films post-treated with different concentrations of EMIM-DCA in THF.

[1] N. Saxena, J. Keilhofer, A. K. Maurya, G. Fortunat, J. Overbeck, P. Müller-Buschbaum, *ACS Appl. Energy Mater.* **1**, 336-342 (2018)

[2] S. Liu, H. Deng, Y. Zhao, S. Ren, Q. Fu, *RSC Adv.* **5**, 1910-1917 (2015)

[3] J. Luo, D. Billep, T. Waechtler, T. Otto, M. Toader, O. Gordan, E. Sheremet, J. Martin, M. Hietschold, D. R. T. Zahn, T. Gessner, *J. Mater. Chem. A* **1**, 7576-7583 (2013)

2.6 Watching metal nanolayer growth on functional polymer thin films for lithium-ion battery applications

S. J. Schaper, F. C. Löhrer, S. Xia, M. Schwartzkopf[1], P. Pandit[1], A. Hinz[2], O. Polonskyi[2], T. Strunskus[2], F. Faupel[2], S. V. Roth[1,3], P. Müller-Buschbaum

[1] DESY, Hamburg, Germany
[2] CAU, Kiel, Germany
[3] KTH, Stockholm, Sweden

Understanding the interface between metals, commonly used as contacts and current collectors, and (ion-)conducting polymers used in organic electronics, organic photovoltaics and polymer lithium-ion batteries (LIBs) is crucial to develop highly reproducible, low-cost and reliable devices. To address these issues, sputter deposition is the technique of choice to fabricate scalable, reproducible, and controllable nanometer and sub-nanometer metal layers on polymer thin films. The sputter deposition process, being well understood and controlled, offers advantages over chemical methods to tailor metal thin-film morphologies on the nanoscale and offers a superior adhesion of the deposited material.[1] In-situ grazing-incidence small-angle X-ray scattering (GISAXS) is used to investigate the formation, growth, and self-assembled structuring on polymer thin films. To exceed the limits of the polymer LIBs unexploited development the deposition and infiltration of sputtered metals onto the polymer thin film needs to be understood.

The diblock copolymer (DBC) polystyrene-block-poly(ethylene oxide) (PS-*b*-PEO) is one of the most promising materials for solid state polymer LIBs. The rigid PS block provides mechanical stability while the soft and ion-conducting PEO block enables Li-ion's migration between the electrodes. Due to the covalent bond between the hydrophobic PS and the hydrophilic PEO block of the PS-*b*-PEO DBC undergoes a microphase separation creating a self-assembled structure in the nanoscale, which can prevent the lithium-dendrite's growth leading to a shortcut in LIBs.

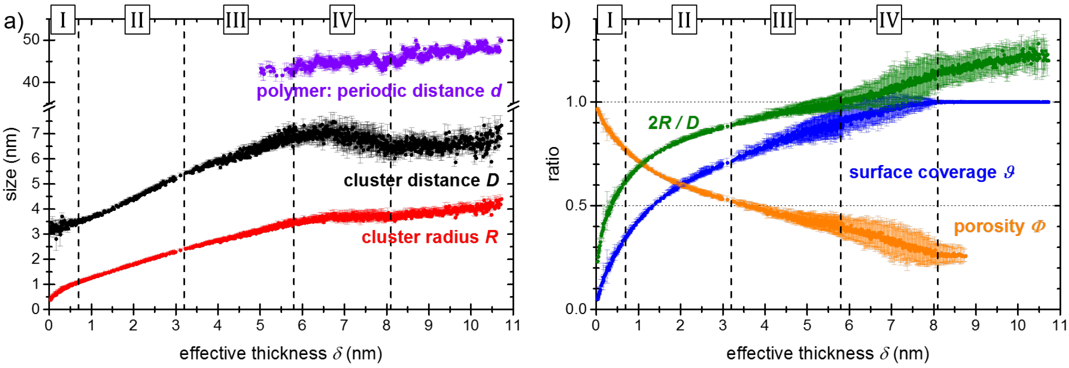

Figure 2.10:
In-situ GISAXS sputter deposition of copper on PS-*b*-PEO DBC thin films: a) Extracted parameters polymeric periodic distance d, cluster distance D and cluster radius R, and b) calculated ratio of $\frac{2R}{D}$, surface coverage θ and porosity ϕ of the deposited copper plotted versus the effective film thickness δ, respectively.

The samples under investigation are 90 nm thin, bare PS-*b*-PEO DBC films on acid-cleaned silicon substrates prepared via spin coating at 2000 rpm from 10 mg ml^{-1} solution with CHCl$_3$ as solvent. Subsequently the samples were solvent annealed with CHCl$_3$. The in-situ GISAXS measurements during sputter deposition of copper nanolayers were done at the beamline P03 at DESY in Hamburg using a DC magnetron sputter chamber. In GISAXS measurements the incoming X-rays with an energy of 13 keV impinge on the sample with an incident angel of 0.4°, while the scattered inetsity is collected with a Pilatus 300k detector at a sample-detector distance of 2.305 m. The 2D GISAXS data is analyzed with vertical line cuts at q_y = 0 to extract the effective film thickness δ and horizontal line cuts at the position of the Yoneda peak to extract the copper cluster distance D and the periodic distance of the PS-*b*-PEO DBC d, respectively. The final thickness of the copper layer is calculated to 10.72±0.11 nm from the intensity modulation along the q_z direction, since the metal layer grows with correlated roughness on the polymer film. As the sputter rate is constant, the effective thickness δ is calculated from the final average copper nanolayer thickness and duration of the sputter process. The evolution during the sputter deposition of D, d and the cluster radius R, which is calculated using a slightly modified model by Schwartzkopf et al.[3] is shown in Fig. 2.10a. Fig. 2.10b shows the calculated ratio of $\frac{2R}{D}$, the surface coverage θ, and porosity ϕ of the deposited copper nanolayer plotted versus the effective film thickness δ.

Taking a closer look at the extracted parameters one can distinguish different stages in the growth mechanism of a copper layer on a the PS-*b*-PEO DBC thin film until a completely covered surface is reached at about $\delta = 8.1$ nm: (I) A nucleation phase until $\delta = 0.7$ nm, where the first copper atoms form small metal clusters which are rapidly growing on the polymer surface while their mean distance to each other stays constantly small. (II) A diffusion driven growth (0.7 nm$< \delta < 3.2$ nm) where the single copper clusters merge on the surface increasing their mean distance D faster than their own radius R. (III) A more adsorption-driven growth (3.2 nm$< \delta < 5.8$ nm) of the clusters where the surface coverage θ has reached values above 70 % and the porosity ϕ is lower than 50 %. Also the increase in the cluster distance D slows down due to the increasing immobilization of the clusters while the cluster radius R is still growing constantly. (IV) At $\delta = 5.8$ nm the percolation threshold is reached meaning the single copper clusters touch each other forming a percolating network providing paths for electrons over the whole surface. The single clusters serve as grains for the growth of the copper layer while the underlaying lateral structure persists. At an effective thickness $\delta = 8.1$ nm the surface is completely covered according to the applied model. The porosity ϕ still stays at about 26% indicating a rough surface of the copper layer. A model describing this growth mechanism is shown in Fig. 2.11.

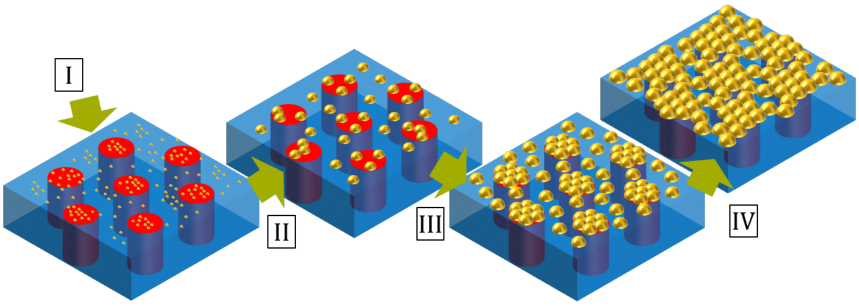

Figure 2.11:
Simplified model for the formation of a copper nanolayer on a PS-*b*-PEO DBC thin film depicting four different stages and a selective growth on the PS domain: (I) nucleation phase, (II) diffusion driven growth, (III) adsorption-driven growth ,and (IV) grain growth.

Concluding, the formation of a copper nanolayer using DC magnetron sputter deposition on a PS-*b*-PEO DBC thin film is not a layer by layer deposition process, but a far more complex growth of clustering metal atoms with different stages. The deposition of only 5.8 nm of copper already forms a percolating metal network on the polymer surface and the sputter deposition of 8.1 nm covers the surface completely.

[1] F. Faupel, V. Zaporojtchenko, T. Strunskus, M. Elbahri, *Adv. Eng. Mater.* **12**, 1177-1190 (2010)

[2] M. Schwartzkopf, A. Hinz, O. Polonskyi, T. Strunskus, F. C. Löhrer, V. Körstgens, P. Müller-Buschbaum, F. Faupel, S. V. Roth, *ACS Appl. Mater. Interfaces* **9**, 5629-5637 (2017)

[3] M. Schwartzkopf, A. Buffet, V. Körstgens, E. Metwalli, K. Schlage, G. Benecke, J. Perlich, M. Rawolle, A. Rothkirch, B. Heidmann, G. Herzog, P. Müller-Buschbaum, R. Röhlsberger, R. Gehrke, N. Stribeck, S. V. Roth, *Nanoscale* **5**, 5053-5062 (2013)

2.7 Exploring the possibilities of PNIPAM microgel films as humidity sensors

T. Widmann, M. Mörtl, P. Müller-Buschbaum

Humidity is the presence of water vapor in the air and has a significant role for life, industry and science. Observing humidity is important for weather forecast, optimization of industrial or experimental processes or just to keep pleasant room atmosphere. Today, various types of humidity sensors exist and one class of such sensors is based on polymers. Polymer based hygrometers typically use the change of electrical parameters with changing humidity [1]. While resistive humidity sensors are based on the change in resistivity upon changing humidity and require conducting polymers, capacitive polymeric humidity sensors use the change of capacity to measure humidity and thus can work with non-conductive polymers.

Therefore, a hygroscopic polymer is placed between two electrodes to form a small capacitor as shown in Fig. 2.12a. Upon change in humidity, the water vapor penetrates through the porous electrodes and enters the polymeric membrane that bonds to the water molecules. This leads to an increase in the polymers permittivity and thereby to an increase in capacity. To keep the sensor as thin and small as possible, the electrodes can be directly attached to the polymer. However, with this a swelling of the polymer leads to a decrease in capacity due to the movement of the electrodes. Nonetheless, the increase of capacity brought by the rise in permittivity is much stronger than the decrease due to the moving plates. As such, for resolution purposes a strongly hygroscopic polymer that does not fully dissolve in water is desired.

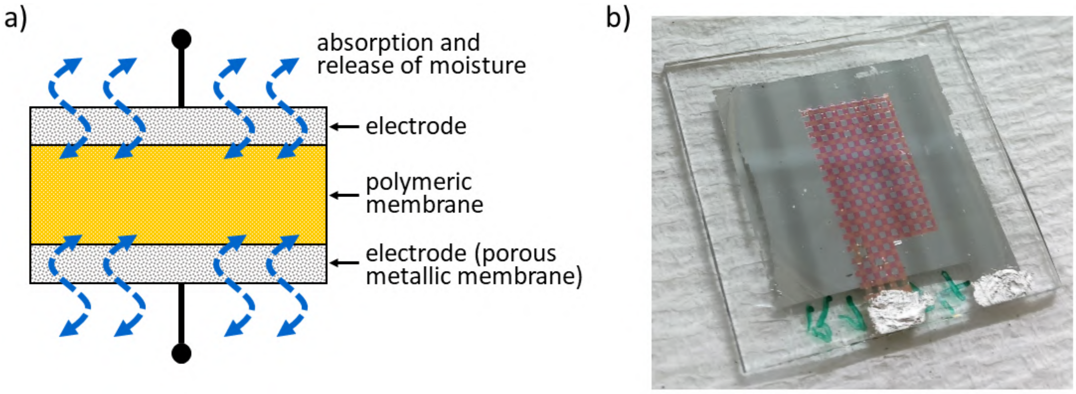

Figure 2.12:
a) Sketch of a capacitative humidity sensor. A hygroscopic polymer is sandwiched by two metallic electrodes to form a capacitor. The humidity sensing ability rises from the change in capacity upon the uptake or release of water. b) PNIPAM microgel based humidity sensor. The thin PNIPAM film is sandwiched between an aluminum and a copper mesh electrode.

Poly(N-isopropylacrylamide) (PNIPAM) is a thermo-responsive polymer that can take up large amounts of water depending on temperature. PNIPAM exhibits a LCST-type phase transition behavior around a temperature of T_c = 32 °C in solution. Cross-linking the polymer chains to form a spherical, interconnected network yields a microgel, which exhibits good stability and a collective responsive nature.

We investigated microgels constituted of PNIPAM and N,N'-methylenebisacrylamide (BIS) as cross-linker in their capability to be used as capacitive humidity sensors. For that purpose we prepared compact layers of microgel colloids and subjected them to varying humidity. The temperature was kept below T_c, so that the microgel is hydrophilic and sensitive to changes in the surrounding humidity.

The completed microgel based humidity sensor is shown in Fig. 2.12b. First, the glass substrate was coated with a layer of aluminum via metal evaporation. A thin PNIPAM microgel layer of around 80 nm was spin-coated on top to cover the whole substrate. On top of that polymer layer, a copper mesh was evaporated to serve as the counter electrode. These sensors were subsequently subjected to varying humidity to calibrate them. However, since the microgel film under the copper mesh does not necessary swell in a homogeneous manner, stress on the electrode on top occurred and lead to material failure of the copper mesh. The microscopy image in Fig. 2.13a shows the sensor device after the polymer film was swollen once. At the edge of the aluminum electrode, but also in some other regions, cracks formed. This could be reduced by using thinner aluminum electrodes and thicker copper electrodes.

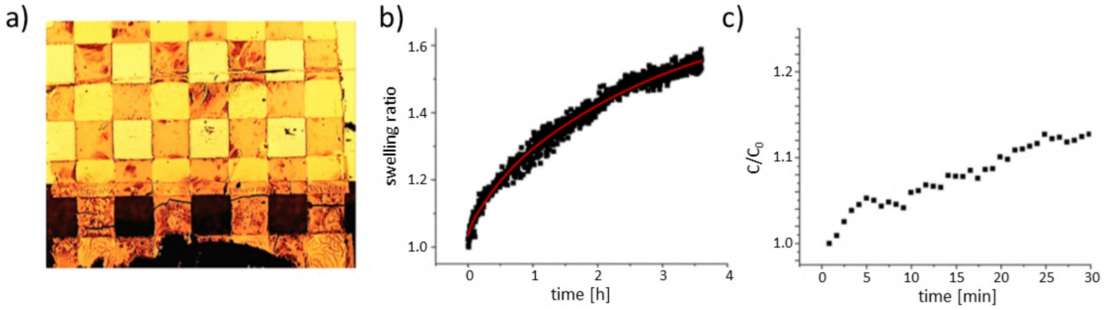

Figure 2.13:
a) Microscopy image (10x) of the PNIPAM humidity sensor after swelling. b) Swelling ratio derived from the spectral reflectance measurement during humidification. c) Capacity ratio derived from an impedance spectroscopy measurement during humidification.

In order to measure the humidity as well as the water content inside of these humidity sensors, we recorded both, the change in capacity, as well as the change in thickness of the polymer film. With that the actual shift in capacity due to the change in permittivity can be decoupled from the one brought from moving the plates of the capacitor. For that purpose, a spectral reflectance measurement was performed simultaneously with an impedance spectroscopy measurement. Both were performed in-situ as a humid atmosphere was created around the polymer films.

The result from the spectral reflectance measurement is shown in Fig. 2.13b. It shows a strong increase in film thickness by a factor of 1.6 over a time of 3.5 h. This is in a similar range to what was observed before for PNIPAM microgel films and shows that the electrode mesh on top doesn't restrict the diffusion of the solvent into the film. The swelling curve is fitted (red line) with a theoretical model that describes the swelling of the polymer film as a combination of a humidity driven and a diffusion driven process [2]. From the fits we obtain a relative time constant of τ = 1.55 h that describes the speed of the swelling process and an effective Flory-Huggins parameter of χ = 0.86, that describes the hydrophilicity of the polymer.

The impedance spectroscopy measurement shown in Fig. 2.13c shows an increase in capacity by a factor of 1.1 over 30 min. Afterwards, the electrode broke and the capacity could no longer be measured. With these first results it is already shown that the PNIPAM microgel film can be used as a capacitive humidity sensor.

[1] Z. Chen, C. Lu, *Sensor letters* **3(4)**, 274-295 (2005)

[2] J. Jaczewska, I. Raptis, A. Budkowski, D.Goustouridis, J.Raczkowska, M.Sanopoulou, E.Pamula, A.Bernasik, J.Rysz, *J. Synth. Met.* **157**, 726-732 (2007))

3 Photovoltaics

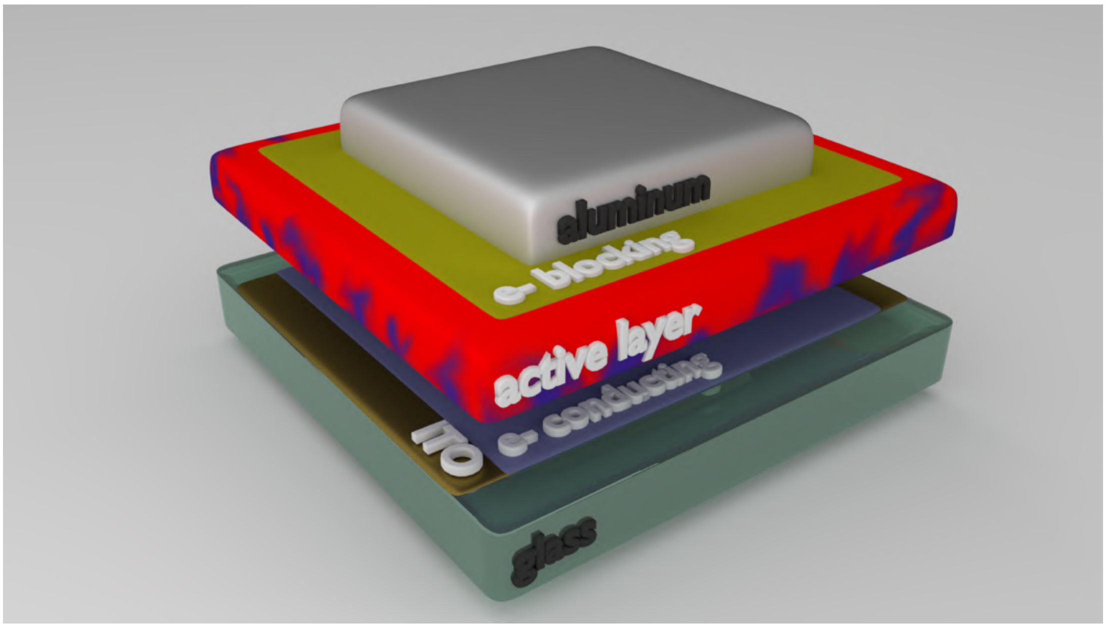

3.1 Organic solar cells in fiber geometry

S. Aeschbach, S. Grott, V. Körstgens, N. Hohn, S. Pratap, A. Davydok[1], C. Krywka[1],
P. Müller-Buschbaum

[1] HZG, Außenstelle DESY, Hamburg, Germany

A promising alternative to silicon solar cells, which are used today to a significant extend for energy conversion, are organic solar cells (OSCs). OSCs have several advantages as compared to silicon solar cells, which render them promising for future use. For example, OSCs are potentially inexpensive, light-weight, flexible and semi-transparent.

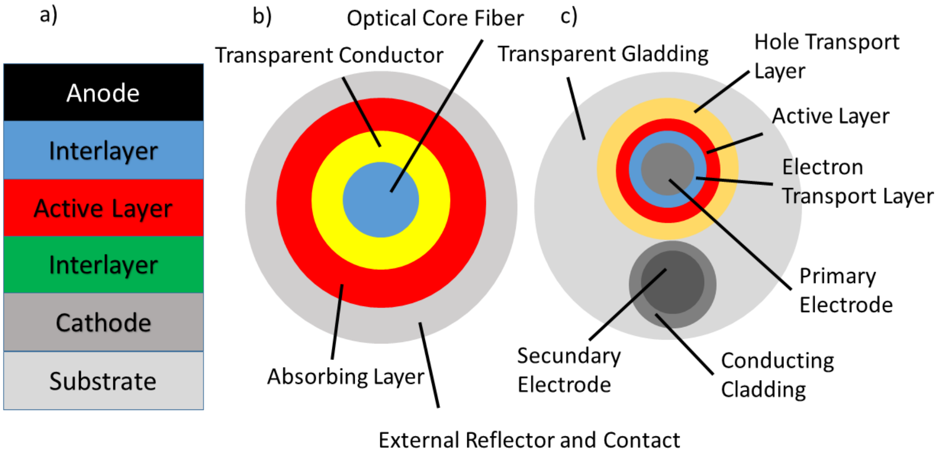

Figure 3.1:
Schematic layout of an organic solar cell a) with the cathode on the substrate and anode as back-electrode [1], b) in a fiber geometry with a single core fiber [2] and c) in a fiber geometry with a two core fiber [3]. The individual laery of the functional stacks are indicated and explained in the text.

OSCs have emerged in two classical designs. Commonly, the bottom layer of an OSC is a transparent substrate. The substrate is covered with a transparent electrode. On the electrode is an interlayer, followed by the so-called active layer, which is responsible for the conversion of light into charge carriers. In OSCs the active layer is a blend consisting of a polymer acting as donor and a small molecule being the acceptor. On top of the active layer another interlayer can be applied. The last layer is the top electrode (Figure 3.1a). In many approaches of OSCs fullerenes are used as acceptor material. Recently, it was realized that alternative small molecule acceptors will be a successful way to adapted and improved the absorption and thereby the entire device efficiency. An example for such non-fullerene acceptor is the small molecule called 3,9-bis(2-methylene-(3-(1,1-dicyanomethylene)-indanone)-5,5,11,11-tetrakis(4-hexylphenyl)-dithieno[2,3-d:2′,3′-d′]-s-indaceno[1,2-b:5,6-b′]dithiophene (ITIC).
A well matching donor polymer is poly[(2,6-(4,8-bis(5-(2-ethylhexyl)thiophen2-yl)benzo[1,2-b:4,5-b′]dithiophene)-co-(1,3-di(5-thiophene-2-yl)-5,7-bis(2-ethylhexyl)benzo[1,2-c:4,5-c′]dithiophene-4,8-dione)] (PBDB-T). Solar cells using this donor-acceptor system are reported to achieve a device efficiency of 11.3%. [1]

The task of a solar cell is to create an electric current from incoming light. The incoming light crosses the transparent outer layers and should be entirely absorbed in the active layer. When the light is absorbed in the donor, it creates a positive-negative charge carrier pair inside the donor. This pair is still strongly bound and is called exciton. To dissociate the exciton into free charge carriers, it has to diffuse to an interface where it can be split, since the thermal energy is not large enough to overcome the Coulomb binding. Then the free positive charge carrier is transferred to the cathode and the negative one to the anode, resulting in an electric current.

Besides the mostly studied thin film solar cells, which have flat geometry, interest in fiber-shaped solar cells has emerged. In the past, there have already been approaches to create solar cells based on fibers. For example one approach is to use an optical core fiber, on which a transparent conductor is applied, followed by an absorbing layer. Finalizing the device with an external reflector and a contact. This fiber is surrounded by a transparent conductor, an absorbing layer and an external reflector and contact (Figure 3.1b). [2] Another approach is a fiber with two cores. One core consists of the primary electrode, surrounded by the electron transport layer, followed by the active layer and the hole transport layer. The other core consists of the secondary electrode surrounded by a conductive cladding, which touches the hole transport layer of the first core. All of this is surrounded by a transparent cladding (Figure 3.1c). [3]

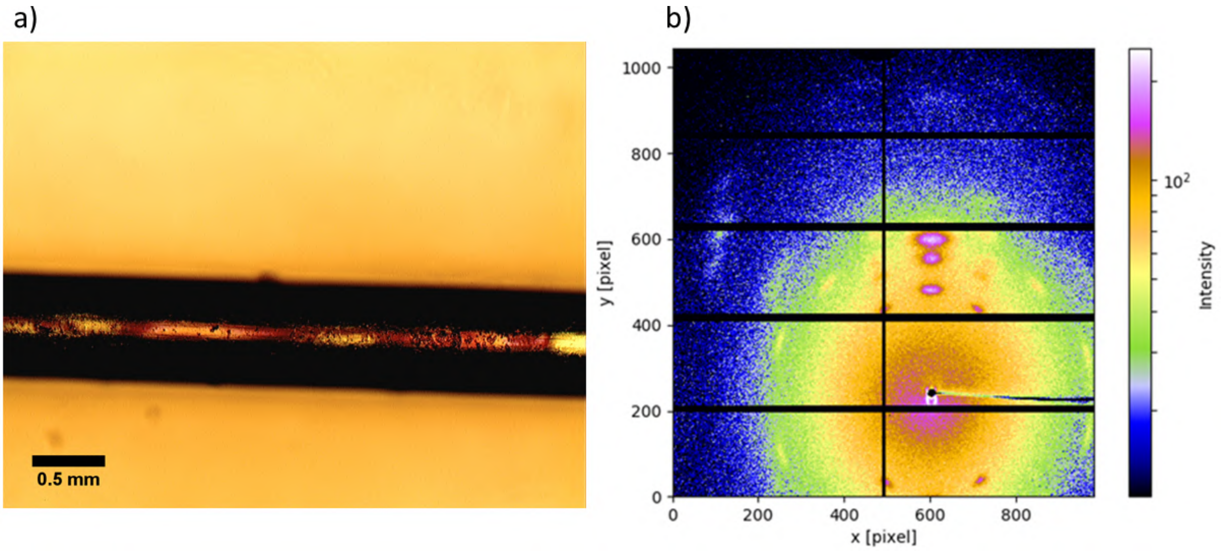

Figure 3.2:
a) Picture of the studied solar cell fiber taken with an optical microscope. b) 2D WAXS data of solar cell fiber with a strong signal from the PET fiber core.

From the possible approaches to realize a solar cell fiber, we focus on a design using a PET fiber core, which is close to the layout shown in Fig. 3.2b. A picture of this so-called power fiber can be seen in Fig. 3.2a. Using advanced scattering techniques, such as grazing incidence wide angle scattering (GIWAXS), we studied the structure of the individual laery of the power fiber. The structure information will be correlated to optoelectronic properties of the power fiber. Fig. 3.2b shows the example of a WAXS image of the power fiber. On the first view, the scattering is dominated by the PET signal as a transmission geometry was used in the scattering experiment.

[1] W. Zhao, S. Zhang, J. Hou, *Sci. China Chem.* **59**, 1574–1582 (2016).

[2] Wake Forrest University, 2006. *Organic optoelectronic devices and applications thereof* . D. L. Carroll, J. Liu, M. A. G. Namboothiry. 01.05.2006, Europe, EP2022108B1.

[3] M. R. Lee, R. D. Eckert, K. F. Forberich, G. Dennler, C. J. Brabec, *Science* **324**, 232-235 (2009).

3.2 Impact of weak and strong acids on structure and composition of PEDOT:PSS polymer electrodes

L. Bießmann, N. Saxena, N. Hohn, Md A. Hossain[1], J. G. C. Veinot[1], P. Müller-Buschbaum

[1] Department of Chemistry, University of Alberta, Edmonton, Canada

One key aspect towards flexible and semi-transparent device applications is the availability of polymeric electrodes to replace the commonly used rigid and brittle metal oxides, such as indium-doped tin oxide (ITO). Among the broad range of available conducting polymers, the polymer mixture poly(3,4-ethylene dioxythiophene):poly(styrene sulfonate) (PEDOT:PSS) gained strong interest due to its easy processibility from water solution and its high conducting properties. It has been shown that different treatments mainly based on high boiling point solvents have a strong impact on the conductivity of PEDOT:PSS [1]. Kim et al. achieved conductivities of $\sim 4000\,\mathrm{S\,cm^{-1}}$ by post-treatment with concentrated H_2SO_4 acid, which he explained with a high amount of extracted PSS [2]. Within this frame, the question was raised if the improved conductivity was exclusively caused by a reduced amount of insulating PSS.

In the present study, the influence of post-treatment with weak and strong acids on the performance of PEDOT:PSS electrodes is investigated and its resilience against water is tested. Therefore, PEDOT:PSS post-treatment with hydrochloric acid (HCl), formic acid (HCOOH), nitric acid (HNO_3) and sulfuric acid (H_2SO_4), is performed and compared to the commonly used ethylene glycol (EG) post-treatment. A significantly enhanced conductivity is found for EG ($1128 \pm 143\,\mathrm{S\,cm^{-1}}$), HCl ($392 \pm 29\,\mathrm{S\,cm^{-1}}$), HCOOH ($1289 \pm 73\,\mathrm{S\,cm^{-1}}$), HNO_3 ($2099 \pm 143\,\mathrm{S\,cm^{-1}}$), and H_2SO_4 ($2938 \pm 325\,\mathrm{S\,cm^{-1}}$) treatment, which goes along with strong thickness reduction (Fig. 3.3).

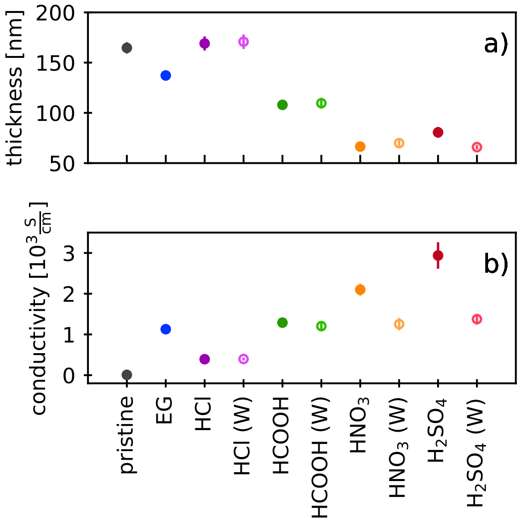

Figure 3.3:
Film thickness (a) and conductivity (b) measurements of post-treated PEDOT:PSS thin films. A correlation between decrease in film thickness and increase in conductivity is observable. Non-washed treatments are depicted with dot-symbols for pristine (gray), EG (blue), HCl (purple), HCOOH (green), HNO_3 (orange), H_2SO_4 (red). Additional washing with water subsequent to the respective acid treatment is represented with circles and the label (W). For high dielectric solvents, a decrease in conductivity after washing is measured [3].

In order to investigate the origin of the increased conductivity in the thin films, the structural change upon acid treatment and its possible reversibility upon H_2O washing is investigated by grazing-incidence wide-angle X-ray scattering (GIWAXS). The obtained 2D scattering images in q_r-q_z representation are depicted in Fig. 3.4a-j) and show a substantially enhanced crystallinity, especially for HNO_3 and H_2SO_4 treated samples, which goes along with the enhanced conductivity. Strong scattering signals are found in q_z direction, which corresponds to an improved lamellar stacking of alternating PEDOT and PSS chains in the range of $\sim 21\,\text{Å}$ and $\sim 12\,\text{Å}$. In addition, pronounced signals are observed in q_r direction that corresponds to an improved PEDOT edge-on π-π stacking distance of $\sim 1.8\,\text{Å}$. Furthermore, the amorphous PSS signal located around $q \approx 1.3\,\text{Å}^{-1}$ is reduced. For a detailed analysis, powder integration cuts have been performed and the peak intensity corresponding to PSS and PEDOT π-π stacking distance has been extracted. Comparison of those intensities yields the PEDOT/PSS ratio of the films that increases for acid treated samples, which is depicted in Fig. 3.4m). The enhanced crystallinity and effective PSS extraction is linked to the acid's strength and dielectric constant (Fig. 3.4k,l). It has been shown, a facilitated phase separation of PEDOT and PSS domains leads to efficient extraction of excess PSS, due to diminished Coulomb screening, owed by the acids' high dielectric constants [3]. Selective PSS removal and structural rearrangement of PEDOT-rich domains due to an enhanced lamellar stacking is identified as major influence on the improvement in electrical conductivity. High conductivities are reached via HNO_3 or H_2SO_4 treatment with the drawback of high sensitivity against H_2O. In contrast, HCl and HCOOH treatment obtaining a medium enhanced conductivity differ in the amount of PSS removal but show higher H_2O resistance.

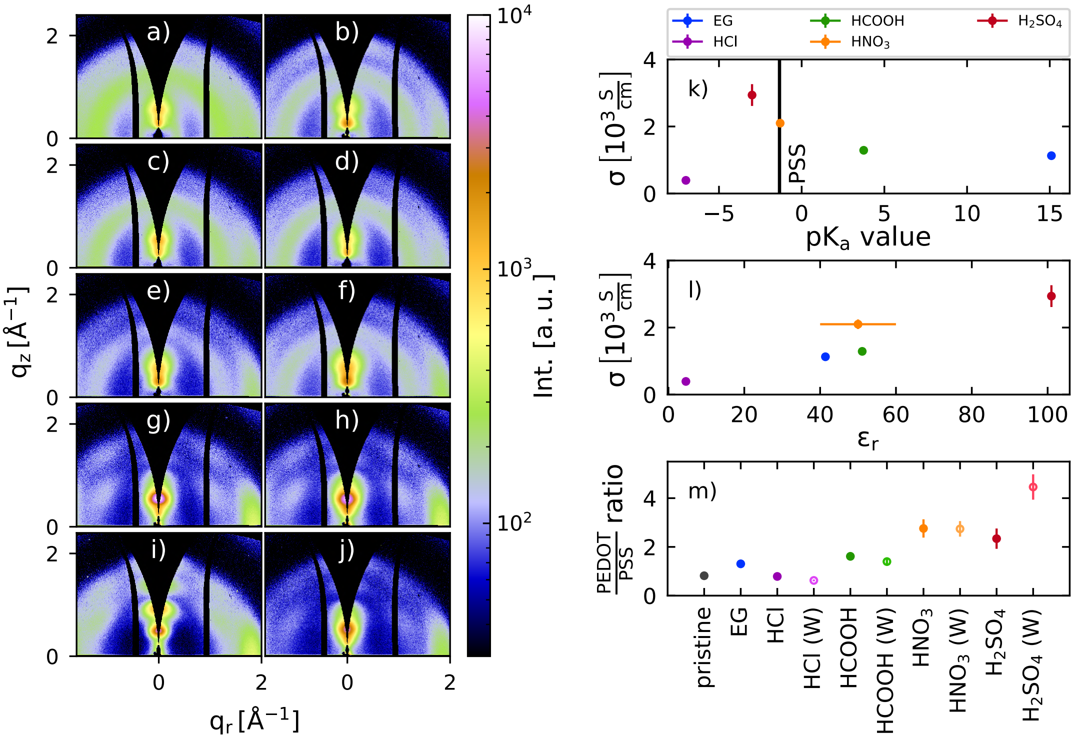

Figure 3.4:
2D GIWAXS patterns of PEDOT:PSS treated samples: a) Pristine, b) EG, c,d) HCl, e,f) HCOOH, g,h) HNO_3, i,j) H_2SO_4 treatment and their H_2O-washed counterparts, respectively. Acid treated samples reveal reduced amorphous PSS signal and high crystalline order. Different lamellar stacking and increased PEDOT edge-on π-π-stacking is observed. k) Relation of conductivity and dissociation constant of acids. l) Relation of conductivity and dielectric constant of acids/solvent. m) PEDOT-to-PSS ratio extracted from powder integration cuts on 2D GIWAXS patterns (a-j). HCl (purple) treatment shows no change in PEDOT-to-PSS ratio, while EG (blue) and HCOOH (green) reveals a slight change. HNO_3 (orange) and H_2SO_4 (red) shows a strong change toward an increased PEDOT-to-PSS ratio, indicating efficient PSS removal [3].

[1] Y. H. Kim, C. Sachse, M. L. Machala, C. May, L. Müller-Meskamp, K. Leo, *Adv. Funct. Mater.* **21**, 1076 (2011), DOI: 10.1002/adfm.201002290

[2] N. Kim, S. Kee, S. H. Lee, B. H. Lee, Y. H. Kahng, Y.-R. Jo, B.-J. Kim, K. Lee, *Adv. Mater.* **26**, 2268 (2014), DOI: 10.1002/adma.201304611

[3] L. Bießmann, N. Saxena, N. Hohn, Md A. Hossain, J. G. C. Veinot, P. Müller-Buschbaum, *Adv. Electron. Mater.*, 1800654 (2019), DOI: 10.1002/aelm.201800654

3.3 Improving compatibility of donor and acceptor materials in ternary organic solar cells by adding BPO

D. Yang, F. C. Löhrer, V. Körstgens, A. Schreiber, S. Bernstorff[1], P. Müller-Buschbaum

[1] Elettra, Trieste, Italy

The urgent society problems of excessive exploitation and consumption of mineral materials, energy shortage and environmental pollution make people to seek for new clean and renewable energy resources. Due to the advantages of low cost, flexibility, solution processing and large-scale fabrication process, enormous attention is focusing on the research and development for higher organic photovoltaics (OPV) performance over the last decades. In OPV architecture, the bulk heterojunction (BHJ), made by blending a donor (D) material with an acceptor (A) material, is introduced to form interpenetrating networks for extending the interfacial area and promoting exciton separation. Fluorine (F) atoms are widely introduced in donor molecules, such as PTB7, PTB7-Th, PffBT4T-2OD, and p-DTS(FBTTh2)2 which can lead a narrow energy band gap of donor materials and then further improve the performance of related devices. In recent years, the power conversion efficiency (PCE) of organic solar cells (OSCs) has been improved by over 17.3% in tandem structure, while the record efficiency for single-junction OSCs is around 14%, which is still behind the performance of inorganic counterparts.[1-2] Based on the previous research, it has been found that further promoting the performance of BHJ organic solar cells is still strongly limited by binary components due to the problems in balancing absorption range, crystallization and compatibility of D/A materials. Therefore, ternary OSCs have been proposed in the photovoltaic field, which can maintain the simple craftsmanship used in binary OSCs and also expand the absorption spectra. However, ternary system suffers from challanges of crystallization and compatibility of D/D/A or D/A/A materials more seriously than binary system. Moreover, the complexity is significantly increased by the addition of a third component.

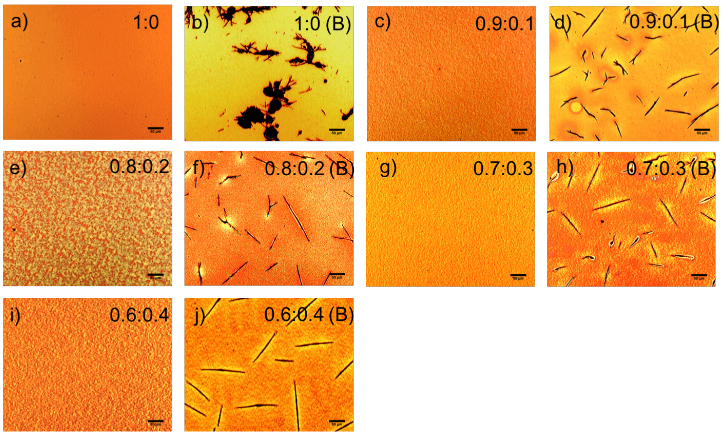

Figure 3.5:
Optical microscopy images of the films with different ratio of PffBT4T-2OD:P3HT:PC_{71}BM: a, c, e, g, i) without BPO, b, d, f, h, j) with 5 wt% BPO, respectively. The scale bar is 50 μm.

To overcome the issues of compatibility of D/D/A or D/A/A materials in ternary OSCs, we doped 4,4'- biphenol (BPO) as an additive in ternary OSCs to modify the BHJ morphology. As the hydrogen bonds can be formed between -OH groups from BPO and F groups in donor materials, the network in the BHJ film can be changed. In the present work, we prepare PffBT4T-2OD:P3HT:PC_{71}BM blend films with five different weight ratios: 1:0:1.2, 0.9:0.1:1.2, 0.8:0.2:1.2, 0.7:0.3:1.2, 0.6:0.4:1.2. Thus, the ratio of PffBT4T-2OD to P3HT is varied, and PC_{71}BM content is constant in all samples. For comparison, 5 wt% of BPO is added into PffBT4T-2OD:P3HT:PC_{71}BM mixture individually. At last, the blends are well dissolved in chlorobenzene and dichlorobenzene (1:1 ratio) with 3 vol% DIO additive.

To investigate the influence of BPO on the BHJ morphology, the BHJ films with and without the BPO were deposited on Si/PEDOT:PSS substrates via spin coating. Then optical microscopy is applied to investigate the surface morphology of these samples. As it shown in Fig. 3.5, the films without BPO are homogenous, but the samples with BPO are quite different to the control samples. When P3HT was absent in the BHJ film, we find large random black dots present on the surface, which indicates the BPO caused a serious aggregation in the BHJ film. However, when P3HT was introduced in the blend solutions, we can observe that some black fibers appear on the surface. At last, we conclude that the morphology of PffBT4T-2OD:P3HT:PC$_{71}$BM films can be modified by BPO addition.

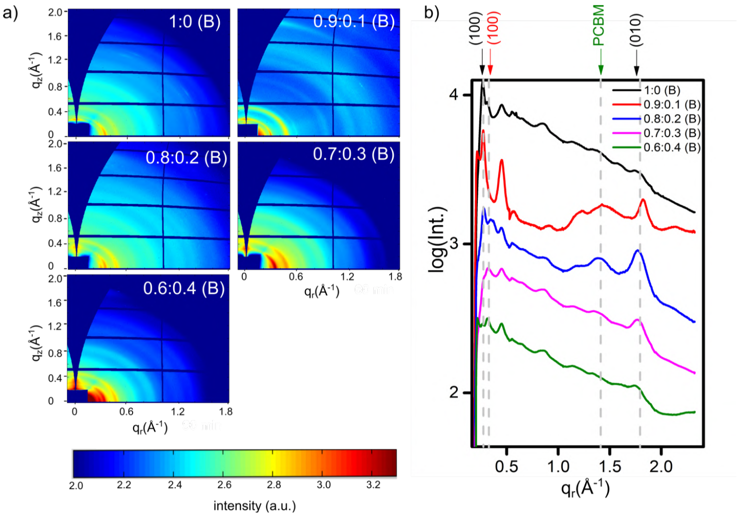

Figure 3.6:
a) 2D GIWAXS images of BPO doping BHJ films with different ratio of PffBT4T-2OD:P3HT:PC$_{71}$BM ; b) Vertical vector integrals of 2D GIWAXS data of different BHJ films. The peaks marked with black arrows are from polymer PffBT4T-2OD. The peak labeled by red arrow is from P3HT. The green arrow indicates the peak of PC$_{71}$BM aggregation.

GIWAXS is applied to probe the crystalline parts of the PffBT4T-2OD:P3HT:PC$_{71}$BM films. The 2D GIWAXS data are shown in Fig. 3.6a. To quantify the GIWAXS data, the vertical sector integrals are taken from the 2D GIWAXS images and the related cuts are plotted in Fig. 3.6b. We can see that the intensity of PffBT4T-2OD (100) peak is more pronounced than the PffBT4T-2OD (010) peak in BPO doped sample without P3HT, which means that an edge-on orientation of PffBT4T-2OD crystals is dominant in these films. While 10 % of P3HT has been inserted into the blend solution, the PffBT4T-2OD (010) peak is more obvious, which stands for more face-on orientation of PffBT4T-2OD crystals appearing in the film. When the weight ratio of P3HT is 20 %, the intensity of PffBT4T-2OD (010) peak is very close to the intensity of PffBT4T-2OD (100) peak, which suggests that the ratio of face-on orientation of PffBT4T-2OD crystals has been further improved. It has been proved that the face-on orientation is more favorable to obtain higher charge mobility than edge-on in the devices, where the charges are collected at the front and back electrodes.[4] Therefore, we claim that the crystallization and compatibility of BHJ films are improved in the ternary OSCs. However, further increasing the content of P3HT leads weak intensity of PffBT4T-2OD peaks, as the overall PffBT4T-2OD content is low in these samples.
Based on the characterizations of optical microscopy and GIWAXS, we clearly see the opportunity of improving the crystallization and compatibility of D/A materials by doping BPO. However, more optimizations are still needed before building the real devices.

[1] C. Yan, S. Barlow, Z. Wang, H. Yan, A. K.-Y. Jen, S. R. Marder, X. Zhan, *Nat. Rev. Mater.* **3**, 18003, 2018.

[2] W. Zhao, S. Li, H. Yao, S. Zhang, Y. Zhang, B. Yang, J. Hou, *J. Am. Chem. Soc.* **139**, 7148, 2017.

[3] H. Sirringhaus, P. J. Brown, R. H. Friend, M. M. Nielsen, K. Bechgaard, B. M. W. Langeveld-Voss, A. J. H. Spiering, R. a. J. Janssen, E. W. Meijer, P. Herwig, D. M. de Leeuw, *Nature* ,**401**, 685, (1999).

3.4 Fullerene-free bulk heterojunction blends for photovoltaic applications - a morphologic study

S. Grott, L. Bießmann, N. Saxena, W. Cao, S. Bernstorff[1], P. Müller-Buschbaum

[1] Elettra Sincrotrone, Trieste, Italy

The continuous demand for energy over the past centuries has driven science and technology to enormous progress concerning energy conversion in a broad field. This has led to an enforced focus of science on renewable energy technologies. One of the most promising technologies are photovoltaic applications, which are capable of generating energy out of sunlight. The already well used inorganic based solar cells, which are operated to harvest sunlight are one step towards dealing with our energy crisis. However, over the past decades research made a huge effort and developed a promising alternative for the commonly used inorganic solar cells. This type of solar cells are based on organic compounds and offer advantages, such as being light weight, semi-transparent and flexible. In addition this kind of solar cells can be produced out of solution, which allows the usage of cheap and large-scale production methods like roll-to-roll printing or spray coating.

Most importantly though, this kind of solar cell is based on organic compounds that are earth abundant. In this case the photoactive layer is build up out of such components and therefore offer a shorter energy payback time than inorganic semiconductor based solar cells.

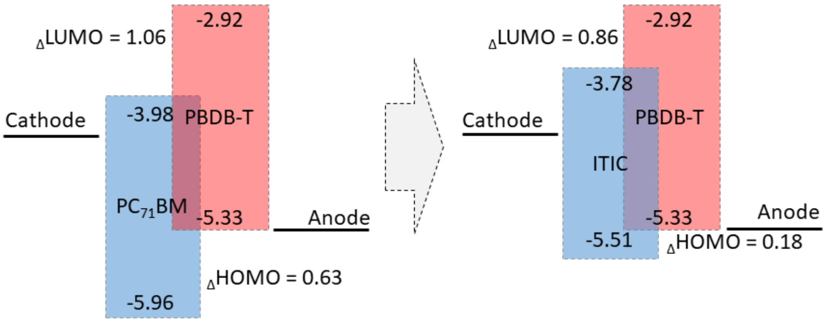

Figure 3.7:
band diagram for PBDB-T:PC_{71}BM and PBDB-T:ITIC.[1]

In this regard the polymer poly(3-hexylthiophen-2,5-diyl) (P3HT) and the fullerene [6,6]phenyl-$C-t61$-butyric acid methyl ester (PCBM) is the most studied donor-acceptor system used as photoactive layer for organic solar cells, which achieved efficiencies of around 4-5 %. To increase the efficiency of organic solar cells, one approach is to tune the absorption properties and bandgaps of the used donor-acceptor system to match the solar spectrum in order to optimize the energy generation. Hence, substituting the fullerene by a none-fullerene small molecule and adjusting the absorption of the acceptor molecule is a promising approach to harvest sunlight more efficient. In Fig. 3.7 the band diagram of the donor polymer poly[(2,6-(4,8-bis(5-(2-ethylhexyl)thiophen-2-yl)-benzo[1,2-b:4,5-b′]dithiophene))-alt-(5,5-(1′,3′-di-2-thienyl-5′,7′-bis(2-ethylhexyl)benzo[1′,2′-c:4′,5′-c′]dithiophene-4,8-dione)] (PBDB-T) and the acceptor molecules [6,6]phenyl-C_{71}-butyric acid methyl ester (PC71BM) and 3,9-bis(2-methylene-(3-(1,1-dicyanomethylene)-indanone))-5,5,11,11-tetrakis(4-hexylphenyl)-dithieno[2,3-d:2′,3′-d′]-s-indaceno[1,2-b:5,6-b′]diethiophene(ITIC)is seen for the respective

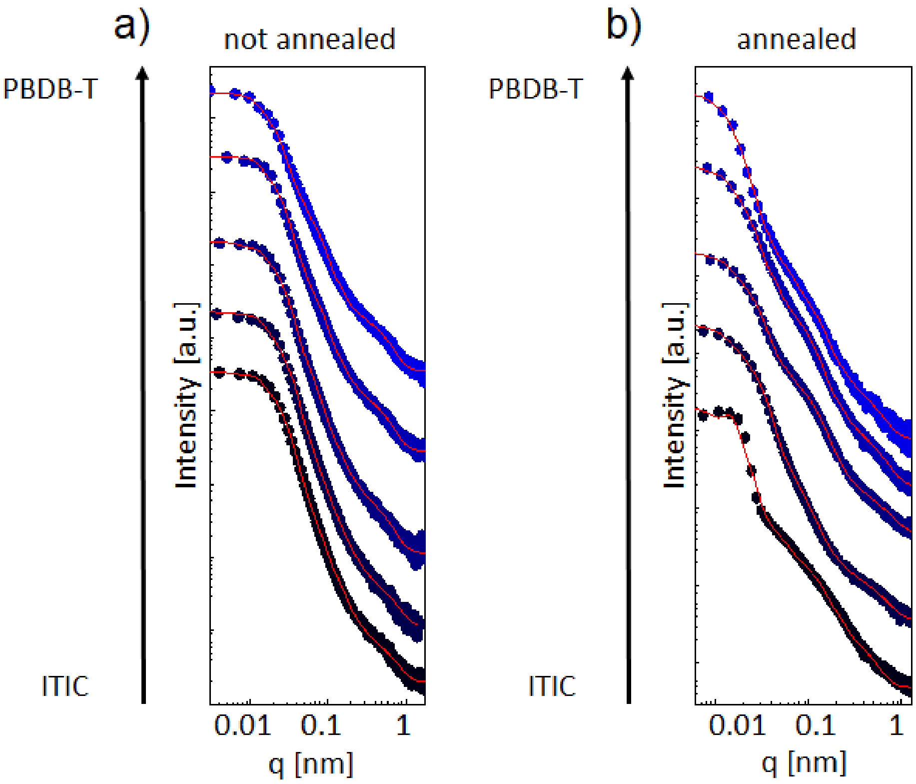

Figure 3.8:
GISAXS horizontal line cuts of the 2D GISAXS data for different PBDB-T:ITIC ratios a) not annealed b) annealed.

donor-acceptor systems.[1]

However, tuning the physical properties of the used compounds is just one approach, to optimize the efficiency of organic photovoltaics. Understanding and improving the inner morphology of the donor-acceptor system is as important as the compounds characteristics. To get insight on the morphology formed by PBDB-T:ITIC, grazing-incidence small angle scattering (GISAXS) is used to probe the structures and domain sizes within thin films. [2] Fig. 3.8a shows the obtained GISAXS cuts for different PBDB-T:ITIC ratios. Fig. 3.8b exhibits the corresponding cuts after thermal annealing. Fig. 3.8a reveals a change of the inner morphology of the prepared thin films by variation of the donor-acceptor ratios. Here, a shift at low q-values can be observed, indicating a growth of large domains found in the thin film. Thermally treating these thin films leads to a change of domain sizes, where this large domain first shrinks and grows again with increasing the PBDB-T content in the thin film (Fig. 3.8b). Correlating these findings with obtained photo-electric measurements is of major importance to fully understand and further improve the performance of organic photovoltaic devices and their power conversion efficiency.

[1] W. Zhao, D. Qian, S. Zhang, S. Li, O. Inganäs, F. Gao, J. Hou, *Adv. Mater.* **28**, 4734-4739 (2016).

[2] P. Müller-Buschbaum, *Anal. Bioanal. Chem.* **376**, 3-10 (2003).

3.5 Effects of annealing time on perovskite material fabricated by the sequential solution deposition

R. J. GUO, L. Reb, B. Predeschly, P. Muller-Buschbaum[1]
[1] MLZ, Garching, Germany

The rapid development of metal halide perovskite solar cells (PSCs) makes such solar cells power conversion efficiency (PCE) comparable with silicon solar cells and the certified PCE has already reached 23.7 percent [1]. The stability of perovskite solar cells had been enhanced to 11000 hours under the light (AM 1.5 G condition) [2], which stands at the position where could be commercialized. There are two spin-coating methods to fabricate the active layer for perovskite solar cells. One method is to spin-coat a mixed solution of methyl-ammonium iodide and lead iodide in the organic solvent like dimethylformamide or dimethyl sulfoxide to produce the active layer of $MAPbI_3$. In order to improve both the coverage of solution on substrates and PCE of solar cells, the so-called sequential deposition method was introduced [3]. For the sequential deposition method, firstly, the mixed PbI_2 and dimethylformamide solution is spin-coated on substrates. After that, substrates are annealing at 70 ^{o}C. When substrates cool down, substrates are dipped into or spin-coated a mixed methyl-ammonium and isopropanol solution, following by annealing at 100 ^{o}C. For this sequential deposition method, the effects of annealing time on both PbI_2 and $MAPbI_3$ films have not been investigated in detail. In this report, the annealing time of PbI_2 layer was controlled to observe the evolution of $MAPbI_3$ films regarding morphology and optic properties. Sample B3 whose PbI_2 layer was annealed at 70 ^{o}C for 1 min and sample B4 whose PbI_2 layer was annealed at 70 ^{o}C for 30 min, after that, both films were spin-coated with mixed methyl-ammonium and isopropanol solution and annealed at 100 ^{o}C for 30 min.

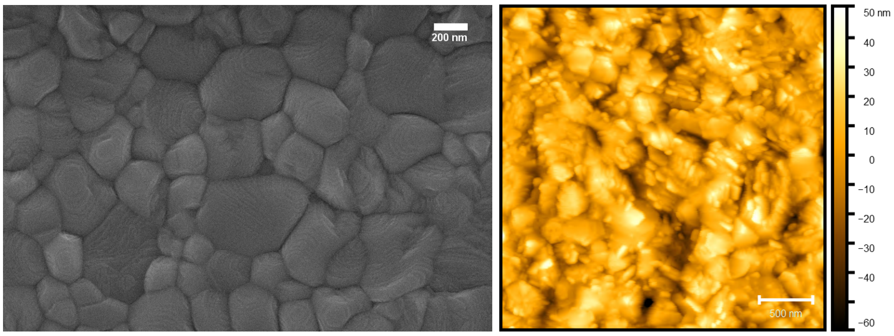

(a) Perovskite film B3 whose lead iodide layer annealed at 70 ^{o}C for 1 min

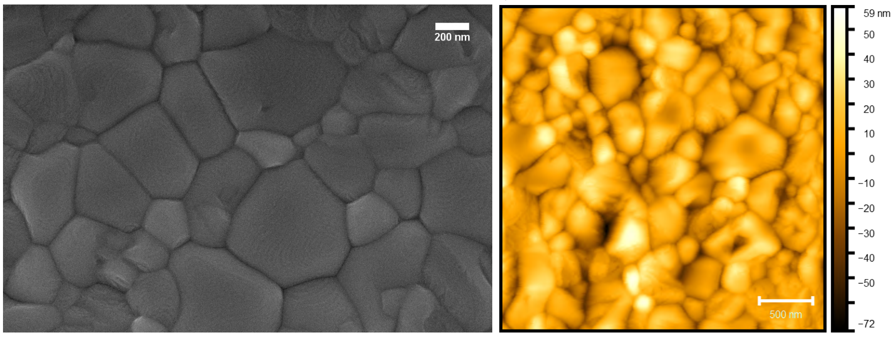

(b) Perovskite film B4 whose lead iodide layer annealed at 70 ^{o}C for 30 min

Figure 3.9: SEM (left) and AFM (right) images of perovskite films

Comparing the SEM images of B3 and B4, we acquire that the rising annealing time can increase the size of crystals of $MAPbI_3$ films, which could have a beneficial effect on the PCE of perovskite solar cells [4]. AFM images of these two films have a huge difference, which shows that AFM is a more sensitive tool to characterize the morphology of $MAPbI_3$ films. Compared with the AFM image of sample B4, there is an amount of second phase in the $MAPbI_3$ films. Due to this second phase, the recombination of perovskite film could be stronger because the grain boundary of films increases, which is not suitable for improving the PCE of PSCs.

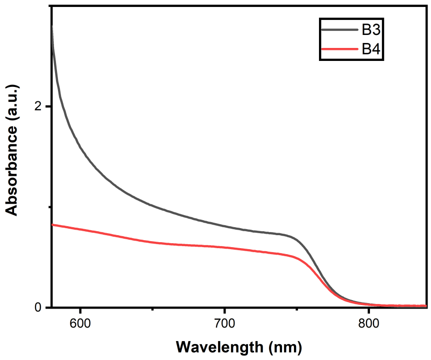

Figure 3.10: UV-Vis absorption spectra of $MAPbI_3$ films

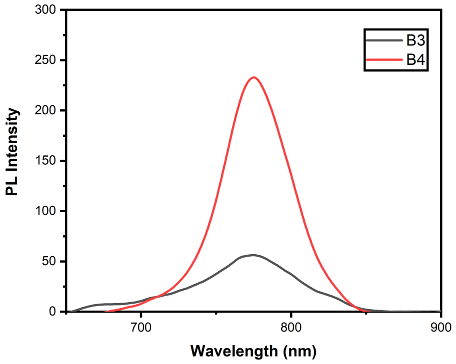

Figure 3.11: Photoluminescence spectra of $MAPbI_3$ films

As shown in UV-Vis absorption spectra of $MAPbI_3$ films, sample B3 shows the film has a stronger light absorption than sample B4. Both sample B3 and B4 have the typical absorption peak of $MAPbI_3$ at 780 nm corresponding to material's optical bandgap E_g= 1.56 eV [5]. For sample B3, light absorption in 450-520 nm is characteristic for light absorption by PbI_2, and it confirms that there is an amount of unreacted PbI_2. This unreacted PbI_2 can improve the stability of PSCs when PSCs are operated under the light [6]. The results of photoluminescence spectra show that sample B3 have much more recombination centers compared with sample B4, which could be related to the second phase induced increasing grain boundary as we mentioned above. Combining the results of UV-Vis absorption spectra and photoluminescence spectra, we can conclude that it is important to find the critical annealing time to obtain $MAPbI_3$ films with both strong light absorption spectra and fewer recombination centers.

To sum up, optimizing the annealing time of PbI_2 film is crucial to achieve $MAPbI_3$ films with strong light absorption and fewer traps so that high PCE of PSCs can be fabricated in following study. Moreover, AFM can offer more informative morphology information compared with SEM.

[1] NREL, https://www.nrel.gov/pv/assets/pdfs/best-reserch-cell-efficiencies.pdf, 2019

[2] G. Grancini, C. Roldán-Carmona,I. Zimmermann, E. Mosconi, X. Lee, D. Martineauand, S. Narbey, F. Oswald, F. De Angelis, M. Graetzel, *Nat. Commun.* **8**, 15684 (2017)

[3] J. Burschka, N. Pellet,S.J. Moon, R. Humphry-Baker, P. Gao, M. Nazeeruddin, M. Grätzel, *Nature* **499**, 316 (2013)

[4] J.H. Im, I.H. Jang, N. Pellet, M. Grätzel, N.G. Park, *Nat. Nanotechnol* **9**, 972 (2014)

[5] S. Kulkarni, T. Baikie,P. Boix, N. Yantara, N. Mathews, S. Mhaisalkar, *J. Mater. Chem. A* **2**, 9221-9225 (2014)

[6] A. Melvin,V. Stoichkov, V.D. Dimitrov, J. Kettle, D. Mogilyansky, E.A. Katz, I. Visoly-Fisher, *Solar Energy* **159**, 794-799 (2018)

3.6 Investigation of the influence of additive to the performance of organic solar cells

H. Kim, X. Jiang, T. Riccitelli, P. Müller-Buschbaum

Bulk heterojunction (BHJ) polymer solar cells (PSCs) sandwich a blend layer of conjugated polymer donor and fullerene derivative acceptor between a transparent ITO positive electrode and a low work function metal negative electrode. In comparison with traditional inorganic semiconductor solar cells, PSCs offer a simpler device structure, easier fabrication, lower cost, and lighter weight. Moreover, these structures can be fabricated into flexible devices. In general, the efficiencies of low-bandgap PSCs decrease considerably when the thickness of active layers go beyond $\sim$ 100 nm because of low crystallinity and a short exciton diffusion length. To solve this problem, solvent additives can be used while fabricating active layers on devices.

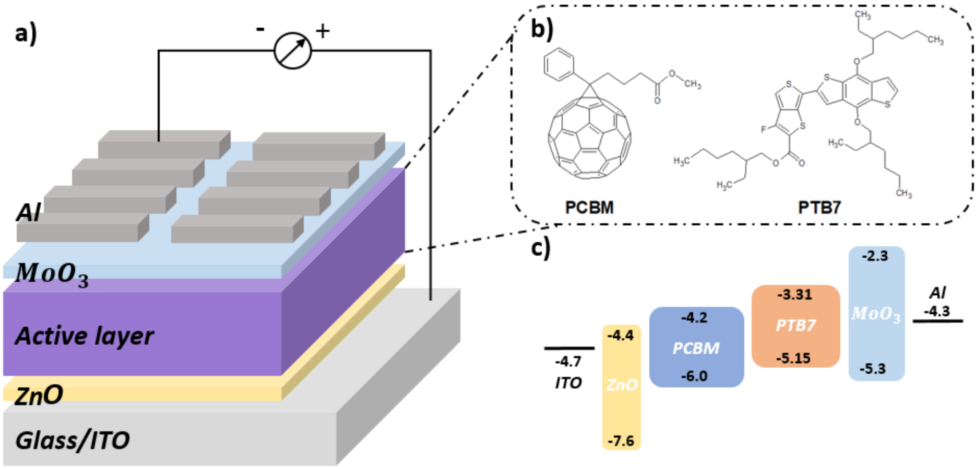

Figure 3.12:
a) Schematic diagram of the probed system: ITO/ZnO/active layer/MoO$_3$(10nm)/Al(100nm). b) Chemical structure of used materials for the active layer, PC$_{71}$BM and PTB7. c) Energy level diagram of the system and path of electrons and holes through the device.

In this experiment, the BHJ solar cells are fabricated with a solvent additive, 1,8-diiodooctane(DIO) and characterized via different thickness. Unfortunately, DIO is an acceptor - selective additive that doesn't enhance the crystallinity sufficiently. To fabricate the devices, it is necessary to prepare ZnO-coated ITO glass substrates and to dissolve the donor and acceptor materials in chlorobenzene (CB) at the first step. ITO glass substrates were cleaned in an ultrasonic bath containing alconex, ethanol, acetone, and 2-propanol successively for 15 minutes each step. Then those substrates were treated with plasma cleaning for 10 minutes. ZnO solution was prepared by dissolving zinc acetate dihydrate $[Zn(CH_3COO)_2 \cdot 2H_2O]$ 1 g in 2-methoxyethanol $[CH_3OCH_2CH_2OH]$ 10 ml and ethanolamine $[NH_2CH_2CH_2OH]$ 0.284 ml under vigorous stirring for 1 day for the hydrolysis reaction in air. The ZnO layer was spin-coated on the top of cleaned ITO substrates by 4,500 rpm for 30 seconds and annealed at 200°C for 1 hour in air. For the active layer, the donor and acceptor materials with the concentrations of 20 mg/mL and 30 mg/mL, respectively, were dissolved in a mixed CB/DIO solution at 90°C for 8 hours under vigorous stirring in a nitrogen glovebox to avoid the high-reaction between oxygen and active layer materials. DIO was added into the CB solution at a ratio of 3 vol %. The mixture of donor/acceptor materials was prepared by mixing them at the same volume ratio. Then the mixture with the total concentration of 25 mg/mL was spin-coated on the ZnO-coated ITO substrates at rates of 1000 rpm and 2000 rpm for 60 seconds. Subsequently, 10 nm MoO$_3$ and 100 nm Al were evaporated as a negative electrode under vacuum. The active area for all devices in the system is 0.12 cm^2.

The final architecture of fabricated BHJ solar cells looks like a sandwich with two different electrodes, ITO/ZnO and Al/MnO_3, surrounding the BHJ active layer in Fig. 3.12 a. In this device, the material $PC_{71}BM$ is the electron acceptor and PTB7 is the electron donor. ZnO and MoO_3 layers work as blocking layers, which are an important for improving the performance of the solar cells by preventing leakage of holes and electrons. Therefore, electrons move to ITO and positive charge carriers move forward to the Al electrode (Fig.).

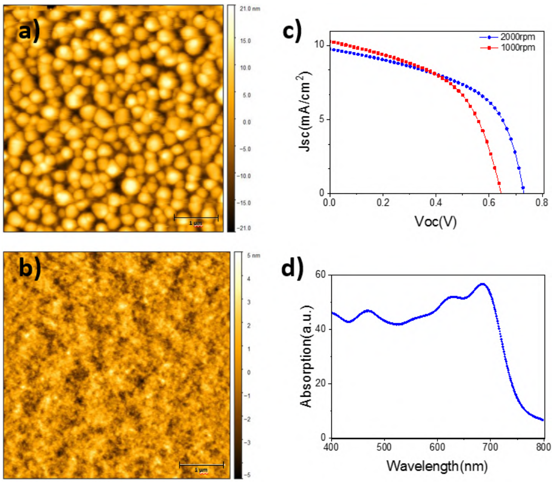

Figure 3.13:
AFM images of the active layers surface a) without DIO additive and b) with DIO additive, demonstrating the influence of the solvent additives on the surface morphology. c) I-V curves of two devices with different active layer thicknesses introduced by controlling the spin-coating speed (1000 rpm / 110 nm & 2000 rpm / 80nm). d) UV-vis absorption spectra of the active layer at 80 nm thickness.

To elucidate the influence of DIO on the BHJ active layer, the morphology is imaged with AFM as seen in Fig. 3.13 a) and b). The active layer without DIO exhibits a more pronounced surface structure (Fig. 3.13 a). With the active addition of 3% DIO the surface of the active layer changes completely. Its roughness significantly decreases (Fig. 3.13 b). Thus, with proper amount of DIO additive, the morphology changes from rough curved features to a substantially smooth appearance.

To investigate the impact of the DIO solvent additive on the BHJ solar cell performance, two devices with different active layer thickness were prepared. One is 80 nm produced via spin coating at 2000 rpm and the other is 110 nm (by 1000 rpm). The active layer on this device absorbs solar energies considerably in the wavelength range between 400 and 700 nm with the highest absorption at 684 nm. Concerning the device efficiency, the short circuit current Jsc increases from 9.74 to 10.26 [mA/cm^2] when the active layer thickness increases between 80 nm and 110 nm while the open circuit voltage Voc decreases from 0.73 to 0.64 [V]. Moreover, the fill factor FF is also decreases from 53.18 % in case of 80 nm to 50.99 % for 110 nm. Thus, the entire device efficiency changes with the use of DIO.

[1] Yifan Zheng, Tenghooi Goh, Pu Fan, Junsheng Yu, and Andre D. Taylor, *ACS Appl. Mater. Interfaces* **8**, 15724-15731 (2016)

[2] Shuai Guo, Christian Brandt, Thomas Andreev, Ezzeldin Metwalli, Weijia Wang, Jan Perlich, and P. Müller-Buschbaum, *ACS Appl. Mater. Interfaces.* **6**, 17902-17910 (2014)

[3] Andrew Wadsworth, Raja S. Ashraf, Maged Abdelsamie, Sebastian Pont, Mark Little, Maximilian Moser, Zeinab Hamid, Marios Neophytou, Weimin Zhang, Aram Amassian, James R. Durrant, Derya Baran, and Iain McCulloch, *ACS Energy Lett.* **2**, 1494-1500 (2017)

[4] Minxia Shang, Xinge Yu, Xu Ye, Hanyu Wang, Lei Zhang, Quan Jiang and Hui Lin, *Journal of Physics D: Applied Physics* Vol.48, No.29, 295105 (2015)

3.7 A transition from fullerene-based to fullerene-free highly efficient organic solar cells

G. I. Ivandekic, S. Grott, P. Müller-Buschbaum

With the rapid increase in energy demand over the last century, science and technology has made enormous progress in the sector of renewable energy in order to overcome the ensuing problems. Furthermore, the growing concerns over environmental issues push the demand for highly efficient, clean and environment-friendly energy solutions. Consequentially, we have seen a huge expansion of the field of photovoltaics, both in academics and in industry. The ever-growing need for energy is motivating the development of new materials with enhanced photoelectrical properties, as well as the study of applicability to large-scale processing techniques to make them commercially viable. Due to their advantageous properties, such as light weight, flexibility and semitransparency, organics solar cells have gained a lot of attention in the last few decades. These properties, along with the possibility to be processed at low cost, give rise to a wide range of application in the field of electronic devices. Contemporary polymer materials have enabled several solution-based processing techniques, such as spin-coating for small scale, spray-coating or different printing methods for large scale fabrication.

Among the different organic photovoltaic devices, solution-processed bulk-heterojunction solar cell have become most prominent due to high power conversion efficiency and tunability. In order to resolve the problems arising from short exciton diffusion lengths in polymers, the active layer of bulk-heterojunction cells, in general, consist of a donor and an acceptor mixed in a specific way so that the formation of a diode junction along the overall length of the cell is guaranteed by the percolation theory. Fullerene derivatives mixed with polymeric semiconductors have been by far the most frequent choice of material for the photo-active layer so far [1]. Even though great progress has been made with fullerene-based solar cells, weak light absorption in the visible spectrum along with high production costs of fullerene derivatives is motivating the increased effort in developing a promising alternatives.

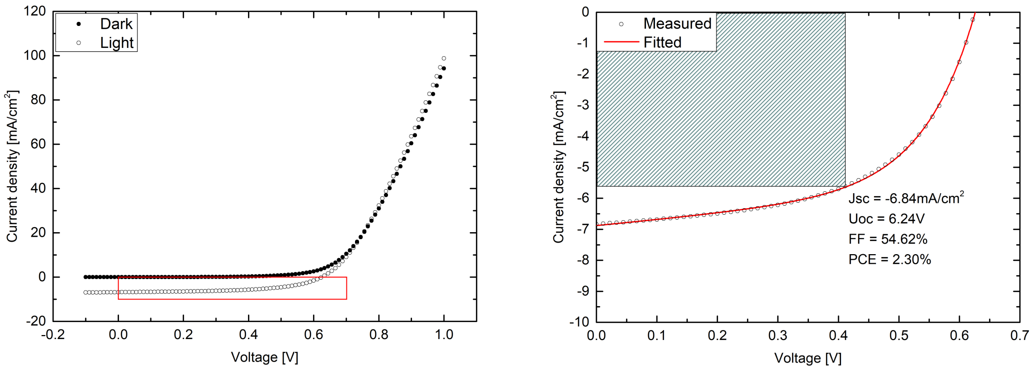

Figure 3.14:
Example of an I-V output characteristic of a P3HT:PCBM solar cell.

The most classical systems in organics solar cells uses poly(3-hexylthiophene):[6,6]-phenyl-C71-butyric acid methyl ester (P3HT:PCBM), despite the fact that it does not lead to the highest power conversion efficiencies.

Many studies have already focused primarily on optimizing the processing procedures of

P3HT:PCBM bulk-heterojunction solar cells. The solar cells were produced in standard or inverse device architecture. The inverse architecture was shown to be more stable. In its functionl stack, on top of the etched ITO-covered glass a hole-blocking layer is inserted. For this purpose, a 20-30 nm layer of ZnO is spin-coated and annealed. Next, the active layer is spin-coated on top of the ZnO, over which an electron-blocking layer of MoO_3 is evaporated. Finally, an Al electrode is evaporated and the finished cell is annealed and left over night in the glove-box. In order to automate the data acquisition and parameter extraction of the I-V measurements, a LabView program is used. In the present study, we have observed that, apart from the ZnO mixing procedure, the time between the annealing of the ZnO layer and the spin-coating of the active layer has a non-negligible influence on the overall performance of the solar cell. A significant increase in power conversion efficiency is observed in every cell produced with an inserted interlayer of either P3HT or PCBM [2]. With the achievement of efficiencies comparable to some of the highest reported, a fabrication route is set to be followed using alternative, fullerene-free polymers.

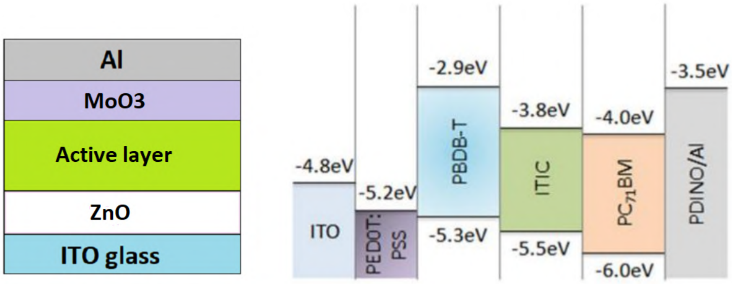

Figure 3.15:
Schematic of solar cell architectures and the energy band diagram of the constituents.

As a substitute for fullerene, a small molecule ITIC (3,9-bis(2-methylene-(3-(1,1-dicyanomethylene)-indanone))-5,5,11,11-tetrakis(4-hexylphenyl)-dithieno[2,3-d:2′,3′-d′]-s-indaceno[1,2-b:5,6-b′]dithiophene) is chosen. The low-bandgap PBDB-T (poly[(2,6-(4,8-bis(5-(2-ethylhexyl)thiophen-2-yl)-benzo[1,2-b:4,5-b′]dithiophene))-alt-(5,5-(1′,3′-di-2-thienyl-5′,7′-bis(2-ethylhexyl)benzo[1′,2′-c:4′,5′-c′]dithiophene-4,8-dione)]) replaces P3HT. In the literature, a power conversion efficiency of above 11% was already reported for the PBDB-T:ITIC sysitem [3]. In the present study, different PBDB-T:ITIC bulk-heterojunction blends are processed by varying the solvents. In order to address the performance issues arising from the use of ZnO, solar cells are fabricated in three different architectures. The prepared solar cells are characterized using several different experimental techniques. To get insight into the inner morphology of the applied bulk-heterojunction grazing-incidence small-angle X-ray scattering (GISAXS) and grazing-incidence wide-angle X-ray scattering (GIWAXS) are used [4]. These information are related to photo-electronic characteristics obtained from UV-vis and photoluminescence measurements and current density-voltage curves, in order to get a full understanding of the applied donor-acceptor system.

[1] M. T. Dang, L. Hirsch, G. Wantz, *Adv. Mater.* **23**, 3597-3602 (2011).

[2] D. Chi, S. Qu, Z. Wang, J. Wang, *J. Mater. Chem. C* **2**, 4383-4387 (2014).

[3] W. Zhao, D. Qian, S. Zhang, S. Li, O. Inganäs, F. Gao, J. Hou, *Adv. Mater.* **28**, 4734-4739 (2016).

[4] P. Müller-Buschbaum, *Anal. Bioanal. Chem.* **376**, 3-10 (2003).

3.8 Influencing the properties of fullerene-free bulk heterojunction blends for photovoltaic applications

A. Kotobi, S. Grott, P. Müller-Buschbaum

Organic solar cells receive high attention, due to their advantages, such as the tuneability of photo-active properties, the possibility to be produced at low-cost, the flexibility and the light-weight, compared to commonly-used inorganic semi-conductors. Bulk heterojunction (BHJ) organic photovoltaic (OPV), consisting of a p-type semi-conducting polymer as the electron donor and a fullerene derivative as the electron acceptor, have received considerable attention for years. However, it should be mentioned that they still have several drawbacks such as weak light absorption in the visible region of the solar spectrum. Therefore, various non-fullerene (NF) acceptors have been developed and applied in OPVs. Promoting the power conversion efficiencies (PCE) is an interesting and important topic in the field of OPVs. In order to achieve higher efficiency, factors such as the active layer composition, the device processing method, the interfacial layers and the device architecture can be taken into consideration.

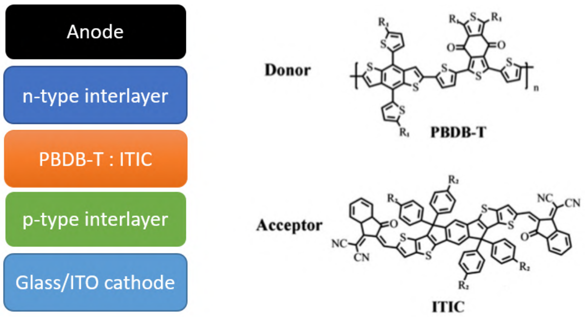

Figure 3.16:
a) Schematic device structure of of an organic solar cell [1]. b) Molecular structures of polymer donor (PBDB-T) and non-fullerene acceptor (ITIC) used in this study.

Among the different post-processing parameters, annealing at different temperatures is of interest because it influences the crystallinity and the absorption. Therefore, after dissolving donor and acceptor materials in chlorobenzene (CB) and spin coating the final solution on glass substrates, different temperatures were used for post-processing. The thin films were fabricated with poly[(2,6-(4,8-bis(5-(2-ethylhexyl)thiophen-2-yl)benzo[1,2-b:4,5-b′]-dithiophene)-co-(1,3-di(5-thiophen-2-yl)-5,7-bis(2-ethylhexyl)benzo[1′,2′-c:4,5-c′]dithiophene-4,8-dione))] (PBDB-T) and 3,9-bis(2-methylene-(3-(1,1-dicyanomethylene)-indanone))-5,5,11,11-tetrakis(4-hexylphenyl)-dithieno[2,3-d:2′,3′-d′]-s-indaceno[1,2-b:5,6-b′]dithiophene) (ITIC) [1]. The glasses were cut in the proper sizes and were cleaned in an acid bath. The active layers were prepared with donor and acceptor materials in which interconnected phase-separated domains with large interfacial areas should be achieved. The domain size should be comparable to the exciton diffusion length for efficient free charge carrier generation and the intermolecular pi–pi interactions of both components must be enhanced to ensure carrier transport [2]. However, in some cases, the ordering and crystallinity of polymer molecules of acceptor and donor is far from ideal. Hence, heat treatment in non-fullerene based OPVs play an important role. For investigating the influence of the annealing temperature, the films were spin-coated without and with annealing. The thermal treatment was performed at 150°. The absorption spectra of the active layers were recorded using a UV-vis spectrometer.

The common structure of fullerene-free BHJs is shown in Fig. 3.16a. This structure is made of ITO covered glass substrates and ZnO spin-coated on these substrates. Moreover, Al/MnO_3 would be deposited after spin-coating the active layer to finalize the devices. However, in our experiment only normal glass was used for spin-coating of the active layer and to device were not finalized.

The UV-vis absorption spectra of neat films of PBDB-T, ITIC, and $PC_{71}BM$ are shown in Fig. 3.17a. The absorption spectrum of the PBDB-T film is dominant in the range from 500 to 700 nm with two peaks centered at 580 and 630 nm. The absorption spectrum of ITIC is mainly in the region of 500–800 nm with two absorption peaks centered at 650 and 720 nm [4]. The absorption spectrum of $PC_{71}BM$ film mainly ranges from 300 to 700 nm, which is complementary to the absorption spectra of PBDB-T and ITIC [3]. Therefore, the absorption of the blends can cover most of the visible region which can be useful for photon absorption and energy conversion of the active layer.

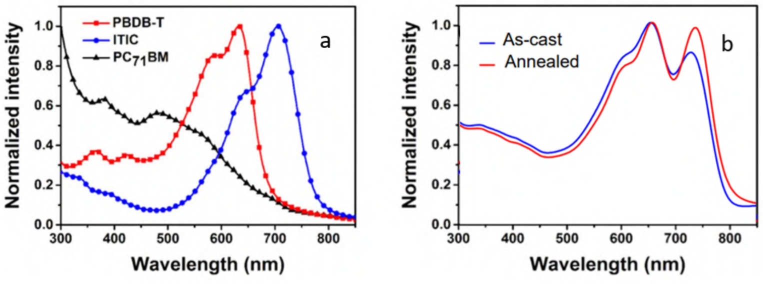

Figure 3.17:
a) UV–vis absorption spectra of PBDB-T, $PC_{71}BM$ and ITIC [4] b) UV-vis absorption spectra of as-cast and annealed PBDB-T:ITIC blend films with a thickness of 100 nm

The morphology has crucial influence on the device performance such as absorption of photons, charge carrier generation and electron mobility. It has been demonstrated that the ideal morphology of the active layer should involve a highly crystalline and interconnected network of phase-separated domains with large donor and acceptor interfacial areas. Therefore, the enhanced crystallinity of acceptor and donor in our blend can increase the electron mobility and diminish charge recombination. For instance, the crystallinity of ITIC can be used in forming pure phases and interpenetrating networks.

In order to better understand the influence of thermal annealing of thin films, the UV-vis absorption spectra of PBDB-T and ITIC are shown in Fig. 3.17b in case of annealing or without annealing after spin-coating of the active layer. The blend film shows a narrow response from 450 nm to 760 nm due to the partially overlapping spectra between PBDB-T and ITIC. As shown in Fig. 3.17b the wavelength range of 450–700 nm is mainly covered by the PBDB-T absorption and the range of 500–760 nm is highly absorbed by ITIC. According to these spectra, it can be concluded that after the thermal annealing of this film, we have increased absorption at 700 nm, which can be related to the higher crystallinity of ITIC during thermal treatment of the films on the substrate.

To better understand the film structure, grazing incidence wide angle X-ray scattering (GIWAXS) and grazing incidence small angle X-ray scattering (GISAXS) will be performed.

[1] Zhao, W., Zhang, S. Hou, J. Sci. China Chem. *ACS Appl. Mater. Interfaces* **8**, (2016) 59: 1574.

[2] Qian, Ye, Zhang, Liang, Li, Huang, Guo, Zhang, Tan, and Hou *Macromolecules* **6**, 2012 45 (24), 9611-9617.

[3] Bi, Xiao, Yang, Niu, Wen, Zhang, Qin, Kong So, Lu, Hao, Liu, Hong, *Nano Energy.* **2**, 2018.01.040.

[4] Liang, Han, Song, Yu, Smilgies, Zhao, Liu, Han, Yanchun, *Journal of Materials Chemistry* A. 6. 10.1039.

3.9 Emergence of lead halide perovskite colloidal dispersions through aggregation and fragmentation: insights from the nanoscale to the mesoscale through spectroscopic signatures

S. Pratap[1], E. Keller, P. Müller-Buschbaum

[1] Advanced Light Source, Lawrence Berkeley National Laboratory, California, USA

The structural properties of colloidal perovskite precursor dispersions are investigated in order to gain perspective on the chemical and physical nature of perovskite sols. Stock precursor dispersion of 2 distinct perovskite compositions, namely $MAPbBr_3$ and $MAPbI_3$ and a 1:1 mixture thereof were prepared in a 4:1 mixture of DMF:DMSO. Their optical characteristics were probed by means of UV-Vis spectroscopy. Other relevant concentrations were attained by sequentially diluting the said precursors with the solvent media, in order to regulate similar physical atmospheric conditions. For $MAPbBr_3$ the absorbance data (Fig. 3.18a) suggest the presence of two distinct (and three identifiable) structural regimes. For precursors of high concentrations ranging from 3M to around 1.3M, the dispersions all display similar absorbance profiles with absorption onsets around 405 nm. The absorption onsets of precursors of concentrations in this high concentration regime (Fig. 3.19), appear slightly red-shifted with each dilution. At intermediary concentrations (regime II), the precursors express stabilized structural sizes wherein the absorbance characteristics remain predominantly invariant with decreasing concentration with minor blue shifts with subsequent dilutions. At yet lower concentrations (regime III), the precursor sols show noteworthy blue-shifts in their absorption onsets with each dilution. For the precursors corresponding to $MAPbI_3$, a stock solution of 1M was prepared. A higher concentration is not intended for the stock solution since the fluid precursor quickly turned translucent due to high supersaturation and the growth of large clusters threatened the integrity of measurements. The absorbance data (Fig. 3.18b) is non-trivial and what at first glance appears as measurement artefacts are in fact, rich optical signatures from plumbo-iodate complexes. Individual absorbance signals are isolated from PbI_2 at around 340 nm; for $[PbI_3]^-$ at 400 nm; for $[PbI_4]^{2-}$ at 438 nm and for $[PbI_5]^{3-}$ as well as $[PbI_6]^{4-}$ at more red shifted wavelengths. For $[PbI_5]^{3-}$ the absorption edge varied strongly with concentration. For $[PbI_6]^{4-}$, the absorption edge is not visualized. It is striking to observe the identical signatures from the plumbo-iodate complexes within the precursor corresponding to $MAPbI_{1.50}Br_{1.50}$ (Fig 3.18c) at the exact wavelengths as designated for the complexes obtained from the $MAPbI_3$ precursor. Moreover, at concentrations beyond 1M, the absorbance data of $MAPbI_{1.50}Br_{1.50}$ provides a rare and fascinating insight into the structure evolution of the concentrated fluid phase. It is observed that

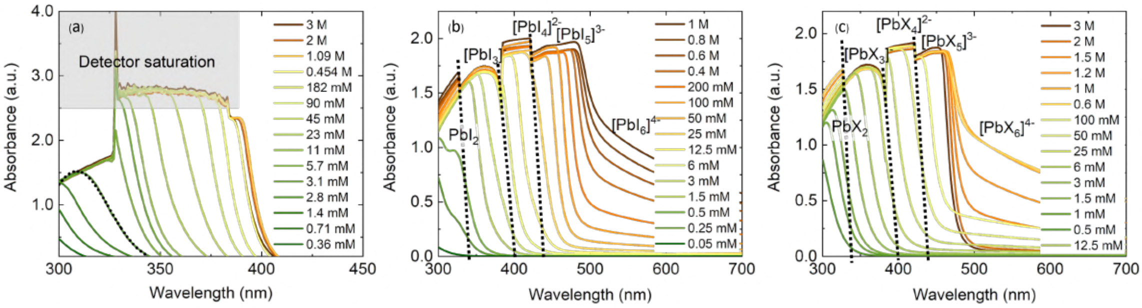

Figure 3.18:
Absorbance data of colloidal perovskite precursors for (a) $MAPbBr_3$, (b) $MAPbI_3$ and (c) $MAPbBr_{1.50}I_{1.50}$.

within the high concentration regime, the absorbance signal corresponding to $[PbI_6]^{4-}$ starts diminishing with increasing concentration and the absorption onsets experiences a blue shift until 3M.

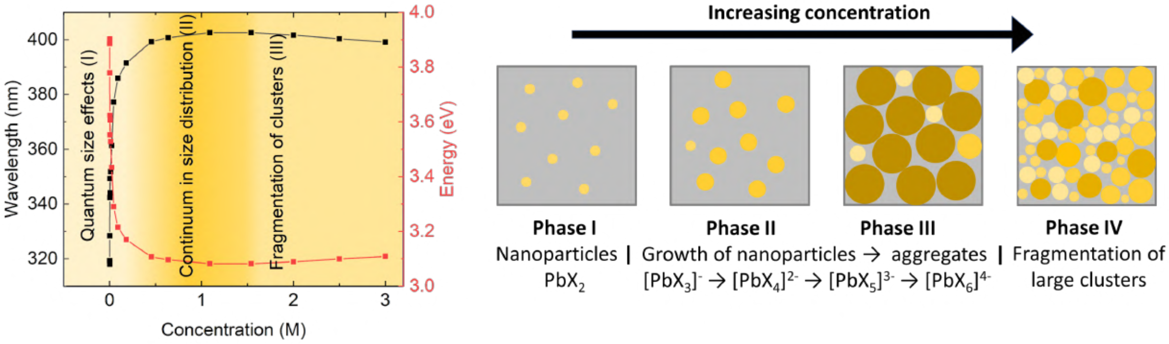

Figure 3.19:
Evolution of structures as a function of precursor concentration: Starting from nanoparticles, followed by increasing size of nanoparticles until an equilibrium size of large aggregates / complex clusters, and thereafter fragmentation of large aggregates.

Fig. 3.19 describes the fate of the colloidal dispersion as a function of increasing concentration of the precursor in the solvent media. At low volume fractions, the dispersed particles are small (nanoparticles). With increasing concentration, red shifts within absorption profiles of growing structural entities is noted. The growth of small entities into larger clusters is favoured over increased number of smaller individual particles, owing to the high degree of translational freedom which affords a larger volume available to the said entities for diffusion (entropy favours growth). As a result, particles with increased size/ increased co-ordination emerge with increasing concentration. These phases also coincide with the quantum size regime observed in the UV-vis measurements and serve as the explanation as to the emergence of new spectroscopic signatures from higher order Pb-X complexes with increasing concentration. Growth of nanoparticles continues until a stable cluster size is obtained by the dispersed phase with the dispersion experiencing an increase in packing density. Once a critical packing density is reached (which varies with chemical composition, owing to changing interactions of the dispersed chemical species with the dispersion medium), any further increase in the concentration of the dispersed phase leads to the jamming of the colloid (phase III) as the volume available to clusters for diffusion (excluded volume) is depleted. Further growth of particle size is no longer favoured due to increased repulsion between the densely packed colloid clusters as the system enters a non-ergodic regime. The diffusion of the particles is arrested and the viscosity induced shear forces in addition to the steric frustrations experienced by the colloidal clusters lead to the fragmentation (or deaggregation) of the erstwhile stable, homeomorphic particles to form smaller, more numerous and dissimilar clusters (phase IV).

Engineering chemical compositions of perovskites for maximizing photovoltaic performances is common practice. In order to increase film thicknesses, precursor concentrations are maximized with little knowledge of the consequence on film morphologies. Thin films based on colloidal precursors grow at the expense of the structural entities present within dispersions. Supersaturated precursor dispersions bear high polydispersity, a property which is then inherited by the thin films. Structural and chemical inhomogeneities within thin films have been linked to variations in photovoltaic performances and bear direct relevance in the case of functional devices. Their origin may very well be correlated to the structures prevalent within the dynamic fluid phase and underlines the need for better understanding of the non-trivial perovskite precursors.

3.10 Optimization pathways of perovskite solar cells

B. Predeschly, L. Reb, P. Müller-Buschbaum

Perovskite solar cells (PSCs) are promising for future energy generation due to their up-scalable low-cost production from solution and their flexibility. Recently, the power conversion efficiency (PCE) of lab-scale produced thin film hybrid solar cells with a mixed cation lead mixed halide perovskite film as active layer exceeded 22% as a result of optimized preparation techniques and material compositions [1, 2]. These high efficiencies are possible because of the special perovskite crystal structure, which is depicted in Fig. 3.20a). In lead-halide solar cells, photons are absorbed in the active perovskite layer and create excitons. In contrast to purely organic active layers, excitons dissociate easily due to a low binding energy. Free electrons and holes reach their individual selective materials, because the diffusion length is typically larger than the perovskite layer thickness.

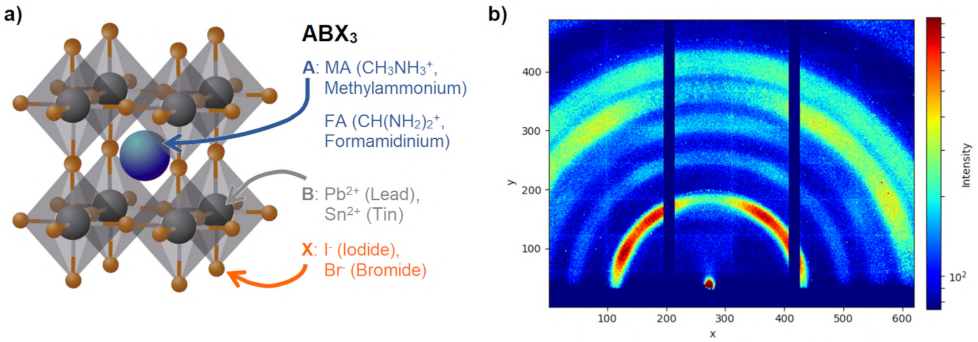

Figure 3.20:
a) Perovskite crystal structure ABX_3 with organic (A), metal (B) and halide (X) part. Image from [3]. b) GIWAXS raw detector image of a perovskite thin film as used for the solar cell.

The preparation of PSCs in the composition under consideration is done in several steps, which will be described briefly below and which are based on production steps as described in Saliba et al. [2]. A key prerequisite is to work in a clean environment but also to use chemicals without impurities to achieve reproducible results. Beside this, the production steps of the PSCs have to be adapted and optimized to the local conditions, which depend on several parameters, as e.g. weather, climate and lab-specific working conditions.

First, the glass substrate with the transparent electrode FTO on it has to be masked and etched according to the desired solar cell geometry. This has to be done in the region where later the top electrode will be contacted in order to avoid a short circuit. Afterwards the substrates are organically cleaned in the ultrasonic bath and subsequently placed into the oxygen plasma oven to get the surface free of any contamination. Next, the hole blocking layer, i.e. compact titania and mesoporous titania are deposited *via* spin-coating. After both depositions, the substrate is annealed on a heating plate and is placed into the calcination oven. When the substrate is cooled down to room temperature and after a further treatment in the plasma oven, the perovskite layer is spin-coated on it. The salts formamidinium iodide (FAI), methylammonium bromide (MABr), lead iodide (PbI_2) and lead bromide ($PbBr_2$) dissolved in dimethylformamide and dimethylsulfoxide (4:1) are needed for the precursor $(FAPbI_3)_{83}(MAPbBr_3)_{17}$. Previous studies showed, that different compositions and concentrations of the precursor changes and influences the crystal growth, size and orientation, the amount and types of defects and therefore the electrical conductivity [4]. But not only the chemical composition plays a crucial role in the final result. Also details of the routine of precursor preparation, spin-coating parameters and details of annealing steps have a high impact on the quality of the perovskite film and might need to be optimized

for the local conditions. After spin-coating the perovskite the anti-solvent chlorobenzene is dynamically spin-coated and induces the crystallization. A subsequent annealing of the substrate delivers the activation energy which is needed for the crystal growth in perovskite structure. Then the electron blocking layer Spiro-OMeTAD together with chlorobenzene and additives for the hole doping is dynamically spin-coated. The usage of the anti-solvent of the perovskite as solvent for Spiro-OMeTAD in this case is advantageous because it does not dissolve the perovskite layer underneath. Lastly, the gold anode is evaporated on the substrate. A mask shields parts of the substrate to get a geometry with defined area of the anode, which is evaporated in two cycles. In the first cycle, a thin gold layer is evaporated with a low rate. In this way we minimize the thermal stress the PSCs are exposed by the impacting gold particles. Finally, with the second evaporation cycle, gold is deposited with a high rate to reach the desired thickness of the anode.
A PSC produced in the way described above is shown in a cross-sectional scanning electron microscope (SEM) picture in Fig. 3.21a). For comparison, Fig. 3.21b) shows a cross-sectional SEM PSC produced by Saliba et al. [2]. The superimposed layers of both PSCs are highlighted with the same colors. In our PSC, the layers reach thicknesses which have about the double layer thicknesses compared to the PSC of Saliba et al. This, together with the different size of our perovskite crystals could be one reason for a smaller PCE. Another method of high statistical relevance to analyze and reveal preferred orientations and sizes of the perovskite crystals is grazing incidence wide angle x-ray scattering (GIWAXS). In Fig. 3.20b) a GIWAXS detector image of the same perovskite as used for our PSC is depicted. It indicates a high crystallinity of the structure, as visible by the sharply defined rings. The scientific findings of such images are very helpful for the investigation of the perovskite layer, important for the optimization of PSCs.

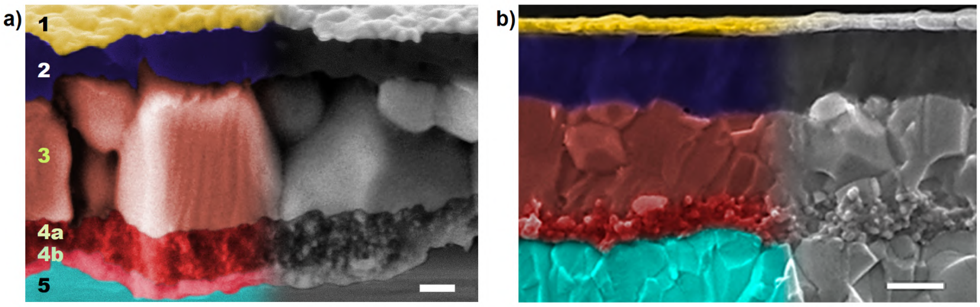

Figure 3.21:
Cross-sectional SEM of a) our superimposed layers on silicon substrate without FTO and b) of a PSC with FTO on glass substrate of Saliba et al. [2]. In both images, the scale bar indicates 200 nm. The image in a) was taken with a 45° tilted stage, whereas that in b) was taken with a perpendicular stage position. The different layers are 1-gold anode, 2-Spiro-OMeTAD, 3-perovskite crystals, 4a-mesoporous titania, 4b-compact titania (not in b)), 5-substrate.

[1] X. Li, D. Bi, C. Yi, J.-D. Décoppet, J. Luo, Jingshan, S. M. Zakeeruddin, A. Hagfeldt, M. Grätzel, *Science* **353**, 58-62 (2016)

[2] M. Saliba, J.-P. Correa-Baena, C. M. Wolff, M. Stolterfoht, N. Phung, S. Albrecht, D. Neher, A. Abate, *Chem. Mater.* **30**, 4193-4201 (2018)

[3] M. Grätzel, *Nature Mater.* **13**, 838 (2014)

[4] T. J. Jacobsson, J.-P Correa-Baena, M. Pazoki, M. Saliba, K. Schenk, M. Grätzel, A. Hagfeldt, *Energy Environ. Sci.* **9**, 1706-1724 (2016)

3.11 High-performance non-fullerene printed organic solar cells

T. Riccitelli, X. Jiang, P. Müller Buschbaum

In recent years, research in the field of polymer based organic photovoltaics has focused on the research of non-fullerene based acceptors because of the drawbacks of fullerene acceptors such as PCBM. Apart from their high production costs, they show poor absorption in the visible light range of the spectrum and they are responsible for morphological instabilities of the active layer [1]. Further advantages of non-fullerene acceptors include a stronger light absorption, the possibility to tune the energy levels and therefore the light absorption and to avoid so-called burn-in efficiency losses, which is a big contribution in the total efficiency loss when using fullerene acceptors [2]. At the same time, research also focused on production techniques which could provide low cost production of organic solar cells and the use of bigger substrates, with printing and roll-to-roll coating gaining growing attention. These techniques could be implemented in industrial production of organic solar cells.

In our work the PffBT4T-2OD:EH-IDTBR donor-acceptor polymer blend is chosen because of the high reported performance, high hole mobility ($10^{-3} - 10^{-2} cm^2 V^{-1} s^{-1}$) and good device stability. In the literature photo conversion efficiencies up to 9.1 % were reported, however, so far the spin coating technique was used for the device fabrication only [2], whereas slot-die coating (printing) is the chosen fabrication method in the present study. Furthermore, this polymer blend allows the use of non-chlorinated solvents, which are less harmfull to the environment, humans and the device performance, requiring lower processing temperatures compared to chlorinated solvents like chlorobenzene. The use of non-chlorinated solvents is a further step towards a possible industrialized production of organic solar cells. Fig. 3.22 shows the printing setup. The solution is pumped into a printer head, suspended over a moving substrate holder. To obtained final film thickness of the printed layer will dependent on a several parameters including the distance from the substrate, the printing speed, the solution flow and the drying time. For the device fabrication we have selected an inverted solar cell architecture as shown in Fig. 3.22, where ZnO is used as an electron blocking layer, molybdenum oxide (MoO_3) as a hole injection layer and Al as back electrode (both are evaporated in vacuum).

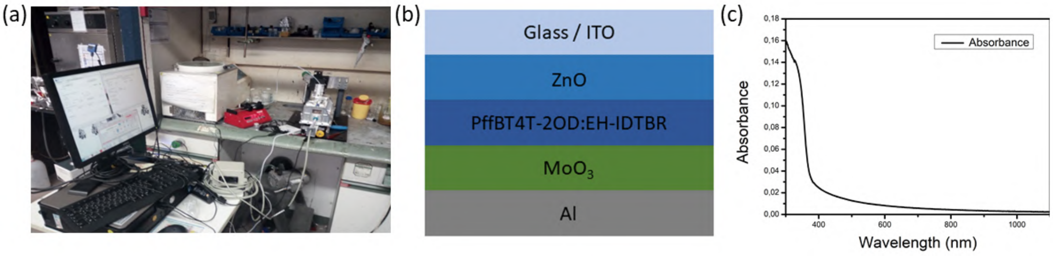

Figure 3.22:
a) printing setup, b) cell structure and c) ZnO absorption

As a start, we focus on the slot-die printing of the ZnO electron blocking layer on both, glass and silicon substrates. In order to obtain information about the structure of the printed ZnO layer, optical microscopy, SEM images and UV-Vis absorption spectra have been used;the latter is shown in Fig. 3.22. Absorption spectrum is taken between 1100 and 300 nm and shows no peak in the visible light region, meaning that the ZnO blocking layer does not interfere with the active layer absorption, which is maximal between 750-550 nm. The low absorption results from a small thickness of the printed film. SEM images show that the structure of the thin ZnO film is homogeneous, with a particle size of around 20 nm Fig. 3.23. The optical microscopy images (Fig. 3.23) show that the film is homogeneous on large scale, although differences in the thickness of the ZnO films is observed when moving from the center to the edge of the substrate.

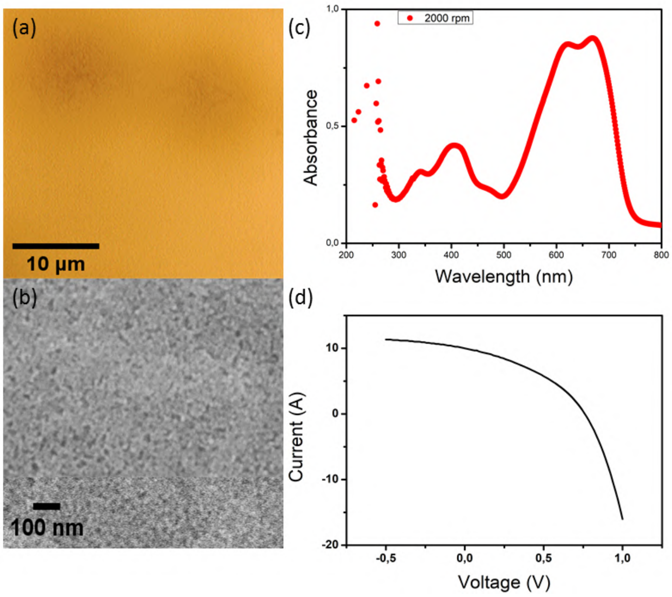

Figure 3.23:
a) optical microscopy, b) SEM image of printed ZnO, c) UV-Vis of the active layer and d) IV curve of 2000 rpm spin coated active layer.

UV-Vis spectra of the active layer are measured to determine where the polymer blend absorption range lies, as shown in Fig. 3.23. The active layer was spin coated at 2000 rpm from an o-xylene solution. The active layer shows three absorption peaks. Two of these peaks are very intense and broad (between 750 and 550 nm) and a second, weaker one, is seen at around 430 nm. For the fabricated solar cell, presently, the PCE reported in literature is not reached. The solar cell fabricated here has an average PCS of 5 %. A representative IV curve of the solar cell is plotted in Fig. 3.23. The average active layer thickness is 100 nm, which could be further optimized to match better literature PCE values. Anyhow, printing will be used to deposit the active layer as it was done for the ZnO blocking layer.

Improvements in the solar cell performance might be obtained by optimizing the ZnO layer thickness, making XRD measurements to determine its thickness, the active layer solution concentration and homogeneity, while it is reported that the latter does not play such a big role in the device performance [3].

[1] A. Wadsworth, R. Ashraf, M. Abdelsamie, S. Pont, M. Little, M. Moser, Z. Hamid, M. Neophytou, W. Zhang, A. Amassian, J.R. Durrant, D. Baran, I. McCulloch, *Acs. En. Let.* **2**, 1494–1500 (2017)

[2] H.Cha, J. Wu, A. Wadsworth, J. Nagitta, S. Limbu, S. Pont, Z. Li, J. Searle, M.F. Wyatt, D.Baran, J-S. Kim, I. McCulloch, J.R. Durrant *Adv. Mat.* **29** , 1701156 (2017)

[3] G. Zhang, R. Xia, Z. Chen, J. Xiao, S. Liu. H-L. Yip, Y. Cao, *Adv. En. Mat*, 1801609 (2018)

3.12 Printed organic solar cells based on non-fullerene acceptor molecules

K. Wienhold, P. Müller-Buschbaum

Organic solar cells have attracted growing interest as a renewable energy source as they consist of highly tunable materials. Their properties can be optimized by modification of the chemical structure of both the electron donor polymer and the small molecule acceptor as well as the choice of processing parameters. To date, a PCE of 13% could be obtained with the conjugated polymer named PBDB-T-SF:IT-4F in an organic solar cell device [1]. Film deposition was done so far with spin coating. However, towards commercialization of organic solar cells, an up-scaling of the film deposition is necessary. Printing of the active layer instead of spin coating can overcome this challenge [2, 3].

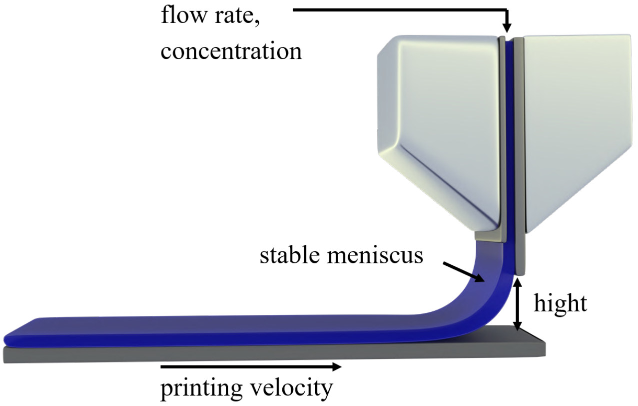

Figure 3.24:
The meniscus guided slot-die coating depends on printing velocity, height of the printer head, flow rate and concentration of the solution.

Understanding the printing process and the influence of processing parameters (Figure -3.24) on the structure and morphology of the active layers is of big significance to optimize the performance of printed organic solar cells. The quality of the printed films depends critically on the printing velocity, the height (distance between substrate and printer head), flow rate and concentration of the solution. Characterization of the printed films with UV/Vis spectroscopy, photoluminescence, optical microscopy, scanning electron microscopy and atomic force microscopy gives insight into the structure and properties of a printed active layer.

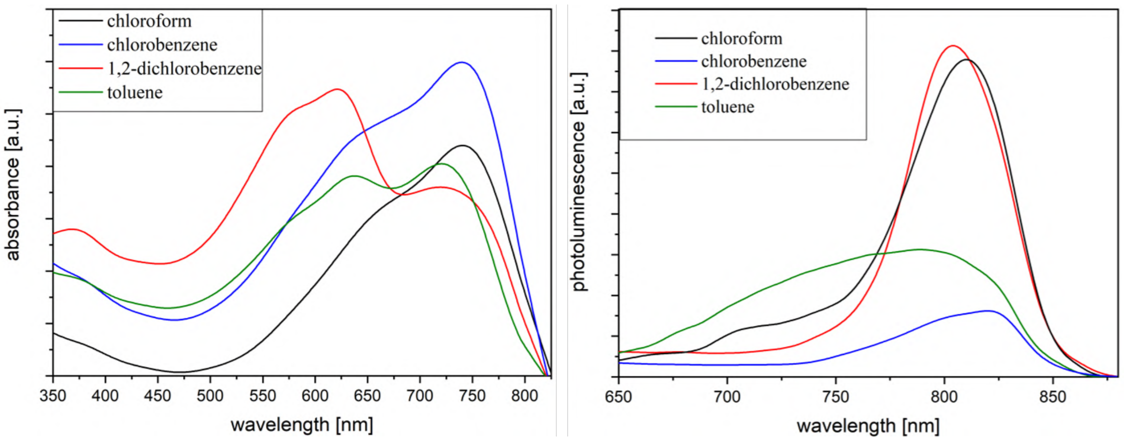

Figure 3.25:
Absorbance (left) and photoluminescence (right) of PBDB-T-SF:IT-4F in chloroform, chlorobenzene, 1,2-dichlorobenzene and toluene.

All samples were prepared by meniscus guided slot-die coating. Therefore, PBDB-T-SF and IT-4F were dissolved in an organic solvent (chloroform, chlorobenzene, 1,2-dichlorobenzene or toluene) to give solutions with a concentration of 10 mg/mL. After priting on a acid-cleaned glass substrate at room temperature, the thin films were post-characterized with optical microscopy, scanning electron microscopy and atomic fore microscopy.
The absorbance and photoluminescence spectra of PBDB-T-SF:IT-4F (Figure 3.25) were measured with a PerkingElmer Lambda 650 S UV/Vis spectrometer and a Perkin Elmer LS55 Fluorescence Spectrometer.

Printed thin films show efficient absorbance over a broad wavelength range in the region of UV/Vis light which is favorable for organic solar cells. Active layers printed with chlorobenzene show much lower photoluminescence compared to chloroform, 1,2-dichlorobenzene and toluene. This indicates an improved charge transfer from the polymer electron donor to the non-fullerene small molecule acceptor.

The surface of the active layers of PBDB-T-SF:IT-4F printed with chlorobenzene on a glass substrate are post-characterized with optical microscopy (Figure 3.26 a), scanning electron microscopy (Figure 3.26 b) and atomic force microscopy (Figure 3.26 c).

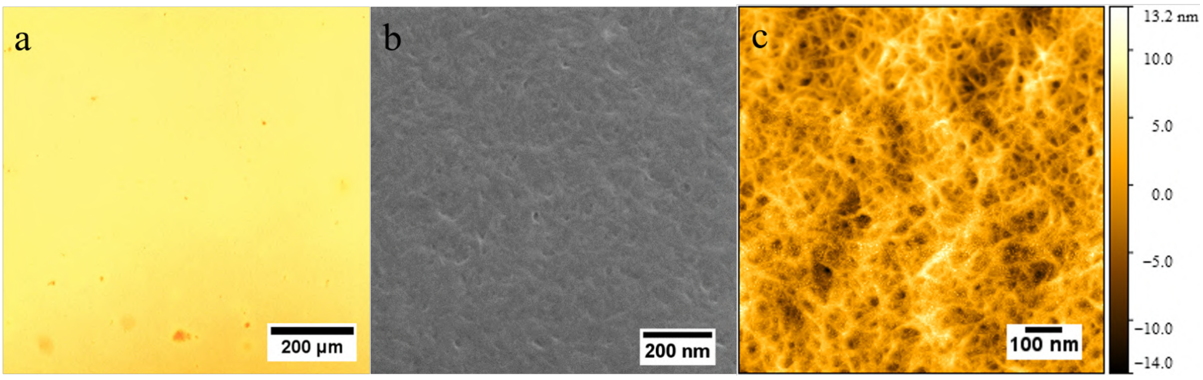

Figure 3.26:
Optical microscopy (a), scanning electron microscopy (b) and atomic force microscopy (c) of printed layers of PBDB-T-SF:IT-4F.

Meniscus guided slot-die coating of active layers with chlorbenzene lead to formation of homogenous thin films as seen with scanning electron microscopy (Figure 3.26 b) and atomic force microcopy (Figure 3.26 c).
Besides the surface structure, however, the investigation of the inner structure of active layers is essential to understand its impact on the photovoltaic device performance and to develop marketable organic solar cells with high efficiency and lifetime. This inner film structure is probed with advanced scattering experiments and the related data analysis is in progress.

[1] W. Zhao, S. Li, H. Yao, S. Zhang, Y. Zhang, B. Yang, J. Hou, *J. Am. Chem.Soc.* **139**, 7148-7151 (2017)

[2] C. N. Hoth, P. I. Schilinsky, S. A. Choulis, C. J. Brabec, *Nano Lett.* **8(9)**, 2806-2813 (2008)

[3] S. Pröller, F. Liu, C. Zhu, C.Wang,T. P. Russell,A. Hexember,P. Müller-Buschbaum, E. M. Herzig *Adv. Energy Mater.* **6**, 1501580 (2016)

4 Polymer-hybrid systems

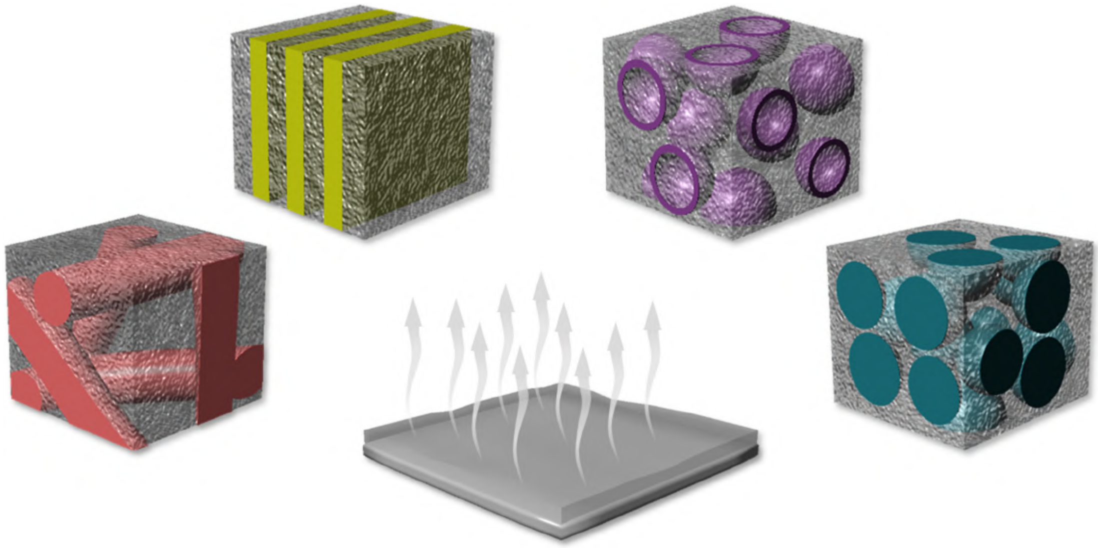

4.1 Printing thin films of water soluble polymers for photovoltaic applications

L. Díaz Piola, V. Körstgens, P. Müller-Buschbaum

Hybrid solar cells aim to combine the advantages of both, inorganic and organic materials in the active layer. The stability and high carrier mobility of the inorganic component, together with the potential low-cost production and feasibility of producing flexible devices from the organic component make the hybrid approach promising. In particular, the possibility for wet chemical device preparation in the organic material allows the use of scalable thin film coating techniques. Most of the research in this direction use organic solvents for the solar cell preparation, which does not lead to a full environmentally friendly approach. Therefore, the use of water soluble components for the organic material is of interest.

Despite the recent efforts to produce efficient devices from aqueous-processed methods [1-2], it still remains a challenge since the charge mobilities of aqueous-soluble conducting polymers are still low compared to those that are soluble in organic solvents. One of the most widely studied water-soluble conducting polymer for use in photovoltaic applications is poly[3-(potassium-6-hexanoate)thiophene-2,5-diyl] (P3P6T), a derivate from the well-known polythiophene poly(3-hexylthiophen-2,5-diyl) (P3HT) (Fig. 4.1a). This polymer, used as a donor material, has shown the feasibility of producing functional solar cells by combining it with TiO_2 nanoparticles, which is the acceptor component of the bulk heterojunction active layer (BHJ). In the active layer the incoming photons are absorbed leading to the formation of an exciton, which then travels to the interface between the donor and acceptor material to be separated into free charge carriers.

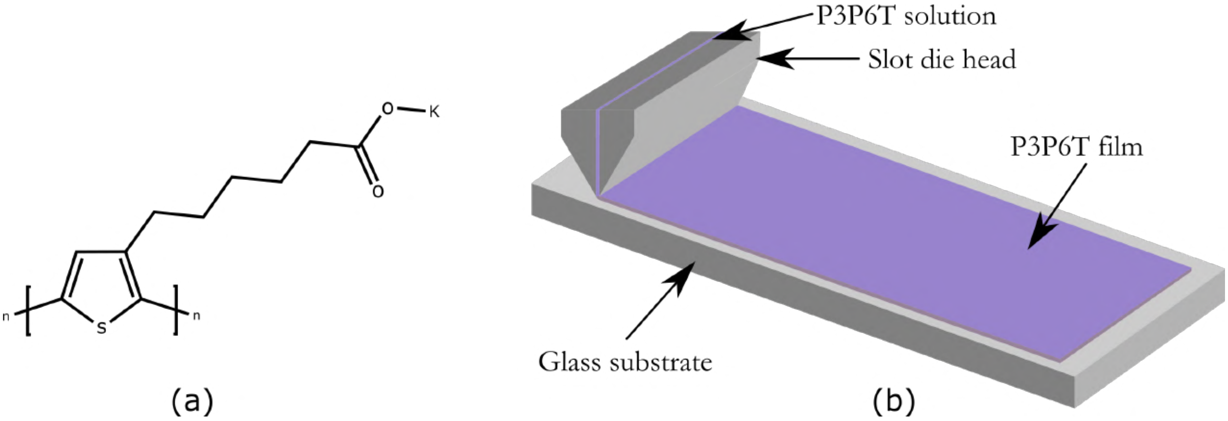

Figure 4.1:
a) Molecular structure of the polymer P3P6T; b) Sketch of the slot-die printing process. The polymer solution is introduced into the slot die head through a syringe pump and the substrate holder velocity is varied through a software controlled motor.

Slot die coating is a well-established technique in the industry due the potential coating over large surfaces, the possibility to coat at high speeds, little material waste in the overall process and the ability to integrate it in roll-to-roll systems. With this technique, the BHJ active layer for a solar cell could be coated onto a substrate for its applications in hybrid solar cells. In the present study we prepare thin films of the polymer P3P6T coated on glass substrates with a slot-die printer, which has been homebuilt in our research group. This setup has been successful to study the morphology formation of active layers in organic solar cells [3].

The basic setup is shown in Fig. 4.1b. The parameters that can be varied with the slot-die printer are: 1) the pumping rate, which is determined by a software controlled syringe, 2) the substrate holder velocity and 3) the dimensions of the slot die head, which are fixed. The glass substrates were first cleaned with DI water and then through an acidic cleaning procedure consisting of sulfuric acid, hydrogen peroxide and water solution at 80 °C during 15 min. The P3P6T solution was prepared by mixing the polymer as purchased in solid state (Rieke Metals) with water at a concentration of 10 mg/mL. After preparation it was stirred for at least 12 h at 60 °C in a sand bath until complete solution. After deposition the thin film was dried on air and then annealed for 10 min at 110 °C.

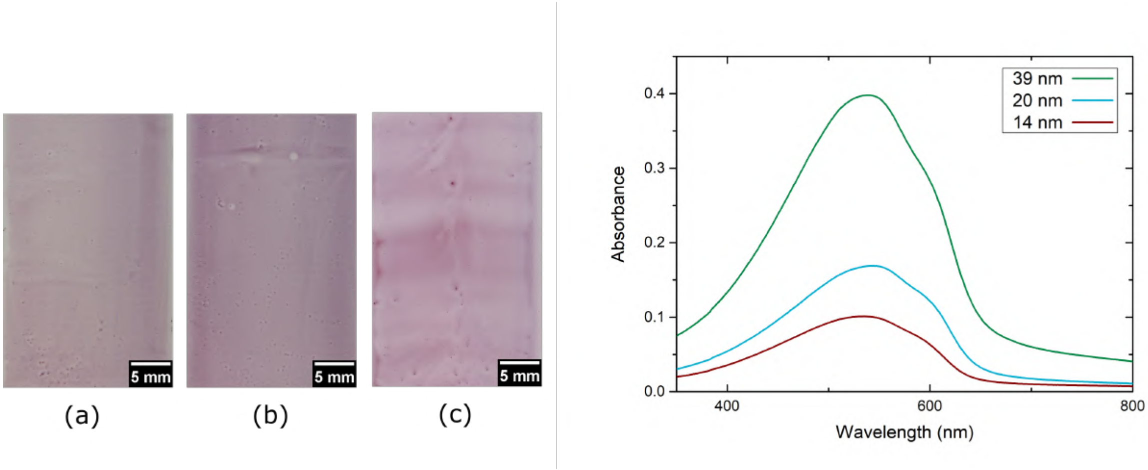

(a) (b) (c)

Figure 4.2:
Absorbance spectra of P3P6T films printed on glass substrates at different experimental conditions (pumping rate and substrate holder velocity). The thickness of the thin films are a) 14 ± 1 nm, b) 20 ± 2 nm and c) 39 ± 8 nm.

One of the important features of the components of the BHJ is their absorbance properties in the visible and ultraviolet range, since this determines the amount of energy that can be captured from solar light. In Fig. 4.2 the samples of different thin film thickness are shown, together with the UV/Vis absorbance spectra measured with a PerkinElmer Lambda 35 UV/Vis spectrometer. The peak of the absorbance spectrum at around $\sim$ 530 nm agrees with those found in the literature [1,4]. The film thickness measured with the DektakXT stylus profiler are also given, and they were measured in at least 5 different positions within the samples.

Further investigation will include the optimization of the parameters to obtain homogeneous and reproducible thin films of the polymer with the slot die coating technique in order to produce functional solar cells with laser-ablated TiO_2 nanoparticles. Furthermore, since the low charge mobility of P3P6T is a crucial limiting factor in the overall performance of these hybrid solar cells, our interest also focuses in finding an additive to this polymer that could enhance its conducting properties.

[1] V. Körstgens, S. Pröller, T. Buchmann, D. M. González, L. Song, Y. Yao, W. Wang, J. Werhahn, G. Santoro, S. V. Roth, Nanoscale, **7**, 2900–2904 (2015).

[2] S. Yao, Z. Chen, F. Li, B. Xu, J. Song, L. Yan, G. Jin, S. Wen, C. Wang, B. Yang, and W. Tian, ACS Appl. Mater. and Interfaces, **7**, 7146-7152 (2015).

[3] S. Pröller, F. Liu, C. Zhu, C. Wang, T. P. Russell, A. Hexemer, P. Müller-Buschbaum, E. M. Herzig, Adv. Energy Mater., **6**, 1501580 (2016).

[4] G. K. V. V. Thalluri, J. C. Bolsee, A. Gadisa, M. Parchine, T. Boonen, J. D'Haen, A. E. Boyukbayram, J. Vandenbergh, T. J. Cleij, L. Lutsen, D. Vanderzande, J. Manca, Sol. Energy Mater. Sol. Cells, **95**, 3262-3268 (2011).

4.2 Crystalline polymer films embedded with magnetite nanoparticles

S. Xia, K. Biswas, M. Opel[1], S. Lafuerza[2], P. Glatzel[2], P. Müller-Buschbaum

[1] WMI, Garching, Germany
[2] ESRF, Grenoble, France

Magnetic films composed of nanostructured diblock copolymer (DBC) matrix and magnetic nanoparticles (MNPs) are promising materials in lots of areas.[1] Most of the involved investigations had focused on the fabrication of polymer templates with highly-ordered nanostructure, or the homogeneity of MNPs' dispersion inside the DBC scaffolds [1]. However, the influence of MNPs on the polymer nanostructure, for example the crystalline structure of the polymer, and the electronic structure of the MNPs at different arrangements were only rarely studied. In the present work, a crystalline DBC, polystyrene-block-poly (ethylene oxide) (PS-*b*-PEO), is used as a template to host magnetite NPs (Fe_3O_4). The employed DBC has a volume fraction of the PS block as 0.29. Therefore, a cylindrical nanostructure can be obtained after microphase separation. To achieve a specific localization of the MNPs inside the PS blocks of the DBC matrix, the surface of the MNPs is functionalized with organic ligands. For a systematic study, hybrid films with different MNP concentrations are fabricated.

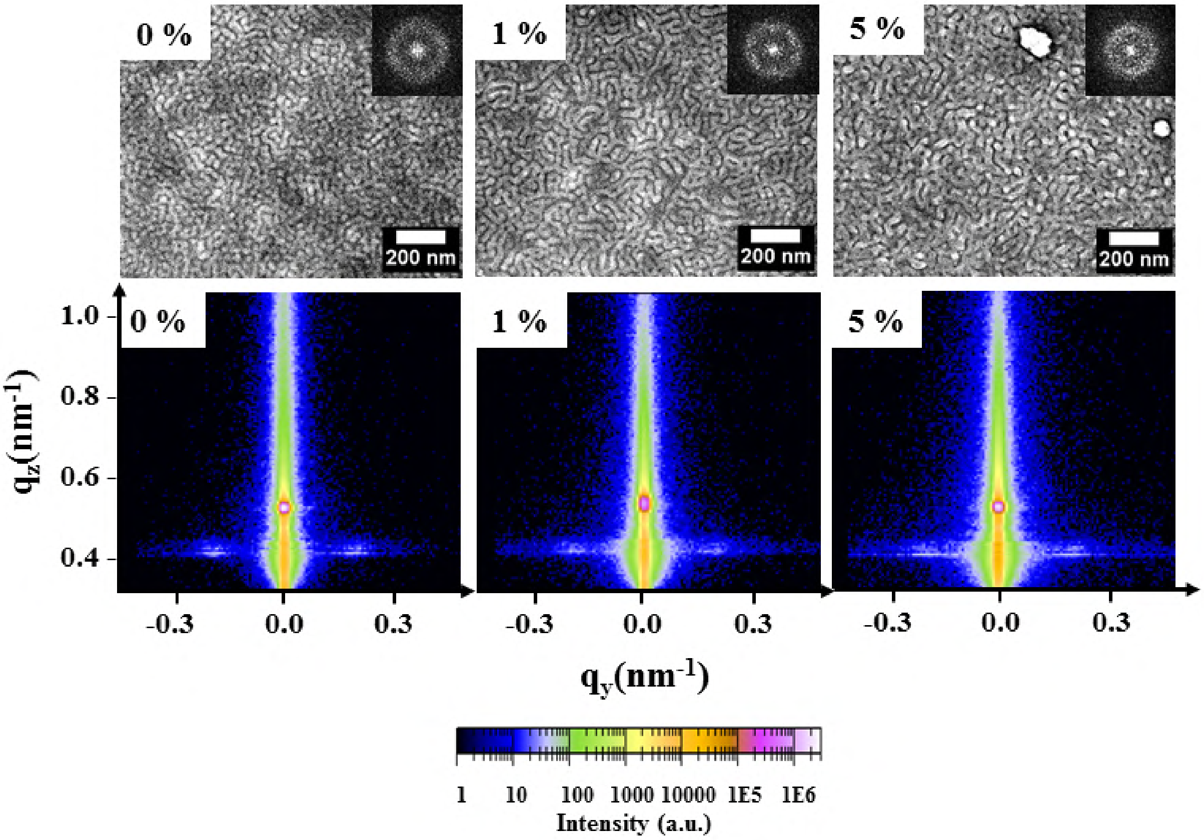

Figure 4.3:
SEM images (top row) and 2D GISAXS data (bottom row) of selected films with different MNP concentrations as indicated. On the right up corner of the SEM images are the corresponding Fast Fourier Transformation graphs.

The surface nanostructure of the as-prepared films is probed via scanning electron microscopy (SEM). Results show that a well-ordered cylindrical nanostructure is obtained for the MNP-free film. Upon incorporation of MNPs (1 wt %), the size of the polymer nanostructure increases obviously, which is caused by the selective accommodation of MNPs inside the PS domains. In addition, the structural order is enhanced, which is similar to previous report using other DBCs. [2] At high MNP concentration (5 wt %), the PS domains are oversaturated and the excess MNPs are squeezed out of the polymer matrix, which results in the presence of MNP aggregates on the film surface. Moreover, the high loading with MNPs leads to a change of the nanostructure into a less ordered one.

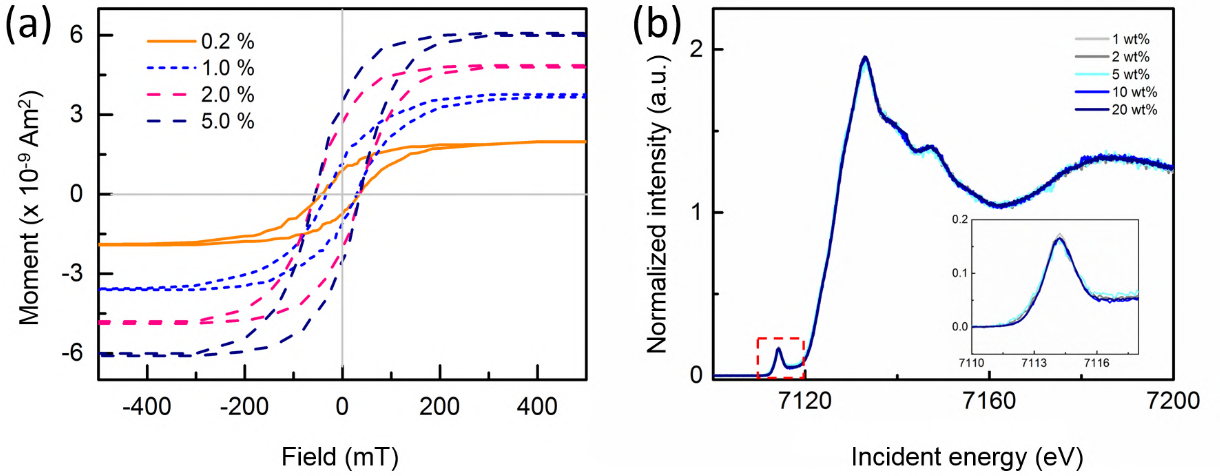

Figure 4.4:
(a) Magnetization curves as a function of magnetic field of hybrid films measured at 2 K.(b)Fe K-edge XANES spectra of hybrid films at different MNP concentrations. The zoomed-in into the pre-edge spectra (marked by a red dashed box) is zoomed in and shown at the bottom-right corner.

The inner nanostructure is studied with grazing incidence small angle X-ray scattering (GISAXS), from which a nanostructure (PS nanocylinder) size of 30.2 ± 0.8 nm is obtained for the pure DBC film. Similar to the SEM observation, the GISAXS data also show a size increase of the PS nanocylinders as the MNP concentration increases. The crystalline structure of PS-*b*-PEO is detected using grazing incidence wide angle X-ray scattering (GIWAXS). Crystallinity of the PEO domains is found to exist at low MNP concentrations. Only a slight decrease of the PEO crystal size is observed at high MNP concentrations (2 wt % and 5 wt %), which might be caused by the swelling behavior of PS domains inside the PEO matrix.

The magnetic behavior of the hybrid films is characterized using a superconducting quantum interference device (SQUID). Through the measurements at different temperatures, a superparamagnetic behavior is observed for all hybrid films irrespective of MNP concentration. Interestingly an exchange bias, which usually appears in a core-shell magnetic structure (with ferromagnetic core and anti-ferromagnetic shell), is observed in the obtained magnetization curves. This suggests that a transition from ferromagnetism to anti-ferromagnetism may occur on the MNPs' surfaces. The electronic structures of MNPs at different concentrations are examined with X-ray absorption near-edge spectroscopy (XANES). The achieved spectra at different MNP concentrations are almost identical, which evidences a stable electronic structure of MNPs at different arrangements.

[1] Y. Yao, E. Metwalli, M A. Niedermeier, M. Opel, C. Lin, J. Ning, J. Perlich, S V. Roth, P. Müller-Buschbaum, *ACS Appl.Mater.Interfaces.* **6**, 5244-5254 (2014)

4.3 Mesoporous titania backfilled with heavy element containing small molecules for hybrid photovoltaics

R. Märkl, N. Hohn, E. Hupf[1], E. Rivard[1], P. Müller-Buschbaum

[1] University of Alberta, Edmonton, Canada

Hybrid photovoltaic devices have recently attracted significant research attention due to improvements in efficiency by tailoring the organic-inorganic interface. Highest efficiencies are reached when the interface between the p-type organic polymer and the n-type inorganic counterpart is as large as possible. At the same time, the distance between the point of exciton generation and the nearest organic-inorganic interface should be smaller than the material specific exciton diffusion length to increase exciton dissociation and thereby maximize charge extraction efficiency [1]. Additional exciton diffusion length can be achieved by adding components that increase the exciton lifetime. It is anticipated that the novel heavy element containing tellurophene denoted Phen-Te-BPinPh exhibits these properties and therefore, is chosen in the present study.

Due to recent success with titania as the inorganic, electron-conducting material in the field of hybrid photovoltaics, a porous titania film is synthesized and intended to be backfilled with the novel material Phen-Te-BPinPh. The amphiphilic diblock copolymer polystyerene-b-polyethylene oxide (PS-b-PEO) is used as a templating agent. By choosing different weight distributions of the diblock copolymer, the pore sizes can be varied. Toluene is chosen as a good solvent for both blocks, while 1-butanol is added as a selective solvent for the hydrophilic PEO block. After addition of the precursor titanium (IV) isopropoxide (TTIP) and cross-linking/gelation triggered by the addition of 6M hydrochloric acid with subsequent stirring for 20 h a sol-gel is obtained. Deposition of the sol-gel onto the chosen substrate (glass or silicon) is done via spin-coating, followed by thermal annealing at 100 °C and 200 °C. To increase the film thickness, spin-coating and annealing steps are repeated five times. Finally, the mesoporous structure is achieved by removing the polymer template through calcination at 500 °C [2].

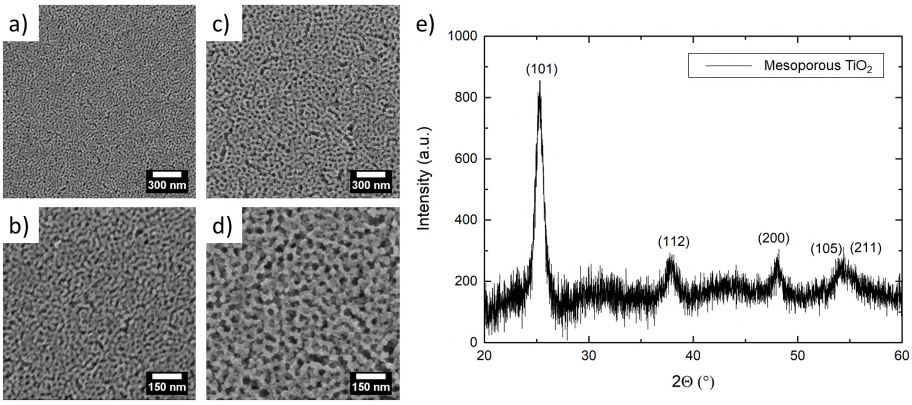

Figure 4.5:
Influence of diblock copolymer weight distribution on pore size of mesoporous titania film: small pores in a) and b) as obtained from a (20.5-b-8) PS-b-PEO template, and big pores in c) and d) as obtained from a (63-b-26) PS-b-PEO template. e) Characterization of mesoporous titania film via X-ray diffraction.

Scanning electron microscopy (SEM) is conducted as initial characterization and resulting images of the mesoporous surface morphology can be seen in Figure 4.5a)-d). Both, films with smaller and larger pore sizes appear homogeneous and the difference in pore size is clearly

visible. A weight distribution of (20.5-b-8) kg · mol^{-1} yields an average pore diameter of (17 ± 1) nm, while a weight distribution of (63-b-26) kg · mol^{-1} creates an average pore diameter of (41 ± 3) nm. Bigger pores are expected to be backfilled easier as compared to smaller pores, which is why the backfilling process is first investigated on the basis of bigger pores.
By conducting X-ray diffraction (XRD) measurements of the titania films, an anatase phase formed during the calcination process can be confirmed as shown in Figure 4.5e). This ensures the suitability for photovoltaic applications as crystallinity is associated with a higher conductivity.
Being a novel material recently developed by the Rivard Group at the University of Alberta, the tellurophene Phen-Te-BPinPh ($C_{28}H_{25}BO_2Te$) is of particular interest for photovoltaic applications. Because this small molecule contains the heavy element tellurium, an enhanced exciton lifetime is expected due to a higher probability of intersystem crossing. Its chemical structure contains conjugated bonds. Therefore an enhancement in conductivity is expected [3]. Additionally, due to the relatively small size backfilling into the mesoporous titania network is facilitated. Optical properties of Phen-Te-BPinPh are measured by UV-Vis spectroscopy as depicted in Figure 4.6a) exhibiting three absorption peaks. The absorbance is clearly dependent on the film thickness, a thicker drop-cast film showing stronger absorbance than a thinner spin-coated sample. The diffraction pattern obtained via XRD and shown in Figure 4.6b) indicates a high degree of crystallinity as many distinct peaks can be observed. A correlated good conductivity appears likely.

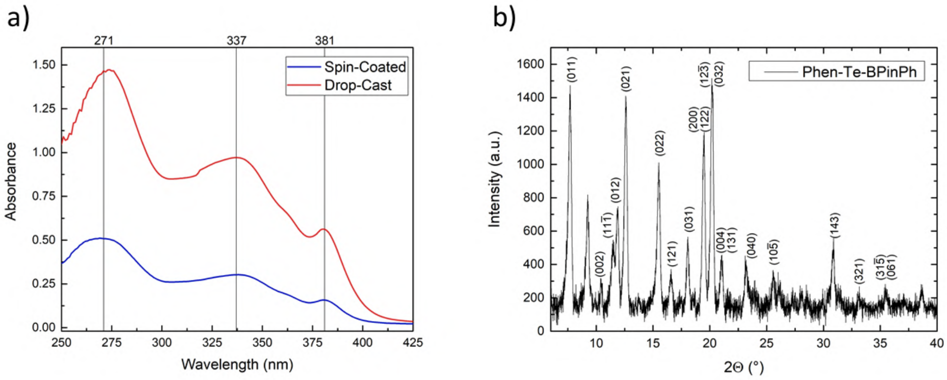

Figure 4.6:
Basic characterization of Phen-Te-BPinPh via a) UV-Vis spectroscopy and b) X-ray diffraction.

In conclusion, Phen-Te-BPinPh appears beneficial to enhance the photovoltaic performance. Together with mesoporous titania films this creates the basis for further research into various possible architectures either as a layer backfilled into the titania matrix or as a dopant in other suitable materials, such as an organic polymer.

[1] P. Müller-Buschbaum, M. Thelakkat, T. F. Fässler, M. Stutzmann, *Adv. Energy Mater.* **7**, 1700248 (2017)

[2] L. Song, W. Wang, S. Pröller, D. Moseguí González, J. Schlipf, C. J. Schaffer, K. Peters, E. M. Herzig, S. Bernstorff, T. Bein, D. Fattakhova-Rohlfing, P. Müller-Buschbaum, *ACS Energy Lett.* **2**, 991-997 (2017)

[3] G. He, B. D. Wiltshire, P. Choi, A. Savin, S. Sun, A. Mohammadpour, M. J. Ferguson, R. McDonald, S. Farsinezhad, A. Brown, K. Shankar, E. Rivard *Chem. Commun.* **51**, 5444-5447 (2015)

4.4 Nano-scale crystallization of poly(3-hexylthiophene) in printed titania pores

N. Li, L. Song, P. Müller-Buschbaum

During the past decade, hybrid solar cells have received considerable attention for solar energy conversion because they possess the combined advantages of conjugated polymers and n-type inorganic semiconductors, such as low cost, ease of production and high efficiencies. Particularly, titania and poly(3-hexylthiophene) (P3HT) have been widely studied as an electron-transport and a hole-transport material, because the anatase titania has a wide bandgap, high electron mobility and long charge-carrier lifetime and P3HT has a high hole mobility and crystallinity. For example, solid-state dye-sensitized solar cells based on TiO_2 and P3HT with quantum-dot sensitizer have been reported to reach the efficiency of 5.2%.[1] Like in organic photovoltaics, the bulk heterojunction concept can also be applied for hybrid solar cells. This means the control over morphology, crystallinity and the polymer chain orientation is of great importance for device performance. So far, the sol-gel chemistry combined with an amphiphilic block copolymer has been proven to be a promising route to tailor the nanostructures of TiO_2 films. However, the studies about the crystallization behavior of P3HT inside the TiO_2 pores are rare, in particular concerning large-scale deposition techniques.

Therefore, in the present work, we provide a new large-scale deposition route, namely printing, to fabricate nanostructured TiO_2 films on an industrial scale. The TiO_2 films with different pore sizes are tailored by the combination of sol-gel chemistry and structure-directing template. Grazing incidence small-angle X-ray scattering (GISAXS) reveals the inner morphology, and the sizes of the nanostructures and pores of the printed TiO_2 films. Additionally, the effect of the pore size on the crystalline properties of P3HT is investigated by grazing incidence wide-angle X-ray scattering (GIWAXS), such as lattice constants and crystal sizes. These detailed studies provide an importance guidance to understand the crystallization behavior of P3HT inside the titania pores, thereby designing a high-efficiency hybrid solar device.

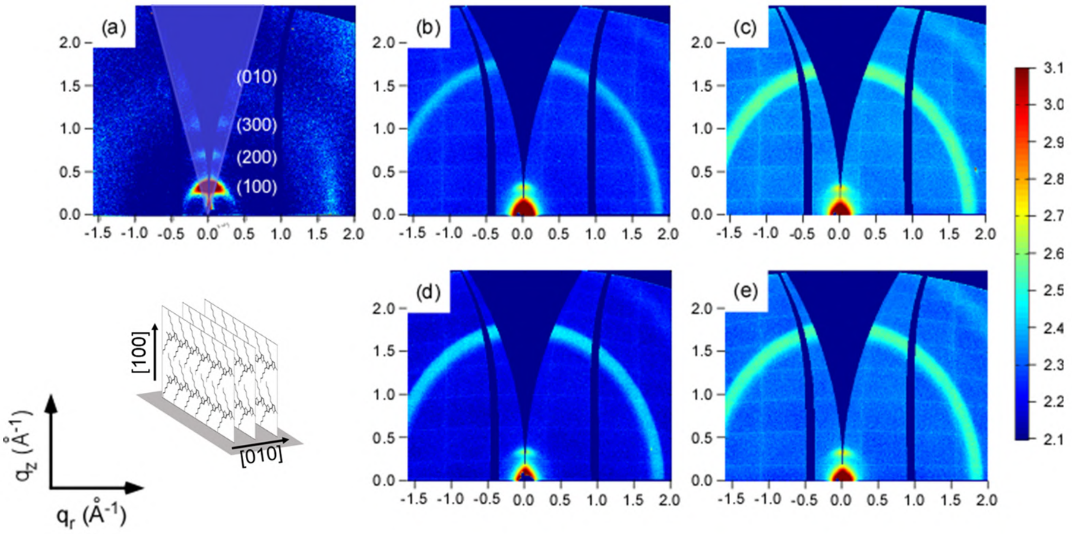

Figure 4.7:
2D GIWAXS data of (a) a pure P3HT reference sample and the printed mesoporous TiO_2 films backfilled with P3HT with varying weight fraction of TTIP: (b) 1.5%, (c) 2.0%, (d) 2.5% and (e) 3.0%.

GIWAXS measurements are performed on the P3HT-backfilled active layers to track the crystallization evolution of P3HT crystallites induced by the printed titania pore sizes. The 2-dimensional (2D) GIWAXS data of the active layers and a reference P3HT sample are shown in Fig. 4.7. The (100) peaks in the vertical direction for all samples exhibit the predominated scattering signals, indicating an edge-on orientation dominates in the P3HT crystallites. Moreover, the P3HT (100) peaks with high intensities appear in all films, whereas the P3HT (200) and (300) peaks are only present in the reference sample. One isotropic ring at q = 17-18 nm^{-1} in all the active layers mainly represents the multi-crystalline anatase titania without orientation (the anatase titania (101) peak is at 17.8 nm^{-1} according to the data from the International Center for Diffraction Data (ICDD, JCPDS # 21-1272)). Besides the titania (101) peak, the P3HT (010) peak is also found at this similar q-position. Combining all the information, we can infer that an overlapped peak of the TiO_2 (101) and P3HT (010) might exist at q = 17-18 nm^{-1} of the active layers.

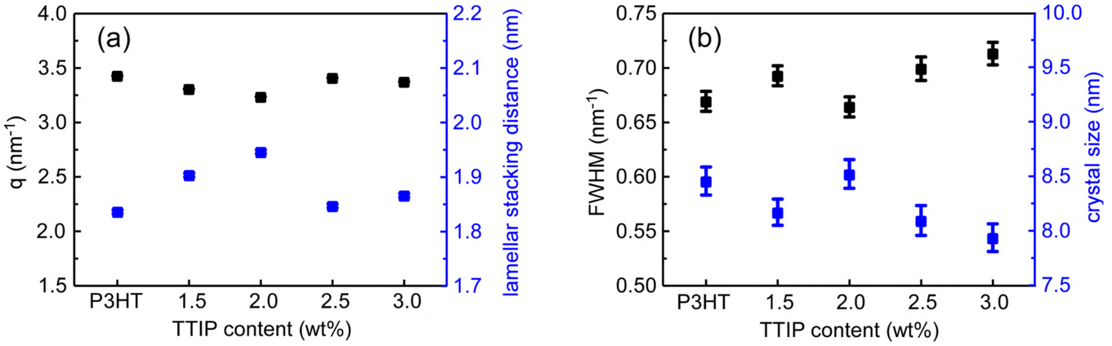

Figure 4.8:
(a) The q values of P3HT (100) peak and the corresponding lamellar stacking distances, and (b) the FWHM values and the corresponding crystal sizes obtained from GIWAXS measurements as a function of weight fraction of TTIP.

For a precise analysis, the vertical-sector integrals are taken from the 2D GIWAXS scattering patterns and fitted with Gaussian functions. The lattice constants and crystal sizes are extracted from the Gaussian fits. Fig. 4.8a shows the q-positions of the P3HT (100) peaks and the related d values, which are also called lamellar stacking distances and calculated by $d = 2\pi q^{-1}$. The full width at half-maximum (FWHM) values are correlated to the crystal sizes as shown in Fig. 4.8b, which are calculated by application from the Scherrer equation under the assumption of a constant paracrystallinity. It is noted that the lamellar stacking distances of the active layers are roughly close to be 1.83 nm of a pure P3HT reference sample. This value is in good agreement with the observations reported by Wang et al.[2] The reference sample has a crystallite size of 8.5 nm, which is a little higher or approximate to the values of the P3HT-backfilled active layers. Pröller et al. observed a crystal size of P3HT crystals is (8.4 ± 0.3) nm in P3HT:[6,6]-phenyl-C61-butyric acid methyl ester (P3HT:PCBM) systems.[3] Moreover, the relationship between the crystalline properties of P3HT, such as the lattice constants the crystal sizes, and the titania pore sizes obtained from GISAXS data will be investigated.

[1] J. A. Chang, J. H. Rhee, S. H. Im, Y. H. Lee, H. J. Kim, M. Gratzel, *Nano Lett.* **10**, 2609 (2010).

[2] W. Wang, L. Song, D. Magerl, D. Moseguí González, V. Körstgens, *Adv. Funct. Mater.* **28**, 1 (2018).

[3] S. Pröller, F. Liu, C. Zhu, T. P. Russell, A. Hexemer, P. Müller-Buschbaum, E. M. Herzig, *Adv. Energy Mater.* **6**, 1 (2016).

4.5 Synthesis of polythiophene derivatives and graphene oxide for organic solar cells

R. Schaffrinna[1], M. Schwager[1], P. Müller-Buschbaum

[1] Hochschule München, München, Germany

Polythiophene derivatives are used as electron donor in organic solar cells [1], as emissive layer in organic light-emitting diodes [2] or as semiconducting layer in organic field effect transistors [3]. The main advantages over conventional inorganic semiconductors are the flexibility, transparency, light weight and the low energy costs per surface [4]. They are also used in special applications where silicon technology fails, e.g. solar cells in glass facades or in clothing. The synthesis of new air-stable organic semiconductors is therefore essential for further progresses in organic electronics.

The homopolymers poly(3-hexylthiophene) (P3HT), poly(3-thiopheneacetic acid) (P3TAA), poly(3-thiopheneethanol) (P3TE) and the related copolymers are prepared starting from the respective monomer units by chemical oxidative polymerization. The synthesized molecules are electrically conductive due to their extended conjugated π-electron system and therefore require neither heavy metals / heavy metal complexes nor dopants for charge transport and can be easily deposited via spin-coating from a solution.

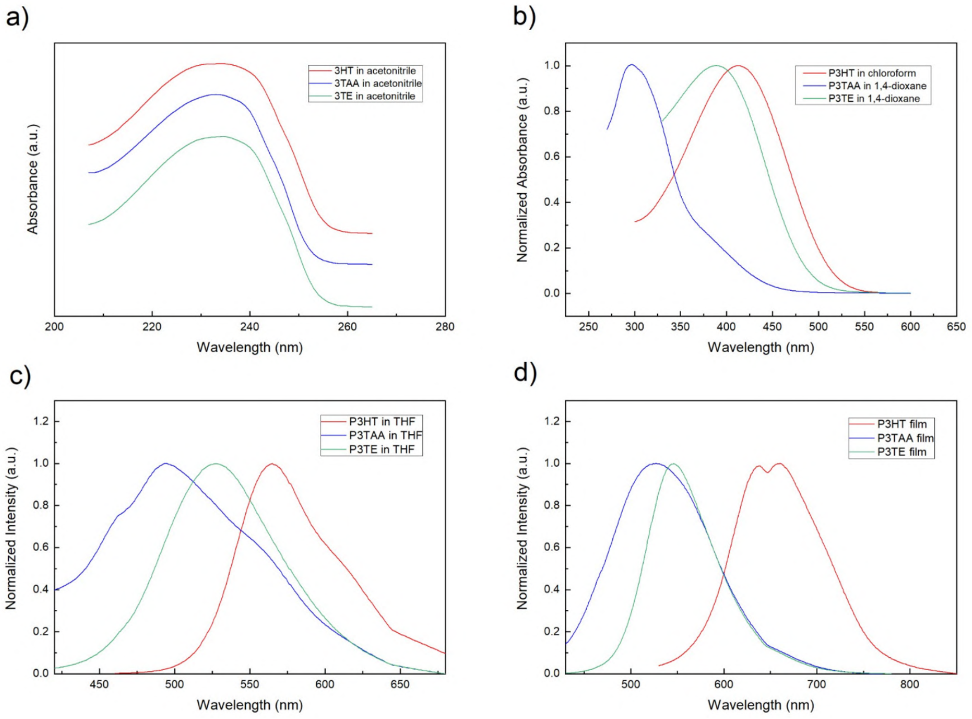

Figure 4.9:
Absorption spectra of a) dissolved monomers and b) dissolved polymers. Fluorescence spectra of c) dissolved polymers and d) polymer films.

The different substitutions of the thiophene ring results in different solubilities in organic solvents and water. The new developed P3TAA is for example very good soluble in polar solvents like acetone due to the acetic acid substituent, while P3HT on the other hand is completely insoluble in it and requires far more hazardous chemicals like chloroform or chlorobenzene, which makes the hexyl substituted molecule less environmental friendly. Shorter and longer conjugated chains can also be separated with different solvents, which also results in different optical properties of the molecule.

Fig. 4.9 a) shows the absorption spectra of the monomers dissolved in acetonitrile. They all exhibit the same absorption shape and a constant maximum at 234 nm, which makes the monomers indistinguishable from each other. The monomers 3-thiopheneacetic acid (3TAA) and 3-thiopheneethanol (3TE) show therefore no auxochromic effect, since the functional groups are located too far away from the thiophene ring. Fig. 4.9 b) shows the absorption spectra of all dissolved polymers with absorption peaks of P3TAA, P3TE and P3HT appearing at 297, 391 and 414 nm respectively, which are all redshifted compared to the respective monomers. The polymer backbone increased with polymerization, which goes along with an increased conjugated π-system and an increased mean conjugation length of the polymers. P3HT is therefore the polymer with the longest mean conjugation length, followed by P3TE and then P3TAA. Fig. 4.9 c) shows the fluorescence of P3TAA, P3TE and P3HT dissolved in THF with maxima at 494, 528 and 565 nm respectively. They also confirm the assumption of an increased polymer backbone and the sequence of the mean conjugation length, since the monomers are not able to fluorescence as they have no extended conjugated π-system, which also indicates the successful synthesis of the polymers. This is also shown in Fig. 4.9 d) where the films are all redshifted and follow the same trend as in solution.

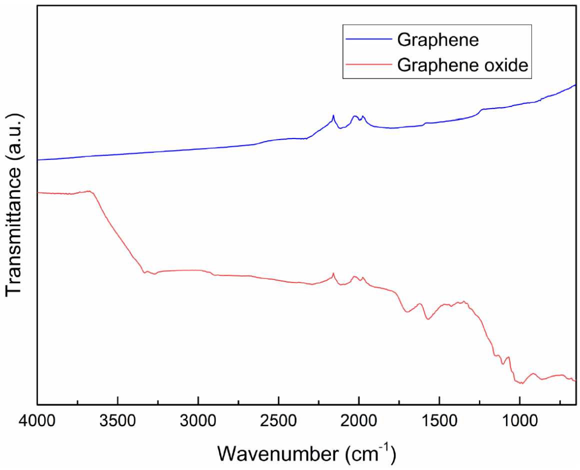

Figure 4.10:
Infrared spectra of graphene and graphene oxide.

The polymers are used together with synthesized graphene oxide as active layer in organic solar cells. Graphene oxide has compared to regular graphene a higher dispersibility in organic solvents and water, is liquid processable and forms more homogeneous layers [5]. These properties result mainly due to the functionalization of graphene oxide with carboxyl (-COOH), hydroxyl (-OH) or other polar groups. The comparison of both infrared spectra in Fig. 4.10 shows for graphene oxide additional hydrogen bond vibrations at around 3700-2500 cm^{-1} and carbonyl group vibrations at 1703 cm^{-1}, which indicate the successful synthesis of the nanomaterial.

[1] J. Li., S. Kim, S. Edington, J. Nedy, S. Cho, K. Lee, A. J. Heeger, M. C. Gupta, Y. T. Yates, *Sol. Energ. Mat. Sol. Cells.* **95**, 1123-1130 (2011)

[2] L. W. Chong,Y. N. Chou, Y. L. Lee, T. C. Wen, T. F. Guo, *Org. Electron.* **10**, 1141-1145 (2009)

[3] J. F. Chang, B. Sun, D. W. Breiby, M. M. Nielsen, T. I. Sölling, M. Giles, I. McCulloch, H. Sirringhaus, *Chem. Mater.* **16**, 4772-4776 (2004)

[4] Y. Li, G. Xu, C. Cui, Y. Li, *Adv. Energy Mater.* **8**, 1701791 (2018)

[5] V. V. Neklyudov, N. R. Khafizov, I. A. Sedov, A. M. Dimiev, *Phys. Chem. Chem. Phys.* **19**, 17000 (2017)

4.6 Comparison of UV-Irradiation and Sintering on Mesoporous Sponge-like ZnO Films

K. Wang, P. Müller-Buschbaum

Zinc oxide (ZnO) has shown great promise for application in multiple fields, especially in dye-sensitized solar cells (DSSCs) due to a broad diversity of accessible morphologies and multiple functionalities [1, 2]. In solid-state DSSCs (ssDSSCs), ZnO is generally used as an electron transport material (ETM), together with dye molecules as light absorber and hole transport materials (HTM) to consist the active layer. Excitons could be generated after light absorption (when the energy of the photons is equal to or larger than the band gap of the dye molecules) and be separated into free charge carriers at the interface between ZnO and dye molecules. The generated negative and positive charge carriers will be extracted from ZnO and the HTM to the corresponding electrode. Thus, to improve the photovoltaic performance of the ssDSSCs, ZnO films with a mesoporous interconnected network structure is beneficial. The large surface area of the mesoporous structure and the good pathway for electron transport promote the exciton separation and reduce the charge recombination in the active layer. Thus, the morphology of ZnO films is of great importance to improve the photovoltaic performance. In the present work, mesoporous sponge-like ZnO films are prepared templated with the diblock copolymer polystyrene-block-poly(4-vinyl-pyridine) (PS-b-P4VP) by sol-gel synthesis. To fabricate the corresponding photovoltaic devices, it is required to remove the diblock copolymer completely from the hybrid films since it is an insulator. Two post-treatment methods, namely UV-irradiation and high-temperature sintering, are compared with respect to the surface and inner morphology of the resulting ZnO films [3]. The post-treatment methods are expected to have a great influence on the morphology of the polymer-removed ZnO films.

For the pure ZnO films after polymer removal, SEM measurements are performed to investigate the surface morphology. As shown in Fig. 4.11, a sponge-like structure is observed for all the ZnO films, independently of the applied polymer removed method. This interconnected network not only can provide a good pathway to promote the charge carrier transport, but is also beneficial for increasing the interface area for exciton separation when application in ssDSSCs. For the ZnO films post-treated with either sintering or UV-irradiation, the pore sizes increase when increasing the polymer-to-zinc precursor (zinc acetate dihydrate, ZAD) ratio from 1:12 to 7:12. With the ratio increasing, small pores grow to larger ones and more mesopores tend to interconnect, preferentially forming larger pores (as marked by red boxes in Fig. 4.11c, d, g and h). In addition, the pore sizes are found to be smaller for the UV-irradiated films as compared to the sintered counterparts. To investigate the inner morphology, grazing-incidence small-angle X-ray scattering (GISAXS) is performed and the corresponding horizontal line cuts are given in Fig. 4.11i and j. A prominent peak at around 0.2 nm^{-1} is observed (marked by a blue box in Fig. 4.11i), and it moves to lower q_y values, which indicates the formation of larger center-to-center distances, independently of the post-treatment method. Fig. 4.11 k and l show the fitting results from the horizontal line cuts of the GISAXS pattern accordingly. It is observed that the pore sizes increase when increasing the polymer-to-zinc precursor ratio. Moreover, the pore sizes of the sintered ZnO films are larger than those of the corresponding UV-irradiated samples, which is also consistent with the SEM results.

To investigate the influence of the mesopore size of the ZnO films on the photovoltaic performance, the corresponding ssDSSCs are fabricated with the layout of FTO/compact ZnO/mesoporous ZnO/indoline dye D205/N^2,N^2,N$^{2'}$,N$^{2'}$,N^7,N^7,N$^{7'}$,N$^{7'}$-octakis(4-methoxyphenyl)-9,9$'$-spirobi[9H-fluorene]-2,2$'$,7,7$'$-tetramine (spiro-OMeTAD)/Au. Fig.

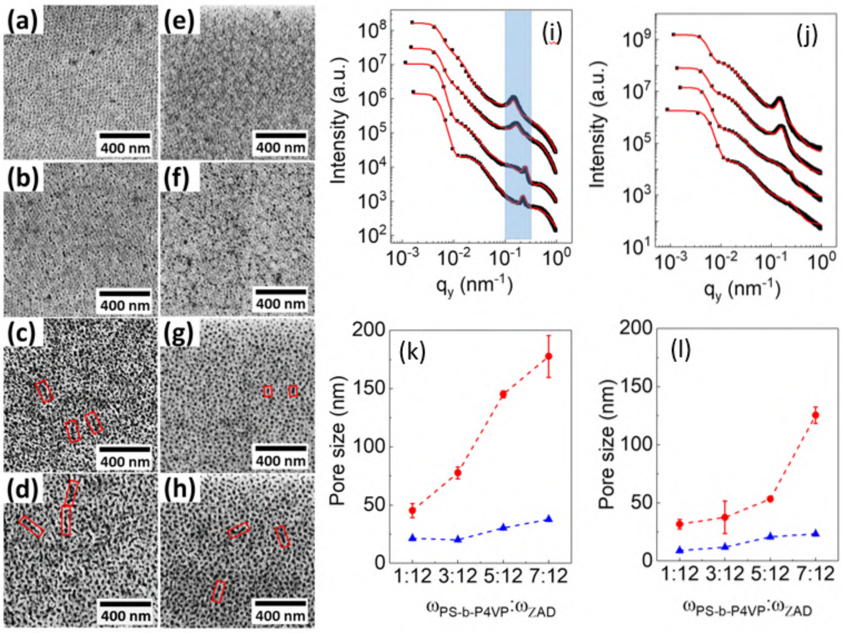

Figure 4.11:
SEM images of mesoporous ZnO films after polymer removal via (a-d) sintering and (e-h) UV irradiation with different polymer-to-ZAD weight ratios of (a, e) 1:12, (b, f) 3:12, (c, g) 5:12, and (d, h) 7:12. The red rectangles in (c), (d), (g), and (h) indicate the presence of connected pores. Horizontal line cuts (i and j) obtained from the 2D GISAXS measurements and the extracted average pore size (k and l) of mesoporous ZnO films with different polymer-to-ZAD ratios of 1:12, 3:12, 5:12, and 7:12 from bottom to top. The polymer is removed by (i, k) sintering, and (j, l) UV-irradiation. The solid red lines indicate the fits to the data.

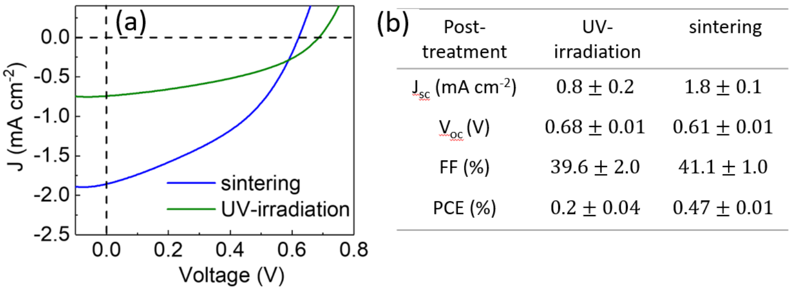

Post-treatment	UV-irradiation	sintering
J_{sc} (mA cm^{-2})	0.8 ± 0.2	1.8 ± 0.1
V_{oc} (V)	0.68 ± 0.01	0.61 ± 0.01
FF (%)	39.6 ± 2.0	41.1 ± 1.0
PCE (%)	0.2 ± 0.04	0.47 ± 0.01

Figure 4.12:
(a) Current density-voltage (J-V) characteristics and (b) device parameters extracted from J-V curves of ssDSSCs based on different post-treated mesoporous ZnO films prepared from the polymer-to-ZAD ratio of 5:12.

4.12a shows the current density-voltage (J-V) curves of the ssDSSCs based on sintered and UV-irradiated ZnO films with the polymer-to-zinc precursor ratio 5:12. The obtained photovoltaic parameters are shown in Fig. 4.12b. The power conversion efficiency (PCE) values of the devices from sintered ZnO films are more than twice of those from UV-irradiated ZnO films, which mainly originates from the improvement of J_{sc}. The increased pore size for the sintered ZnO films enhances the possibility for dye molecules and HTM to be backfilled into the ZnO films and thereby improves the connection at the interfaces of ZnO/dye/HTM.

[1] C. Y. Lin, Y. H. Lai, H. W. Chen, J. G. Chen, C. W. Kung, R. Vittal, K. C. Ho, *Energy. Environ. Sci.* **4**, 3448-3455 (2011)

[2] F. X. Liang, Y. Gao, C. Xie, X. Y. Tong, Z. J. Li, L. B. Luo, *J. Mater. Chem.C* **6**, 3815-3833 (2018)

[3] K. Wang, S. Xia, W. Cao, N. Hohn, S. Grott, L. P. Kreuzer, M. Schwartzkopf, S. V. Roth, P. Müller-Buschbaum, *J. Appl. Nano Mater.* **1**, 7139-7148 (2018)

4.7 Quantum dot solids as studied with grazing-incidence X-ray scattering

W. Chen, K. Wang[1], P. Müller-Buschbaum

[1] Southern University of Science and Technology, Shenzhen, China

Colloidal quantum dots (QDs) are promising in photovoltaic and photodetector devices due to their tunable semiconductor properties and the solution processability.[1-3] High-quality and mono-disperse colloidal QDs are synthesized normally through a hot-injection method, and one single final colloidal QD is configured as an inorganic semiconductor core and an organic outer layer of long chain ligands, like oleic acid. Moreover, comparing with cadmium chalcogenide QDs, like CdSe and CdTe, lead chalcogenide QDs, PbSe and PbS, are more suitable for those charge extraction devices, because of their intrinsic weaker exciton binding energy and more suitable absorption spectrum. In a classic device fabrication process, the QD solid is functionalized after a ligand exchange treatment, in which the organic component was substituted by short chain ligands or ions. The work function of the solid can also be changed and play a role as a specific functional layer, such as an active layer or a blocking layer in a real device. Due to the solution processability, colloidal QDs can be deposited via various methods. Not only standard methods can be used such as lab-scaled spin-coating, dip-coating, drop-casting and solution-casting, but also industrial relevant methods like printing and spray deposition are feasable. These deposition techniques integrated with various surface treatments will result in different configuration of the inner structure as well as different electronic properties of the solids.

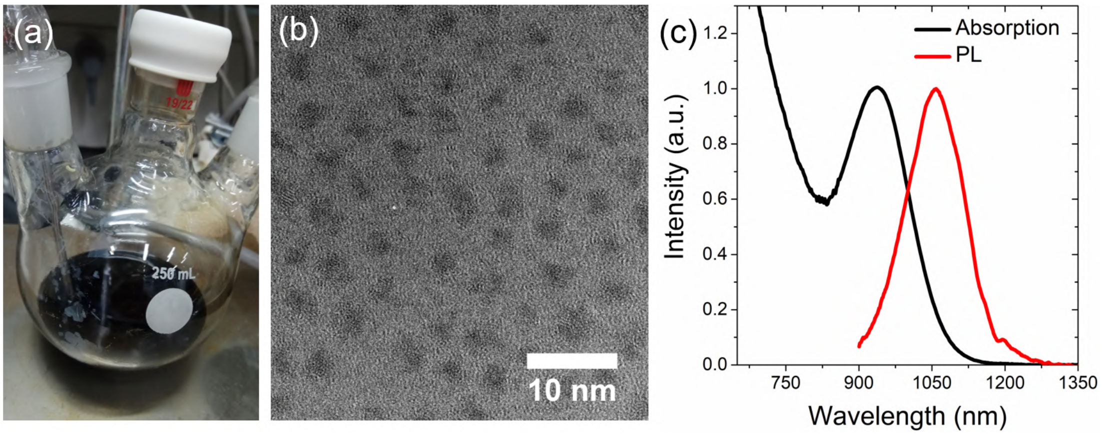

Figure 4.13:
a) As synthesized colloidal PbS QDs via hot ions injection method, b) HRTEM image of the colloidal QDs and c) the absorption and emission spectra of the QDs in solution.

In the present study, we make use of the powerful capabilities of grazing-incidence X-ray scattering (GIXS) techniques for the characterization of nanostructured films. We study the inner structure of QD solids fabricated by different deposition methods or treated by different methods. An hot ions injection method has been used to obtain high-quality oleic acid capped colloidal QDs as illustrated in Fig. 4.13(a). The size and morphology of the QDs are probbed by high resolution transmission electron microscopy (HRTEM) as seen in Fig. 4.13(b)and the optical band-gap is determined by the first exciton peak from the absorption spectrum in solution, as seen in Fig. 4.13(c). After purification and pretreatment, the QDs with certain concentration are deposited on a substrate to get the colloidal solid. To functionalize it, short ligands or ions solution were applied to perform the ligand exchange by soaking in solution for a certain time. With a rinsing process afterwards, one single cycle is accomplished. A layer-by-layer (LBL) process integrated with several cycles is performed to achieve a desired solid thickness and obtain a final close packed solid. A regular LBL process for halide ions treated QD solid is shown in Fig. 4.14(a), integrated with spray deposition, soaking, rinsing and drying processes. The 2D GIXS pattern in the small angle range (GISAXS) is shown in Fig. 4.14(b). The solid density could be evaluated from the Yoneda position derived from the vertical line cut at q_y=0. Moreover, the horizontal line cut provides information about the inter-dot spacing between neighboring QDs and on the larger domain size and the distributions, which originated from the colloidal structure collapse of the particles stacking by ligand exchange. The crystal orientation distribution of the QDs in functional solids is also investigated by GIXS in wide angle range (GIWAXS).

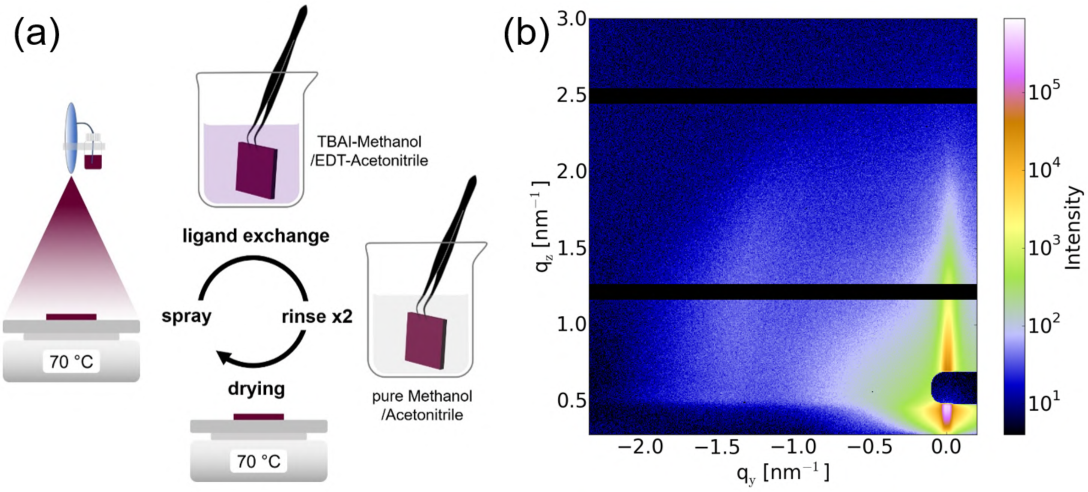

Figure 4.14:
a) LBL cycle used for spray-coating and ligand exchange treatment by iodine ions (TBAI, tetrabutylammonium iodide) and short chain EDT (1,2-ethandithiol) via soaking and rinsing processes and b) 2D GISAXS pattern of as deposit QD solid via LBL.

Beside the GIXS based structure analysis, we also use femtosecond laser based transient absorption spectroscopy (fs-TAS) to investigate the energy states distribution around the first exciton peak region. The ability to generate hot excitons of the treated solids has been evaluated and analyzed by the correspondingt spectrum at maximum deep position in the TAS map. The evolution of the energy peak position and the decay time is used to confirm the path distribution for charge hopping as well as the life time of hot excitons. The inner energy state distribution is strongly related to the inner structure distribution. In summary, these fundamental studies are very important for further improvements of complex fabrication process of the QD solids, to enable future application in optoelectronic devices.

[1] M. Liu, O. Voznny, R. Sabatini, F. Pelayo, R. Munir, A. H. Balawi, X. Lan, F. Fan, G. Walters, A.R. Kirmani, S. Hoogland, F. Laquai, A. Amassian, E. H. Sargent, *Nat. Mater.* **16**, 258-263 (2017)

[2] J. Xu, O. Voznny, M. Liu, A. R. Kirmani, G. Walters, R. Munir, M. Abdelsamie, A. H. Proppe, A. Sarkar, F. Pelayo, M. Wei, B. Sun, M. Liu, O. Ouellette, R. Quintero-Bermudez, J. Li, J. Fan, L. Quan, P. Todorovic, H. Tan, S. Hoogland, S. O. Kelley, M. Stefik, A. Amassian, E. H. Sargent, *Nat. Nanotechnol.* **13**, 456-462 (2018)

[3] O. Voznny, B. R. Sutherland, A. H. Ip, D. Zhitomirsky, E. H. Sargent, *Nat. Rev.* **2**, 17026 (2017)

4.8 The influence of carbon nano onions on the surface morphology of organic solar cells

C. Weindl, F. C. Löhrer, P. Müller-Buschbaum

Carbon nano onions (CNOs) are already widely used in science especially in the field of energy storage systems as batteries and capacitors.[1] Comparatively advantages of this fullerene like particles are a large external surface area and a high conductivity. In this work the aim is to implement them into solar cells for enhancing device parameters.

The most practical way for the production of CNOs is the thermal annealing of detonation nanodiamond powders.[2,3] The transformation of nanodiamonds to carbon onions is processed in a few steps. At the beginning, the sp^3-hybridized carbon is heated up to 200 °C to remove oxygen-containing functional groups and water. The removal of functional groups like carboxyl, anhydride and lactone groups at temperatures of about 800 °C results in dangling bonds which combine to build π-bonds. The formation of a carbon onion shell starts to begin at 900 °C. Structural defects of the nanodiamond surface ease the formation of sp_2-hybridized carbon. At temperatures of about 1100 °C an ordered graphitic structure starts to form which results in a highly ordered carbon nano onion. [1]

The particles have properties which are very interesting for solar cells. The first one is the relatively high conductivity (2-4 S/cm). Due to a ZnO conductivity of 0.015 S/cm CNOs may be able to enhance the charge carrier extraction before recombination in the ZnO layer.[4] Another aspect is the improvement of the conductivity of the active layer which may lead to a better mobility of charger carriers to the electrodes. Due to its high surface area and a particle size in the range of 5-10 nm the CNOs may also be beneficial for nanostructuring, which can improve device performance significantly via optimizing the morphology of the active layer. The last benefit may be the huge surface area of 420 m^2/g (see fig. 4.15a). This may also have a positive effect in case of artificial nanostructuring.[1]

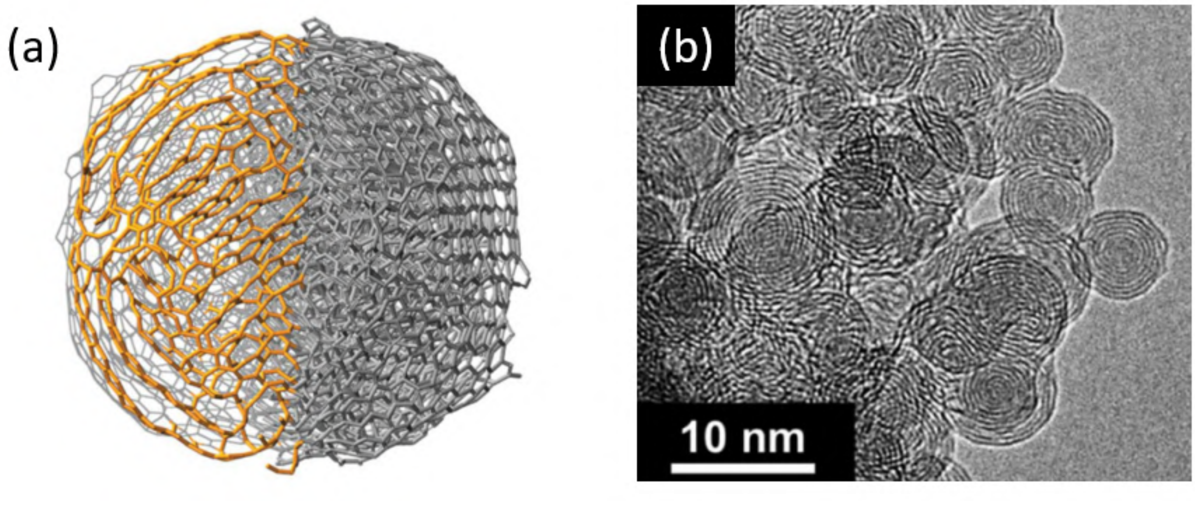

Figure 4.15: a) Sketch of the the structure of a carbon nano onion. b) Transmission electron microscopy image of CNO. Both figures are adapted from reference [1].

The surface morphology comes into account whether the CNOs lead to a change in the topography of the active layer. This characterization is done with atomic force microscopy (AFM) to probe length scales relevant to the CNOs.

measured variable	AL	ALO
Maximum height	19.36 nm	15.45 nm
Mean roughness (Sa)	0.85 nm	0.83 nm
Area texture parameter (Sku)	3.72	4.35

Table 1: AFM roughness parameters of AL and ALO

The implementation of CNOs leads to a decrease in the maximum height of the active layer, whereas there is no significant difference for the mean roughness. The Sku values determine if the specimen shows bumpy or spiky character. For solar cells a spiky surface may lead to better performance because of a higher surface area. The layers with the CNO show also a higher texture parameter which leads to sharper peaks on the surface. To get more precise data about the roughness the height profiles are plotted.

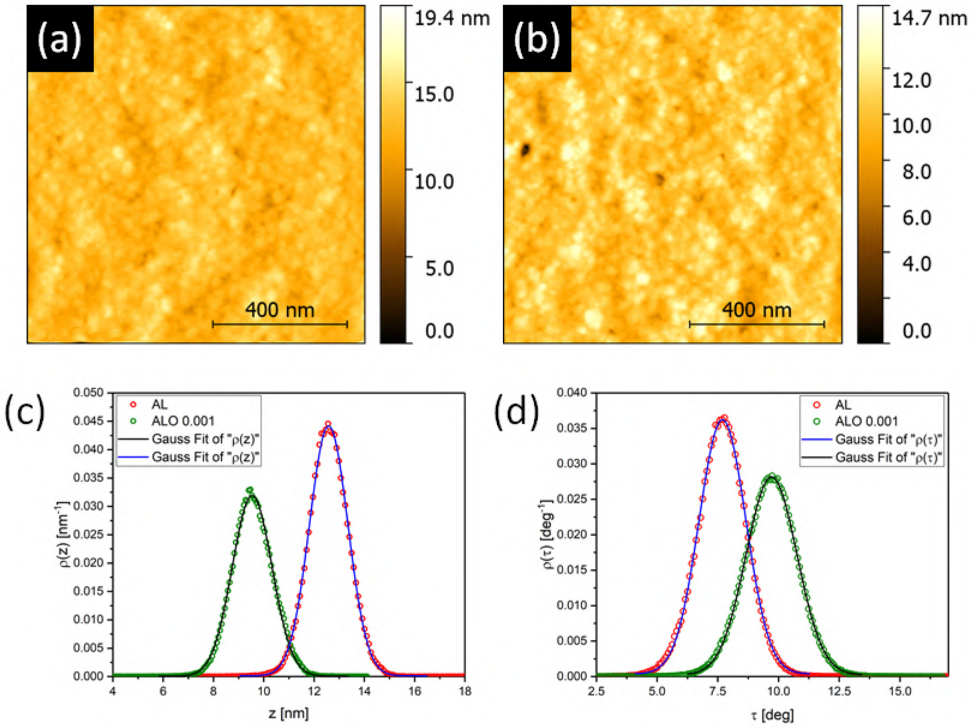

Figure 4.16: Represenatative AFM images of the active layer a) without (AL) and b) with CNOs (ALO). Distribution of c) heights and d) phase in the AFM data.

The height distributions do only differ significantly in the peak height and position, but not in the FWHM values. In case of the mechanical contrast probed by the phase in the AFM images, also a change in the FWHM is found. Thus, the CNOs have a weak impact on the film surface.

[1] M. Zeiger, N. Jäckel, V. N. Mochalin, V. Presser, *J. Mater. Chem. A* 4.9 (2016)

[2] J. K. McDonough, Y. Gogotsi, *The Electrochemical Society Interface* **22.3**, 61–66 (2013)

[3] V. L. Kuznetsov, A. L. Chuvilin, Y. V. Butenko, I. Y. Mal'kov, V. M. Titov, *Chemical Physics Letters* **222**, 343-348 (1994)

[4] S. H. Liao, H. J. Jhuo, Y. S. Cheng, S. A. Chen *Advanced Materials* **25**, 4766-4771 (2013)

4.9 Preparation of various intriguing TiO_2 structures via amphiphilic diblock copolymer assisted sol-gel chemistry

S. Yin, P. Müller-Buschbaum

In the past decades, many applications of the nanostructured TiO_2 thin films have established in our daily life. In specific applications, TiO_2 thin films with unique structures usually possess more advantages than its corresponding bulk materia.[l] Because of the low costs and an operation compatibility with the ambient conditions, amphiphilic block copolymer assisted sol-gel chemistry has been confirmed as a powerful approach towards nanostructured TiO_2 films. During the block copolymer assisted synthetic route, the hydrolysis and condensation of the TiO_2 precursor can be specifically confined into one of the blocks of the diblock copolymer through hydrogen bonds. As a consequence, the morphology control of TiO_2 can be realized by tuning the phase separation behavior of the block co-polymer in the sol-gel solution. Cheng and co-authors have successfully synthesized a variety of TiO_2 nanostructures by controlling the relative content of each component in the stock solution[2], and the huge influence of HCl addition on the resulting thin film morphology was also pointed out[3]. However, besides the HCl addition, the solvent effect during the block copolymer assisted sol-gel preparation process has rarely been studied, which is also crucial to the resulting TiO_2 morphology[4]. In the present work, the morphology evolution of the TiO_2 thin films as a function of the catalyst content and solvents category is investigated. Specifically, THF and 1,4-dioxane are used as a solvent to prepare the stock sol-gel solution, and five parallel samples with exponentially increased HCl content are prepared for each solvent. After sufficient stirring, the micellar solution is spin coated onto silicon substrates to form hybrid TiO_2/polymer composite thin films. After removing the PS-b-PEO template by calcination, different TiO_2 nanostructures are characterized with scanning electron microscopy (SEM).

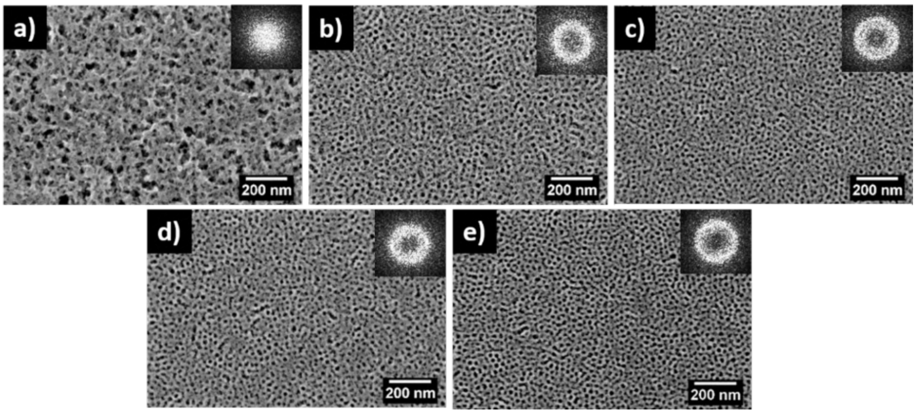

Figure 4.17:
SEM images of the TiO_2 thin films prepared with THF solvent. The up-right insets of the images refer to the corresponding FFT patterns. The volume fraction of HCl is exponentially increased from a) 0.5% to e) 8%.

Fig.4.17 shows SEM images of TiO_2 thin films prepared with THF solvent. The volume fraction of TTIP in each sample is kept constant, while the HCl content from Fig.4.17a to Fig.4.17e increases (0.5%, 1%, 2%, 4%, and 8%). As shown in Fig. 4.17, a structural transition from disorder to order is exhibited with the increase of HCl content in the stock solution, which can also be reflected by the FFT patterns of the corresponding SEM images. The appearance of the ring-like pattern from Fig.4.17b to Fig.4.17e hints the existence of isotropic and narrow distributed pores. The structure transition mechanism with respect to the HCl content can be explained as follows. In the case of the sol-gel solution with low HCl content, like the volume fraction of 0.5% in Fig. 4.17a, the electrostatic repulsion among the hydrolyzed particles resulting from the small amount of HCl is not sufficient to inhibit their further growth and agglomeration. In addition, the extension of the hydrophobic PS blocks has not been fully suppressed by the low surface energy in the solution. As a result, the randomly arranged pore structures in Fig. 4.17a is obtained. However, with the increase of the HCl content, the greatly enhanced surface energy and effectively suppressed aggregation of the hydrolyzed TiO_2 jointly lead to the formation of the neatly arranged porous structures from Fig. 4.17b to Fig. 4.17e.

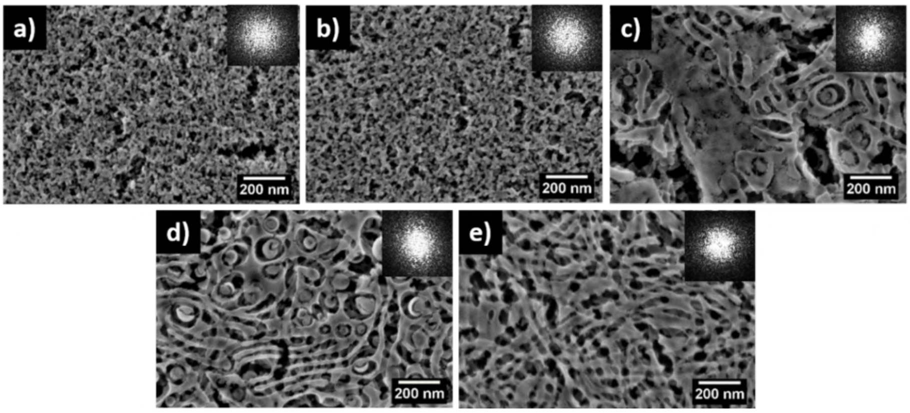

Figure 4.18:
SEM images of TiO_2 thin films prepared with 1,4-dioxane. The up-right insets of the images refer to the corresponding FFT patterns. The volume fraction of HCl in the samples exponentially increased from a) 0.5% to e) 8%.

Fig.4.18 exhibits the SEM images of TiO_2 thin film prepared with 1,4-dioxane as solvent. As seen in Fig. 4.18a and Fig. 4.18b, a similar foam-like structure (similar with respect to Fig. 4.17a can be obtained when the volume fraction of HCl is 0.5% and 1%, respectively. The formation of the foam-like structure can also be assigned to the low surface energy and aggregation of the nanoparticles in the solution. However, with the increase of the HCl content in the solution, like the volume fraction of 2% in Fig.4.18c, a coexisting structure of vesicles, nanowires and large aggregates is obtained. The formation of this inhomogeneous structures could be attributed to the variation of the surface energy between PS blocks and the surrounding solvent. Compared with the random structures, the appearance of the vesicle and nanowire structures in Fig.4.18c effectively accommodate the extra surface energy caused by the higher HCl content. However, the decreased surface energy associated with the formation of the vesicles and nanowires makes it very difficult to maintain the stability of the new sol-gel system. As a result, some large aggregates are formed. With the further increase of the HCl content, the resulting higher surface energy effectively inhibits the aggregation of the particles in the solution, which leads to the formation of the high specific surface area structures in Fig. 4.18d and Fig.4.18e.

[1] Y. Mai, A. Eisenberg, *Chemical Society Reviews* **41**, 5969 (2012)

[2] Y. Cheng, J. Gutmann, *J. Am. Chem. Soc.* **128**, 4658-4674 (2005)

[3] N. Hohn, S. Schlosser, L. Bießmann, L. Song, S. Grott, S. Xia, K.Wang, M. Schwartzkopf, S. Roth, P. Müller-Buschbaum, *ACS Appl.Nano Mater.* **1**, 4227-4235 (2018)

[4] C. Wang, Y. Ying, *Chem. Mater.* **11**, 3113-3120 (1999)

5 Real-time characterization

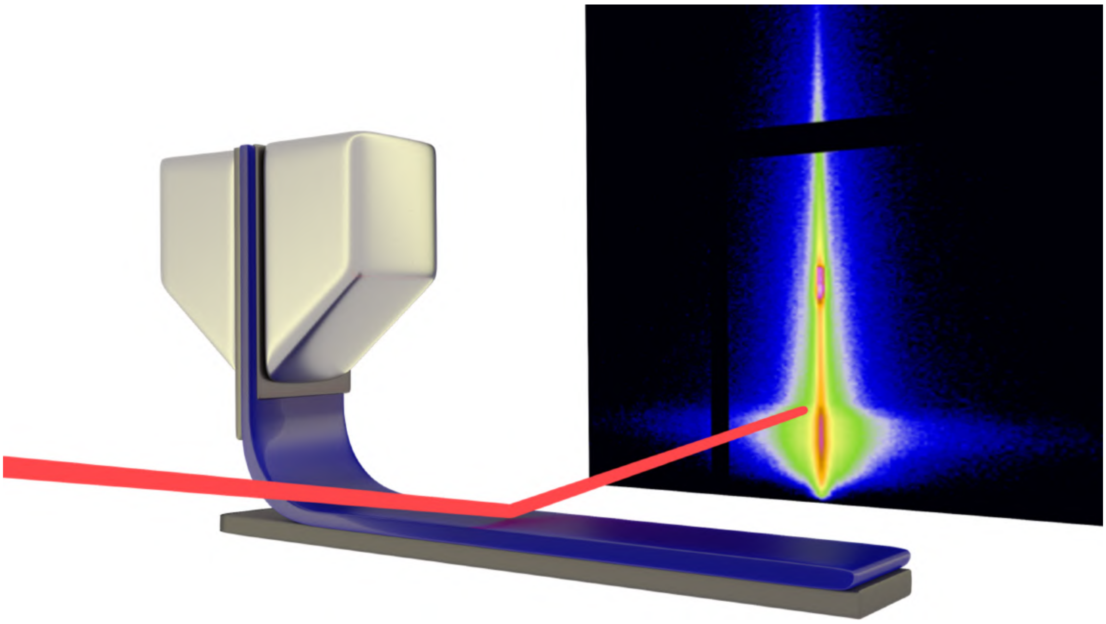

5.1 In-situ GISAXS investigation of silver sputter deposition on conjugated block copolymer thin films

M. Gensch[1,2], P. Müller-Buschbaum[2], S. V. Roth[1,3]

[1] DESY, Hamburg, Germany
[2] TUM, Garching, Germany
[3] KTH, Stockholm, Sweden

Understanding the growth of metals on and inside polymer thin films is crucial for many applications e.g. solar cells [1] or sensor applications [2]. The need of controlling the polymer structure for solar cell applications is substantial for the performance of the device. Therefore, rod-coil copolymer thin films with a conjugated block can be a route to create these nanostructures. Rod-coil copolymers are used as a template for organic solar cells, in case the amorphous layer will be removed and replaced by an acceptor material [3]. Common techniques to prepare these nanocomposites of metal/polymer films are solution casting for thin polymer thin films in the nanometer range and subsequent sputter deposition to create a thin metal film. The sputter process can be controlled precisely to create a thin nanostructured metal film. During the sputter deposition the samples were investigated by grazing incidence small angle X-ray scattering (GISAXS) to obtain information about the lateral and vertical arrangement of the metal clusters on the polymer template. The thickness of the samples are in the nanometer range, smaller than the domain period length of the copolymer film. The films were deposited by solution casting on organic cleaned silicon substrates. The concentration of the solution is 5 mg/mL for the copolymer thin film. The *in situ* GISAXS experiments were performed at the beamline P03 in Hamburg DESY [4]. The P03 sputter deposition chamber was used with RF sputter deposition and a silver target. The measurements were done at an incident angle of α_i= 0.4° and beam energy of 0.985 Å. The sample to detector distance was SSD = 2529 mm. The detector was a Pilatus 1M with a pixel size of 172x172 μm^2. The direct and specular beam, which is reflected from the sample to the detector, are shielded by beamstops to protect the detector from damage. At the Yoneda peak, which is characteristic for every material, horizontal line cuts were made to analyse the lateral formation of the silver clusters on the polymer domains.

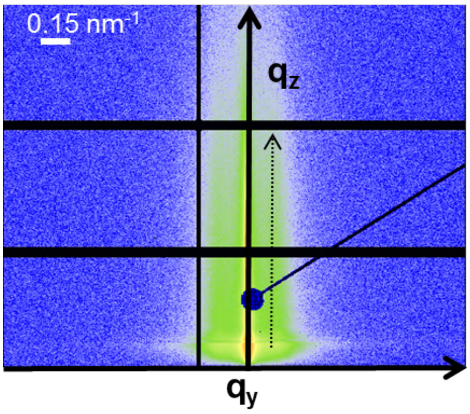

Figure 5.1:
The GISAXS pattern of the PMMA-b-P3HT copolymer thin film shows a clear domain peak for the thin films indicated by a dashed arrow.

Fig. 5.1 shows the GISAXS pattern of PMMA-b-P3HT. From the results of the GISAXS measurements one gain the size of the domain period of the copolymer template of around L = (42 ± 3) nm for the 20 nm thin layer. The domains are seen as lateral strips in the Yoneda cut in fig. 5.2

(dashed arrow). The approaching silver cluster peak is clearly visible on the thin copolymer film (black arrow). Due to the ordered hexagonal copolymer film, a continuous growth on the polymer blocks is achieved. The decorating of the metal clusters on the domains is clearly visible in fig. 5.2a by the increasing density contrast of the polymer blocks. In fig. 5.2b the result of the cluster and domain peak fitting is shown in the 2D-Colorplot, compared to the experimental GISAXS results in fig. 5.2a, which are in good agreement. From the GISAXS measurements, the average mean distance and the radii from the clusters were extracted by the geometrical model from Schwartzkopf et al. [5] see fig. 5.2c. The percolation threshold (2R/D=1), where conductive pathways start to form, was determined and shown in fig. 5.2d.

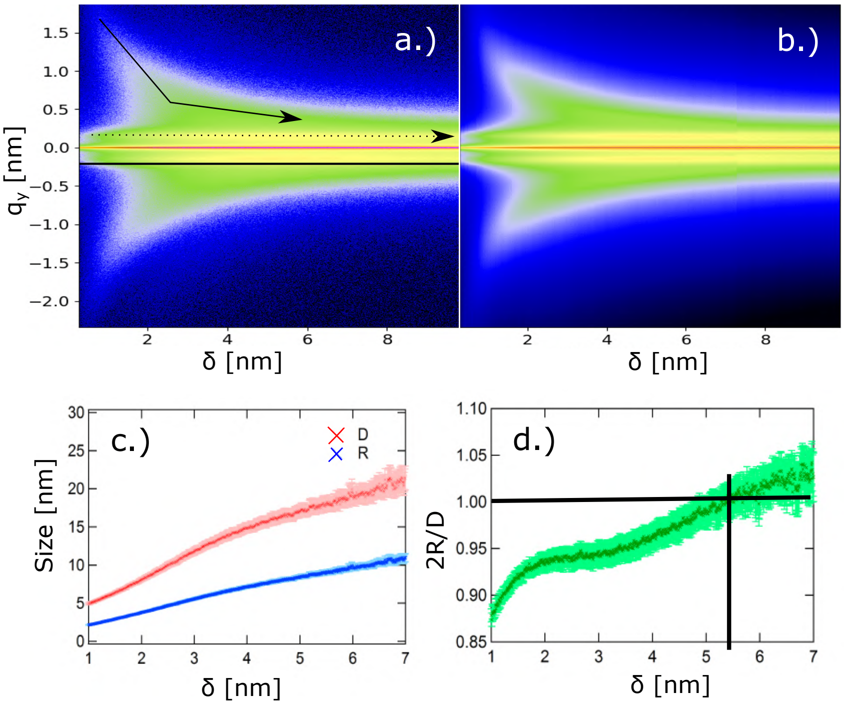

Figure 5.2:
a) Map of the horizontal line cuts from 2D GISAXS data of the metal/polymer composite measured during increasing silver thickness via sputter deposition. b) Corresponding fit of the cuts being in good agreement to the data. c) Radii and the distances of the silver clusters on the copolymer film and d) percolation threshold, determined by the ratio between the radii and the average distance of the clusters.

[1] G. Kaune, M. A. Ruderer, E. Metwalli, W. Wang, S. Couet, K. Schlage, R. Röhlsberger, S. V. Roth, P. Müller-Buschbaum, *ACS Appl. Mater. Interfaces* **1**, 353–360 (2009)

[2] F. Faupel, V. Zaporojtchenko, T. Strunskus, M. Elbahri, M. *Adv. Eng. Mater.* **12**, 1117–1190 (2010)

[3] I. Botiz, S.B. Darling, *Macromolecules* **42**, 8211–8217, (2009)

[4] A. Buffet, A. Rothkirch, R. Döhrmann, V. Körstgens, M. M. A. Kashem, J. Perlich, G. Herzog, M. Schwartzkopf, R. Gehrke, P. Müller-Buschbaum, S. V. Roth *Journal of Synchrotron radiation* **19**, 647–653 (2012)

[5] M. Schwartzkopf, G. Santoro, C. J. Brett, A. Rothkirch, O. Polonskyi, A. Hinz, E. Metwalli, Y. Yao, T. Strunskus, F. Faupel, P. Müller-Buschbaum, S. V. Roth *ACS Appl. Mater. Interfaces* **7(24)**, 13547–13556 (2015)

5.2 In-situ GISAXS investigation of spray deposited ß-lactoglobulin/titania films

J. Heger, W. Chen, C. Brett[1], W. Ohm[2], S. V. Roth[1],[2], P. Müller-Buschbaum

[1] KTH, Stockholm, Sweden
[2] DESY, Hamburg, Germany

Hybrid solar cells are promising systems for photovoltaic energy conversion. Their active layer consist of an organic/inorganic semiconductor junction. The organic part enables light-weighted, flexible and semitransparent characteristics. The inorganic part brings high charge carrier mobility and long-term stability with respect to degradation. Since being all-solvent processable, the hybrid systems can be fabricated on large industrial scales, e.g. by spray deposition. The tight binding of photo-generated Frenkel-like excitons in organic semiconductors challenges charge carrier separation and therefore the power converting efficiency of the solar cell. Before recombination, which happens within about 10 nm, the exciton must be separated at an electrochemical interface, so that the carriers can move to their corresponding electrodes. Thus, tailoring morphology of the active layer is a crucial issue in organic photovoltaic. Hybrid solar cells are able to be fabricated by filling a nanostructured inorganic scaffold with the organic material [1]. So far, our group successful uses sol-gel chemistry assisted templating of inorganic materials by diblock copolymers [2] and in-situ spray deposition [3]. However, this process is linked to organic solvents and environmentally toxic conditions.

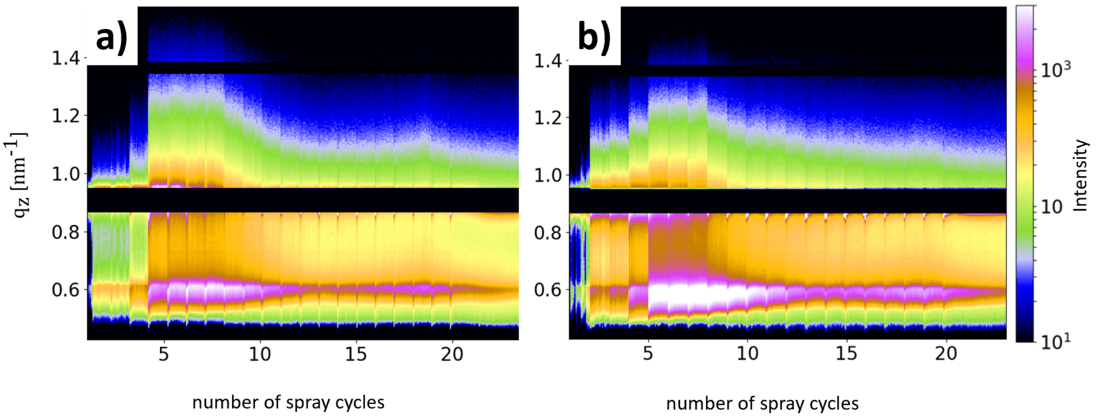

Figure 5.3:
2D color plots of vertical cuts at q_y = 0 nm^{-1} of samples denaturated at a) pH = 2 and b) pH = 5.

As a novel approach, we introduce the bovine whey protein ß-lactoglobulin as tailoring agent. It is water-soluble and forms different structures within denaturation, e.g. from fibrils to spheres. We want to understand the influence of ß-lactoglobulin on the morphology of TiO_2 at different acidic conditions and the film development during spray deposition. Therefore, titanium tetraisopropoxide (TTIP) serves as titania precursor. It is mixed with ß-lactoglobulin, purified water and different amounts of hydrochloric acid, yielding a pH of 2 and 5. The protein is denaturated by heating the blend at 90° C for 24 h under stirring. Next, the resulting sol-gels are sprayed on a cleaned silicon substrate.

The in-situ GISAXS experiments were carried out at P03 beamline, DESY. The substrate was placed in a distance of 20 cm to the spray nozzle on top of a heating plate at 120° C and in 5 m to the detector at an incident angle of 0.4°. Nitrogen was used as carrier gas with a pressure of 1 bar. The whole setup was mounted on a linear stage, which periodically moved the sample perpendicular to the beam, in order to avoid beam damage. An individual spray cycle lasted 3 s, 0.2 s of spray pulse, followed by 2.8 s of drying. This was repeated 20 times, followed by 10 s annealing. GISAXS measurements were performed every 0.1 s.

Figure 5.3 shows a 2D color plot of vertical cuts at q_y = 0 nm^{-1} for both samples during the whole spray process. One can see periodically changes of the Yoneda and specular peak position, which is related to the spray cone pressing against the substrate. For both samples the Yoneda peak at around q_z = 0.6 nm^{-1} shows a maximum between the 6th and 7th spray cycle followed by a second side maximum between the 18th and 19th pulse. The sample prepared at the pH of 5 has a stronger intensity in diffuse scattering and the Yoneda region compared to the sample at pH of 2. Differences have to be evaluated in more detail, comparing the individual cuts in vertical and horizontal direction.

After spray deposition, the samples are calcined at 500° C for 2 hours and a heating ramp of 5° C per minute. This removes the protein template and improves the crystallinity of the remaining nanostructured titania. Scanning electron microscopy images before and after calcination of samples denaturated at pH of 2 are shown in figure 5.4 a) and b), respectively. The as deposited sample shows interconnected fibrils within a jellylike protein phase, covering TiO_2. During spray deposition, the ß-lactoglobulin/TiO_2 composites are atomized by a nozzle and distributed randomly along the substrate by nitrogen, yielding a surface of high roughness. The calcined sample shows TiO_2 with different structure sizes. Larger channels with 200 nm to 300 nm of diameter are separated by titania consisting of pores around 20 nm to 30 nm and spherical TiO_2 nanoparticles of about 10 nm in diameter. The large structures are tailored by bundles of protein fibrils while the smaller pores are caused by the jellylike protein phase.

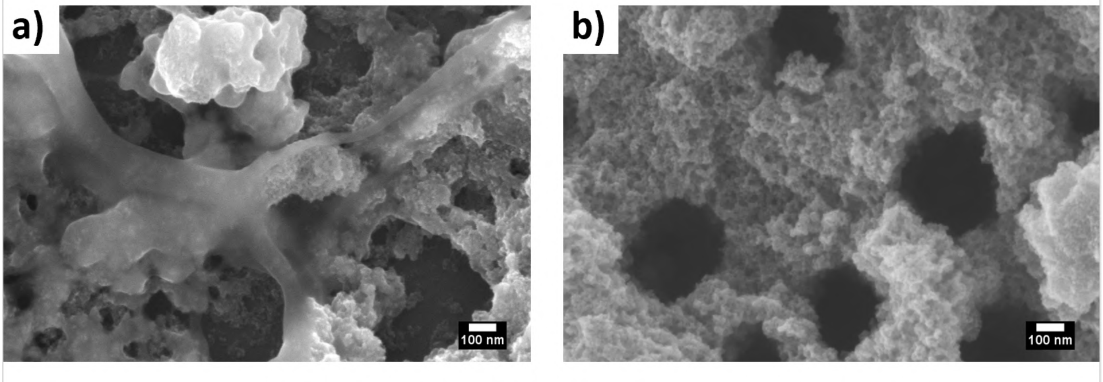

Figure 5.4:
Scanning electron microscopy images of spray-coated samples a) as deposited and b) after calcination at 500° C.

In a solar cell these channels can enhance the backfilling efficiency of organic polymers. The radii of the pores fit with around 15 nm the exciton diffusion length very well. The overall roughness of the sprayed sample increases the light scattering, which reduces efficiency loss due to reflection. This assumptions have to be investigated by further experiments.

[1] M. Rawolle, K. Sarkar, M. A. Niedermeier, M. Schindler, P. Lellig, J. S. Gutmann, J.-F. Moulin, M. Haese-Seiler, A. Wochnik, C. Scheu, P. Müller-Buschbaum, *ACS Appl. Mater. Interfaces* **5**, 719-729 (2013)

[2] G. Kaune, M. Haese-Seiler, R. Kampmann, J.-F. moulin, Q. Zhong, P. Müller-Buschbaum, *J. Poly. Sci. Part B.* **48**, 1628-1635 (2010)

[3] N. Hohn, S. J. Schlosser, L. Bießmann, L. Song, S. Grott, S. Xia, K. Wang, M. Schwartzkopf, S. V. Roth, P. Müller-Buschbaum, *ACS Appl. Nano Mater.* **1**, 4227-4235 (2018)

5.3 Impact of catalytic additive on spray deposited and nanoporous titania thin films observed via *in situ* X-ray scattering: implications for enhanced photovoltaics

N. Hohn, S. J. Schlosser, L. Bießmann, L. Song, S. Grott, S. Xia, K. Wang, M. Schwartzkopf[1], S. V. Roth[1,2], P. Müller-Buschbaum

[1] DESY, Hamburg, Germany
[2] KTH, Stockholm, Sweden

Mesoporous titania thin films play a key role in the development of hybrid or dye sensitized solar cells. To fabricate mesoporous titania thin films, the amphiphilic diblock copolymer polystyrene-b-poly(ethylene oxide) (PS-b-PEO) is used as a template in a sol-gel synthesis approach. *In situ* grazing incidence small angle X-ray scattering (GISAXS) is applied to investigate the structure formation process during spray deposition. Note that the selected deposition technique (spray deposition) is upscalable for potential industrial application.

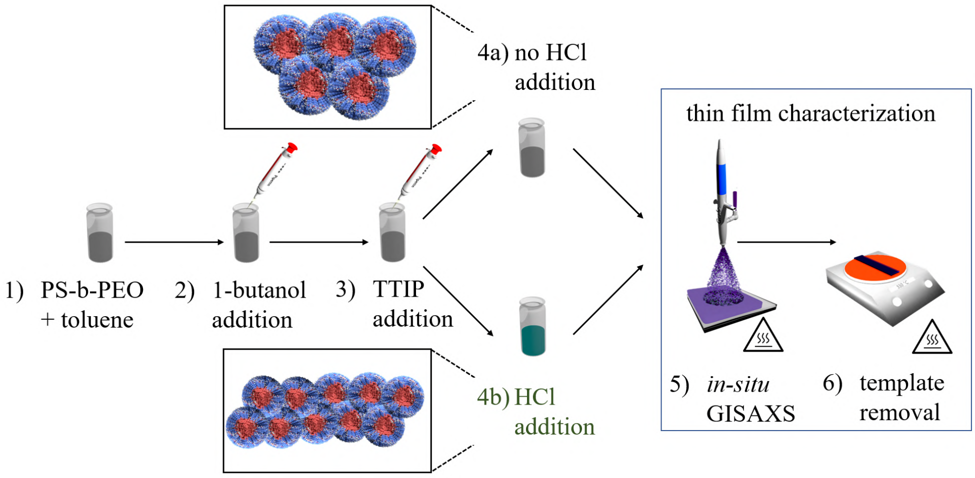

Figure 5.5:
Schematic overview of steps involved in the preparation of mesoporous titania thin films. (1) The initial solution is prepared based on the diblock copolymer PS-b-PEO in toluene and followed by (2) the addition of the bad solvent 1-butanol. (3) TTIP is selectively incorporated into the PEO domain of formed micelles. Unlike (4a) step (4b) consists of HCl addition to the solution. (5) *In situ* GISAXS measurements during spray deposition and (6) subsequent template removal through high-temperature treatment. Reprinted with permission from [2]. Copyright 2018 American Chemical Society.

A schematic overview of the mesoporous titania thin film synthesis routine is shown in Figure 5.5. Initially, the good solvent toluene is used to dissolve the diblock copolymer PS-b-PEO. The poor solvent is added to induce phase separation of the employed diblock copolymer. Note, that the volume mixing ratio of toluene and 1-butanol was chosen to yield an azeotrope solvent mixture. In step 3) the precursor titanium (IV) isopropoxide (TTIP) is selectively incorporated into the PEO phase of the polymer template. Two solutions are prepared to analyze the impact of HCl on the structure formation process of composite PS-b-PEO/titania thin films. While WHCl labeled solutions do contain HCl as a catalytic additive, NHCl labeled solutions do not contain any HCl. *In situ* GISAXS is then applied during spray deposition. Afterwards, template removal is performed through high temperature annealing and a mesoporous titania thin film is obtained.

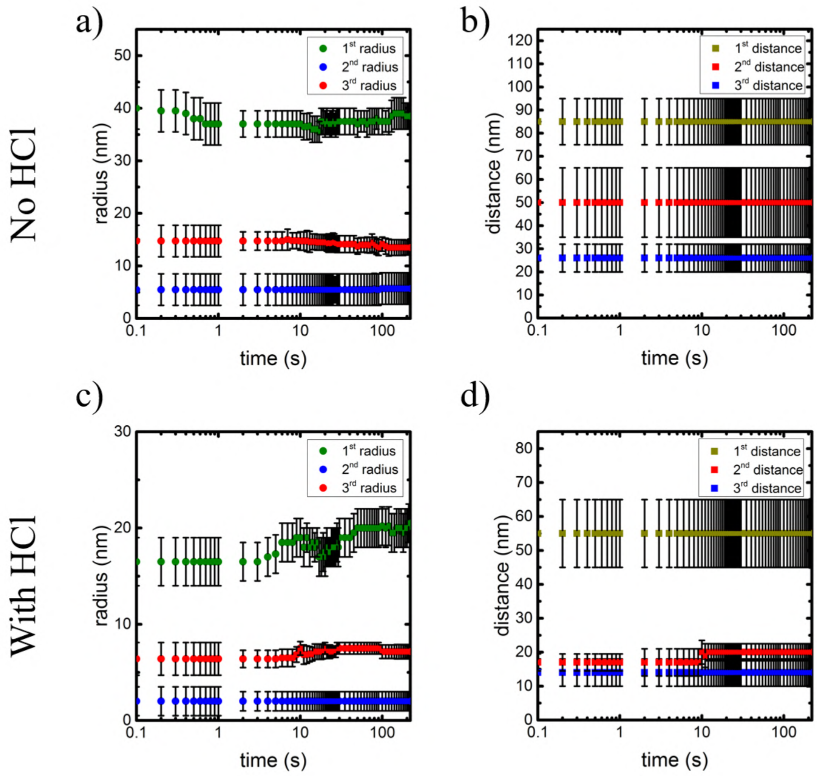

Figure 5.6:
Time evolution of (a, c) radii and (b, d) distances for the sprayed titania thin films obtained from modeling of in situ GISAXS data. (a, b) Modeling results for NHCl-based solutions and (c, d) same parameters for WHCl solutions. In general, distances and radii are decreased for WHCl-based thin films (better surface-to-volume ratio), and structural rearrangement is exclusively happening with the presence of HCl. Reprinted with permission from [2]. Copyright 2018 American Chemical Society.

In situ GISAXS characterization was carried out at the MiNaXS beamline P03 of the PETRA III storage ring at DESY, Hamburg ($\lambda = 0.94$ Å, sample-detector distance = 4377 mm, incident angle = 0.35°, vertical beam size = 12 μm, horizontal beam size = 24 μm) [1]. A time resolution of 0.1 s was chosen to observe structure formation dynamics while maintaining sufficiently high statistics for data modeling. Through GISAXS data modeling average structural radii and distances were extracted and results are shown in Fig. 5.6.

Through the addition of HCl an enhanced templating effect was observed. Exclusively for solutions containing HCl, structural changes of the average radii were found through modeling (Fig. 5.6c). Furthermore, overall structures were found with improved order (smaller error bars in Fig. 5.6) and smaller average distances as compared to films made from NHCl solutions. The improved templating effect was furthermore confirmed via ex-situ AFM and SEM measurements [2].

[1] A. Buffet, A. Rothkirch, R. Döhrmann, V. Körstgens, M. M. Abul Kashem, J. Perlich, G. Herzog, M. Schwartzkopf, R. Gehrke, P. Müller-Buschbaum, S. V. Roth, *J. Synchrotron Radiat.* **19**, 647-653 (2012)

[2] N. Hohn, S. J. Schlosser, L. Bießmann, L. Song, S. Grott, S. Xia, K. Wang, M. Schwartzkopf, S. V. Roth, P. Müller-Buschbaum, *ACS Appl. Nano Mater.* **1**, 4227-4235 (2018)

5.4 In-situ Tracking of Composition and Morphology of a Diblock Copolymer Film with GISAXS during Exchange of Solvent Vapors at Elevated Temperatures

F. Jung, A. V. Berezkin, D.-M. Smilgies[1], D. Posselt[2], C. M. Papadakis

[1] Cornell University, Ithaca, NY, USA
[2] Roskilde University, IMFUFA, Denmark

Block copolymer (BCP) thin films have attracted a lot of interest due to their ability to self-assemble and form ordered structures with length scales of 10-100 nm. This so-called bottom-up approach offers a wide range of interesting applications, e.g. for nanolithography. Imperative for use in these applications is a defect-free, controllable morphology and orientation.

Solvent vapor annealing (SVA) is a widely used method to obtain highly ordered BCP thin films and to modify the BCP film morphology [1]. In a selective solvent, chemically different nanodomains swell to a different extent, which implies a change in the effective volume fraction of the BCP, thus enabling order-order transitions. This effect is highly controllable by using mixtures of solvents of varying selectivity. Recently, SVA has been combined with thermal annealing (solvo-thermal vapor annealing, STVA), which is expected to significantly improve kinetics of structural rearrangements.

In this work, a thin film from the cylinder-forming diblock copolymer polystyrene-*block*-poly(dimethyl siloxane) (PS-*b*-PDMS), with PDMS the minority block, is investigated during STVA with solvent mixtures [2]. The solvents used are toluene and *n*-heptane, which are weakly selective for PS and strongly selective for PDMS, respectively. Thus, swelling in toluene mostly swells the glassy PS matrix, while *n*-heptane increases the effective volume fraction of PDMS and enables a transition from the initial cylindrical to the lamellar morphology. The experimental setup is shown in Fig. 5.7: Saturated solvent vapors are produced by means of bubblers and subsequent mixing. By changing the flow rates, different compositions of the solvent vapor can be achieved. Additionally, several parts of the setup are temperature-controlled to enable experiments at higher temperatures. For *in situ* characterization of the film morphology, the sample cell is equipped with a glass window for film thickness measurements using a spectral reflectance device and kapton windows for grazing-incidence small-angle x-ray scattering (GISAXS) measurements. Measurements were performed at beamline D1 at the Cornell High Energy Synchrotron Source (CHESS).

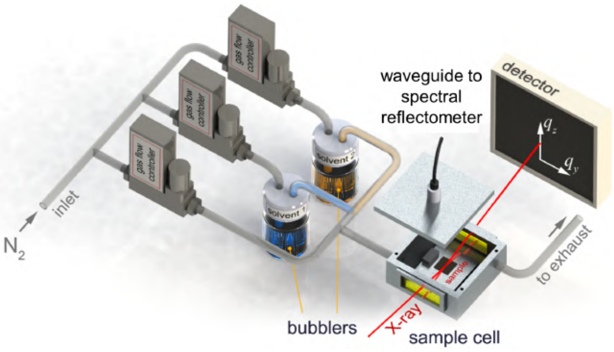

Figure 5.7:
Schematics of the experimental setup for *in situ* GISAXS investigations during STVA in mixtures of two solvents. For clarity, the electrical heating and thermal insulation are not shown.

This way, a PS-*b*-PDMS film having a thickness of 187 nm and a cylindrical morphology with no distinct orientation was swollen in pure *n*-heptane for 1 h (Fig. 5.8). In order to probe different vapor compositions, the *n*-heptane was exchanged by toluene in 10 steps lasting 300 s each. Afterwards, the film was dried with pure N_2 gas. The sample was kept at a temperature of 44 °C. The GISAXS map of the initial film is shown in Fig. 5.8a at 0 s. It reveals a cylinder morphology with random orientation. During swelling in *n*-heptane, standing cylinders are observed for a short time at 1200 s, which change back to unoriented cylinders at longer swelling times. Using the time-dependent intensity of a Bragg reflection along with the time-dependent swelling ratio,

S_R (Fig. 5.8b), we were able to exctract the distribution of the solvents among the PS- and the PDMS-domains. This allows for a calculation of the effective volume fraction of the PDMS-rich domain, f_{eff}, which, together with the polymer volume fraction $\phi_P = 1/S_R$, defines a trajectory of the film through its state diagram during STVA (Fig. 5.8c). f_{eff} increases to ∼0.5 during further swelling in *n*-heptane and, according to the theoretical BCP phase diagram, a transition to the lamella morphology is expected. This is not observed, but instead, the randomly oriented cylinder morphology is maintained, which is attributed to the still glassy PS matrix hindering restructuring. Only after initiating the solvent exchange, thus mobilizing the matrix, the transition takes place and results in standing and lying lamellae at 5100 s. By increasing the toluene fraction, thus decreasing f_{eff}, first standing and lying cylinders are observed at 5500 s which finally reorder to lying cylinders with very high order, as seen from the second-order Bragg peaks at 6000 s. At the highest swelling ratios, the system crosses an order-disorder transition (not shown). During drying, lying cylinders of two different orientations are observed, indicated by the additional Bragg peaks at 7200 s. This morphology persists in the fully dried film with slightly decreased long range order.

In conclusion, we successfully navigated a PS-*b*-PDMS film through its state diagram by exchange of solvent vapors at elevated temperatures and simultaneously determined the morphology and solvent composition in the film.

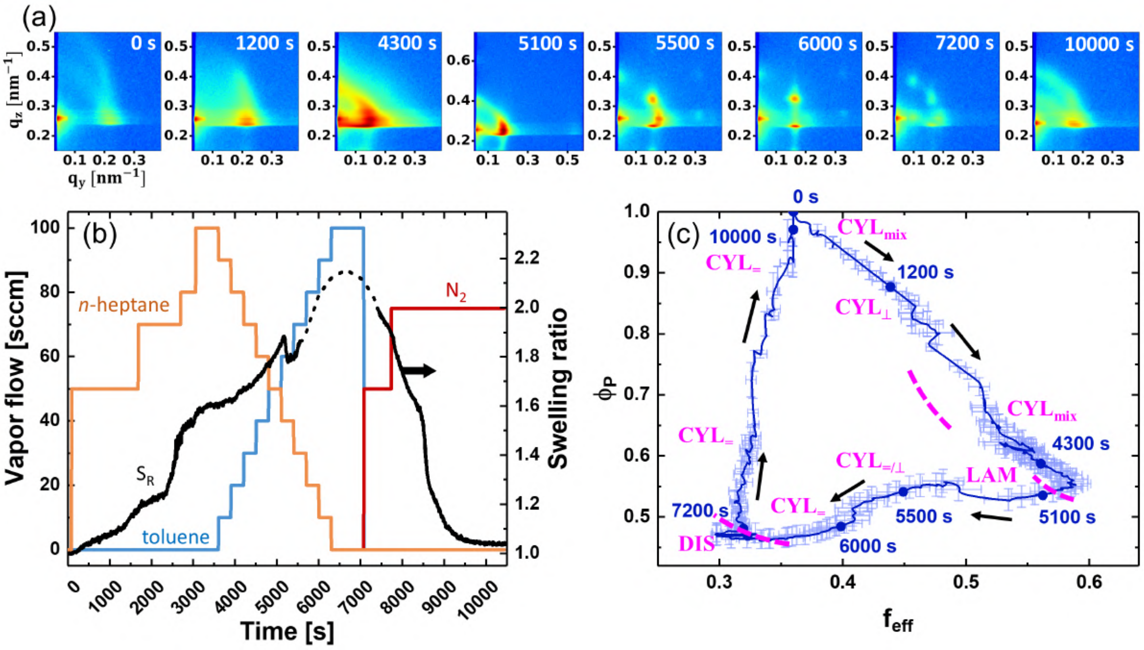

Figure 5.8:
(a) Measured 2D GISAXS maps at selected times. (b) Variation of the vapor flows (all left axis) and the resulting swelling ratio S_R (right axis). (c) Trajectory of the system during STVA as a function of the effective volume fraction of PDMS, f_{eff}, and the polymer volume fraction, ϕ_P. The observed morphologies are indicated. CYL, LAM and DIS stand for cylinders, lamellae and disordered. The subscript ”=”and ”⊥”denote lying and standing cylinders, respectively. Adapted from [2] with permission from John Wiley and Sons.

The project is funded by DGF (Pa771/10-2) and the Russian Foundation for Basic Research.

[1] D. Posselt, J. Zhang, D.-M. Smilgies, A. V. Berezkin, I. I. Potemkin, C. M. Papadakis, *Prog. Polym. Sci.* **66**, 80-115 (2017)

[2] A. V. Berezkin, F. Jung, D. Posselt, D.-M. Smilgies, C. M. Papadakis, *Adv. Funct. Mater.* **28**, 1706226 (2018)

5.5 In-situ investigation of phase transition kinetics in stimuli-responsive block copolymer thin films

L. Kreuzer, T. Widmann, L. Bießmann, J. F. Moulin[1], V. Hildebrand[2], A. Laschewsky[2],
C. M. Papadakis, P. Müller-Buschbaum

[1] MLZ, Garching, Germany
[2] Institute of Chemistry, University of Potsdam, Germany

Responsive polymers belong to the class of smart materials since they are capable of undergoing drastic changes in properties by varying an external stimulus in their surrounding environment such as temperature, relative humidity or salt concentration. Especially in thin film morphology this behavior can be exploited in a manifold of application fields such as (nano-) sensors and switches, soft-robotics and artificial pumps or muscles [1]. In order to implement responsive thin polymer films in the aforementioned applications a controlled sorption and diffusion of gaseous and liquid penetrants, usually small molecules such as H_2O and CO_2, through the polymeric network is of essential importance [2]. A promising candidate that could fulfill these requirements is a newly synthesized diblock copolymer that consists of a zwitterionic poly(sulfobetaine) (PSPP) block and a second non-ionic poly(N-isopropylmethacrylamide) (PNIPMAM) block (Fig.5.9a). The block copolymer is doubly thermoresponsive as the non-ionic block exhibits a lower critical solution temperature (LCST) and the PSPP block shows an upper critical solution temperature (UCST) (Fig.5.9b). In aqueous solution, this constellation induces upon temperature change a structure inversion of the polymers, which is called schizophrenic micelle (Fig.5.9c) [3].
However, it is not clear yet, whether this interesting behavior can be transferred from solution to thin film morphology since there, the geometrical restriction of the polymer and the increased area of interfaces (substrate – polymer, interfaces within polymer film, polymer – air) might affect the diffusion processes in a non-negligible manner compared to the bulk material or their dilute solutions.

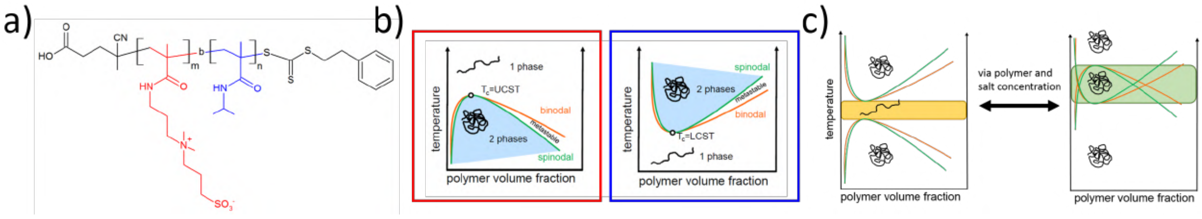

Figure 5.9:
a) Chemical structure of PSPP-b-PNIPAM with typical end groups. The PSPP block is colored red, whereas the PNIPAM block is colored blue. The chemical structure of PNIPMAM includes an additional methyl group at the marked carbon atom (purple star) b) phase diagram of an LCST-type polymer (left) and an UCST-type polymer (right) c) reversible inversion of relative positions of UCST and LCST via polymer and salt concentration in aqueous solution.

In our recent work, we investigate in-situ the phase transition kinetics in responsive PSPP-b-PNIPMAM thin films upon temperature change. During these studies, custom-made sample environments enable control over key parameters such as temperature and relative humidity and furthermore, allow following the phase transition in-situ. With time-of-flight neutron reflectometry (TOF-NR) we are able to distinguish between the separate regimes by swelling (relaxed polymer chains) and de-swelling (coiled polymer chains) of the polymer film. Information about swelling ratio d/d_{ini} and refractive index n is gained with in-situ spectral reflectance (SR) (Fig. 5.10a), which can be used to directly determine the amount of absorbed water within the PSPP-b-PNIPMAM film. Fourier-transformed infrared spectrsocopy (FTIR) is used to gain insights in the molecular interactions between the water molecules and the polymer upon swelling (increasing relative humidity) and upon temperature increase (Fig. 5.10b). Since H_2O and D_2O molecules differ in their rotation and vibration energies, FTIR can distinguish between water and deuterated water. This is beneficial especially during kinetic processes where deuterated water is involved since it yields educated information about the complex interplay of different water species (H_2O, D_2O and OHD) and possible deuteration of the polymer chain.

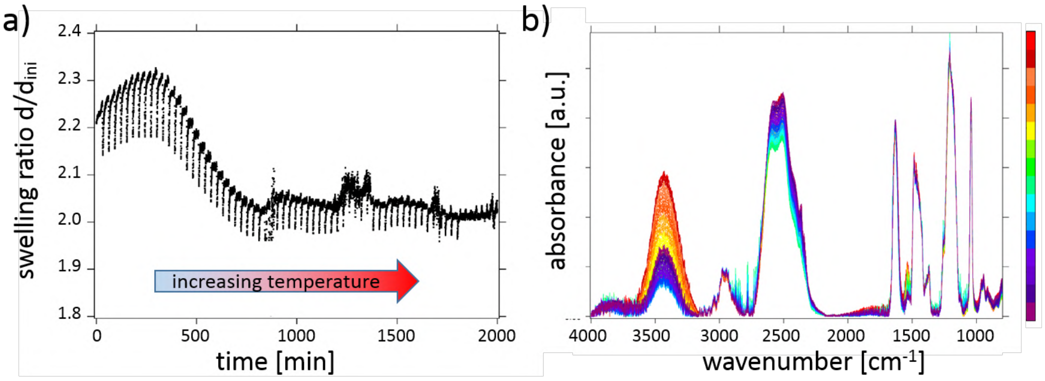

Figure 5.10:
In-situ spectral reflectance (a) and Fourier-transform infrared spectroscopy (b) measurements upon increasing temperature

In-situ SR experiments reveal only one phase transition, LCST-type at lower temperature as compared to the corresponding LCST in aqueous solution. An UCST-type phase transition was not detected (Fig. 5.10a). Apparently, the change from diluted (solution) to highly concentrated (thin film) polymer regime has major impact on both phase transition temperatures. TOF-NR measurements confirm these findings. Detailed analysis of FTIR spectra yields information about the amount of water molecules within the polymer film. Furthermore, the extracted data can be fitted with a theoretical model that provides conclusions about the water - polymer interactions but also gives insights on which time scales the dynamic phase transitions are happening.

In summary, we introduce a complementary in-situ investigation of the phase transition kinetics in responsive PSPP-b-PNIPMAM thin films. Relaxed and collapsed polymer regimes are detected via TOF-NR and SR, while information about the interaction between characteristic groups of the polymer chain and water molecules are obtained via FTIR. This investigation demonstrates the potential of in-situ measurements for the understanding of fundamental mechanisms behind phase transition kinetics, which is needed to take the next step towards the implementation in commercial applications.

[1] M. A. Cohen Stuart, W. T. S. Huck, J. Genzer, M. Müller, C. Ober, M. Stamm, G. B. Sukhorukov, I. Szleifer, V. V. Tsukruk, M. Urban, F. Winnik, S. Zauscher, I. Luzinov *Nature Materials* **9**, 101-113 (2010)

[2] M. Philipp, V. Körstegens, D. Magerl, C. Heller, Y. Yao, W. Wang, G. Santoro, S. V. Roth, P. Müller-Buschbaum, *Langmuir* **31**, 9619-9627 (2015)

[3] V. Hildebrand, M. Heydenreich, A. Laschewsky, H. M. Möller, P. Müller-Buschbaum, C. M.Papadakis, D. Schanzenbach, E. Wischerhoff *Polymer* **122**, 347-357 (2017)

5.6 Following the sputter deposition of gold contacts on thin films of photoactive polymers

F. C. Löhrer, V. Körstgens, M. Schwartzkopf[1], A. Hinz[2], O. Polonskyi[2], T. Strunskus[2], F. Faupel[2], S. V. Roth[1], P. Müller-Buschbaum

[1] DESY, Hamburg, Germany
[2] FAU Kiel, Kiel, Germany

With their easy processability, high flexibility and tuneable optical properties, organic electronics (OE) offer a wide range of potential applications. Especially photoactive polymers have received high attention in recent years as candidates for organic photovoltaics (OPV) or light emitting diodes (OLED). Due to their well-known advantages, OPV or OLED devices could combine functionality with design in fields as diverse as mobility, architecture or clothing. Although those devices mainly consist of organic materials, their electrodes are in many cases still made from metals. Thus, polymer-metal interfaces are inherently present in most organic electronic devices. Understanding the growth mechanisms of metal contacts on polymer thin films plays a crucial role in identifying potential ways to enhance the performance of organic electronics. Recent research efforts focus on engineering the optical bandgap of photoactive polymers by tuning their side groups, thereby creating families of polymers with the same backbone, but tunable optoelectronic behavior. Amongst those polymer families, especially PTB7 and its derivatives are interesting. Fig.5.11 illustrates the change in the bandgap and therefore the absorption behavior between PTB7 and PTB7-Th. By introducing a thiophene ring into the side-chains, the bandgap of PTB7-Th is significantly decreased, which leads to absorption of less energetic photons and thereby higher solar cell efficiencies.

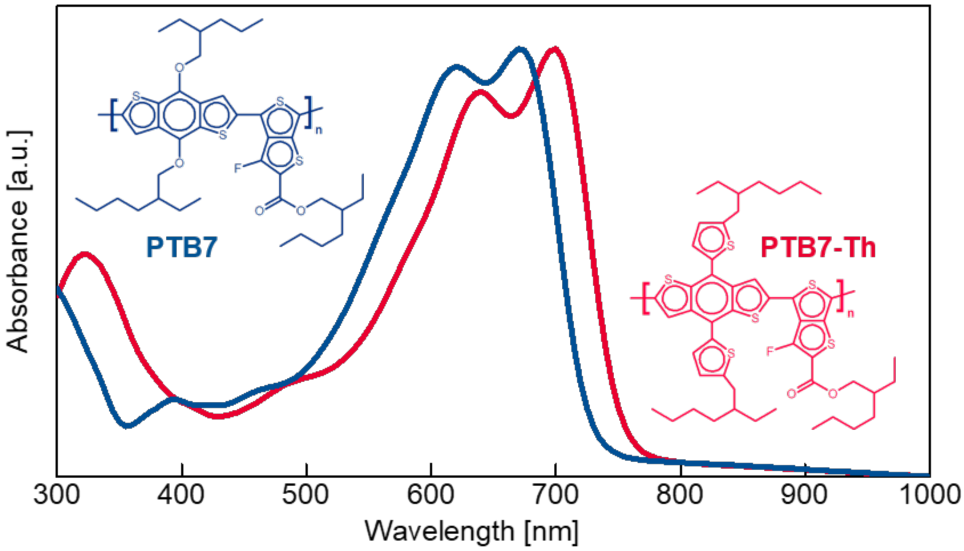

Figure 5.11:
a) Monomer units of PTB7 (blue) and PTB7-Th (red) and b) the corresponding UV/vis absorption spectra in comparison to the solar emission spectrum.

We investigated the morphological changes during the sputter deposition of gold electrodes onto thin films of both polymers, PTB7 and PTB7-Th, via in-situ grazing incidence small angle X-ray scattering (GISAXS). [1] This technique allows for time-resolved insights into the deposition behavior of the metal on the organic film, which strongly depends on the film structure. Making use of the outstanding time resolution at the P03 instrument at DESY in Hamburg, we compared the deposition behavior of sputtered gold particles on both semi-conducting polymer films. With a mobile sputter chamber, which was implemented directly into the beamline, we followed the creation and growth of gold clusters and the subsequent layer formation. The acquired large data sequences were analyzed using the fast data reduction software DPDAK. Hereby, the 2D raw data were cut at specific regions of interest, such as the horizontal line cuts shown in Fig. 5.12, which give information about the lateral film morphology during film growth.

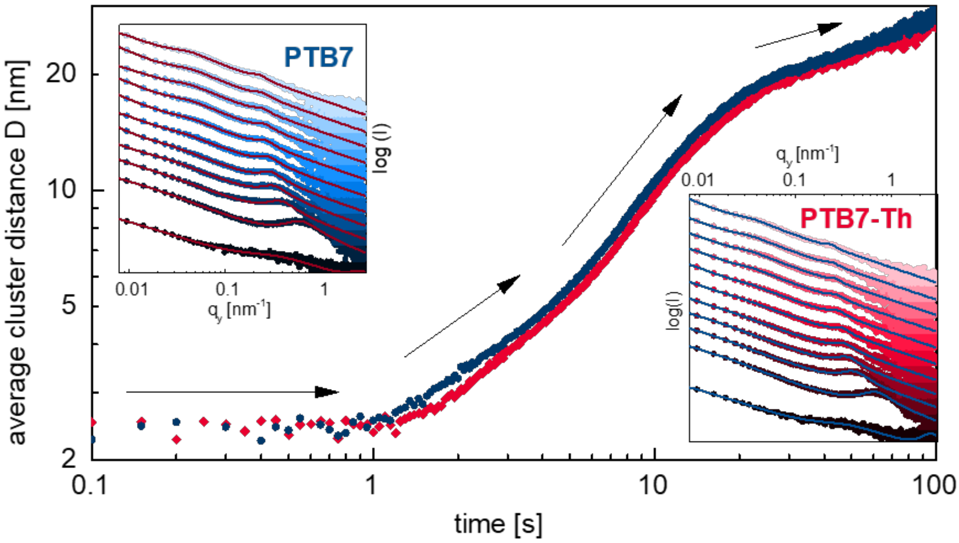

Figure 5.12:
Exemplary direct data analysis with a) horizontal line cuts from the 2D GISAXS data taken after certain time intervals for PTB7 (top graph) and PTB7-Th (bottom graph) and b) the evolution of the corresponding correlation distance during the deposition process for PTB7 (blue) and PTB7-Th (red).

The evolution of the maximum over time can be translated into a real-space value, the average cluster distance D, which is a measure for the mean distance of gold clusters on the polymer surface. This direct data analysis gives an insight into the different growth phases during the deposition process. The results are in good accordance with a step-like growth shown in other works. [2, 3, 4] In a first analysis, only small differences in the growth behavior of gold on both polymer films could be distinguished, which demonstrates that the change in the side group has a weak influence on the overall growth behavior.

[1] P. Müller-Buschbaum, *Adv. Mater.* **26**, 7692–7709 (2014)

[2] G. Kaune, M. A. Ruderer, E. Metwalli, W. Wang, S. Couet, K. Schlage, R. Röhlsberger, S. V. Roth, P. Müller-Buschbaum, ACS Appl. Mater. Interfaces **1**, 353-360 (2009)

[3] M. Schwartzkopf, G. Santoro, C. J. Brett, A. Rothkirch, O. Polonskyi, A. Hinz, E. Metwalli, Y. Yao, T. Strunskus, F. Faupel, P. Müller-Buschbaum, S. V. Roth, *ACS Appl. Mater. Interfaces* **7**, 13547-13556 (2015)

[4] M. Schwartzkopf, A. Hinz, O. Polonskyi, T. Strunskus, F. C. Löhrer, V. Körstgens, P. Müller-Buschbaum, F. Faupel, S. V. Roth, *ACS Appl. Mater. Interfaces* **9**, 5629-5637 (2017)

5.7 Analysis of metal nanostructure evolution on polymer surfaces by in-situ GISAXS during sputter deposition

V. Munteanu, S. J. Schaper, V. Körstgens, M. Schwartzkopf[1], P. Pandit[1], A. Hinz[2], O. Polonskyi[2], T. Strunskus[2], F. Faupel[2], S. V. Roth[1,3], P. Müller-Buschbaum

[1] DESY, Hamburg, Germany
[2] CAU zu Kiel, Kiel, Germany
[3] KTH, Stockholm, Sweden

A good understanding of the fabrication process of reproducible functional metal-polymer interfaces is of high importance for their use in organic electronics. Sputter deposition offers the ability to precisely control and tailor the fabrication of metal-polymer interfaces. During sputter deposition, the evolution of the metallic layer morphology is monitored in situ with time-resolved grazing-incidence small-angle X-ray scattering (GISAXS). The resulting in-situ scattering data is processed and analyzed using the DPDAK software package. By fitting the processed data, structure parameters can be extracted which temporal evolution reveals the mode of metal growth on polymer surfaces.

For each sample, vertical line cuts are performed at $q_y = 0$. These cuts are fitted with Gaussian functions as displayed in Figure 5.13. The measured distance Δq_z between two adjacent vertical peaks allows the determination of an average film thickness δ using the simple relation $\delta = \frac{2\pi}{\Delta q_z}$.

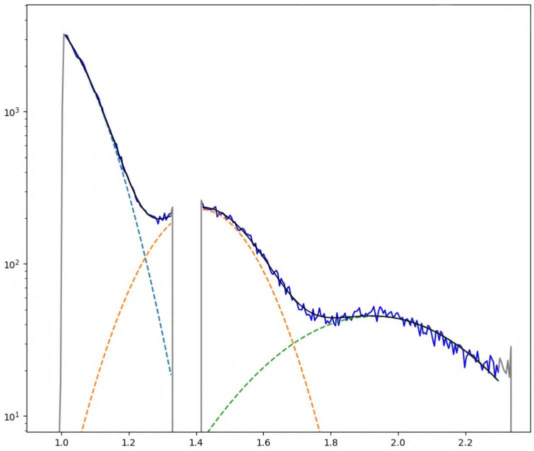

Figure 5.13:
Example of fitting a vertical line cut using 3 Gaussian functions with DPDAK to determine the film thickness.

For each sample, two narrow horizontal cuts are performed at the Yoneda positions of the corresponding metal and polymer as well as one broad Yoneda cut. The cuts are fitted with a combination of Lorentzian and Gaussian functions, which allows tracking of the position of the side peaks and, consequently, the determination of the temporal evolution of the cluster distance $D = \frac{2\pi}{q_y}$ and the periodic distance of the polymer superstructure d. The cluster radius R is computed by employing a simplified geometrical model in which the clusters are hemispheroids positioned in a 2D hexagonal lattice [1]. The exact spheroid factor will be chosen by comparing the experimental GISAXS data with the results of simulations made with BornAgain for different shapes of the spheroids. The plot of the extracted sizes as a function of effective thickness for a sample of Cu sputtered on PS-b-PEO is displayed in Figure 5.14.

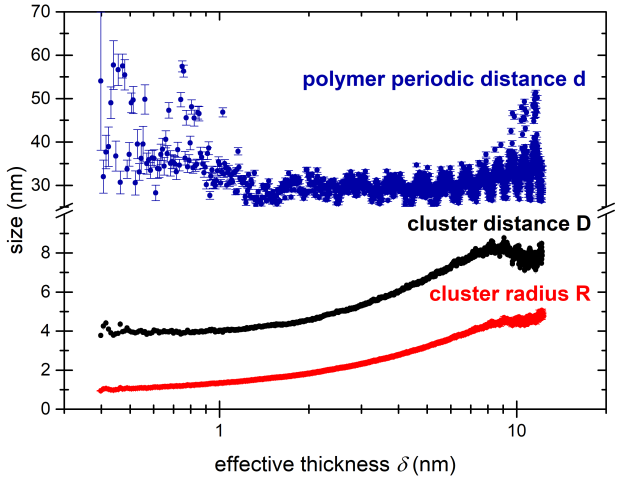

Figure 5.14:
Extracted sizes as a function of the effective thickness.

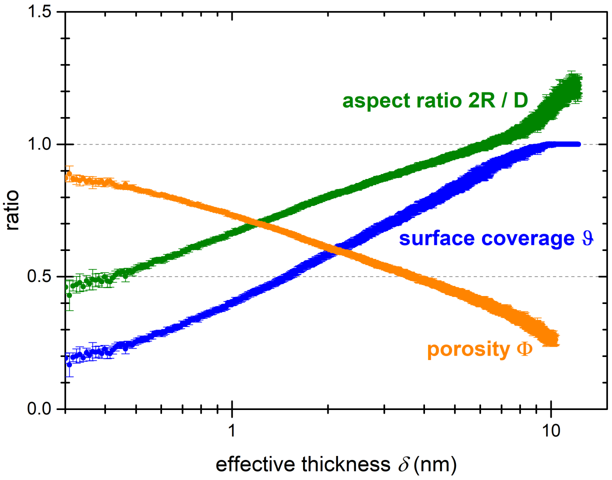

Figure 5.15:
Aspect ratio, surface coverage and layer porosity versus the effective thickness.

The aspect ratio 2R/D, the surface coverage and the layer porosity are also computed from the geometrical model [2-3], and shown in Figure 5.15 as a function of the effective thickness. A more detailed data analysis is in progress.

[1] M. Schwartzkopf, A. Buffet, V. Körstgens, E. Metwalli, K. Schlage, G. Benecke, J. Perlich, M. Rawolle, A. Rothkirch, B. Heidmann, G. Herzog, P. Müller-Buschbaum, R. Röhlsberger, R. Gehrke, N. Stribeck, S. V. Roth, *Nanoscale* **5**, 5053 (2013)

[2] M. Schwartzkopf, G. Santoro, C. J. Brett, A. Rothkirch, O. Polonskyi, A. Hinz, E. Metwalli, Y. Yao, T. Strunskus, F. Faupel, P. Müller-Buschbaum, S. V. Roth,*ACS Appl. Mater. Interfaces* **7**, 13547-13556 (2015)

[3] M. Schwartzkopf, A. Hinz, O. Polonskyi, T. Strunskus, F. C. Löhre, V. Körstgens, P. Müller-Buschbaum, F. Faupel, S. V. Roth, *ACS Appl. Mater. Interfaces* **9**, 5629-5637 (2017)

5.8 In-situ GISAXS investigation of gold sputter deposition on perovskite films

L. Reb, M. Schwartzkopf[1], S. V. Roth[1],[2], P. Müller-Buschbaum

[1] DESY, Hamburg, Germany
[2] KTH, Stockholm, Sweden

Thin metal electrodes are applied in industrial photovoltaics, but are also of great interest in electronics for transistors in e.g. photodiodes [1]. Therefore, understanding and controlling the interface of the active layer and the metal electrode is of key importance to develop devices of high efficiency and reproducibility. To deposit metal layers of nanometer thickness, sputtering is promising because it is a well controllable, cost-effective, and an up-scalable process. In addition, sputtering preserves the thin layer beneath it, compared to chemical or thermal deposition techniques and typically results in a better adhesion on the organic surface [2].
Recently, hybrid organic-inorganic perovskite gained large attention due to its unique optoelectronic properties, i.e. efficient light-driven charge separation and large charge carrier diffusion length. For example, perovskite solar cells reached power conversion efficiencies in harvesting light energy exceeding 22 per cent in the last years - properties which are unprecedented for thin-film materials and therefore promising for the application in such thin-film future devices [3]. Perovskite thin films with high quality crystals are produced easily at low temperatures in the lab-scale spin-coating process, but could be processed equally well in up-scalable deposition techniques as printing or spray-casting. In all cases, the perovskite surface morphology i.e. the crystal sizes and surface roughness, which in turn depend on processual details, play a crucial role in determining the interface characteristics.

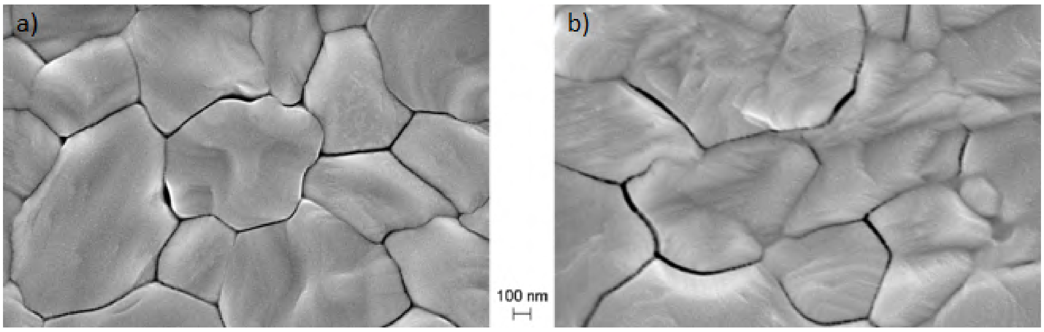

Figure 5.16:
Surface scanning electron microscopy images of differently processed perovskite layers a) *'left'* and b) *'right'* with a different surface roughness but a similar crystal size distribution.

In order to study the interface formation, *in-situ* grazing incidence small angle X-ray scattering (GISAXS) can be performed during the sputter deposition, to gain insight into the detailed steps of aggregation and growth of the sputtered metal layer. Thereby, GISAXS offers an non-destructive way to gain information of high statistical relevance about the time evolution of metal grain size and inter-grain distance in the crucial steps of interface formation.
In the present study, perovskite (methylammonium-lead-iodide, $MAPbI_3$) thin films were deposited onto silicon substrates *via* spin-coating and subsequent annealing. Different surface roughnesses, as visible in Fig. 5.16, were achieved by varying the processing parameters, and give the opportunity to study their impact on the development of the sputtered gold interface. In this report, the two perovskite layers of different surface are referred to as *'left'* and *'right'*, according to the ordering of their respective figures. The *in-situ* GISAXS experiments were conducted at the P03 beamline at DESY, Hamburg, using a DC magnetron sputter chamber [4]. The micrometer-scale beam impinged on the sample with a photon energy of 12.6 keV, below the

lead absorption edge, and with an incident angle of 0.4°, above the critical angle of gold. A Pilatus 1M detector registered the scattered X-rays, where direct and specular beam were shielded by beamstops. The main focus in the analysis of the resulting *in-situ* data is on the Yoneda region - characteristic for every material - which contains the desired information of the bulk and surface morphology in reciprocal space. To access this information, horizontal line cuts reveal details of the lateral formation of the gold clusters, i.e. parallel to the surface, and vertical cuts of the vertical growth, i.e. along the surface normal.
Such line cuts are presented in Fig. 5.17. A closer look at the time-evolution of both '*right*'-side plots, reveals a rougher surface than both '*left*'-side plots, since in the Yoneda region the scattered intensity is lower. Comparing the vertical line cuts, one can see a co-evolution of intensity peaks moving downwards. These height modulations demonstrate a steadily increasing layer thickness of gold over time of a certain rate for both the '*left*' and '*right*' perovskite and underline the accurate sputter deposition rate and high reproducibility of the experiment. Regarding the lateral growth of the first gold aggregates on the perovskite surface, we focus on the first seconds of deposition in the horizontal line cuts and especially on the highlighted regions. In Fig. 5.17b), intensity peaks originate at high q-values, i.e. far away from the central Yoneda region located at the apparent symmetry axis, and then close the low-intensity gap towards the center by broadening and moving to the center after a few seconds. In contrast to that, in Fig. 5.17d) the appearing intensity in the high q-region does not have such defined q-values, but instead a quite broad q-distribution from the very beginning. In this case no well-defined intensity peaks nor a gap towards the center occur. The perovskite surface morphology seems to influence details of gold aggregation. In Fig. 5.17b) at first aggregates of a certain size and spacing seem to form, which grow and merge until a closed layer is formed eventually. In contrast, the rougher surface in Fig. 5.17d) seems to cause a broader size distribution of the gold clusters.

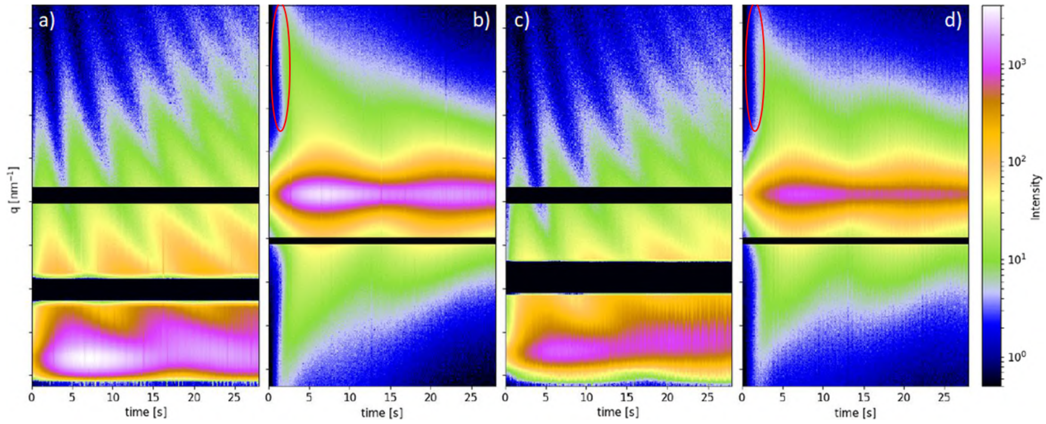

Figure 5.17:
(a,c) Vertical and (b,d) horizontal line cut of the *in-situ* sputtering for the (a,b) '*left*' and (c,d) '*right*' type, respectively. Along the q axes two vertical tics span 0.2 nm^{-1}. Red ellipses highlight special regions (see text).

[1] Y. Dong, Y. Zou, J. Song, X. Song, H. Zeng, *J. Mater. Chem. C* **5**, 11369-11394 (2017)

[2] F. Faupel, V. Zaporojtchenko, T. Strunskus, M. Elbahri, *Adv. Eng. Mater.* **12**, 1177-1190 (2010)

[3] M. Saliba, J.-P. Correa-Baena, C. M.Wolff, M. Stolterfoht, N. Phung, S. Albrecht, D. Neher, A. Abate, *Chem. Mater.* **30**, 4193-4201 (2018)

[4] A. Buffet, A. Rothkirch, R. Döhrmann, V. Körstgens, M. M. A. Kashem, J. Perlich, G. Herzog, M. Schwartzkopf, R. Gehrke, P. Müller-Buschbaum, S. V. Roth, *Journal of Synchrotron radiation* **19**, 647-653 (2012)

5.9 In-situ investigation on sprayed polymer films embedded with magnetic nanoparticles

S. Xia, L. Song, V. Körstgens, M. Opel[1], M. Schwartzkopf[2], S. V. Roth[2 3], P. Müller-Buschbaum

[1] WMI, Garching, Germany
[2] DESY, Hamburg, Germany
[3] KTH, Stockholm, Sweden

For magnetic sensor applications, magnetic films composed of dibock copolymers (DBCs) and magnetic nanoparticles (MNPs) are promising candidates. [1] However, most studies so far have only focused on the properties of the finally obtained films. [2] Less attention has been paid to the formation process of the magnetic films and the kinetic arrangement of the MNPs during the film fabrication. The establishment of tailored nanostructures in MNPs-DBC films is a complex procedure, which involves kinetic processes until the final static hybrid structure is obtained. Accordingly, *in situ* experiments are extremely useful in order to gain profound understanding of the involved multifaceted kinetic process. In this regard, spray-coating is applied to fabricate MNPs-DBC films from solution precursors containing polystyrene-block-polyN-isopropylacrylamide (PS-*b*-PNIPAM) and magnetite NPs (Fe_3O_4, 2 wt %). Kinetic processes during the spray deposition are followed by *in situ* grazing incidence small angle X-ray scattering (GISAXS) measurements with a high time resolution. To probe the influence of the MNPs on the morphology evolution, a reference film without MNPs is also spray-deposited under identical conditions.

Compared to the pure polymer reference film, the hybrid films exhibit a larger inter-domain distance and domain size during the whole spray process. Such size increase is caused by the preferential localization of MNPs inside the PS blocks. Due to the surface modification of the MNPs with oleic acid chains, the MNPs show a stronger affinity to the PS blocks than to the PNIPAM blocks. The selective dispersion of the MNPs leads to the expansion of the PS domains, ending up with an increased domain size of the microphase separation structure. In addition, the evolution of a closed film from polymer islands also features differently in the two studied systems. By modeling the *in situ* GISAXS data, a faster local film formation is found for the hybrid system as compared to the reference. Such observation can be explained by the presence of MNPs inside the polymer matrix. In the present investigation, the MNPs are dispersed in the hybrid film during the entire deposition process. The affinity of the MNPs to the substrate contributes to an improved wetting behavior of the hybrid film. Due to the preferential localization of the MNPs inside the PS domains, the PS cores tend to follow the movement of the MNPs, leading to a faster merging of the polymer islands. Therefore, a quicker establishment of complete local film is observed for the hybrid system compared with the pure one where no MNPs are present.

Surface nanostructures of the final dry films are characterized *via* atomic force microscopy (AFM). Results show that a parallel cylindrical morphology (with respect to the substrate) is obtained for the reference, while a vertical orientation of the morphology appears in the hybrid film. The change in orientation is attributed to the selective incorporation of MNPs inside the PS cylinders. Due to the oleic acid capping layer of MNPs, the energetic compatibility between MNPs and the PS block is strongly enhanced while selective incorporation into the PNIPAM block is much weaker in comparison. Entropic effects lead to accumulation of the MNPs at the substrate surface. Due to the affinity of PS cores to the MNPs, an upstanding cylinder ordering is more likely as compared to the reference sample and a parallel cylinder orientation does inherently not allow for contact between PS cores and MNPs on the surface of the substrate. In addition to the vertically aligning cylinders, some parallel ones can also be found on the surface of the hybrid film, which is due to the non-equilibrium nature of the investigation hybrid system. MNPs agglomerates can be discovered inside the films, resulting in a rougher surface as compared to the reference. Magnetic measurements were collected using a superconducting quantum interface device (SQUID). Results prove that the sprayed magnetic hybrid film follows a superparamagnetic behavior. The blocking temperature is calculated as 121 ± 19 K, which coincides with our previous investigation where identical MNPs were employed.[2]

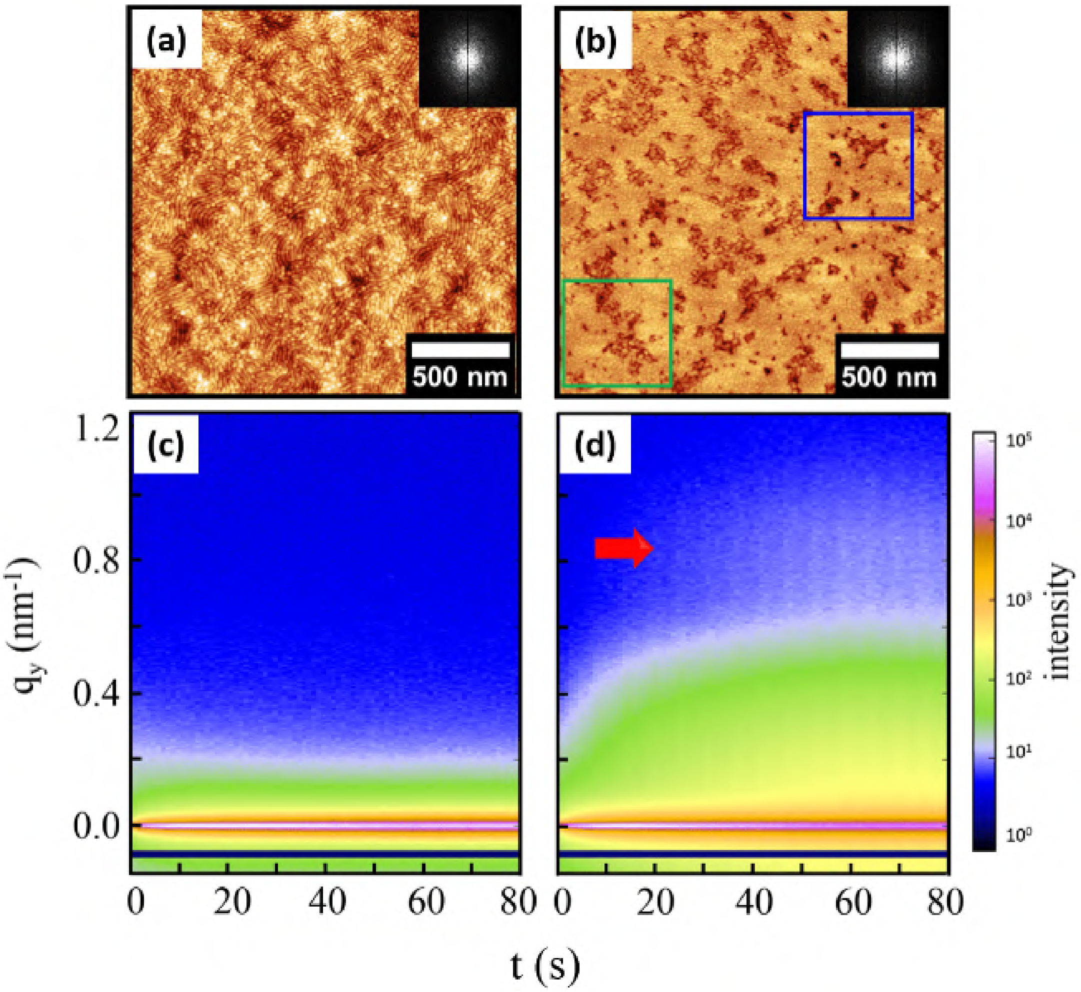

Figure 5.18:
AFM height images of (a) pure DBC reference film and (b) magnetic hybrid film containing 2 wt % of MNPs. On the top right corner are the Fast Fourier Transform images. In figure (b), the blue and green boxes show the MNP aggregates and partially parallel cylinders, respectively. Mapping extracted from horizontal line cuts from the 2D GISAXS data of (c) the reference film and (d) the hybrid film. All horizontal line cuts are integrated over $\Delta\, q_z$ = 0.51- 0.56 nm^{-1} and plotted versus spray time.

[1] T. Kimura, H. Ago, M. Tobita, M. Kyotani, M. Yumura, B. *Adv. Mater.* **14**,1380-1383 (2002)

[2] Y. Yao, E. Metwalli, M A. Niedermeier, M. Opel, C. Lin, J. Ning, J. Perlich, S. V. Roth, P. Müller-Buschbaum, *ACS Appl.Mater.Interfaces.* **6**, 5244-5254 (2014)

5.10 In-situ investigating morphology formation of printed non-fullerene active layer for solar cells

X. Jiang, S. Grott, T. Riccitelli, V. Körstgens, K. Wienhold, M. Schwartzkopf[1], S. V. Roth[1],[2], P. Müller-Buschbaum

[1] DESY, Hamburg, Germany
[2] KTH, Department of Fibre and Polymer Technology, Stockholm, Sweden

Bulk heterojunction (BHJ) polymer solar cells have gained significant improvements via novel organic synthesis and easy fabrication methods. Especially their potential roll-to-roll processing and large-area processing ability on low cost makes conjugated polymer-based organic solar cells very attractive as a cost-effective solution to today's energy-shortage problem. Usually, typical BHJ solar cell devices are a functional stack, which consists of many layers with different functions. On top of the substrate is the cathode, followed by the transparent electron blocking layer, which can prevent the diffusion of electrons to the anode. Next is the active layer, in which light is transferred into charger carriers and on top the anode, if no top blocking layer is needed. The active layer is the most important part of the device. The so-called bulk heterojunction (BHJ) morphology was established to be best working. It is a mixture of a p-type organic semiconductor (p-OS) as the donor and an n-type organic semiconductor (n-OS) as the acceptor making a large interface morphology. Fig. 5.19 shows a typical device configuration of BHJ solar cells. By using conventional fullerene derivatives as acceptors, the rational design of both, polymer and small molecule p-OS donor structures has significantly improved the achieved power conversion efficiencies (PCEs) of OSCs, now exceeding 11 % [1]. Despite the success of fullerene acceptors, they still suffer from several limitations, such as limited visible light absorption, high costs and poor thermal stability of the morphology due to fullerene mobility. Non-fullerene n-OS small molecule acceptors have some remarkable advantages as compared to fullerene derivatives, including a well-defined molecular structure, good batch reproducibility, easy tuning of film absorption and electronic energy levels, high morphological stability and potentially low costs. Recently, the PCEs of non-fullerene polymer solar cells (PSCs) with small molecule acceptors have rapidly increased to over 14 % [2]. Despite this success in the achieved PCE values, fundamental understanding in the systems with the rather novel non-fullerene acceptors is still limited. For example, morphology evolution of the active layer during the fabrication process is not well established. Given its importance in the fabrication of high performance solar cells, it needs to be addressed in future research.

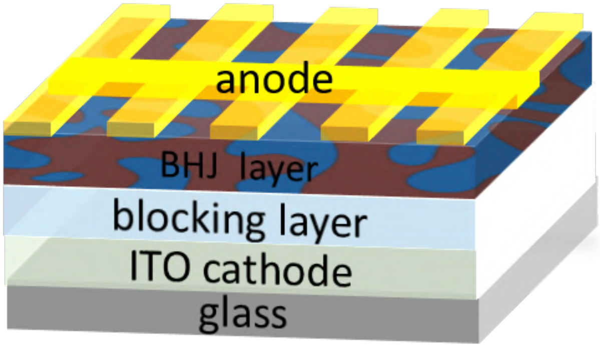

Figure 5.19:
A typical BHJ solar cell architecture .

In the present work, we investigate an active layer, which contains a low band gap donor polymer named pffBT4T-2OD and a non-fullerene acceptor named EH-IDTBR. Films are prepared with the slot-die printing technique. To observe the structure formation of the polymer domains on the mesoscale, grazing incidence small-angle X-ray scattering (GISAXS) is used in-situ during the printing process. Active layer solutions (PffBT4T-2OD:EH-IDTBR) are prepared from

TMB solutions at 80 °C overnight with a total concentration of 15 mg/ml. The in-situ GISAXS experiments are performed at the beamline P03 in Hamburg at DESY [3]. The measurements are done at an incident angle of 0.4 ° at a wavelength of 0.96$\AA$. The sample-detector distance is 3174 mm. Using a Pilatus 1M detector, the direct beam and the specular reflected beam are shielded by beamstops to protect the detector from damage. At the Yoneda peak, which is characteristic for the studied material, horizontal line cuts are made to analyze the formation of lateral polymers structures during the drying of the initially wet layer.

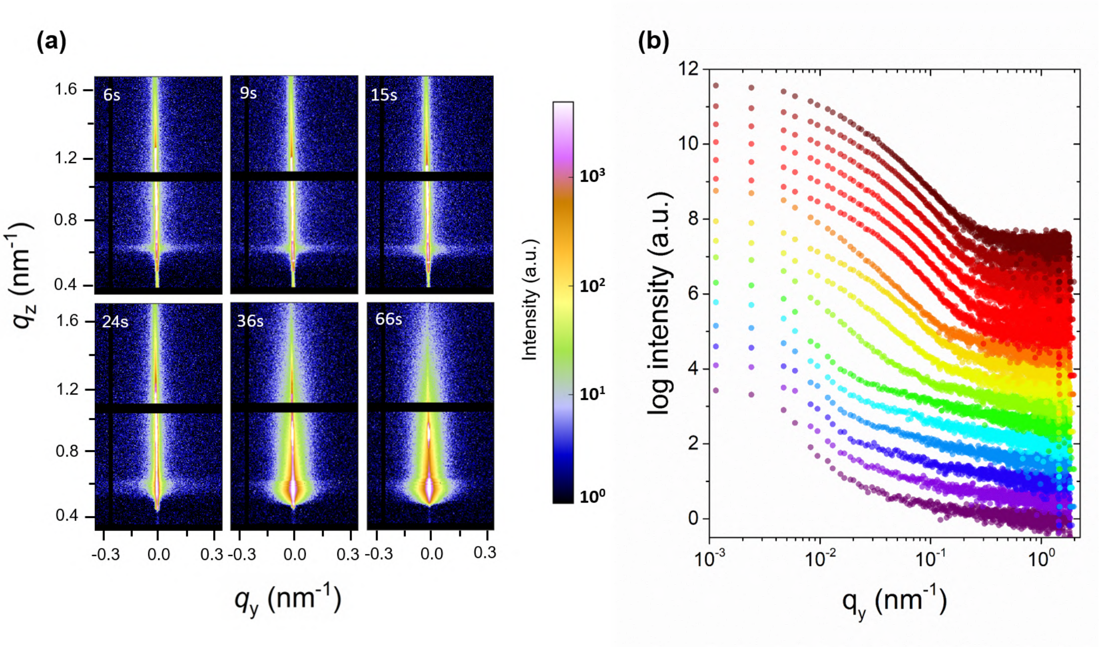

Figure 5.20:
(a) Selected 2D GISAXS data during the in-situ printing process at times as indicated. (b) Horizontal line cuts extracted from the in-situ GISAXS data, from the bottom to the top time increases during the formation of the thin BHJ film.

Fig. 5.20a) shows selected 2D GISAXS data to illustrate the evolution of the active layer during the printing. The intensity of the Yoneda peak is increasing with increasing time, due to the solvent evaporation and the solidification of the polymer:small molecule blend film in BHJ morphology. Fig. 5.20b) shows horizontal line cuts of the in-situ GISAXS data, which reveal the evaporation of the solvent, the formation and the rearrangement of the polymer domains [4]. A detailed data analysis is in progress and will give the understanding the kinetic process during film formation via printing.

[1] H. Cha, J. Wu, A. Wadsworth, J. Nagitta, S. Limbu, S. Pont, Z. Li, J. Searle, M. F. Wyatt, D. Baran, J. S. Kim, I. McCulloch, J. R. Durrant,*Advanced Materials* **29**, (2017)

[2] Z. Zheng, Q. Hu, S. Zhang, D. Zhang, J. Wang, S. Xie, R. Wang, Y. Qin,W. Li, L. Hong, N. Liang, F. Liu, Y. Zhang, Z. Wei, Z. Tang, T. P. Russel, J. Hou, H. Zhou, *Advanced Materials* **30**, 1801801 (2018)

[3] G. Herzog, M. M. A. Kashem, G. Benecke, A. Buffet, R. Gehrke, J. Perlich, M. Schwartzkopf, V. Korstgens, R. Meier, M. A. Niedermeier, M. Rawolle, M. A. Ruderer, P. Müller-Buschbaum, W. Wurth, S. V. Roth, *Langmuir* **28(21)**, 8230-8237 (2012)

[4] S. Pröller, F. Liu, C. Zhu, T. P. Russel, A. Hexemer, P. Müller-Buschbaum, E. M. Herzig, *Advanced Energy Materials* **6**, (2015)

6 Instrumentation and new materials

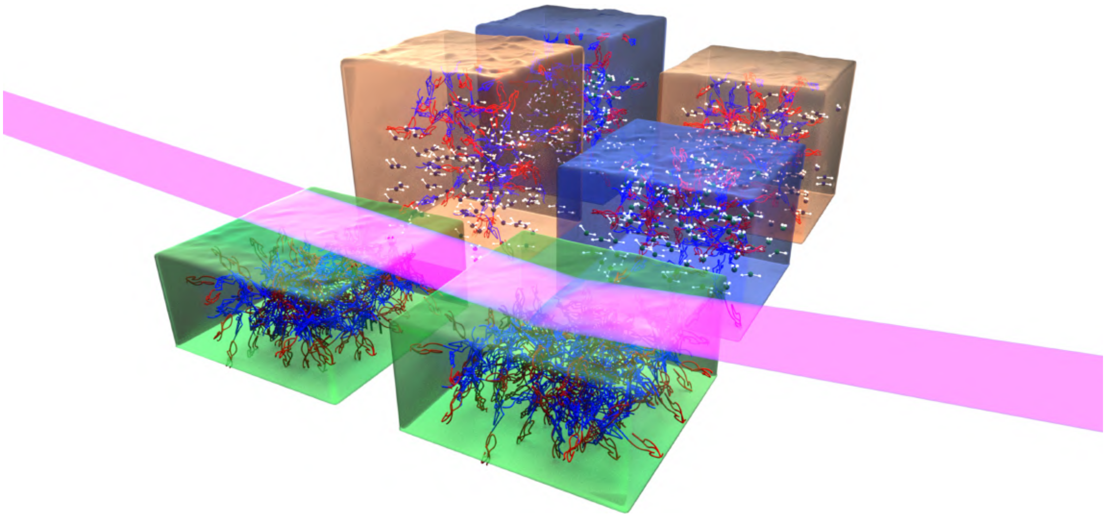

6.1 Thermo-mechanical behavior of silver-filled thermoplastic polymers

A. Baccari, P. Müller-Buschbaum

Filled thermosetting and thermoplastic polymers are used for silver-filled, electrically conductive adhesives in the printed circuit board industry [1]. These are a type of glue containing usually 80 % of a conductive material and 20% of a polymer matrix that has the necessary mechanical and thermal properties. The produced electronic devices need to pass several thermo-mechanical tests using dynamic mechanical analysis and thermal mechanical analysis (DMA and TMA) [2] techniques in order to get a good expectancy of the lifetime performance and behavior of the final products. For the manufacturing of electronics, experiments and simulation are beneficial for assessing new adhesives, e.g. if they are based on a thermoplastic polymer matrix instead of the usual epoxy-based composite adhesive. Thermo-mechanical material models of polymers are essential for obtaining meaningful results from thermo-mechanical simulation.

Today, the electronics packaging community has an acceptable understanding of the thermo-mechanical behavior of thermosetting epoxy polymers, but not yet of alternative composites such as for example silver-filled thermoplastic polymer matrices. Consequently, in the present work we focus on such conductive composites.

In general, thermoplastics are completely different from thermosets. A thermoplastic polymer is a material that has a liquid phase (melt) when it is heated. The internal structure of thermoplastics is not based on cross-links. Therefore, when a thermoplastic polymer is heated, first the glass transition occurs. Then, in the absence of cross-links, a melt is obtained at sufficiently high temperatures. Concerning some kind of applications, such behavior is rather an advantage as thermoplastics can be shaped and reshaped several times via heating and cooling. In contrast, for thermosets, high temperatures lead to material decomposition and they cannot be reshaped. Commonly, thermosets are amorphous, as the cross-links do not allow an ordered arrangement of the polymer chains, whereas thermoplastics can be either amorphous or semi-crystalline polymers. Amorphous thermoplastics show only a glass transition temperature and no melting temperature on a DSC graph. Semi-crystalline polymers undergo crystallization and melting processes, which are recognized in DSC.

The study of some typical thermoplastics like polypropylene gives a general understanding of the thermo-mechanical behavior of this type of polymers. This first understanding would be helpful for the study of thermoplastic-based glues.
For polypropylene (PP), the storage modulus curve as a function of temperature shows a smooth stiffness drop from 3900 MPa to very low values (Fig. 6.1). In fact, the presence of a crystalline phase (with quite strong bonds between polymer molecules) prevents the stiffness from decreasing suddenly. However, we do not observe a plateau before and after the glass transition. The loss modulus curve shows the glass transition peak. We observe as well another secondary transition between 50 °C and 100 °C. It is probably an α transition which corresponds to the relaxation of rigid amorphous PP chains in the crystalline phase.

For the silver-filled adhesive, the storage modulus curve as a function of temperature shows a stiffness drop at 93 °C (Fig. 6.2), the glass transition temperature of the polymer composite. Above T_g, the storage modulus decreases until 225 °C where a sudden drop is observed. This drop should correspond to the melting of the thermoplastic phase of the polymer matrix, as a typical signature for semi-crystalline thermoplastics. In fact, thermoplastic polymers does not

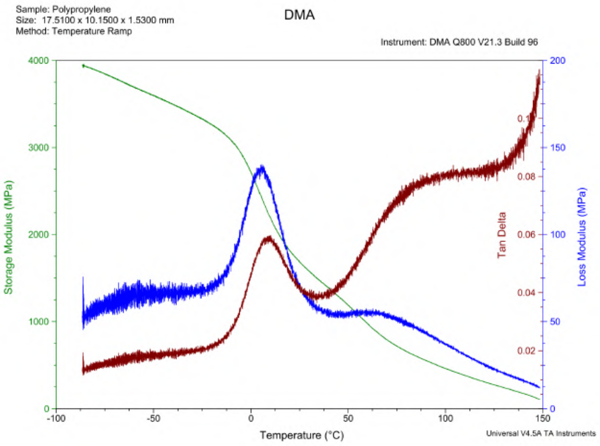

Figure 6.1:
DMA analysis of polypropylene (1 Hz)

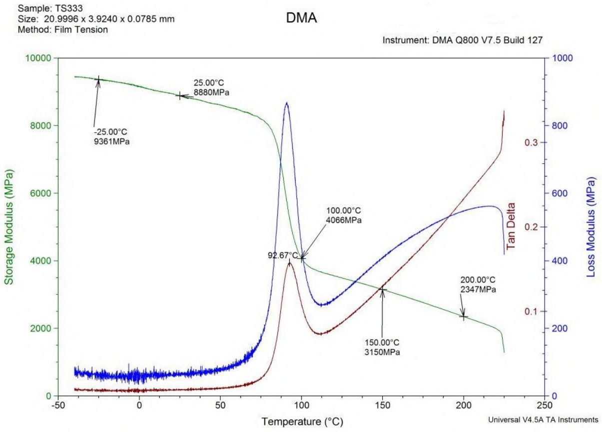

Figure 6.2:
DMA analysis of the studied silver-filled adhesive (1 Hz)

contain cross-links. The polymer chains/molecules are linked via weak bonds.
As the temperature increases, the energy is sufficiently increased to break these weak bonds. Therefore, the stiffness of the material becomes extremely low with a drop to approximately 0 MPa (at the melting temperature).
For thermosetting polymers, the irreversible curing step prevents this type of material from reaching very low stiffness values. However, for thermoplastics (especially amorphous ones), the softening of the polymer is pronounced and results in the sudden drop of the storage modulus.

The understanding of the general behavior of thermoplastics allows to assess the influence of fillers (glass fibers, silver, carbon nanotubes...etc.) on the thermo-mechanics of these materials. It would be suitable afterwards to study some mineral-filled thermoplastics using DMA experiments and SAXS measurements to investigate their internal structure.

[1] Y. Li, D. Lu, C.P. Wong, *Electrical Conductive Adhesives with Nanotechnologies*, Springer US, 2010

[2] D. Menczel, R. Bruce Prime, *Thermal analysis of polymers: fundamentals and applications*, John Wiley & Sons, 2009

6.2 Tack properties of dry adhesive electrodes

A. Zheng, V. Körstgens, E. Herth[1], H.-Y. Chiang[2], P. Müller-Buschbaum

[1] University Paris-Sud, France

[2] dreem, Paris, France

The type of electrodes commonly used in medical applications to measure electric potentials are usually wet electrodes. The use of wet electrodes however, can cause skin irritation and the signal quality decreases as the gel of the electrode dehydrates. Hence, wet electrodes are not suitable for long-time measurements. Dry adhesives, based on a microstructured surface are a useful alternative. In order to obtain biosignals, additionally to the adhesion to the skin, electrical conductivity has to be ensured. One way to achieve this is to introduce conductive fillers into the polymer matrix [1]. Assuring that the percolation threshold of the filler is exceeded a conductive dry adhesive can be obtained. We produced microstructured conductive adhesive patches with a combination of carbon black and graphene sheets dispersed in polydimethylsiloxane (PDMS).

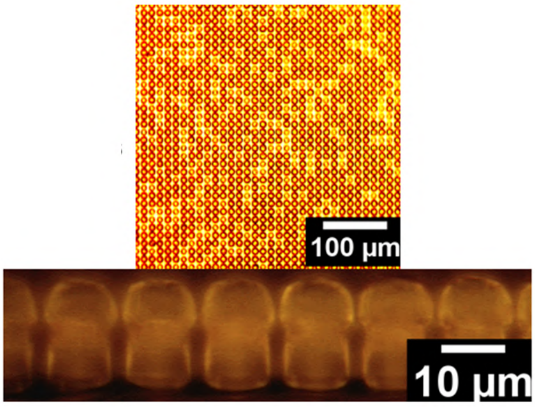

Figure 6.3:
Optical microscopy images before tack measurement for an example PDMS pattern achieved with a mold. The top view showing ≈ 83% of reproduced pillars and side view in higher magnification showing the mushroom tip shape.

One example for a dry adhesive patch of PDMS obtained from a microstructured mold is given in Fig. 6.3. It was aimed for a pillar structure with a flat-ended mushroom shape. Fig. 6.3 has been chosen as an example for the evaluation of the integrity of the adhesive patches, meaning the percentage of successfully reproduced pillars. For this example the pillar radius is 3.5 μm and the pillar density is 6.4 $\cdot 10^5/cm^2$. With different molds an integrity of the pillar structures close to 100 % has been achieved in our studies. Tack measurements are a well introduced method in the area of pressure sensitive adhesives (PSAs) [2]. Based on a home-built setup for the investigations of PSAs [3] we modified the method to address dry adhesives. The basic components of the measurement device are given in Fig. 6.4a. Following the scheme in Fig. 6.4b, a punch with a defined surface is moved vertically towards the sample surface with a preset constant velocity. On contact with the sample, the punch will apply a preset loading force and the contact with the sample is maintained for a preset duration (Fig. 6.4c), before the punch is retracted with a constant, preset velocity in vertical direction (Fig. 6.4d). An important detail for the measurement is the punch geometry and material. Different geometries will contact the sample differently. A cylindrical punch has the benefits of knowing the exact contact area and having the preload force distributed over the contact area homogeneously. These well defined conditions however require a parallel alignment of the surfaces of punch and the dry adhesive patch. In this work, measurements are done with a polished aluminum punch, an aluminum foil tip punch and a leather tip punch. Given a sufficient transparency of the investigated sample the use of a polished metal surface allows for the microscopic observation of debonding mechanism of adhesive patches (as indicated with the camera symbol in Fig. 6.4b-d.

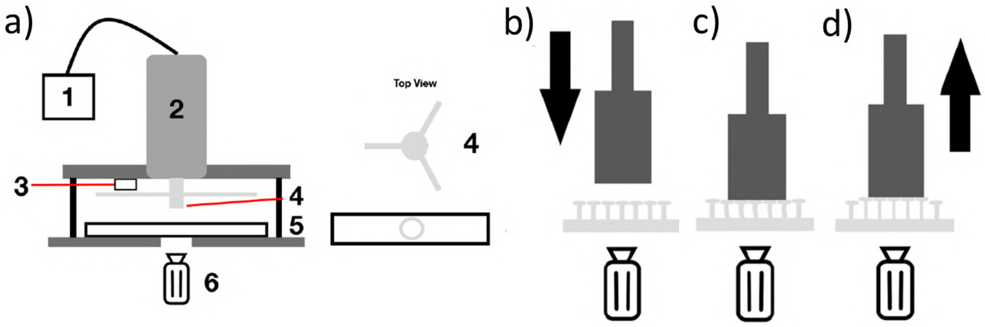

Figure 6.4:
Tack measurement: a) Schematic overview of the custom-built Tack setup 1) linear actuator with DC motor 2) force sensor 3) distance sensor 4) punch holder 5) sample holder 6) microscope and camera b) approach of punch c) stand still at defined applied force d) rectracting punch and measurement of tack.

In Fig. 6.5 tack measurements for a sticky note and a dry adhesive with pillar microstructure are compared. The course of the experiments corresponds to the stages described in Fig. 6.4b-d. Most important value to extract from the tack measurement is usually the force maximum measured during retraction. Furthermore in Fig. 6.5a it can be observed that for the sticky note the debonding occurs over a longer distance compared to the dry adhesive patch in Fig. 6.5b. This can be explained by the fibrillation acrylate copolymer used in the coating of the sticky note.

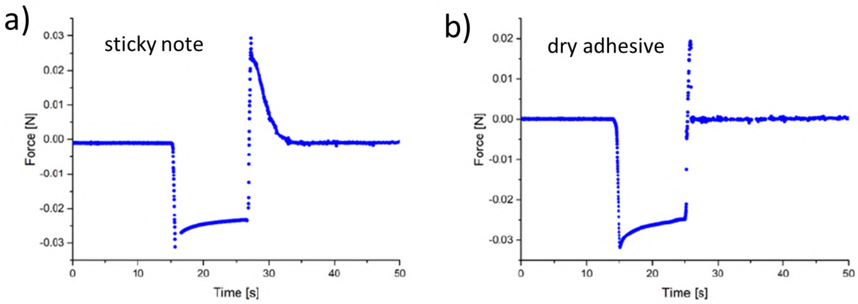

Figure 6.5:
Tack experiments for a) a sticky note (adhesive coated paper) and b) a dry adhesive with pillar microstructure.

The characterization of dry electrodes concerning their potential use in medical and scientific applications complies the measurement of electrical conductivity as well as tack investigations as a measure for achievable skin adhesion. Despite these basic characterizations it is important to monitor the dry electrodes in devices for the measurement of electroencephalograms (EEGs). For our conductive dry adhesive electrodes with microstructured pillars we achieved comparable properties to wet electrodes in terms of signal quality in such measurements.

[1] T. Kim, J. Park, J. Sohn, D. Cho, S. Jeon, *ACS Nano* **10**, 4770-4778 (2016)

[2] P. Müller-Buschbaum, T. Ittner, E. Maurer, V. Körstgens, W. Petry, *Macromol. Mater. Engin.* **292**, 825-834 (2007)

[3] M. Schindler, M. Koller, P. Müller-Buschbaum, *ACS Appl. Mater. Interfaces* **7**, 12319 (2015)

6.3 Photochromic films based on WO_3 nanoparticles and cellulose nanocrystals

V. Körstgens, J. Thalhammer, P. Müller-Buschbaum

In the emerging field of printable electronics there is a growing demand for transparent, flexible substrate and coating materials [1]. Films based on cellulose nanofibrils are a promising sustainable alternative to fully synthetic polymers [2]. Transparent films can be obtained of cellulose nanofibrils (CNFs) or even more downsized particles, cellulose nanocrystals (CNCs). These cellulose materials can be extracted out of soft wood with an oxidative process with 2,2,6,6-tetramethyl-piperidine-1-oxyl radicals [3]. The TEMPO-oxidation converts hydroxyl-groups into carboxyl functional groups on the surface of fibrils and nanocrystals, respectively. In this investigation we demonstrate how photochromic thin films can be produced out of such CNCs. Photochromism is defined as the light induced, reversible transformation of a chemical species between two forms with different absorption spectra. A well-known example to exhibit this behavior is tungsten trioxide whose photochromic mechanism especially in combination with the cellulose polymer shall be further explained in the following: In a CNC-WO_3 composite the oxygen atoms of the tungsten trioxide can form H-bonds with the six OH-groups of the cellubiose units of the cellulose polymer. To explain the photochromic behavior of tungsten(VI) oxide and cellulose nanocrystals Adachi et al. concluded that the WO_3 colloids responsible for the change in color are mainly $WO_3{\cdot}2H_2O$ crystallites [3, 4]. If these particles are radiated with UV light electron-hole pairs can be generated in the conduction and valence band which can weaken the O-H bonds of the water molecules of $WO_3{\cdot}2H_2O$ causing the H_2O to decompose into H^+, O_2 and free electrons. While the oxygen molecules are released in the ambient air, the protons subsequently bind with remaining oxygen atoms, again forming H_2O. The change of color due to the UV radiation can now be explained through the reduction of colorless W^{6+} into colored W^{5+} ions [4]. We investigated composite films of cellulose nanocrystals (BGB ultra, Blue Goose Biorefineries Inc.) and WO_3 nanoparticles (P-10, Avantama). Different ratios of the two components have been applied with a number of coating techniques ranging from simple drop casting on glass substrates, blade coating and spray deposition.

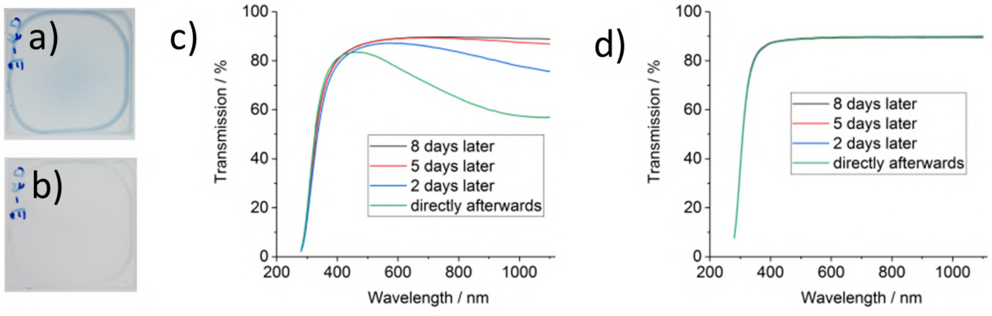

Figure 6.6:
Composite films of cellulose nanocrystals and WO_3 nanoparticles after UV light illumination a) film on glass substrate directly after illumination b) colorization faded after 192 h c) transmission measured at different times d) control experiment with pure cellulose nanocrystals

In Fig. 6.6a it is shown how an initially colorless transparent film prepared with solution casting changes to blue color after illumination with UV light for 2 h. The color change is most obvious in the rim around the edge of the sample. This elevated structure is a consequence of the solution casting process and can be avoided by an alternative coating technique like spray deposition. With UV-vis measurements the transmission of the sample is followed with time in the central part of the sample. In Fig. 6.6c) it is shown that over the course of approximately 200 h the initial state is reestablished leading to a colorless film again as shown in Fig. 6.6b). The reversibility of the process proves that the composite is photochromic. For comparison the pure cellulose nanocrystal film is shown without any photochromic effect (Fig. 6.6d)).

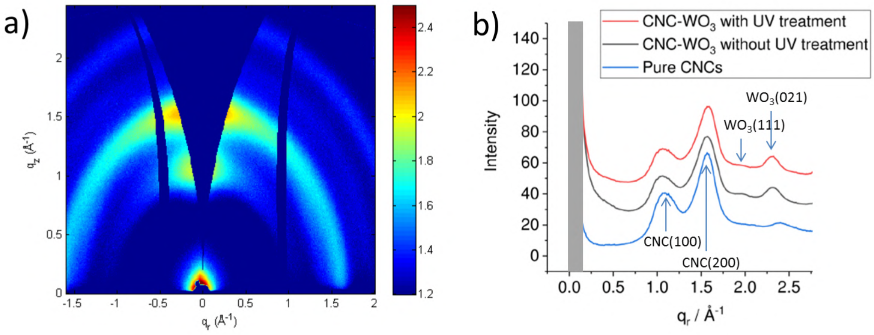

Figure 6.7:
GIWAXS investigation of composite films. a) 2D GIWAXS pattern of composite of cellulose nanocrystals and WO_3 nanoparticles with UV treatment b) comparison of pure cellulose nanocrystals and composites with WO_3 before and after UV treatment, the curves are shifted along the intensity axis for clarity.

In order to evaluate if the color change of the composite films is accompanied with distinct structural changes, grazing incidence wide angle scattering measurements (GIWAXS) were performed. The measurements were performed with a GANESHA instrument from SAXSLAB operating with a wavelength of 0.154 nm and a sample to detector distance set to 106.2 mm. In Fig. 6.7a the obtained GIWAXS pattern for a composite of cellulose nanocrystals and WO_3 nanoparticles with UV treatment is shown. The radial integrated intensities are given in Fig. 6.7b for films of pure cellulose nanocrystals and the composites with WO_3 before and after UV treatment. The pure cellulose nanocrystal film show a peak at $q_r \approx 1.1\ \text{Å}^{-1}$ corresponding to a superposition of (110) and $(\bar{1}10)$ lattice planes. From the (200) at $q \approx 1.1\ \text{Å}^{-1}$ reflection in Fig. 6.7a it can be concluded that the cellulose nanocrystal are preferentially aligned parallel to the substrate surface. The corresponding lattice spacing is ≈ 0.4 nm in accordance with investigations on other cellulose systems [2]. In the composite films additional peaks from WO_3 without preferential orientation can be assigned to lattice planes (111) at $q_r \approx 2.0\ \text{Å}^{-1}$ and (021) at $q_r \approx 2.4\ \text{Å}^{-1}$. The slight differences in the scattering pattern before and after UV illumination require further investigation. For the photochromic effect of WO_3 nanoparticles the occurrence of $WO_3 \cdot 2H_2O$ crystallites is required [3,4]. For this reason the water retention properties of the cellulose component in the composite films are expected to play a major role in applications. Further studies on the photochromic effect of composite films with cellulose (CNCs and CNFs, respectively) will include the influence of humidity.

[1] H. Zhu, W. Luo, P.N. Ciesielski, Z. Fang, J.Y. Zhu, G. Henriksson, M.E. Himmel, L. Hu, *Chem. Rev.* **116**, 9305-9374 (2016)

[2] W. Ohm, A. Rothkirch, P. Pandit, V. Körstgens, P. Müller-Buschbaum, R. Rojas, S. Yu, C. J. Brett, D. L. Söderberg, S. V. Roth, *J. Coat. Techn. Res.* **15**, 759-769 (2018)

[3] A. Isogai, T. Saito, H. Fukuzumi, *Nanoscale* **3**, 71-85 (2011)

[4] S. Stoenescu, S. Badilescu, T. Sharm, R. Brüning, V.-V. Truong, *Opt. Engin.* **55**, 127102 (2016)

[5] K. Adachi, T. Mita, S. Tanaka, K. Honda, S. Yamazaki, M. Nakayama, T. Goto, H. Watari, *RSC Adv.* **2**, 2128-2136 (2012)

6.4 Laser-Neutron pump-probe experiment at the neutron time-of-flight spectrometer TOFTOF

D. Schwaiger, W. Lohstroh[1], J. Pieper[2], P. Müller-Buschbaum

[1] MLZ, Garching, Germany
[2] TU Tartu, Tartu, Estonia

In biological systems, function is often closely related to dynamics and conformational changes of protein molecules. One example for this dynamics – function correlation is the operation of photosystem II, which features the absorption of photons by pigments and subsequent creation of a reaction potential, which is the basis for further steps in photosynthesis. In order to study such systems, neutrons are suited very well due to the possibilities of observing light elements (mainly Hydrogen), very abundant in proteins, and of introducing contrast between different motions by (partial) deuteration of the sample. In order to observe functional dynamics, an optical activation is needed to start the dynamic processes. For this reason we develop a setup, which is designed for the operation in the time-of-flight spectrometer TOFTOF [1] and will be used to illuminate a sample with laser pulses of certain wavelength, energy and frequency.
After synchronization with the neutron spectrometer, we hope to be able to follow the dynamics of the sample after light activation. As a model system, the light-driven proton pump bacteriorhodopsin (BR) is chosen. This protein is embedded in the purple membrane of Halobacterium salinarum. After activation, the system runs through a photocycle on a timescale of 0.1 – 1s, which is well studied by time resolved optical absorption techniques [2][3].

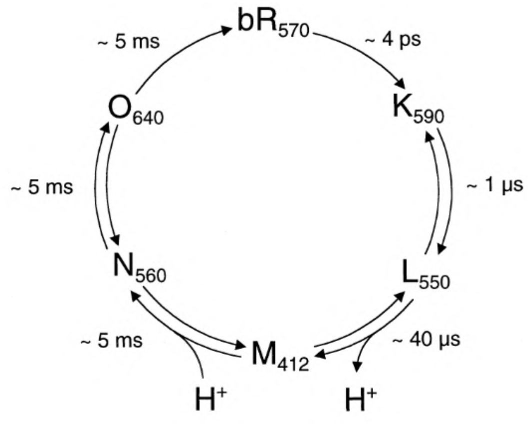

Figure 6.8:
Photocycle of BR at room temperature. Ground state and intermediates are characterized by their absorptoin maxima in [nm] (subscripts) and decay times. [3]

As shown in fig. 6.8, there are several metastable intermediates (K – O), adopted by BR, which all have specific absorption maxima and decay times. The most prominent intermediate state is represented by M. It stands out by an absorption maximum, which is clearly distinct from the absorption maxima of all the other substates and the fact that the actual conformational change, including the transport of an external proton into the thylakoid - lumen, takes place at this stage of the photocycle. In the figure, this is indicated by the loss of a proton before, and the regain of a proton after M. For this reason, the M intermediate has been addressed particularly in previous studies of the system and will also be our first object of study.

In preparation for the neutron experiments, time resolved optical absorbance difference experiments have been performed in Tartu, Estonia. Samples of purple membrane (PM) films of certain hydration levels were prepared, using salt solutions to adjust relative humidity in closed atmospheres. The absorption changes at a probe wavelength of 412 nm were observed and logged on an oversampled logscale to ensure sufficient time resolution at any time. For the activation, a laser of the wavelength 532 nm and a pulse energy of 280 mJ was chosen, but beam intensity was attenuated with optical greyfilters by a factor of 0.9 or 0.99 respectively to create similar conditions to those, planned at the neutron spectrometer.

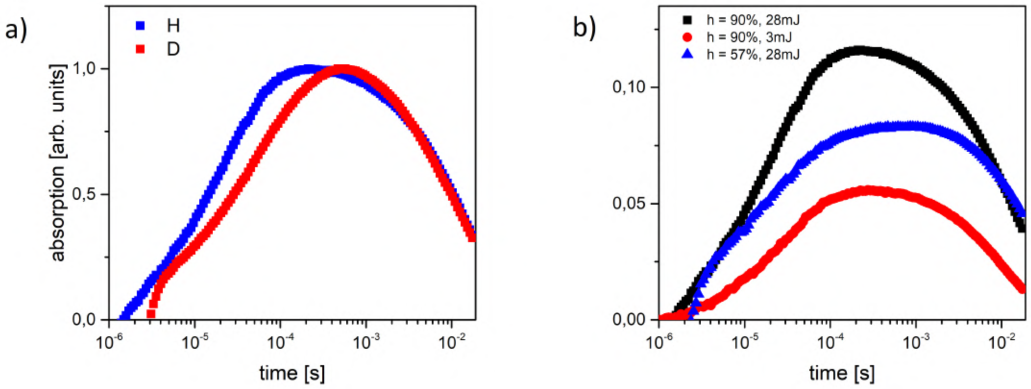

Figure 6.9:
Time resolved absorption spectra for a probe wavelength of 412 nm. Time = 0 represents the moment of activation. a) shows the difference in kinetics between H_2O (blue curve) and D_2O (red curve) hydrated BR for h = 0.9 and pulse energy = 28mJ (values normalized to a max. of 1). b) compares absorption between the black curve (same parameters as the blue one in a)) and both, one for a lower pulse energy (3mJ, red) and one for a lower hydration level (0.57, blue) respectively

Fig. 6.9 reveals the kinetics of accumulation and decay of the M intermediate in the BR-photocycle. It becomes apparent, that formation of M starts at times smaller than 0.001 ms after activation and most of M is gone 100 ms after activation (not covered by the time range of this figure), whereas the maximum is reached after about 0.1-1 ms. This gives the timeframe for the neutron measurements. Additionally the kinetic difference of hydrated and deuterated PM are displayed in fig. 6.9 a). The effect of the introduction of D_2O on kinetics is often neglected, but fig. 6.9 a) suggests a shift of the maximum concentration of M by almost one magnitude towards longer times. This has to be accounted for in further experiments.
Fig. 6.9 b) compares different hydration levels and pulse energies. It is obvious, that kinetics are strongly influenced by hydration. Reducing the water content (blue curve) of the sample not only slows the dynamics, it also reduces the quantum yield in the light absorption process. By decreasing the pulse energy (red curve), the percentage of activated molecules is decreased, which is manifested in a lower relative absorption of samples which were exposed to low intensity pulses. This can be attributed to the very high absorption of PM and thus a more incomplete illumination of the sample. A very slight shift of the absorption maximum towards smaller times can be inferred for higher energy pulses, which becomes way more prominent for even higher energies [3]. This indicates forced changes in the photocycle, leading to irreversible changes and finally bleaching and destruction of the sample. For a QENS experiment, lasting several hours, a laser pulse energy of well below 27 mJ but preferably still above 3 mJ is suggested by the results, in order to keep the sample stable and ensure good signal.

[1] T. Unruh, J. Neuhaus, W. Petry, *Nuclear Instruments and Methods in Physics Research Section A: Accelerators, Spectrometers, Detectors and Associated Equipment* **580**, 1414-1422 (2007)

[2] G. Varo, J. K. Lanyi, *Biochemistry* **29**, 2241-2250 (1990)

[3] J. Pieper, A. Buchsteiner, N. A. Dechner, R. E. Lechner, T. Hauß, *Photochem. Photobiol.* **85**, 590-597 (2009)

6.5 Polymers for lithium ion batteries - investigating composite electrodes

C. Telescu, S. Schaper, P. Müller-Buschbaum

With the development of new technologies, the demand for reliable, cheap and long life batteries with high specific energy and high efficiency is constantly increasing. Therefore, a significant effort is devoted to the improvement of battery performance. The lithium-ion polymer battery is a prospective candidate for powering the new generation of electrical devices and vehicles due to outstanding advantages as low weight, high negative potential and high specific capacity. These features are of critical significance for the automotive and electronics industries. Improving materials, composition, and interfaces is still necessary to exploit the possibilities of polymer based lithium-ion batteries (LIB). This project has the aim to study LIB cells with different polymer composite cathodes.

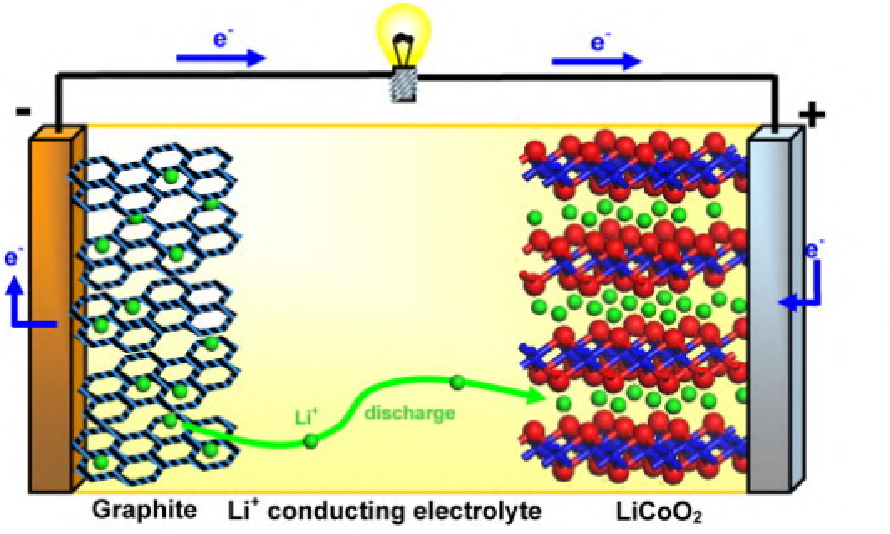

Figure 6.10:
Schematic setup of a Li-ion battery with $LiCoO_2$ and graphite electrode [1].

A rechargeable battery in general consists of five main components: Two current collectors, a positive electrode, a negative electrode, and an electrolyte in between the electrodes. The current collectors are responsible for electron transport; generally, copper and aluminum are used as these materials have very good electrical conductivity and match electrochemically with the used electrodes. Organic solvents enriched with different lithium salts serve as liquid electrolytes. There are also ceramic and polymer based solid electrolytes. Liquid electrolytes show a way higher conductivity ($\sigma \sim 10^{-2}\, S/cm$) [2] than the solid block co-polymer electrolytes ($\sigma \sim 10^{-4}\, S/cm$) [3] at room temperature, but liquid electrolytes are mostly flammable and also they require a separator to prevent a short cut and lithium dendrite formation between the electrodes. The electrode on which the oxidation reaction during discharging takes place is called anode, and cathode is the electrode where the reduction reaction is performed.

The first commercial Li-ion battery, introduced by Sony Corporation in 1991, was based on a $LiCoO_2$ cathode and a carbon anode, a simplified sketch of a LIB can be seen in figure 6.10. When an electrical current is applied to charge the cell, lithium ions move out of the cathode ($LiCoO_2$) and become intercalated inside the graphite anode. Upon battery discharge, the lithium ions travel back to the cathode and an electrical current is created by the electrons moving externally from the anode to cathode.

During the last decade in the Li-ion battery industry, many alternative cathode materials have been exploited. These materials include compositional variations of $LiCoO_2$ structure, such as $LiNi_{0.8}Co_{0.15}Al_{0.05}O_2$ (lithium nickel-cobalt-aluminium-oxide, NCA) [4], cobalt-free compounds in the $Li_{1+x}Mn_{2-x}O_4$ system [4] and lithium-iron(II)-phosphate (LFP) with the chemical sum formula $LiFePO_4$, this material has an olivine-type structure.

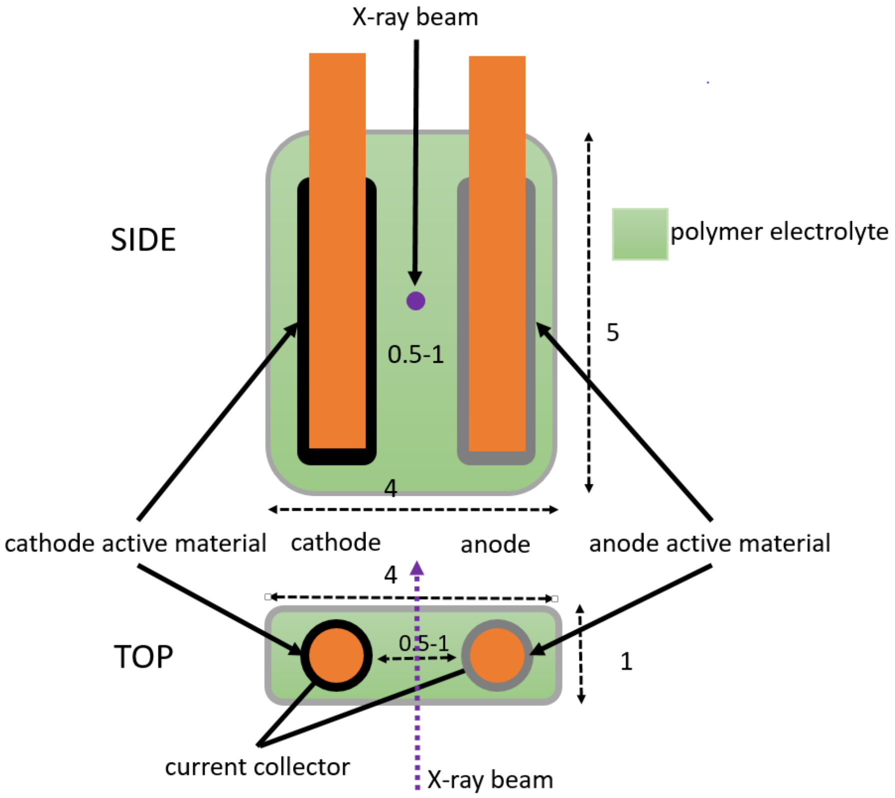

Figure 6.11: Detailed drawing of the cell geometry in SIDE and TOP views. All dimensions are given in millimeters.

The main disadvantage of the $LiMnO_2$ systems are the structural transformations to the spinel phase during electrochemical cycling, which hinders subsequent Li insertion and/or removal, also the required temperature for oxygen evolution and Li vacancy formation is too high to be compatible with any practical synthesis temperature. NCA provides a higher practical capacity $160 - 180\,mAh/g$, but its thermal instability on delithiation due to the presence of the high valence Ni compromises the safety of Li-ion cells, another disadvantage is the cobalt, which is toxic and quite expensive for the large scale production. The theoretical capacity of LFP is at $160\ mAh/g$, while the capacity is slightly lower, LFP still performs better at aspects of environment, health and cost. A study of polymer composite cathodes is done with lithium iron phosphate (LFP), lithium nickel cadmium aluminum oxide (NCA) and graphite as active materials. Lithium salt doped polystyrene-block-polyethylene oxide is used as a solid polymer electrolyte. The morphology of the polymer can be investigated with small-angle X-ray scattering (SAXS). It is also possible to observe important structural changes inside the battery during charge or discharge. Using SAXS, in-operando studies were performed on specifically designed capillary based micro-batteries. A sketch of a capillary battery assembly is shown in Figure 6.11.

[1] P. G. Bruce, *Solid State Ionics* **21-26**, 752–760 (2008)

[2] M. Deepa, N. Sharma, S. A. Agnihotry, S. Singh, T. Lal, R. Chandra, *Solid State Ionics* **152-153**, 253-258 (2002)

[3] E. Metwalli, M. V. Kaeppel†, S. J. Schapert, A. Kriele, R. Gilles, K. N. Raftopoulost, P. Müller-Buschbaum, *ACS Appl. Energy Mater.* **1**, 666-675 (2018)

[4] H. J. Bang, H. Joachin, H. Yang, K. Amine, J. Prakash, *J. Electrochem. Soc.* **153**, A731 (2006)

6.6 Inelastic Neutron Scattering on FeNiCo High-Entropy Alloys

J. Costa, W. Petry, M. Leitner

High-entropy alloys, equiatomic alloys of five or more principal elements, have recently been the focus of much attention due to their superior structural properties [1]. The stability of these materials is a matter of great concern for application, where it is still not settled whether the prototypical examples are thermodynamically stable phases or just metastable on accessible timescales. In this respect, a profound knowledge of lattice vibrations (phonons) is necessary as they are responsible for phase stabilities and thermodynamic properties, but also for other properties such as thermal conductivity. However, these issues have so far scarcely been studied directly [2].

Equiatomic FeNiCo is of specific interest as a medium-entropy analogue of the prototypical Cantor alloy CoCrFeMnNi [3]. In this class of materials, clearly also the role of magnetic effects has to be considered, with a richness of phenomena expected due to the interactions between the different atomic moments arranged on the face-centred cubic lattice with potential short-range order, and the interplay between magnonic and phononic excitations at elevated temperatures.

We present here our results obtained by inelastic neutron scattering. So far, such experiments have mostly been conducted with triple-axis-spectrometers. For this experiment, however, there are other criteria: a profound knowledge of lattice vibrations requires an as wide as possible two-dimensional spectrum of the density of states, the polycrystalline FeNiCo-samples give only access to $|Q|$ and future developments in the field of instrumentation will be dominated by the upcoming pulsed neutron facility ESS (European Spallation Source). An instrument which fulfills all points is the time-of-flight spectrometer TOFTOF at the MLZ Garching.

To ensure that the spectrum obtained from the new method contains the desired result, it was initially necessary to validate the experimental technique: Nickel, which has properties and interactions similar to a single-phase FeNiCo, is used for this purpose. For nickel the inelastic neutron spectrum is simulated in Fig. 6.12 (left) via the already known Born-von-Karman parameters taken from [4]. The experimentally obtained spectrum (Fig. 6.12, right) contains the intensity of the scattered and counted neutrons with a certain energy E in THz and a specific scattering angle $|Q|$ in Å^{-1}. Brightly shining, sharp edges belong to van Hove singularities. Since the experiment agrees well with the simulation, it can be said that the instrument used delivers the desired result.

To determine the chemical disorder inherent to the highly-entropic character of FeNiCo, its short-range order was investigated via the elastically diffracted line at $E = 0\,\mathrm{THz}$ at different temperatures. The plot at room temperature is displayed in Figure 6.13 (left). It shows the counted neutrons at a certain scattering angle. The second and third Bragg peak belongs to FeNiCo, the first and fourth one to niobium, the material the sample holder is made of. The counting rate is composed of coherent (Bragg peak), incoherent (flat line) and diffuse-coherent scattering (flat line). The diffuse-coherent part originates from the different scattering lengths of Fe, Ni and Co. It makes up roughly 30%. The whole line declines due to the Debye-Waller factor (DWF). Since no other patterns are contained, short-range order is not present. The spectra at elevated temperatures result in quite similar curves (not shown). At least for the measured period of time ($\approx 2\mathrm{h}$) FeNiCo is chemically stable there.

Further we looked for an influence of the randomly arranged Fe, Ni, Co atoms on the fcc lattice with respect to the phonon spectrum by comparing FeNiCo with Ni below and above the Curie temperature T_C. This is ongoing work.

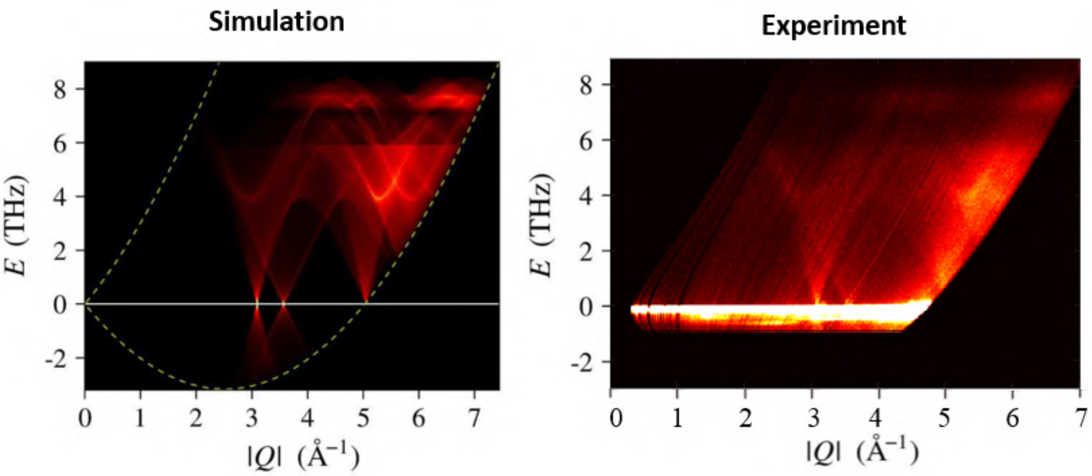

Figure 6.12:
The inelastic neutron spectrum of Nickel is shown with the wavelength $\lambda = 2.5$ Å at room temperature. The intensity is plotted against the energy E and the scattering vector $|Q|$. The polycrystalline sample gives only access to $|Q|$. On the *left*-hand side the simulation is displayed, on the *right*-hand side the experimentally obtained spectrum. The elastic line corresponds to the value $E = 0$.

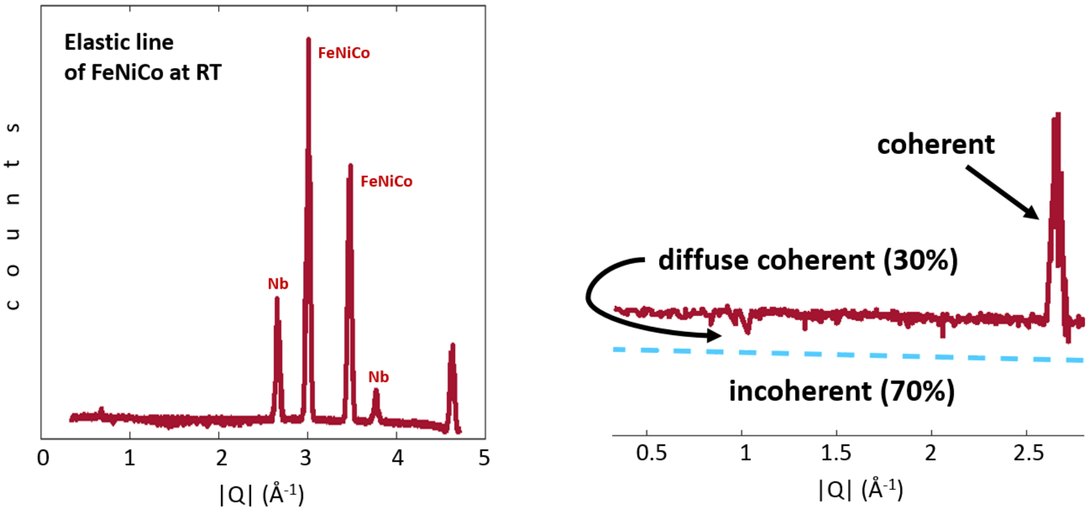

Figure 6.13:
(left) Elastic line of FeNiCo at room temperature. The counted neutrons are plotted against the scattering angle $|Q|$. The niobium peaks belong to the sample holder. *(right)* The counting rate consists of the coherent (Bragg peak), incoherent (flat line) and diffuse-coherent cross-section (flat line). The line declines due to the Debye-Waller factor. Since no other patterns are contained, short-range order is not present in FeNiCo — at least for the measured period of time ($\approx 2\mathrm{h}$).

[1] J.-W. Yeh, *Ann. Chim. Sci. Mat.* **31**, 633–648 (2006)

[2] F. Körmann, Y. Ikeda, B. Grabowski, M. H. Sluiter, *npj Comput. Mater.* **3**, 36 (2017)

[3] B. Cantor, *Entropy* **16**, 4749–4768 (2014)

[4] M. Kresch, O. Delaire, R. Stevens, J. Y. Y. Lin, and B. Fultz, *Phys. Rev. B*, **75**, 104301 (2007)

6.7 Magnetic and chemical microstructures of Mn-based Heusler compounds studied by small-angle neutron scattering

U. Zweck[1], P. Neibecker[1], S. Mühlbauer[1], P.-Y. Chiu[1], W. Petry[1], M. Leitner[1]

[1] MLZ, Garching, Germany

Ni_2MnZ based Heusler compounds have attracted a considerable amount of attention due to their various appealing properties such as the ferromagnetic shape-memory effect or the magnetocaloric effect. As full-Heusler alloys, their low-temperature equilibrium structure corresponds to $L2_1$ order, which can be described by four nested fcc lattices. Two of those sublattices, α_1 and α_2, are occupied solely by Ni atoms, while β and γ hosts Mn and Z atoms, respectively. At high temperatures a state of increased entropy is preferred, leading to a random distribution of the Mn and Z atoms over the β and γ sublattices, corresponding to B2 order. Quenching a crystal from the B2 stable regime preserves its disordered structure at low temperatures, where atomic diffusion is inactive. During subsequent annealing, $L2_1$-ordered domains nucleate independently and grow, leading to a division of the crystal into anti-phase domains according to Mn occupying either the β or γ sublattice [1]. Disregarding the α sites, the nearest neighbours of the β sites belong to the γ sublattice and vice versa, thus the boundaries of these domains host Mn-Mn and Z-Z neighbour pairs.

In Ni_2MnZ compounds the magnetic moments are mainly carried by Mn atoms, whose exchange interaction depends strongly on the distance between them. While the moments of next-nearest neighbour Mn atoms interact ferromagnetically, neighbouring Mn spins couple anti-ferromagnetically. Therefore, the Mn spins on the β and γ sublattices always align antiparallel with respect to each other. According to this argumentation, a reversal of magnetization when crossing an APD boundary should be expected. Using TEM and Lorentz TEM a reversal of magnetization at structural APD boundaries has indeed been observed in $Ni_{50}Mn_{25}Al_{12.5}Ga_{12.5}$ bulk samples, implying that structural and magnetic domains are identical [2]. Also the width of the magnetic domain walls in these systems is unusually thin, about 10 nm [2]. The magnetic properties of these systems are therefore strongly dependent on the microstructure, with anti-ferromagnetic and ferromagnetic exchange interactions being present [3].

To study this interplay of magnetic and structural order as well as the mechanism of coupling of ferromagnetic domains across APD boundaries, we have applied small-angle neutron scattering (SANS) to investigate the magnetization microstructure of $Ni_2MnAl_{0.5}Ga_{0.5}$ powder samples. To obtain samples with a distinct APD size, solution annealed ingots have been crushed and manually ground to powder of diameter $< 125\ \mu$m. The preparation process induces lattice defects to the samples, which are removed by recovery annealing the powders for 4 h in the B2-stable regime at 1073 K. The samples were subsequently quenched in room temperature water and afterwards annealed in the $L2_1$ stable regime at 623 K for 30 min, 3 h and 10 d, to obtain distinct APD sizes. The magnetic transition temperatures T_C of the powder samples have been determined using Differential Scanning Calorimetry (DSC), with T_C ranging from 314.5 K for the as quenched powder sample to 387.1 K for the one with a 10 d annealing duration. These results are in good agreement with the magnetic transition temperatures of $Ni_2MnAl_{0.5}Ga_{0.5}$ bulk samples, which were prepared under identical annealing conditions. In case of the as quenched samples, the powder shows a 20 K higher T_C than in the bulk, indicating that quenching powder samples is less effective than for the bulk ones. All powder samples were packed between two pure Al foils and pressed under 180 bar at room temperature. The SANS measurements have been performed under zero magnetic field at the SANS-1 at the FRM II, Garching. For each sample three detector distances, 2 m, 8 m and 20 m, were used in order to acquire a complete diffractogram. The samples were measured in the temperature range from 4.2 K to 450 K. Instead of stabilizing the temperature the data were collected continuously during temperature

sweeps, to acquire them in the whole temperature range.
Figure 6.14 a) displays SANS profiles in a temperature range from 50 K to 450 K of the $Ni_2MnAl_{0.5}Ga_{0.5}$ powder sample with a 10 day annealing duration. SANS profiles measured below the magnetic transition temperature of 387 K display a shoulder at around 0.05 Å^{-1} which weakens with increasing temperature. Above T_C this contribution has vanished completely from the profile. Since structural change due to atomic diffusion cannot be the reason for any additional temperature-dependent signal at such low temperatures, its nature must be magnetic. Clearly, a shoulder at 0.05 Å^{-1} corresponds in real space to a characteristic magnetic domain size of about 125 Å.

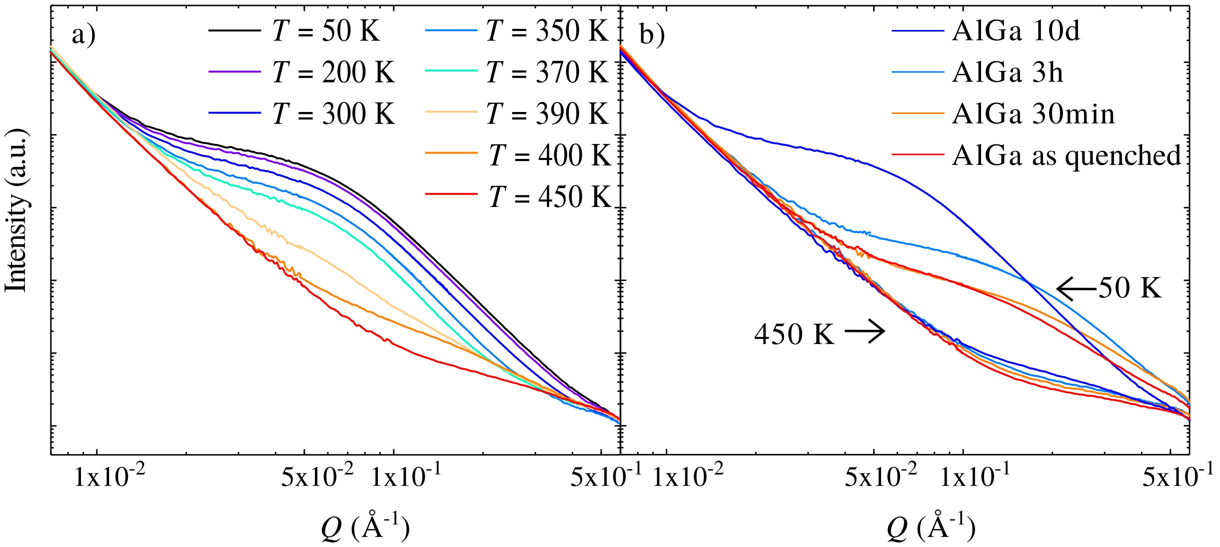

Figure 6.14:
a) Temperature-dependent SANS profiles of the $Ni_2MnAl_{0.5}Ga_{0.5}$ sample annealed for ten days at 623 K, b) SANS profiles of the $Ni_2MnAl_{0.5}Ga_{0.5}$ samples measured at 50 K and 450 K.

In figure 6.14 b) the measurements at 50 K and 450 K of $Ni_2MnAl_{0.5}Ga_{0.5}$ samples with increasing annealing times and consequently increasing APD sizes are compared. The profiles of all samples display the same temperature-dependent characteristics as discussed above for the sample with a 10 d annealing duration. The shoulder is most distinctive for the profile of the sample with the longest annealing duration and weakest for the as quenched one. Its position varies for each sample, corresponding to characteristic lengths of the magnetic domain from 60 Å for the as quenched case to 125 Å for the one with a 10 d annealing duration.
From the presented results it can be clearly seen that APD size and the characteristic length of magnetic domains are correlated. Specifically, larger APD size has a positive effect on the magnetic domain size. This supports our microscopic model of Mn and Z atoms aligning at APD boundaries as well as the exchange interaction of spins across APD boundaries.

[1] H. Ishikawa, R. Y. Umetsu, K. Kobayashi, A. Fujita, R. Kainuma, K. Ishida, *Acta Mater.* **56**, 4789 (2008)

[2] T. Yano, Y. Murakami, R. Kainuma, D. Shindo, *Mat. Trans.* **48**, 2636 (2007)

[3] P. Neibecker, M. Leitner, G. Benka, W. Petry, *Appl. Phys. Lett.* **105**, 261904 (2014)

7 Teaching and outreach

7.1 Lectures, seminars and lab courses

Spring Term 2018

Prof. Dr. Peter Müller-Buschbaum, *Experimentalphysik 2 für MSE*
Prof. Dr. Christine Papadakis, *Angewandte Physik: Polymerphysik 2*
Prof. Dr. Peter Müller-Buschbaum, Dr. Volker Körstgens,
Nanostructured Soft Materials 2
Dr. Michael Leitner, *Materialphysik auf atomarer Skala 2*
Prof. Dr. Peter Müller-Buschbaum, Prof. Dr. Christian Große, *Mess- und Sensortechnologie*
Prof. Dr. Winfried Petry, *Physics with neutrons 2*
Prof. Dr. Christine Papadakis, *Höhere Physik 2*
Prof. Dr. Peter Müller-Buschbaum, *Seminar: Current problems in organic photovoltaics*
Prof. Dr. Peter Müller-Buschbaum, Prof. Dr. Christine M. Papadakis,
Master Seminar: Soft Matter Physics
Prof. Dr. Peter Müller-Buschbaum, Prof. Dr. Christine M. Papadakis,
Bachelor-Seminar: Funktionelle weiche Materialien
Prof. Dr. Peter Böni, Dr. Alexandros Koutsioumpas, Dr. Christoph Morkel, Prof. Dr. Peter Müller-Buschbaum, Dr. Markos Skoulatos, *Seminar Neutronen in Forschung und Industrie*
Prof. Dr. Peter Müller-Buschbaum, Prof. Dr. Christine M. Papadakis,
Seminar: Structure und dynamics of condensed matter
Prof. Dr. Peter Müller-Buschbaum, Prof. Dr. Christine M. Papadakis, *Seminar: Polymers*
Prof. Dr. Winfried Petry, *Erasmus Mundus MaMaSELF Summer School*
Montpellier, France, 6 – 15 Sep 2018

Autumn Term 2018/2019

Prof. Dr. Christine Papadakis, *Angewandte Physik: Polymerphysik 1*
Prof. Dr. Peter Müller-Buschbaum, Dr. Volker Körstgens, *Nanostructured Soft Materials 1*
Prof. Petry, Dr. Markus Kellermeier, *Master Course "Radiation Biology"*
Dr. Michael Leitner, *Materialphysik auf atomarer Skala 1*
Prof. Dr. Peter Müller-Buschbaum, Prof. Dr. Winfried Petry, Dr. Sebastian Busch,
Physics with neutrons 1
Prof. Dr. Christine Papadakis, *Höhere Physik 1*
Prof. Dr. Peter Müller-Buschbaum, *Seminar: Current problems in organic photovoltaics*
Prof. Dr. Peter Müller-Buschbaum, Prof. Dr. Christine M. Papadakis,
Master Seminar: Soft Matter Physics
Prof. Dr. Peter Böni, Dr. Alexandros Koutsioumpas, Dr. Christoph Morkel, Prof. Dr. Peter Müller-Buschbaum, Dr. Markos Skoulatos, *Seminar Neutronen in Forschung und Industrie*
Prof. Dr. Peter Müller-Buschbaum, Prof. Dr. Christine M. Papadakis,
Seminar: Structure und dynamics of condensed matter
Prof. Dr. Peter Müller-Buschbaum, Prof. Dr. Christine M. Papadakis, *Seminar: Polymers*

Lab Courses 2018

Rasterkraftmikroskopie (Fortgeschrittenenpraktikum)
Neutron scattering at FRM II (Fortgeschrittenenpraktikum)
Theoretische und praktische Einführung in AFM (Fortgeschrittenenpraktikum)
Thermische Analyse (Fortgeschrittenenpraktikum)
Darstellung von DNS im Rasterkraftmikroskop (Fortgeschrittenenpraktikum)

7.2 Conferences and public outreach

FRM II and MLZ
Research neutron source Heinz Maier-Leibnitz under new leadership
31 Mar/1 Apr 2018

Professor Petry's term as Scientific Director ended on March 31, 2018. FRM II and MLZ welcomed Prof. Dr. Peter Müller-Buschbaum as their new Scientific Director.

Prof. Dr. Peter Müller-Buschbaum, Prof. Dr. Winfried Petry
credits: A. Heddergott/TUM

P. Müller-Buschbaum, W. Petry

Lehrerfortbildung "Große Instrumente für große Fragestellungen"

42. Edgar-Lüscher-Seminar

Zwiesel, 27 – 29 Apr 2018

Programm

Freitag, 27. April 2018

13.00 - 14.15	**Einführungsvortrag für Schüler** *Dr. Andreas Kratzer – TUM School of Education*
14.15 - 14.45	Diskussion und Kaffeepause
14.45 - 15.15	**Begrüßung**
15.15 - 16.30	**Aktuelle Projekte bei GSI und zukünftige Möglichkeiten bei FAIR** *Prof. Dr. Peter Senger – GSI Helmholtzzentrum für Schwerionenforschung, Darmstadt*
16.30 - 17.15	Diskussion und Kaffeepause
17.15 - 18.30	**Materialphysikalische Experimente in Schwerelosigkeit - Forschen ohne Oben und Unten** *Prof. Dr. Andreas Meyer –* *DLR, Institut für Materialphysik, Köln*
18.30 - 18.45	Diskussion

Samstag, 28. April 2018

09.00 - 10.15	**PETRA IV – neue Möglichkeiten mit Synchrotronstrahlung** *Prof. Dr. Stephan V. Roth –* *DESY, Hamburg & KTH, Stockholm, Schweden*
10.15 - 11.00	Diskussion und Kaffeepause
11.00 - 12.15	**Freie Elektronenlaser, ein neues Werkzeug zur Suche nach Strukturen und Wechselwirkungen** *Dr. Rafael Abela – PSI, Villigen, Schweiz*
12.15 -12.30	Diskussion
14.30 - 15.45	**Spallationsneutronenquelle ESS – neue Möglichkeiten für die Forschung mit Neutronen** *Prof. Dr. Andreas Schreyer –* *European Spallation Source ERIC, Lund, Schweden*
15.45 - 16.30	Diskussion und Kaffeepause
16.30 - 17.45	**Neue Ergebnisse von der Neutronenquelle FRMII** *Prof. Dr. Winfried Petry – FRM II, München*
17.45 - 18.00	Diskussion

Sonntag, 29. April 2018

09.00 - 10.15	**CERN - geplante Experimente und die Zukunft** *Dr. Michael Hauschild – CERN, Genf, Schweiz*
10.15 - 11.00	Diskussion und Kaffeepause
11.00 - 12.15	**Neutrino- und Gammastrahlen-Astronomie mit IceCube, MAGIC und CTA** *Dr. Christian Fruck – TU München*
12.15 - 13.00	Diskussion, Themenfindung für das 43. Edgar-Lüscher-Seminar

Organisation

Prof. Dr. Peter Müller-Buschbaum
TUM

Prof. Müller-Buschbaum ist Sprecher für das Netzwerk „Regenerative Energien (NRG)" in der Munich School of Engineering (MSE) der TU München, Leiter des KeyLabs „TUM.solar" im Forschungsnetzwerk „Solar Technologies Go Hybrid", Deutscher Vertreter bei der European Polymer Federation (EPF) für den Bereich Polymerphysik und Associate Editor der Zeitschrift „ACS Applied Materials & Interfaces" der „American Chemical Society" (ACS). Er befasst sich in seiner Forschungsarbeit mit der Entwicklung polymerbasierter Materialien mit neuartigen Struktur-Eigenschaftsbeziehungen.

Prof. Dr. Winfried Petry
TUM

Prof. Petry ist Ordinarius am Lehrstuhl für Funktionelle Materialien (E13) des Physik Departments der TU München, Betreuungsprofessor für die Bayerische Eliteakademie und Wissenschaftlicher Direktor der Forschungsneutronenquelle Heinz Maier-Leibnitz (FRM II). Er forscht auf dem Gebiet der Materialwissenschaften mit Neutronen.

Organisatorische Hinweise

Organisation vor Ort:

OStD Heribert Strunz,	*Gymnasium Zwiesel*
OStR Christian Stoiber,	*Gymnasium Zwiesel*
StR Claus Starke,	*Gymnasium Zwiesel*
StR Thomas Kufner,	*Gymnasium Zwiesel*

E-Mail: luescherseminar@gymnasium-zwiesel.de

Hinweise:

- Alle Vorträge finden in der Aula des Gymnasiums Zwiesel statt.
- Für 5,- € erhalten die Teilnehmer am Ende des Seminars eine CD mit sämtlichen freigegebenen Vorträgen und den bisherigen Festschriften.
- In den ausgewiesenen Kaffeepausen wird in der Mensa des Gymnasiums Kaffee und Kuchen gegen eine freiwillige Spende angeboten.
- Am Rande der Aula findet eine Ausstellung verschiedener Lehrmittelausstatter und Verlage statt.

Titelfoto: ALICE-Experiment am CERN ©

42. Edgar-Lüscher-Seminar

Große Instrumente für große Fragestellungen

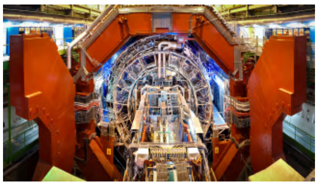

am Gymnasium Zwiesel

Freitag, 27. April 2018 bis Sonntag, 29. April 2018

Schirmherr:

Prof. Dr. Dr. h.c. mult. Wolfgang A. Herrmann,
Präsident der TUM

Veranstalter:

Ltd. OStD Anselm Räde,
Ministerialbeauftragter für die Gymnasien in Niederbayern

Wissenschaftliche Leitung:

Prof. Dr. Peter Müller-Buschbaum, *TUM*
Prof. Dr. Winfried Petry, *TUM*

Referenten

Dr. Andreas Kratzer
TUM School of Education, München

Dr. Andreas Kratzer ist akademischer Oberrat an der TUM School of Education. Er beschäftigt sich mit Physik-Fachdidaktik und entwickelt Projekte für Schülerinnen und Schüler und Möglichkeiten der Kooperation zwischen Schule und Universität (TUMLab im Deutschen Museum, TUM Science Labs, TUM Schulcluster, Schülerforschungszentrum Berchtesgadener Land, TheoPrax-Kommunikationszentrum München, Lernort-Labor). In seinem Vortrag wird er verschiedene „große Instrumente" vorstellen. Dabei soll sowohl ein Einblick in technische Grundlagen als auch in weitgefächerte Fragestellungen gegeben werden. Der Vortrag soll insbesondere eine Einführung für Schüler in die folgenden spannenden Vorträge sein.

Prof. Dr. Peter Senger
GSI Helmholtzzentrum für Schwerionenforschung

Professor Senger ist Abteilungsleiter am GSI Helmholtzzentrum für Schwerionenforschung in Darmstadt. Als Sprecher einer internationalen Kollaboration war er verantwortlich für die Entwicklung eines der vier großen Experimentierprogramme, die an der zukünftigen Facility for Antiproton and Ion Research (FAIR) durchgeführt werden.

In seinem Vortrag wird er sowohl auf die bisherige Forschung an der GSI eingehen, als auch die geplanten FAIR-Experimente beschreiben, die Antworten auf fundamentale Fragen auf den Gebieten Hadronen-, Kern-, Atom- und Plasmaphysik sowie Strahlenbiologie und Materialwissenschaft suchen.

Prof. Dr. Andreas Meyer
DLR, Institut für Materialphysik , Köln

Professor Meyer ist Direktor des Instituts für Materialphysik im Weltraum, Deutsches Zentrum für Luft- und Raumfahrt in Köln und Ordinarius der Fakultät für Physik und Astronomie an der Ruhr Universität Bochum.

In seinem Vortrag wird er über den wissenschaftlichen Nutzen von Experimenten in Schwerelosigkeit für die (Weiter-)entwicklung von erdgebundenen Messverfahren einerseits und für experimentelle Ergebnisse unter gut definierten Versuchsbedingungen ohne störende Einflüsse der Gravition anderseits berichten. Die zugehörigen Experimente werden auf Großanlagen wie dem Parabelflugzeug Zero-G, dem ZARM-Fallturm, Höhenforschungsraketen und der Internationalen Raumstation ISS durchgeführt.

Referenten

Prof. Dr. Stephan Roth
DESY, Hamburg & KTH, Stockholm, Schweden

Professor Roth ist außerordentlicher Professor für Synchrotronstrahlungscharakterisierung in der Faser- und Polymertechnologie.

Seine Forschung umfasst die Installation und Nanostrukturierung von Dünnschichten auf dem Gebiet der Nanowissenschaften und Materialien für die Informationstechnologie.

Die Selbstorganisation spielt eine entscheidende Rolle bei der Nanostrukturierung. Daher nutzt er die Klein- und Weitwinkel-Röntgenstreuung, um die Nanostrukturierung in Echtzeit durch sogenannte In-situ-Experimente zu beobachten. Sein Ziel ist es, die Beziehung zwischen Nanostruktur und Funktion aufzuklären, z.B. die Nanostruktur und Morphologie mit ihren optischen Eigenschaften in Beziehung setzen.

Dr. Rafael Abela
PSI, Villigen, Schweiz

Dr. Abela ist Projektleiter SwissFEL, Photonik und Forschung am Paul Scherrer Institut in Villigen. Anfang 2019 startet am Röntgenlaser SwissFEL der reguläre Nutzerbetrieb. Die neue Großforschungsanlage des PSI wird sehr kurze Pulse von Röntgenlicht mit Lasereigenschaften erzeugen. Damit werden Forschende extrem schnelle Vorgänge wie die Entstehung neuer Moleküle bei chemischen Reaktionen verfolgen, die detaillierte Struktur lebenswichtiger Proteine bestimmen oder den genauen Aufbau von Materialien klären. Die Erkenntnisse werden zu praktischen Anwendungen führen wie etwa neuen Medikamenten, effizienteren Prozessen in der chemischen Industrie oder neuen Materialien in der Elektronik.

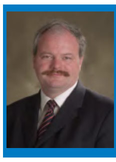

Prof. Dr. Andreas Schreyer
European Spallation Source ERIC, Lund, Schweden

Professor Schreyer ist seit 2016 Direktor für Forschung an der Europäischen Spallationsquelle (ESS) in Lund, einer Kollaboration von 15 europäischen Ländern. Zudem lehrt er an der Universität Hamburg und forscht im Bereich der Leichtbaumaterialien, Biomaterialien und magnetischen Nanostrukturen mit Neutronen- und Synchrotronstrahlung.

Die ESS wird neue Möglichkeiten der Forschung mit Neutronen im Bereich der Material- und Lebenswissenschaften eröffnen. Der Nutzerbetrieb soll 2023 beginnen. Nach einem Überblick über den aktuellen Stand des Projekts folgt eine Einführung in die zukünftigen Forschungsmöglichkeiten an der ESS mit einigen konkreten Beispielen.

Referenten

Prof. Dr. Winfried Petry
FRM II, München

Prof. Petry ist seit der Inbetriebnahme der Forschungsneutronenquelle Heinz Maier-Leibnitz (FRM II) an der Technischen Universität München im Jahr 2004 deren Wissenschaftlicher Direktor. Unter seiner Federführung wurde die Instrumentierung des FRM II konzipiert und realisiert. 2011 führte er deren wissenschaftliche Nutzung in das Heinz Maier-Leibnitz Zentrum Garching (MLZ) über. In seinem Vortrag wird er aufzeigen wie Neutronen Licht in das Dunkel der Materie bringen, die molekularen Prozesse bei der Speicherung von Energie in Batterien aufklären, wie Bakterien Antibiotika unwirksam machen und die Bedeutung von Radioisotopen erzeugt mit Neutronen für die Nuklearmedizin aufzeigen.

Dr. Michael Hauschild
CERN, Genf, Schweiz

Dr. Michael Hauschild ist Physiker am Europäischen Forschungszentrum für Teilchenphysik CERN in Genf (Schweiz), an dem der größte Teilchenbeschleuniger der Welt, der Large Hadron Collider LHC betrieben wird. Dort hat er die Entdeckung des Higgs-Teilchens im Juli 2012 unmittelbar miterlebt.

In seinem Vortrag werden neben der Vorstellung des CERN mit seinen aktuellen Forschungsgebieten und zukünftigen Forschungseinrichtungen die Grundlagen der Teilchenphysik und des Standardmodells beschrieben. Einen Schwerpunkt wird dabei das Higgs-Teilchen mit seinen Auswirkungen auf unser Verständnis der Physik insbesondere der Erzeugung von Masse bilden.

Dr. Christian Fruck
TU München

Dr. Fruck ist Post-Doc an der Technischen Universität München, Mitglied der IceCube und MAGIC Kollaborationen und beschäftigt sich in seiner Forschung mit extrem energiereichen Objekten und Ereignissen im Universum. Spezielle Großinstrumente für die Beobachtung hoch-energetischer Gammastrahlen und Neutrinos erlauben es mit Röntgenstrahlung und Radiowellen in Kombination mit Beobachtungen im Optischen neue Einblicke in die höchst-energetischen physikalischen Prozesse im Universum zu erlangen. Dr. Fruck wird in seinem Vortrag einen Einblick in sein Forschungsgebiet geben und dabei aktuelle Beobachtungsinstrumente, sowie laufende und geplante Erweiterungen und Neuentwicklungen vorstellen.

S. Grigoriev (NRC KI – PNPI), W. Petry
CREMLIN workshop "Engineering for advanced neutron instrumentation and sample environment"
St. Petersburg, Russia, 13 – 16 May 2018

In view of the upcoming commissioning of the Russian PIK reactor engineers and scientists from Russian and European neutron research facilities gathered at the New Peterhof Hotel to share their experiences, requirements and strategies on how to cope with challenging issues. The workshop, which was organized by Professor Sergey Grigoriev (NRC KI – PNPI) and Prof. Petry (TUM-FRM II) took place within the CREMLIN project aiming at strengthening the interaction between Russian and European large-scale infrastructures. The CREMLIN project was funded by the European Commission.

credit: Tatyana Potapova, PNPI

P. Müller-Buschbaum, C.M. Papadakis
Summer School Polymer Physics
Obertauern, Austria, 12 – 15 Jun 2018

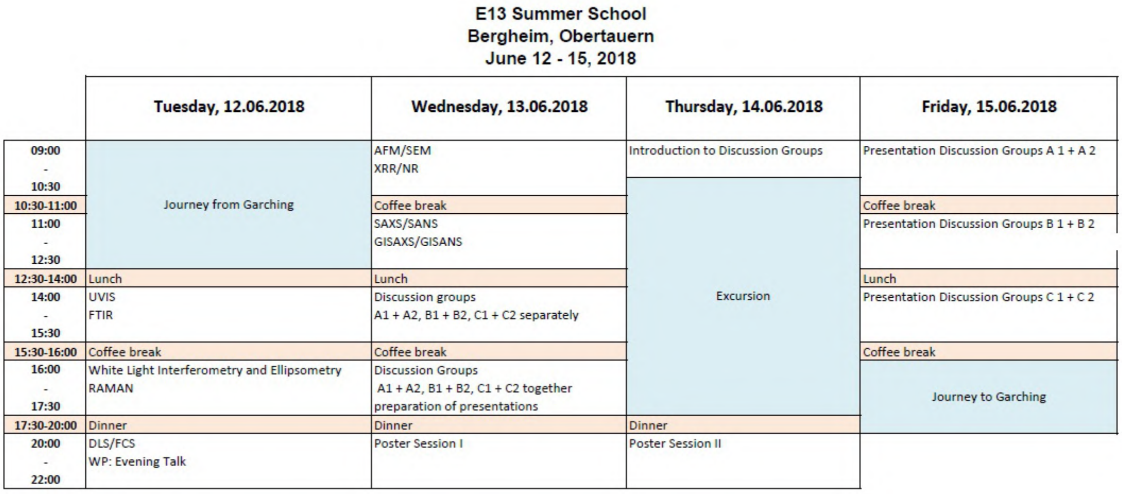

E13 Summer School
Bergheim, Obertauern
June 12 - 15, 2018

	Tuesday, 12.06.2018	**Wednesday, 13.06.2018**	**Thursday, 14.06.2018**	**Friday, 15.06.2018**
09:00 - 10:30	Journey from Garching	AFM/SEM XRR/NR	Introduction to Discussion Groups	Presentation Discussion Groups A 1 + A 2
10:30-11:00		Coffee break	Excursion	Coffee break
11:00 - 12:30		SAXS/SANS GISAXS/GISANS		Presentation Discussion Groups B 1 + B 2
12:30-14:00	Lunch	Lunch		Lunch
14:00 - 15:30	UVIS FTIR	Discussion groups A1 + A2, B1 + B2, C1 + C2 separately		Presentation Discussion Groups C 1 + C 2
15:30-16:00	Coffee break	Coffee break		Coffee break
16:00 - 17:30	White Light Interferometry and Ellipsometry RAMAN	Discussion Groups A1 + A2, B1 + B2, C1 + C2 together preparation of presentations		Journey to Garching
17:30-20:00	Dinner	Dinner	Dinner	
20:00 - 22:00	DLS/FCS WP: Evening Talk	Poster Session I	Poster Session II	

Excursion to Burg Mauterndorf

W. A. Herrmann, T. Hamacher, N. Adams, H. Gasteiger, W. Lang, M. Lienkamp, P. Müller-Buschbaum, H. Spliethoff, W. Wall
8th Colloquium of the Munich School of Engineering: "Advances in Energy Transition"
Garching, 19 Jul 2018

Munich School of Engineering
Technische Universität München

8th Energy Colloquium of the Munich School of Engineering

Advances in Energy Transition

July 19, 2018 – 8:30 a.m. to 8:00 p.m.
TUM – Quantum, Garching-Hochbrück

8:30 – 9:00 a.m.
Registration

9:00 – 9:15 a.m.
Opening: Prof. Thomas Hamacher
Director Munich School of Engineering

9:15 – 9:45 a.m.
Keynote: Shell Hydrogen Study – Energy of the Future?
Dr. Jurgen Louis, Shell Global Solutions GmbH

9:45 – 11:00 a.m.
Electrochemical Energy Storage: From Fundamentals to Experiments
Session Chair: **Prof. Peter Müller-Buschbaum**

Watching Metal Nanolayer Growth on Functional Polymer Thin Films for Lithium-Ion Battery Applications
Simon Schaper, Chair of Functional Materials

Towards Graphite/V2O5 Na Ion Batteries
Lukas Seidl, Electrochemical Research Group

Activity of Oxygen and Hydrogen Evolution Reaction Electrocatalysts under Industrially Relevant Conditions
Sebastian Watzele, Physics of Energy Conversion and Storage

11:00 – 11:30 a.m.
Poster Presentation and Coffee Break

11:30 – 12:45 p.m.
Power Generation and Storage: From Micro to Macro
Session Chair: **Prof. Hartmut Spliethoff**

Monitoring a Commercial µ-CHP SOFC-Stack by Electrochemical Impedance Spectroscopy
Tobias Herrmann, Chair of Plant and Process Technology

Biomass Combustion from Lab-Scale to Full-Scale: A Holistic Approach for CHP Plants
Richard Nowak Delgado, Chair of Energy Systems

Distributed Residential Battery Energy Storage Systems in a Microgrid Environment
Stefan Englberger et al., Institute for Electrical Energy Storage Technology

12:45 – 2:00 p.m.
Poster Presentation and Lunch Break

Please register: http://www.mse.tum.de

2:00 – 2:30 a.m.
Keynote: Potential of Sustainable Campuses in Driving Energy Transition
AStA Umweltreferat, TUM

2:30 – 3:45 p.m.
Renewable Energies: From Prediction to Market
Session Chair: **Prof. Carlo L. Bottasso**

An Analytical Weather Generator: Energy Source Data for Renewable Energy Models
Franz Christange, Chair of Renewable and Sustainable Energy Systems

Numerical Simulation of a Scaled Wind Farm
Chengyu Wang, Chair of Wind Energy

Renewable Auctions – A Real Options Approach
David Matthäus, Chair of Management Accounting

3:45 – 4:15 p.m.
Poster Presentation and Coffee Break

4:15 – 5:30 p.m.
Energy-Water-Nexus: From Munich to Harare
Session Chair: **Prof. Werner Lang**

Multi Energy Management and Aggregation Platform
Alexandre Capone, Chair of Renewable and Sustainable Energy Systems

Thermal Use of Shallow Groundwater in Munich's Energy Planning
Fabian Böttcher, Chair of Hydrogeology

Promoting Rural Electrification in Sub-Saharan Africa: Least-Cost Modeling of Decentralized Energy-Water-Food Systems
Johannes Winklmaier, Chair of Renewable and Sustainable Energy Systems

5:30 – 6:00 p.m.
Keynote: Designing with Nature - The Potentials of Green Technologies in the Context of Climate Change and the Transition to Renewable Energy
Prof. Ferdinand Ludwig, TUM

6:00 – 6:15 p.m.
Summary and Closing

6:15 – 8:00 p.m.
Poster and Presentation Award with Colloquium Dinner

Heinz Maier-Leibnitz Zentrum Garching
MLZ-Conference "Neutrons for Culture and Arts"
Lenggries, 19 – 22 Jun 2018

In 2018, the MLZ Conference was dedicated to Neutrons for Culture and Arts; archaeologists and conservators from museums and universities met at the Arabella Brauneck Hotel in Lenggries (Bavaria) to present their views on the potential of neutrons in cultural heritage research.

Credits: MLZ

Heinz Maier-Leibnitz Zentrum
German Conference for Research with Synchrotron Radiation, Neutrons and Ion Beams at Large Facilities 2018
Garching, 12 - 15 Sep 2018

A wealth of new contacts, ideas and information was taken home by more than 520 scientists who attended the German Conference for Research with Synchrotron Radiation, Neutrons and Ion Beams at Large Facilities 2018 in mid September 2018. Three intensive days – many participants even came to the welcome reception on the night before the start of the conference in elegant ambience of the Münchner Künstlerhaus am Lenbachplatz. The conference was organised by the user committees KFS, KFN and KFSI in cooperation with MLZ

SNI participants in front of the Faculty of Engineering of TUM
credits: Wenzel Schürmann/TUM

P. Müller-Buschbaum
Lehrerfortbildung "Physik der Ozeane und Atmosphäre "
Edgar-Lüscher Lectures Dillingen, 26 – 28 Sep 2018

EDGAR–LÜSCHER–LECTURES DILLINGEN/DONAU 2018
Thema: Physik der Ozeane und Atmosphäre
Datum: Mittwoch, 26. September bis Freitag, 28. September 2018
Tagungsort: Akademie für Lehrerfortbildung Dillingen
Veranstalter: Akademie für Lehrerfortbildung Dillingen und TU München
wissenschaftliche Leitung: Prof. Dr. Peter Müller-Buschbaum,
Technische Universität München.

Programm

Mittwoch, 26. 09. 2018
15:00 – 15:30 Begrüßung
StD Werner Ettinger / Prof. Dr. Peter Müller-Buschbaum (Physik-Department, TUM)

15:30 – 17:00 Prof. Dr. Thomas Birner (Meteorologische Institut München, LMU)
Atmosphärische Dynamik

18:30 – 20:00 Priv. Doz. Dr. rer. nat. Hans-Dieter Wizemann (Institut für Physik und Meteorologie, Universität Stuttgart)
Eddy-Kovarianz-Messungen als Instrument der modernen Meteorologie

Donnerstag, 27. 09. 2018
8:30 – 10:00 PD Dr. Tijana Janjic-Pfander (Hans-Ertel-Zentrum für Wetterforschung, LMU)
Data assimilation and ensemble forecasting in meteorology and oceanography

10:00 – 10.30 Kaffeepause

10:30 – 12:00 Dr. Gerd Schädler (Institut für Meteorologie und Klimaforschung, KIT)
Regionales Klima und Wasserkreislauf

15:30 – 17:00 Prof. Dr. Bernhard Mayer (Meteorologische Institut München, LMU)
Wolken — Fernerkundung und Klimawirkung

18:30 – 20:00 Dr. Aiko Voigt (Institut für Meteorologie und Klimaforschung, KIT)
Wolken und Sturmzugbahnen

Freitag, 28. 09. 2018
8:30 – 10:00 Professor Hans-Peter Schmid (Institut für Meteorologie und Klimaforschung, KIT)
Effekt von Umweltveränderungen auf Wetter und Klima

10:00 – 10.30 Kaffeepause

10:30 – 12:00 Prof. Dr. Stephan Pfahl (Institut für Meteorologie, FU Berlin)
Klimaschwankungen und Extrema

Ab 12:00 Lehrgangsabschluss
Prof. Dr. Peter Müller-Buschbaum / StD Werner Ettinger

Technische Universität München
Prof. i.R. Dr. Winfried Petry was awarded the honorary title of Emeritus of Excellence of the Technical University of Munich (TUM)
9 Oct 2018

TUM-President Prof. Dr. Dr. h.c. mult. Wolfgang A. Herrmann bestowed the certificate appreciating his academic achievements

Winfried Petry (l.) receives the award from TUM-President Wolfgang Herrmann (r.)

© Uli Benz/TUM

TUM FRM II, Lehrstuhl für Funktionelle Materialien
Scientific colloquium for Professor Winfried Petry
25 Oct 2018

About 300 guests joined the official farewell ceremony for Prof. Petry on 25 October. Among them, high ranking officials from science and politics. All of them highly appreciated Winfried Petry's merits as science manager and scientist and welcomed Prof. Müller-Buschbaum as the new Director of FRM II and MLZ.

Programm, 25. Oktober 2018

15:00-16:00 Uhr
Begrüßungskaffee

16:00-17:00 Uhr
Grußansprachen

Prof. Dr. Dr. h.c. mult. Wolfgang A. Herrmann, Präsident der Technischen Universität München

Prof. Dr. med. Marion Kiechle
Bayerische Staatsministerin für Wissenschaft und Kunst

Bundesministerium für Bildung und Forschung, N.N.

Prof. Dr. Dr. h.c. mult. Sebastian M. Schmidt
Mitglied des Vorstandes
Forschungszentrum Jülich GmbH

Prof. Dr. Stefan Schönert
Prodekan des Physik Departments
Technische Universität München

17:00-18:00 Uhr
Wissenschaftliche Vorträge

Prof. Dr. Andreas Meyer
Direktor des Instituts für Materialphysik im Weltraum
Deutsches Zentrum für Luft- und Raumfahrt (DLR)
Verlangsamung der Dynamik:
Verständnis auf molekularer Ebene

Prof. Dr. Helmut Schober
Direktor Institut Max von Laue – Paul Langevin (ILL)
Anpassung durch Evolution:
Wie sich die Neutronenstreuung den Anforderungen unserer Zeit stellt.

18:00 Uhr
Ausklang der Veranstaltung mit Imbiss
im Foyer des Physik-Departments

Moderation:
Prof. Dr. Peter Müller-Buschbaum
Wissenschaftlicher Direktor FRM II und MLZ

Sehr geehrte Damen und Herren,
liebe Kolleginnen und Kollegen,

seit 1992 war Herr Prof. Dr. Winfried Petry Lehrstuhlinhaber am Physik Department der Technischen Universität München und hat sich von diesem Zeitpunkt an mit großem persönlichen Einsatz für Bau und wissenschaftliche Nutzung der Forschungs-Neutronenquelle Heinz Maier-Leibnitz (FRM II) engagiert.

Im März 2018 endete die Amtszeit von Professor Petry als Wissenschaftlicher Direktor der Forschungs-Neutronenquelle, als Direktor am Heinz Maier-Leibnitz Zentrum (MLZ) und als Inhaber des Lehrstuhls für Funktionelle Materialien.

In Würdigung all seiner Verdienste um die Forschung mit Neutronen veranstaltet der FRM II zusammen mit dem Lehrstuhl für Funktionelle Materialien ein wissenschaftliches Festkolloquium, zu dem ich Sie sehr herzlich einlade.

Es findet am Donnerstag, 25. Oktober 2018, im Physik-Department der Technischen Universität in Garching statt.

Prof. Dr. Peter Müller-Buschbaum
Wissenschaftlicher Direktor FRM II und MLZ

Prof. Dr. Dr. h.c. mult. Wolfgang Herrmann, Albert Berger, Prof. Winfried Petry, Prof. Dr. med. Marion Kiechle, Prof. Dr. Peter Müller-Buschbaum, Dr. Anton Kastenmüller
Foto: Andreas Heddegott/TUM

P. Müller-Buschbaum
Colloquium „150 Years of Physics at TUM“
Garching, 8 Nov 2018

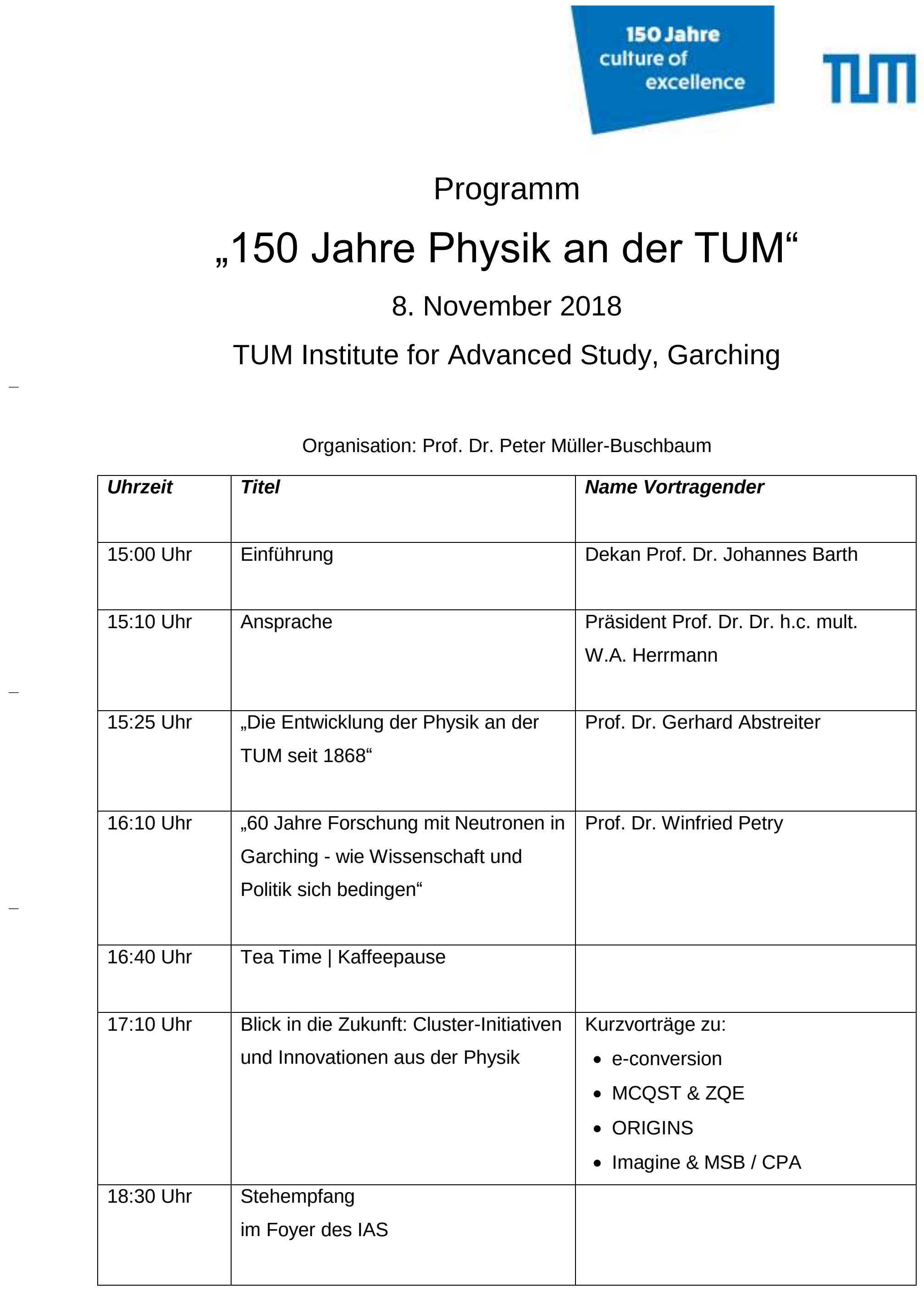

Programm

„150 Jahre Physik an der TUM“

8. November 2018

TUM Institute for Advanced Study, Garching

Organisation: Prof. Dr. Peter Müller-Buschbaum

Uhrzeit	***Titel***	***Name Vortragender***
15:00 Uhr	Einführung	Dekan Prof. Dr. Johannes Barth
15:10 Uhr	Ansprache	Präsident Prof. Dr. Dr. h.c. mult. W.A. Herrmann
15:25 Uhr	„Die Entwicklung der Physik an der TUM seit 1868“	Prof. Dr. Gerhard Abstreiter
16:10 Uhr	„60 Jahre Forschung mit Neutronen in Garching - wie Wissenschaft und Politik sich bedingen“	Prof. Dr. Winfried Petry
16:40 Uhr	Tea Time | Kaffeepause	
17:10 Uhr	Blick in die Zukunft: Cluster-Initiativen und Innovationen aus der Physik	Kurzvorträge zu: • e-conversion • MCQST & ZQE • ORIGINS • Imagine & MSB / CPA
18:30 Uhr	Stehempfang im Foyer des IAS	

credits: Wenzel Schürmann/TUM

Heinz Maier-Leibnitz Zentrum
MLZ Review
Garching 19 – 21 Nov 2018

Ten international experts in neutron science have been solicited to take part in the review of the Heinz Maier-Leibnitz Zentrum

Reviewers, MLZ and institute-Directors, and MLZ science group coordinators in the Neutons Guide Hall East – photo taken by W. Schürmann/TUM

7.3 Service to the community

Prof. Dr. Peter Müller-Buschbaum:

- Since 7/2017 member of the Aptitude Committee of master course Materials Science and Engineering (MS and E) at TUM
- Since 9/2016 spokesman and board member of the Graduate School of ”Munich School of Engineering” (MSE) at TUM
- Since 6/2016 member of the doctoral committee of ”Munich School of Engineering” (MSE) at TUM
- Since 3/2015 member of “Advanced Light Source (ALS) Review Panel”
- Since 9/2014 member of “Heinz Maier-Leibnitz Zentrum (MLZ) Review Panel“
- Since 6/2014 member of Stanford Synchrotron Radiation Lightsource (SSRL) Review Panel
- Since 9/2012 Associate Editor of journal ”ACS Applied Materials & Interfaces” of the American Chemical Society
- Since 3/2012 head of KeyLab ”TUM.Solar” at TUM
- Since 1/2012 member of the Scientific Selection Panel of the Helmholtz-Zentrum Berlin für Materialien und Energie (HZB)
- Since 2011 member of European Spallation Source (ESS) Scientific Advisory Panel (Reflectivity)
- Since 2011 German representative at the European Polymer Federation (EPF) for polymer physics
- Since 2010 spokesman of the regenerative engergies section (NRG) at the Munich School of Engineering (MSE) of TUM
- Since 2010 member of TUM Energie at TUM
- Since 2010 German representative at the European Synchrotron User Organization (ESUO)
- Since 2008 chairman of “DESY Photon Science User Committee“ at the synchrotron radiation laboratory DESY in Hamburg

Prof. Dr. Christine M. Papadakis:

- Since 4/2015 Editor-in-Chief for Colloid & Polymer Science, Springer-Verlag
- Member of the Review Panel ″Soft Matter″ of the Heinz Maier-Leibnitz Zentrum
- Vice women′s representative of the Physics Department at TUM

Prof. Dr. Winfried Petry:

- Since 2018 TUM Emeritus of Excellence
- Since 2016 member of the Evaluation Panel for Neutron Research of the Swedish Research Council
- Since 2015 member of the Neutron Scientific Advisory Committee of the National Research Center Kurchatov Institute "Petersburg Nuclear Physics Institute" (PNPI, Gatchina)
- Since 2012 member of the Scientific Advisory Board of NaWi Graz
- Since 2007 member of the Steering Comittee of the Laue Langevin Institute (ILL)
- Since 1999 liaison professor of Bayerische Eliteakademie (Bavarian Leadership Academy) and since May 2011 member of the Board of Trustees

8 Publications, talks and funding

8.1 Publications

- D. Aravopoulou, K. Kyriakos, A. Miasnikova, A. Laschewsky, C. M. Papadakis, A. Kyritsis
  Comparative investigation of the thermoresponsive behavior of two diblock copolymers comprising PNIPAM and PMDEGA blocks
  J. Phys. Chem. B **122**, 2655-2668 (2018)

- B. Baumeister, C. Schwarz, Ch. Steyer, H. Breitkreutz, W. Petry
  Manufacturing processes for inert monolithic mini-size fuel foils with thickness gradient
  Proceedings RRFM 2018, München (2018)

- B. Baumeister, Ch. Schwarz, Ch. Steyer, W. Petry, J. Allenou, B. Stepnik
  Production of surrogate fuel plates with monolithic gradient foils
  Proceeding RERTR 2018, Edinburgh (2018)

- A. V. Berezkin, F. Jung, D. Posselt, D.-M. Smilgies, C. M. Papadakis
  In situ tracking of composition and morphology of a diblock copolymer film with GISAXS during exchange of solvent vapors at elevated temperatures
  Adv. Funct. Mater. 1706226 (2018)

- L. Bießmann, L.P. Kreuzer, T. Widmann, N. Hohn, J.-F. Moulin, P. Müller-Buschbaum
  Monitoring the swelling behavior of PEDOT:PSS electrodes under high humidity conditions
  ACS Appl. Mater. Interfaces **10**, 9865-9872 (2018)

- B.J. Bohn, Y. Tong, M. Gramlich, M.L. Lai, M. Döblinger, K. Wang, R.L.Z. Hoye, P. Müller-Buschbaum, S.D. Stranks, A.S. Urban, L. Polavarapu, J. Feldmann
  Boosting tunable blue luminescence of halide perovskite nanoplatelets through post-synthetic surface trap repair
  Nano Lett. **18**, 5231-5238 (2018)

- P. Böni, W. Petry
  Neutron science with highly brilliant beams
  Applications of Laser-Driven Particle Acceleration, 315-332 CRC Press, ISBN 9781498766418 (2018)

- J. Boudaden, M. Steinmaßl, H.-E. Endres, A. Drost, I. Eisele, C. Kutter, P. Müller-Buschbaum
  Polyimide-based capacitive humidity sensor
  Sensors **18**, 1516 (2018)

- H. Breitkreutz, J. Shi, R. Jungwirth, T. Zweifel, H.Y. Chiang, W. Petry
  Heavy ions irradiation as a tool to minimize the number of in-pile tests in UMo fuel development
  ATW - Int. Journal for Nuclear Power **63 (5)**, 325 (2018)

- H. Breitkreutz, A. Heldmann, J. Hingerl, R. Jungwirth, J. Shi, W. Petry
  Quantitative comparability of heavy ion and in-pile irradiations on UMo fuel systems
  Journal of Nuclear Materials **507**, 276-287 (2018)

- H.-Y.Chiang, T. Wiss, S.-H. Park, O. Dieste-Blanco, W. Petry
  TEM-Analysis for irradiation-induced interaction layers in coated UMo/X/Al trilayer systems

(X1/4 Ti, Nb, Zr and Mo)
Journal of Nuclear Materials **499**, 588 – 566 (2018)

- M. Coriç N. Saxena, M. Pflüger, P. Müller-Buschbaum, M. Krumrey, E.M. Herzig
  Resonant grazing-incidence small-angle x-ray scattering at the sulfur K-edge for material-specific investigation of thin film nanostructures
  J.Phys.Chem.Lett. **9**, 3081-3086 (2018)

- H. Gabold, Z. Luan, N. Paul, M. Opel, P. Müller-Buschbaum, M. Law, A. Paul
  Structural and magnetic properties of cobalt iron disulfide (CoxFe1-xS2) nanocrystals
  Sci. Rep. **8**, 4835, 1-16 (2018)

- N. Giesbrecht, J. Schlipf, I. Grill, T. Bein, A. Hartschuh, P. Müller-Buschbaum, P. Docampo
  Single-crystal-like optoelectronic-properties of MAPbI3 perovskite polycrystalline thin films
  J. Mater. Chem. **A 6**, 4822-4828 (2018)

- N. Hohn, S.J. Schlosser, L. Bießmann, S. Grott, S. Xia, K. Wang, M. Schwartzkopf, S.V. Roth, P. Müller-Buschbaum
  Readily available titania nanostructuring routines based on mobility and polarity controlled phase separation of an amphiphilic diblock copolymer
  Nanoscale **10**, 5325-5334 (2018)

- N. Hohn, S.J. Schlosser, L. Bießmann, L. Song, S. Grott, S. Xia, K. Wang, M. Schwartzkopf, S.V. Roth, P. Müller-Buschbaum
  Impact of catalytic additive on spray deposited and nanoporous titania thin films observed via in situ x-ray scattering: Implications for Enhanced Photovoltaics
  ACS Appl. Nano Mater. **1**, 4227-4235 (2018)

- T.K. Huber, H. Breitkreutz, D.E. Burkes, A.J. Casella, A.M. Casella, S. Elgeti
  Thermal conductivity of fresh and irradiated U-Mo fuels
  Journal of Nuclear Materials **503**, 304-313 (2018)

- D. Jost, J.-R. Scholz, U. Zweck, W. R. Meier, A. E. Böhmer, P. C. Canfield, N. Lazareviç, R. Hackl
  Indication of subdominant d-wave interaction in superconducting $CaKFe_4As_4$
  Phys. Rev. B **98**, 020504(R) (2018)

- L. Karge, D. Lang, J. Schatte, R. Gilles, S. Busch, P. Leibenguth, H. Clemens
  Characterization of anisotropic pores and spatially oriented precipitates in sintered Mo-base alloys using small-angle neutron scattering
  Journal of Applied Crystallography **51 (6)**, 1706-1714 (2018)

- J. Kehrle, T. K. Purkait, S. Kaiser, K. N. Raftopoulos, M. Winnacker, T. Ludwig, M. Aghajamali, M. Hanzlik, K. Rodewald, T. Helbich, C. M. Papadakis, J. G. C. Veinot, B. Rieger
  Superhydrophobic silicon nanocrystal–silica aerogel hybrid materials: synthesis, properties, and sensing application
  Langmuir **34**, 4888-4896 (2018)

- T.M. Koh, V. Shanmugam, X. Guo, S.S. Lim, O. Filonik, E.M. Herzig, P. Müller-Buschbaum, V. Swamy, T.C. Sum, S.G. Mhaisalkar, N. Mathews
  Enhancing moisture tolerance in efficient hybrid 3D/2D perovskite photovoltaics
  J. Mater. Chem. **A 6**, 2122-2128 (2018)

- S. Koutsoumpis, P. Klonos, K. N. Raftopoulos, C. M. Papadakis, D. Bikiaris, P. Pissis
Morphology, thermal properties and molecular dynamics of syndiotactic polystyrene (s-PS) nanocomposites with aligned graphene oxide and graphene nanosheets
Polymer **153**, 548-557 (2018)

- S. Koutsoumpis, J. Ozimek, K. N. Raftopoulos, E. Hebda, P. Klonos, C. M. Papadaks, K. Pielichowski, P. Pissis
Polyurethanes with POSS pendent on flexible hard segments: morphology and glass transition
Polymer **147**, 225-236 (2018)

- M. Leitner and I. Kühn
Dispersal in Plants and Animals
in ”Diffusive Spreading in Nature, Technology and Society” edited by A. Bunde, J. Caro, J. Kärger, and G. Vogl, Springer (Cham 2018)

- X.H. Li, P. Saal, W.M. Gan, M. Hoelzel, W. Volk, W. Petry, M. Hofmann
Strain-induced martensitic transformation kinetic in austempered ductile iron (ADI)
Metallurgical and Materials Transactions **A 49 (1)**, 94-104 (2018)

- S.-Z. Liang, X.-Y. Wang, Y.-G. Xia, S. Xia, E. Metwalli, B. Qiu, Q. Ji, S.-S. Yin, S. Xie, K. Fang, L.-Y. Zheng, M.-M. Wang, X.-X. Zuo, R.-J. Li, Z.-P. Liu, J.Zhu, P. Müller-Buschbaum, Y.-J. Cheng
Scalable synthesis of hierarchical antimony/carbon micro-/nanohybrid lithium-ion battery anodes based on dimethacrylate monomer
Acta Metallurgica Sinica (English Letters) **31**, 910-922 (2018)

- E. Metwalli, M.V. Kaeppel, S.J. Schaper, A. Kriele, R. Gilles, K.N. Raftopoulos, P. Müller-Buschbaum
Conductivity and morphology correlations of ionic-liquid/lithium-salt/block copolymer nanostructured hybrid electrolytes
ACS Appl. Energy Mater. **1**, 666-675 (2018)

- G.E. Möhl, E. Metwalli, R. Bouchet, T.N.T. Phan, R. Cubitt, P. Müller-Buschbaum
In operando small angle neutron scattering study of single-ion copolymer electrolyte for Li-metal batteries
ACS Energy Lett. **3**, 1-6 (2018)

- G.E. Möhl, E. Metwalli, P. Müller-Buschbaum
In operando Small Angle X-ray Scattering investigation of nanostructured polymer electrolyte for lithium-ion batteries
ACS Energy Lett. **3**, 1525-1530 (2018)

- B.-J. Niebuur, L. Chiappisi, X. Zhang, F. Jung, A. Schulte, C. M. Papadakis
Formation and growth of mesoglobules in aqueous poly(N-isopropylacrylamide) solutions revealed with kinetic small-angle neutron scattering and fast pressure jumps
ACS Macro Lett. **7**, 1155-1160 (2018)

- B.-J. Niebuur, J. Puchmayr, C. Herold, L.P. Kreuzer, V. Hildebrand, P. Müller-Buschbaum, A. Laschewsky, C.M. Papadakis
Polysulfobetaines in aqueous solution and in thin film geometry
Materials **11**, 850 (2018)

- F. Nübling, D. Yang, P. Müller-Buschbaum, M. Brinkmann, M. Sommer
  In-situ synthesis of ternary block copolymer / homopolymer blends for organic photovoltaics
  ACS Appl. Mater. Interfaces **10**, 18149-18160 (2018)

- W. Ohm, A. Rothkirch, P. Pandit, V. Körstgens, P. Müller-Buschbaum, R. Rojas, S. Yu, C.J. Brett, D.L. Söderberg, S.V. Roth
  Morphological properties of air-brush spray deposited enzymatic cellulose thin films
  J. Coat. Technol. Res. **15**, 759–769 (2018)

- K. Rathinam, Y. Oren, W. Petry, D. Schwahn, R. Kasher
  Calcium phosphate scaling during wastewater desalination on oligoamide surfaces mimicking reserve osmosis and nanofiltration membranes
  Water Research **12**, 271-225 (2018)

- C. Reiter, H. Breitkreutz, W. Petry
  High precision neutronic calculations for transient simulations of compact cores
  Proceedings of Physor 2018, Cancun, Mexiko (2018)

- L. Rodrigues, K. N. Raftopoulos, S. T. Schmidt, F. Schneider, H. Dietz, T. Rades, H. Franzyk, A. E. Pedersen, C. M. Papadakis, D. Christensen, G. Winter, C. Foged, M. Hubert
  Immune responses induced by nano-self-assembled lipid adjuvants based on a monomycoloyl glycerol analogue after vaccination with the chlamydia trachomatis major outer membrane protein
  J. Control. Release **285**, 12-22 (2018)

- N. Saxena, J. Keilhofer, A.K. Maurya, G. Fortunato, J. Overbeck, P. Müller-Buschbaum
  Facile optimization of thermoelectric properties in PEDOT:PSS thin films through acido-base and redox dedoping using readily available salts
  ACS Appl. Energy Mater. **1**, 336-342 (2018)

- J. Schlipf, A.M. Askar, F. Pantle, B.D. Wiltshire, A. Sura, P. Schneider, L. Huber, K. Shankar, P. Müller-Buschbaum
  Top-down approaches towards single crystal perovskite solar cell
  Sci. Rep. **8**, 4906, 1-8 (2018)

- J. Schlipf, L. Bießmann, L. Oesinghaus, E. Metwalli, L. Porcar, P. Müller-Buschbaum
  Ingression of moisture into hybrid perovskite thin films probed with in-situ GISANS
  J.Phys.Chem.Lett. **9**, 2015-2021 (2018)

- J. Shi, H. Breitkreutz, J. Hingerl, W. Petry
  Quantitatively simulating fission-enhanced diffusion in U-Mo/Al systems by swift heavy io irradiation
  Proceedings RRFM 2018, München (2018)

- L. Song, M. Rawolle, N. Hohn, J.S. Gutmann, H. Frielinghaus, P. Müller-Buschbaum
  Deformation of mesoporous titania nanostructures in contact with D2O vapor
  Small **14**, 18011461 (2018)

- L. Song, T. Wang, V. Körstgens, W. Wang, N. Saxena, C.J. Schaffer, T. Fröschl, N. Hüsing, S. Bernstorff, P. Müller-Buschbaum
  Wet-imprinting of channel-type superstructures in nanostructured titania thin films at low temperatures for hybrid solar cells
  ChemSusChem **11**, 1179-1186 (2018)

- R.E. Stene, B. Scheibe, C. Pietzonka, A.J. Karttunen, W. Petry, F. Kraus
  MoF5 revisited. A comprehensive study of MoF5
  Journal of Fluorine Chemistry **211**, 171-179 (2018)

- B. Stepnik, M. Grasse, C. Rontar, D. Geslin, Y. Guinard, S. Van den Berghe, A. Leenaers, H. Breitkreutz, W. Petry, H. Palancher, E. Hervieu, Y. Calzavara, H. Guyon
  Manufacturing of the SEMPER FIDELIS UMo irradiation experiment
  Proceedings RRFM 2018, München (2018)

- Y. Tong, E.-P. Yao, A. Manzi, E. Bladt, K. Wang, M. Döblinger, S. Bals, P. Müller-Buschbaum, A.S. Urban, L. Polavarapu, J. Feldmann
  Spontaneous self-assembly of perovskite nanocrystals into electronically coupled supercrystals: toward filling the green gap
  Adv. Mater. **30**, 1801117 (2018)

- C. Tsitsilianis, G. Serras, C.-H. Ko, F. Jung, C. M. Papadakis, M. Rikkou-Kalourkoti, C. S. Patrickios, R. Schweins, C. Chassenieux
  Thermoresponsive hydrogels based on telechelic polyelectrolytes: from dynamic to 'frozen' networks
  Macromolecules **51**, 2169-2179 (2018)

- N.S. Vishnevetskaya, V. Hildebrand, M.A. Dyakonova, B.-J. Niebuur, K. Kyriakos, K.N. Raftopoulos, Z. Di, P. Müller-Buschbaum, A. Laschewsky, C.M. Papadakis
  Dual, orthogonal switching of the "schizophrenic" self-assembly of diblock copolymers
  Macromolecules **51**, 2604-2614 (2018)

- K. Wang, L. Bießmann, M. Schwartzkopf, S.V. Roth, P. Müller-Buschbaum
  Tuning of the morphology and optoelectronic properties of ZnO/P3HT/P3HT b PEO hybrid films via the spray deposition method
  ACS Appl. Mater. Interfaces **10**, 20569-20577 (2018)

- K. Wang, V. Körstgens, D. Yang, N. Hohn, S.V. Roth, P. Müller-Buschbaum
  Morphology control of low temperature fabricated ZnO nanostructures for all solid-state transparent dye-sensitized solar cells
  J. Mater. Chem. **A 6**, 4405-4415 (2018)

- R. Wang, Y. Tong, A. Manzi, K. Wang, Z. Fu, E. Kentzinger, J. Feldmann, A.S. Urban, P. Müller-Buschbaum, H. Frielinghaus
  Preferential orientation of crystals enables amplified spontaneous emission in mixed dimensional hybrid perovskite films
  Adv. Optical Mater. **6**, 1701311 (2018)

- W. Wang, L. Song, D. Magerl, D. Moseguí González, V. Körstgens, M. Philipp, J.-F. Moulin, P. Müller-Buschbaum
  Influence of solvent additive 1,8-octanedithiol on P3HT:PCBM solar cells
  Adv. Funct. Mater. **28**, 1800209 (2018)

- S. Xia, E. Metwalli, M. Opel, P.A. Staniec, E.M. Herzig, P. Müller-Buschbaum
  Printed thin magnetic films based on diblock copolymer and magnetic nanoparticles
  ACS Appl. Mater. Interfaces **10**, 2982-2991 (2018)

- S. Xia, L. Song, V. Körstgens, M. Opel, M. Schwartzkopf, S.V. Roth, P. Müller-Buschbaum
  Magnetic nanoparticles containing soft-hard diblock copolymer films with high order
  Nanoscale **10**, 11930-11941 (2018)

- S. Yin, D. Zhao, Q. Ji, Y. Xia, S. Xia, X. Wang, M. Wang, J. Ban, Y. Zhang, E. Metwalli, X. Wang, Y. Xiao, X. Zuo, S. Xie, K. Fang, B. Qiu, Z. Yang, Y. Lin, L. Chen, C. Wang, Z. Liu, J. Zhu, P. Müller-Buschbaum, Y. Cheng
  Si/Ag/C nanohybrids with in situ Incorporation of super-small silver nanoparticles using epoxy resin as solvent and carbon source: tiny amount, huge impact
  ACS Nano **12**, 861-875 (2018)

- X. Zhang, P. Chytil, T. Etrych, W. Kiu, L. Rodrigues, G. Winter, S. K. Filippov, C. M. Papadakis
  Binding of HSA to macromolecular pHPMA based nanoparticles for drug delivery: an investigation using fluorescence methods
  Langmuir **34**, 7998–8006 (2018)

- X. Zhang, B.-J. Niebuur, P. Chytil, T. Etrych, S.K. Filippov, A. Kikhney, D.C.F. Wieland, D.I. Svergun, C.M. Papadakis
  Macromolecular pHPMA-based nanoparticles with cholesterol for solid tumor targeting: behavior in HSA protein environment
  Biomacromolecules **19**, 470-480 (2018)

- X. Zhang, Y. Rui, Y. Wang, J. Xu, H. Wang, Q. Zhang, P. Müller-Buschbaum
  SnO2 nanorod arrays with tailored area density as efficient electron transport layers for perovskite solar cells
  J. Power Sources **402**, 460-467 (2018)

- L. Zheng, X. Wang, Y. Xia, S. Xia, E. Metwalli, B. Qiu, Q. Ji, S. Yin, S. Xie, K. Fang, S. Liang, M. Wang, X. Zuo, Y. Xiao, Z. Liu, J. Zhu, P. Müller-Buschbaum, J. Zhu, Y. Cheng
  Scalable in situ synthesis of Li4Ti5O12/carbon nanohybrid with super-small Li4Ti5O12 nanoparticles homogeneously embedded in carbon matrix
  ACS Appl. Mater. Interfaces **10**, 2591-2602 (2018)

- Q. Zhong, L. Mi, E. Metwalli, L. Bießmann, M. Philipp, A. Miasnikova, A. Laschewsky, C.M. Papadakis, R. Cubitt, M. Schwartzkopf, S.V. Roth, J. Wang, P. Müller-Buschbaum
  Effect of chain architecture on the swelling and thermal response of star-shaped thermo-responsive (poly(methoxy diethylene glycol acrylate)-block-polystyrene)3 block copolymer films
  Soft Matter **14**, 6582-6594 (2018)

8.2 Talks

- A. V. Berezkin, F. Jung, D. Posselt, D.-M. Smilgies, C. M. Papadakis
  Solvothermal annealing of a diblock copolymer film in solvent vapor mixtures
  DPG-Frühjahrstagung, Dresden, 11 – 16 Mar 2018

- A. V. Berezkin, F. Jung, D. Posselt, D.-M. Smilgies, C. M. Papadakis
  Morphologies and solvent distribution during solvent vapor annealing of block copolymer thin films: in situ, real-time GISAXS investigations
  4th International GISAS Conference, Gyeongju, South Korea, 4 – 7 Sep 2018

- L. Bießmann, L. P. Kreuzer, T. Widmann, N. Hohn, J.-F. Moulin, P. Müller-Buschbaum
  Monitoring the swelling behavior of PEDOT:PSS electrodes under high humidity conditions
  DPG-Frühjahrstagung, Berlin, 11 – 16 Mar 2018

- L. Bießmann, W. Cao, F. Jung
  AFM/SEM
  Polymer Physics Summer School Obertauern, Austria, 12 – 15 Jun 2018

- W. Chen, S. Grott, S. Pratap
  Small angle X-ray and neutron scattering
  Polymer Physics Summer School Obertauern, Austria, 12 – 15 Jun 2018

- J. Costa, W. Petry, M. Leitner
  Inelastic neutron scattering on FeNiCo high-entropy alloys
  4th German SNI Conference, Garching, 17 – 19 Sep 2018

- C. Geiger, C. Henschel, L. P. Kreuzer, T. Widmann, A. Laschewsky, C. M. Papadakis, P. Müller-Buschbaum
  Co-nonsolvency in thermo-responsive block copolymer thin films
  2nd BornAgain School and User Meeting, Garching, 19 – 21 Dec 2018

- M. Gensch, M. Schwartzkopf, W. Ohm, C. Brett, A. Stierle, Peter Müller-Buschbaum, Stephan V. Roth
  Optoelectronic properties of Ag clusters on polymer thin films during sputter deposition
  DPG-Frühjahrstagung, Berlin, 11 – 16 Mar 2018

- M. Gensch, M. Schwartzkopf, W. Ohm, C. Brett, A. Stierle, Peter Müller-Buschbaum, Stephan V. Roth
  Optoelectronic properties of Ag clusters on polymer thin films during sputter deposition
  4th GERMAN-CZECH workshop on nanomaterials, Budweis, Czech, 10 – 11 May 2018

- M. Gensch, M. Schwartzkopf, W. Ohm, C. Brett, A. Stierle, Peter Müller-Buschbaum, Stephan V. Roth
  Optoelectronic properties of metal clusters on polymer thin films during sputter deposition
  4th International GISAS Conference, Gyeongju, South Korea, 4 – 7 Sep 2018

- S. Grott, S. J. Schaper
  grazing-incidence scattering techniques
  SolTech Symposium: Solar Technologies go Hybrid, Würzburg, 2 – 3 Oct 2018

- S. Grott, A. Davydok, D. Chakraborty, S. Pratap, N. Hohn, V. Körstgens, C. Krywka, P. Müller-Buschbaum

Structure determination during functional stack build-up of power fibers
DESY Photo Science Users' Meeting, Hamburg, 24 – 25 Jan 2018

- S. Grott, L. Bießmann, N. Saxena, W. Cao, S. Bernstorff, P. Müller-Buschbaum
  Morphological investigations on fullerene-free bulk heterojunction blends for photovoltaic applications
  4th International GISAS Conference, Gyeongju, South Korea, 4 – 7 Sep 2018
- J. Heger, N. Hohn, D. Yang
  GISAXS/GIWAXS/GISANS
  Polymer Physics Summer School Obertauern, Austria, 12 – 15 Jun 2018
- N. Hohn, S. J. Schlosser, L. Bießmann, S. Grott, S. Xia, K. Wang, M. Schwartzkopf, S. V. Roth, P. Müller-Buschbaum
  Investigation of mobility controlled amphiphilic diblock copolymer templating for hybrid photovoltaic applications
  DPG-Frühjahrstagung, Berlin, 11 – 16 Mar 2018
- N. Hohn
  Inorganic-organic hybrid photovoltaic solar cells using novel hybrid materials
  Seminar Talk, Garching, 16 Mai 2018
- N. Hohn, M. Giebel, S. J. Schlosser, A. E. Hetzenecker, L. Bießmann, S. Grott, S. Xia, K. Wang, M. Schwartzkopf, S. V. Roth, T. F. Fässler, P. Müller-Buschbaum
  Approaching photovoltaic industry - Morphological tuning of inorganic thin films through amphiphilic diblock copolymer templating on the basis of large scale coating techniques
  ATUMS: Novel Concepts in Hybrid Structures, Tutzing, 29 – 30 Mai 2018
- N. Hohn, P. Müller-Buschbaum
  Diblock copolymer templating – A powerful tool for versatile nanostructure fabrication
  ATUMS: Annual Meeting 2018, Garching, 15 Nov 2018
- X. Jiang, N. Li, R. Schaffrinna
  UV/VIS spectroscopy
  Polymer Physics Summer School Obertauern, Austria, 12 – 15 Jun 2018
- F. Jung, P. A. Panteli, D.-M. Smilgies, D. Posselt, C. Tsitsilianis, C. S. Patrickios, C. M. Papadakis
  GISAXS investigation of multi-responsive block copolymer thin films during solvent vapor annealing
  4th International GISAS Conference, Gyeongju, Korea, 4 – 7 September 2018
- J.-J. Kang, C.-H. Ko, S. Xia
  Dynamic investigation on polymer solutions by DLS and FCS
  Polymer Physics Summer School Obertauern, Austria, 12 – 15 Jun 2018
- V. Körstgens, S. Xia, F. Martin, C.J. Brett, W. Ohm, M. Schwartzkopf, D. Söderberg, S.V. Roth, P. Müller-Buschbaum
  In situ spray deposition of conductive cellulose–PEDOT:PSS composites
  DESY user's meeting, SAXS WAXS workshop, Hamburg, 25 – 26 Jan 2018
- V. Körstgens, S. Xia, F. Martin, C.J. Brett, W. Ohm, M. Schwartzkopf, D. Söderberg, S.V. Roth, P. Müller-Buschbaum

Spray deposition of conducting composite films studied with in situ GISAXS
DPG-Frühjahrstagung, Berlin, 11 – 16 Mar 2018

- V. Körstgens, C. Mayr, F. Buschek, A. Haussmann, F. Löhrer, W. Ohm, M. Schwartzkopf, H. Iglev, A. Hinz, O. Polonskyi, T. Strunskus, S.V. Roth, F. Faupel, R. Kienberger, P. Müller-Buschbaum
  Spray deposition of water-processed active layers of hybrid solar cells investigated with in situ GISAXS and GIWAXS
  4th International GISAS Conference, Gyeongju, South Korea, 4 – 7 Sep 2018

- L. P. Kreuzer, T. Widmann, N. Hohn, K. Wang, J.-F. Moulin, V. Hildebrand, A. Laschewsky, C. M. Papadakis, P. Müller-Buschbaum
  Multi-stimuli responisve polymer films analyzed by in-situ neutron reflectometry
  29. Edgar Lüscher Seminar, Klosters, Switzerland 3 – 9 Feb 2018

- L. P. Kreuzer, T. Widmann, N. Hohn, K. Wang, J.-F. Moulin, V. Hildebrand, A. Laschewsky, C. M. Papadakis, P. Müller-Buschbaum
  Water swelling and exchange kinetics of multi-stimuli responisve polymer thin films
  DPG-Frühjahrstagung, Berlin, 11 – 16 Mar 2018

- L. P. Kreuzer, T. Widmann, N. Hohn, K. Wang, J.-F. Moulin, V. Hildebrand, A. Laschewsky, C. M. Papadakis, P. Müller-Buschbaum
  Water swelling and exchange kinetics in multi-stimuli responsive polymer thin films followed with in-situ time of flight neutron reflectometry
  Macro 18 Conference, Cairns, Australia, 1 – 5 Jul 2018

- L. P. Kreuzer, F. Löhrer, T. Widmann
  Fourier transform infrared spectroscopy
  Polymer Physics Summer School 2018, Obertauern, Austria, 12 – 15 Jun 2018

- L. P. Kreuzer, T. Widmann, V. Körstgens, P. Müller-Buschbaum
  Flexible sample environment for the investigation of soft matter for implementation at the ESS
  Verbundprojekttreffen FlexiProb, Bielefeld, 10 Dez 2018

- M. Leitner, P. Neibecker, M. Opel, X. Xu, R. Kainuma, W. Petry
  Continuous transition from antiferro- to ferromagnetic state via moment canting in $Ni_{2-x}Co_xMnAl$
  DPG-Frühjahrstagung, Berlin, 11 – 16 Mar 2018

- M. Leitner, P. Neibecker, J. Schmidbauer, W. Petry
  Premartensite in $Ni_2MnAl_0.5Ga_0.5$
  ESOMAT 2108, Metz, 27 – 31 Aug 2018

- M. Leitner
  Atomic diffusion studied by coherent X-ray scattering
  Fakultät für Physik, Universität Wien, Vienna, Austria, 20 Nov 2018

- F. Löhrer, V. Körstgens, S. J. Schaper, M. Schwartzkopf, A. Hinz, O.Polonskyi, T. Strunskus, F.Faupel, S.Roth, P. Müller-Buschbaum
  Following the formation of metal electrodes on photoactive polymer thin film
  DPG-Frühjahrstagung, Berlin, 11 – 16 Mar 2018

- F. Löhrer, C. Senfter, P. Müller-Buschbaum
  Investigation of degradation processes in low bandgap polymers for organic photovoltaics
  DPG-Frühjahrstagung, Berlin, 11 – 16 Mar 2018
- F. Löhrer, D. Yang, C. Schaffer, W. Wang, D. Moseguí González, S.V. Roth, S. Bernstorff, P. Müller-Buschbaum
  Understanding morphological degradation in organic photovoltaics with advanced scattering techniques
  4th German SNI Conference, Garching, 17 – 19 Sep 2018
- F. Löhrer, L. P. Kreuzer, T. Widmann
  Fourier Transform Infrared Spectroscopy
  Polymer Physics Summer School 2018, Obertauern, Austria, 12 – 15 Jun 2018
- P. Müller-Buschbaum
  Polymer and hybrid nanostructures for applications in organic solar cells investigated with advanced scattering techniques
  Neutrons for Science and Industry Seminar an TU München, Garching, 15 Jan 2018
- P. Müller-Buschbaum
  Report of the Users Committee (DPS-UC) - report 2017
  DESY Users' Meeting, Hamburg, 25 – 26 Jan 2018
- P. Müller-Buschbaum
  Report by Chair of the DESY Photon Science User Committee
  DESY POF Begutachtung; Hamburg, 7 – 8 Feb 2018
- P. Müller-Buschbaum
  Next generation solar cells studied with GISANS
  GISANS workshop for new reactor based instrument at MLZ, Jülicher Zentrum für Forschung mit Neutronen, Garching 1 Feb 2018
- P. Müller-Buschbaum
  Big data and automatization challange in grazing incidence scatterin
  Digitale Agenda – Workshop des KFS/KFN, Hamburg 22 Feb 2018
- P. Müller-Buschbaum
  GISANS – basics, challenges and possibilities
  Leuchtturmberufung der TUM in Garching, 5 Mar 2018
- P. Müller-Buschbaum, W. Wang, L. Song, D. Magerl, D. Moseguì González, V. Körstgens, M. Philipp, J.-F. Moulin
  Influence of solvent additive 1,8-octanedithiol on P3HT:PCBM solar cells
  DPG-Frühjahrstagung, Berlin, 11 – 16 Mar 2018
- P. Müller-Buschbaum, C.J. Schaffer, C.M. Palumbiny, S.V. Roth
  Watching aging in organic solar cells - an in-operando stud
  255th American Chemical Society National Meeting, New Orleans, USA, 18 – 22 Mar 2018
- P. Müller-Buschbaum
  FRMII in the European Neutron Landscape
  SINE 2020 General Assembly Meeting, Parma, Italy, 5 – 6 Jun 2018

- P. Müller-Buschbaum
  Thermoelectric thin hybrid films based on conducting polymers
  Thermoelektrik Workshop, Leipzig, 8 – 9 Jun 2018

- P. Müller-Buschbaum
  MLZ Conference Neutrons for Culture and Art - Welcome
  MLZ Conference Neutrons for Culture and Art, Lenggries, 19 – 22 Jun 2018

- P. Müller-Buschbaum
  Polymer and hybrid nanostructures for applications in organic solar cells investigated with advanced scattering techniques
  Physikalisches Kolloquium Universität Wuppertal, 25 Jun 2018

- P. Müller-Buschbaum
  A first step into space with organic solar cells
  DLR Seminar des Instituts für Materialphysik im Weltraum 2018, Köln, 26 Jun 2018

- P. Müller-Buschbaum
  Studying soft matter surfaces and interfaces with in-situ and in-operando x-ray and neutron scattering
  World Polymer Congress – MACRO 2018, Cairns, Australia, 1 – 5 Jul 2018

- P. Müller-Buschbaum
  Next generation solar cells studied with GISANS
  GISAS2018, Gyeongju, South Korea, 4 - 7 Sep 2018

- P. Müller-Buschbaum
  VDI-TUM Expertenforum – Begrüßung am FRM II
  7. VDI-TUM Expertenforum, Garching, 13 Sep 2018

- P. Müller-Buschbaum
  SNI Welcome
  German Conference for Research with Synchrotron Radiation, Neutrons and Ion Beams at Large Scale Facilities, 17 – 19 Sep 2018

- P. Müller-Buschbaum
  The GISANS technique and its application
  ILL and ESS European Users Meeting, Grenoble, 10 - 12 Oct 2018

- P. Müller-Buschbaum
  Next generation solar cells
  MSE Workshop Solarforschung, Garching, 30 Nov 2018

- P. Müller-Buschbaum
  GISAS for soft matter
  BornAgain Workshop, Garching 19 – 21 Dec 2018

- B.-J. Niebuur, L. Chiappisi, X. Zhang, F. Jung, A. Schulte, C. M. Papadakis
  Multi-step kinetics of mesoglobule formation in aqueous PNIPAM solutions during pressure jumps
  DPG-Frühjahrstagung, Berlin, 11 – 16 Mar 2018

- B.-J. Niebuur, K.-L. Claude, S. Pinzek, C. Cariker, K. N. Raftopoulos, V. Pipich, M.-S. Appavou, A. Schulte, C. M. Papadakis

Pressure-dependence of poly(N-isopropylacrylamide) mesoglobule formation in aqueous solution
16th Conference of the International Association of Colloid and Interface Scientists, Rotterdam, the Netherlands, 21 – 25 May 2018

- B.-J. Niebuur, L. Reb, D. Schwaiger
  Raman spectroscopy
  Polymer Physics Summer School, Obertauern, Austria, 12 – 15 Jun 2018
- C. M. Papadakis, M. A. Dyakonova, G. Gotzamanis, S. K. Filippov, C. Tsitsilianis
  pH responsiveness of hydrogels formed by telechelic polyampholytes
  82nd PMM conference and the 24th Polymer Networks Group Meeting - Polymer Networks and Gels 2018, Prague, Czech Republic, 17 – 21 Jun 2018
- W. Petry
  Forschungscampus Garching – eine Erfolgsgeschichte
  Neujahrempfang der CSU Garching, Rathaus Garching, 19 Jan 2018
- W. Petry
  Neutrons for basic research, industry and medicine
  EC Conference on Medical, Industrial and Reseach Applications of Nuclear and Radiation Technology, Brussels, 20/21 Mar 2018
- W. Petry
  Mit Neutronen die Welt erforschen – auf der Suche nach dem Wissen von morgen
  42. Edgar-Lüscher Lehrerfortbildungs-Seminar, Gymnasium Zwiesel, 27 - 29 Apr 2018
- W. Petry
  Fuel development for European high performance research reactors
  3rd International Symposium on Highly Enriched Uranium Minimization, Oslo, Norway, 5 – 7 Jun 2018
- W. Petry
  Neutrons for medicine
  E13 Summerschool, Obertauern, Austria, Jun 12, 2018
- W. Petry
  Neutrons for medicine
  RACIRI Summer School 2018, Rügen Island, 31 Aug 2018
- W. Petry
  Neutrons – for what?
  Institute for Material Physics in Space, German Aerospace Center (DLR), Cologne 17 Oct 2018
- W. Petry
  60 Jahre Forschung mit Neutronen auf dem Campus Garching – wie Politik und Neutronen sich bedingen
  Festveranstaltung des Physik Departments anlässlich 150 Jahre Technische Universität München, Garching, 8 Nov 2018
- N. Saxena, B. Pretzl, X. Lamprecht, D. Yang, N. Li, C. Bilko, S. Bernstorff, P. Müller-Buschbaum

Ionic liquid post-treatment of PEDOT:PSS thin films for improvement of thermoelectric properties
DPG-Frühjahrstagung, Berlin, 11 – 16 Mar 2018

- N. Saxena, K. Wang, K Wienhold
X-ray reflectivity and neutron reflectivity
Polymer Physics Summer School 2018, Obertauern, Austria, 12 – 15 Jun 2018

- R. Schaffrinna, M. Schwager, P. Müller-Buschbaum
Thiophene based semiconductors
1th Ko-op Symposium of the Munich School of Engineering, Garching, 29 Nov 2018

- S. J. Schaper, F. C. Löhrer, V. Körstgens, S. Xia, M. Schwartzkopf, P. Pandit, A. Hinz, O. Polonskyi, T. Strunskus, F. Faupel, S. V. Roth, P. Müller-Buschbaum
In-situ GISAXS during sputter deposition of metal nanolayers on functional polymer thin films for lithium-ion batteries
DPG-Frühjahrstagung, Berlin, 11 – 16 Mar 2018

- S. J. Schaper, F. C. Löhrer, V. Körstgens, S. Xia, M. Schwartzkopf, P. Pandit, A. Hinz, O. Polonskyi, T. Strunskus, F. Faupel, S. V. Roth, P. Müller-Buschbaum
Watching metal nanolayer growth on functional polymer thin films for lithium-ion battery applications
8th Colloquium of the Munich School of Engineering, Garching, 19 Jul 2018

- S. J. Schaper, J. Schlipf, S. Yin
White light interferometry (WLI) & ellipsometry
Polymer Physics Summer School 2018, Obertauern, Austria, 12 – 15 Jun 2018

- S. J. Schaper, F. C. Löhrer, V. Körstgens, S. Xia, M. Schwartzkopf, P. Pandit, A. Hinz, O. Polonskyi, T. Strunskus, F. Faupel, S. V. Roth, P. Müller-Buschbaum
Watching metal nanolayer growth on functional polymer thin films for lithium-ion battery applications
2nd BornAgain School and User Meeting, Garching, 19 – 21 Dec 2018

- J. Schlipf, L. Bießmann, L. Oesinghaus, E. Berger, E. Metwalli, J. A. Lercher, L. Porcar, P. Müller-Buschbaum
Ingression of moisture into hybrid perovskite thin films probed with in-situ GISANS
DPG-Frühjahrstagung, Berlin, 11 – 16 Mar 2018

- J. Schlipf, L. Bießmann, L. Oesinghaus, E. Berger, E. Metwalli, J. A. Lercher, L. Porcar, P. Müller-Buschbaum
Ingression of moisture into hybrid perovskite thin films probed with in-situ GISANS
NIM-GP Winter Meeting, München, 10 Apr 2018

- J. Schlipf, P. Müller-Buschbaum
Fundamentals of GISANS and selected examples
SwedNess Annual Meeting & Swedish Neutron Week, Göteborg, 23 – 24 Apr 2018

- L.Song, B.Su, K.Wang, G.Santoro, S.V.Roth, P. Müller-Buschbaum
Spray deposition of titania films for application in photovoltaics
17th SAXS/WAXS/GISAXS Satellite Workshop of DESY Users' Meeting, Hamburg, 25 – 26 Jan 2018

- N. S. Vishnevetskaya, V. Hildebrand, B.-J. Niebuur, P. Müller-Buschbaum, A. Laschewsky, C. M. Papadakis
  Orthogonally and doubly switchable diblock copolymers: Schizophrenic behavior
  DPG-Frühjahrstagung, Berlin, 11 – 16 Mar 2018

- N. S. Vishnevetskaya, V. Hildebrand, P. Müller-Buschbaum, A. Laschewsky, C. M. Papadakis
  Schizophrenic micelles from doubly and orthogonally switchable block copolymers
  16th Conference of the International Association of Colloid and Interface Scientists, Rotterdam, The Netherlands, 21 – 25 May 2018

- N. S. Vishnevetskaya, V. Hildebrand, P. Müller-Buschbaum, A. Laschewsky, C. M. Papadakis
  'Schizophrenic' micelles from doubly and orthogonally switchable block copolymers
  University of Ioannina, Greece, 3 Oct 2018

- N. S. Vishnevetskaya, V. Hildebrand, P. Müller-Buschbaum, A. Laschewsky, C. M. Papadakis
  'Schizophrenic' micelles from doubly and orthogonally switchable block copolymers
  14th European Detergents Conference EDC, Berlin, 10 Oct 2018

- N. S. Vishnevetskaya, V. Hildebrand, P. Müller-Buschbaum, A. Laschewsky, C. M. Papadakis
  'Schizophrenic' micelles from doubly and orthogonally switchable diblock copolymers
  Cracow University of Technology, Poland, 23 Nov 2018

- K. Wang, V. Körstgens, D. Yang, N. Hohn, S. V. Roth, P. Müller-Buschbaum
  Morphology control of low temperature fabricated ZnO nanostructures for transparent all solid-state dye-sensitized solar cells
  DPG-Frühjahrstagung, Berlin, 11 – 16 Mar 2018

- T. Widmann, L. P. Kreuzer, N. Hohn, L. Bießmann, K. Wang, J-F. Moulin, Y. Hannappel, T. Hellweg, P. Müller-Buschbaum
  Water uptake and diffusion in thin PNIPAM microgel films
  DPG-Frühjahrstagung, Berlin, 11 – 16 Mar 2018

- T. Widmann, L. P. Kreuzer, N. Hohn, L. Bießmann, K. Wang, J-F. Moulin, Y. Hannappel, T. Hellweg, P. Müller-Buschbaum
  In situ studies on the H2O/D2O swelling and exchange kinetics in PNIPAM microgel thin films followed with time of flight neutron reflectometry
  Macro 2018, Cairns, Australia, 1 – 5 Jul 2018

- T. Widmann, L. P. Kreuzer, P. Müller-Buschbaum
  Flexible sample environment for the investigation of soft matter for implementation at the ESS
  FlexiProb Meeting, Lund, Sweden, 29 May 2018

- D. Yang, F. C. Löhrer, V. Körstgens, A. Schreiber, S. Bernstorff, J. M. Buriak, P. Müller-Buschbaum
  Investigating the degradation of PffBT4T-2OD: PC70BM solar cells by in-operando GISAXS/GIWAXS measurements
  DPG-Frühjahrstagung, Berlin, 11 – 16 Mar 2018

- D. Yang, B. Cao, T. Hauger, E. J. Luber, P. Müller-Buschbaum, J. M. Buriak
  How to rationally select an interfacial modifier for high performance organic photovoltaics
  ATUMs annual meeting, Garching, 12–16 Nov 2018

- X. Zhang, P. Chytil, S. K. Filippov, D. I. Svergun, C. M. Papadakis
  Self-assembled polymeric nanoparticles for drug delivery: Do they interact with blood proteins?
  12th Hellenic Polymer Society International Conference 2018, Ioannina, Greece, 30 Sep – 3 Oct 2018

8.3 Posters

- N. Aldosari, L. P. Kreuzer, J. Pantle, V. Hildebrand, A. Laschewsky, C. M. Papadakis, P. Müller-Buschbaum
  Smart nano-sensors made of stimuli-responsive polymers in thin films
  Polymer Physics Summer School 2018, Obertauern, Austria, 12- 15 Jun 2018
- N. Aldosari, L. P. Kreuzer, J. Pantle, V. Hildebrand, A. Laschewsky, C. M. Papadakis, P. Müller-Buschbaum
  Smart nano-sensors made of stimuli-responsive polymers in thin films
  8th Colloquium of the Munich School of Engineering, Garching, 19 Jul 2018
- A. V. Berezkin, F. Jung, D. Posselt, D.-M. Smilgies, C. M. Papadakis
  Morphologies and solvent distribution during solvent vapor annealing of block copolymer thin films: In situ, teal-time GISAXS investigations
  4th German SNI Conference, Garching, 17 – 19 Sep 2018
- L. Bießmann, N. Saxena, P. Müller-Buschbaum
  Investigations on PEDOT:PSS polymeric electrodes for OLED applications
  8th Colloquium of the Munich School of Engineering, Garching, 19 Jul 2018
- L. Bießmann, N. Saxena, K. Wang, D. Yang, C. Bilko, S. Bernstorff, P. Müller-Buschbaum
  Structural investigations on PEDOT:PSS polymeric electrodes by means of GISAXS and GIWAXS
  4th German SNI Conference, Garching, 17 – 19 Sep 2018
- K. Biswas, S. Xia, S. Lafuerza, P. Glatzel, M. Opel, P. Müller-Buschbaum
  Magnetic nanoparticles in diblock copolymer matrix
  DPG-Frühjahrstagung, Berlin, 11 – 16 Mar 2018
- K. Biswas, S. Xia, S. Lafuerza, P. Glatzel, M. Opel, P. Müller-Buschbaum
  Magnetic nanoparticles in diblock copolymer matrix
  Polymer Physics Summer School 2018, Obertauern, Austria, 12- 15 Jun 2018
- W. Cao, S. Xia, M. Appold, M. Gallei, P. Müller-Buschbaum
  Thin films of ultrahigh molecular weight diblock copolymers
  DPG-Frühjahrstagung, Berlin, 11 – 16 Mar 2018
- W. Cao, S. Xia, M. Appold, M. Gallei, P. Müller-Buschbaum
  Thin films of ultrahigh molecular weight diblock copolymers
  Polymer Physics Summer School 2018, Obertauern, Austria, 12- 15 Jun 2018
- W. Cao, S. Xia, M. Appold, N. Saxena, L. Bießmann, S. Grott, M. Gallei, P. Müller-Buschbaum
  Thin films of ultrahigh molecular weight diblock copolymers
  4th German SNI Conference, Garching, 17 – 19 Sep 2018
- D. Chakraborty, P. Müller-Buschbaum
  Spray deposition of polymer thin films for photovoltaic application
  DPG-Frühjahrstagung, Berlin, 11 – 16 Mar 2018
- D. Chakraborty, P. Müller-Buschbaum
  Spray deposition of polymer thin films for photovoltaic application
  Polymer Physics Summer School 2018, Obertauern, Austria, 12- 15 Jun 2018

- W. Chen, P. Müller-Buschbaum
  Colloidal quantum dot solids for photovoltaics
  DPG-Frühjahrstagung, Berlin, 11 – 16 Mar 2018
- W. Chen, P. Müller-Buschbaum
  Colloidal quantum dot solids for photovoltaics
  8th Colloquium of the Munich School of Engineering, Garching, 19 Jul 2018
- W. Chen, P. Müller-Buschbaum
  Colloidal quantum dot solids for photovoltaics
  4th German SNI Conference, Garching, 17 – 19 Sep 2018
- R. Delgado, S. Grott, P. Müller-Buschbaum
  Printed fullerene free thin films for photovoltaic applications.
  DPG-Frühjahrstagung, Berlin, 11 – 16 Mar 2018
- R. Delgado, S. Grott, P. Müller-Buschbaum
  Printed fullerene free thin films for photovoltaic applications.
  Polymer Physics Summer School 2018, Obertauern, Austria, 12 – 15 Jun 2018
- R. Delgado, S. Grott, P. Müller-Buschbaum
  Printed fullerene free thin films for photovoltaic applications.
  8th Colloquium of the Munich School of Engineering, Garching, 19 Jul 2018
- S. Grott, C. Ott, M. Schwartzkopf, N. Hohn, S. Xia, K. Wang, S. V. Roth, T. Nilges, P. Müller-Buschbaum
  Influence of inorganic nanoparticles on the morphology of polymer blends for photovoltaic applications
  DESY Photo Science Users' Meeting, Hamburg, 24 – 25 Jan 2018
- S. Grott, L. Bießmann, N. Saxena, W. Cao, S. Bernstorff, P. Müller-Buschbaum
  Morphological investigations on fullerene-free bulk heterojunction blends for photovoltaic applications
  DPG-Frühjahrstagung, Berlin, 11 – 16 Mar 2018
- S. Grott, C. Ott, N. Hohn, S. Xia, K. Wang, T. Nilges, P. Müller-Buschbaum
  Influence of SnIP nanoparticles on organic thin films for photovoltaic applications
  8th Colloquium of the Munich School of Engineering, Garching, 19 Jul 2018
- S. Grott, C. Ott, M. Schwartzkopf, N. Hohn, S. Xia, K. Wang, S. V. Roth, T. Nilges, P. Müller-Buschbaum
  Effect of inorganic SnIP nanoparticles on the morphology of polymer blends for photovoltaic applications
  4th German SNI Conference, Garching, 17 – 19 Sep 2018
- S. Grott, C. Ott, M. Schwartzkopf, N. Hohn, S. Xia, K. Wang, S. V. Roth, T. Nilges, P. Müller-Buschbaum
  Morphology of a polymer blend influenced by inorganic SnIP nanocrystals
  7th SolTech Conference: Solar Technologies go Hybrid, Würzburg, 3 – 5 Oct 2018
- J. Heger, P. Müller-Buschbaum
  Directional, hierarchical films via spray coating
  8th Colloquium of the Munich School of Engineering, Garching, 19 Jul 2018

- J. Heger, W. Chen, S. Grott, X. Jiang, S. Bernstorff, P. Müller-Buschbaum
  Directional, hierarchical films via spray coating
  4th German SNI Conference, Garching, 17 – 19 Sep 2018
- X. Jiang, P. Müller-Buschbaum
  Printed low bandgap polymer films
  DPG-Frühjahrstagung, Berlin, 11 – 16 Mar 2018
- X. Jiang, W. Cao, P. Müller-Buschbaum
  Printed high-transparent blocking layer for photovoltaics
  8th Colloquium of the Munich School of Engineering, Garching, 19 Jul 2018
- X. Jiang, P. Müller-Buschbaum
  Morphology of printed active layers for organic solar cells as studied with advanced scattering techniques
  4th German SNI Conference, Garching, 17 – 19 Sep 2018
- X. Jiang, W. Cao, W. Chen, P. Müller-Buschbaum
  Printed high-transparent blocking layer for photovoltaics
  7th SolTech Conference: Solar Technologies go Hybrid, Würzburg, 3 – 5 Oct 2018
- F. Jung, P. A. Panteli, C. Tsitsilianis, C. S. Patrickios, C. M. Papadakis
  Structural investigations of multi-responsive physical hydrogels
  DPG-Frühjahrstagung, Berlin, 11 – 16 Mar 2018
- F. Jung, P. A. Panteli, C. Tsitsilianis, C. S. Patrickios, C. M. Papadakis
  Light and X-ray scattering study of a temperature and pH responsive physical hydrogel
  82nd Prague Meeting on Macromolecules and 24th Polymer Networks Group Meeting, Prague, 17 – 21 June 2018
- F. Jung, P. A. Panteli, D.-M. Smilgies, D. Posselt, C. Tsitsilianis, C. S. Patrickios, C. M. Papadakis
  In situ GISAXS investigations of pH and temperature responsive block copolymer thin films during swelling in water vapor
  4th German SNI Conference, Garching, 17 – 19 Sep 2018
- J.-J. Kang, J. Zhao, S. Pispas, C. M. Papadakis
  Morphology of amphiphilic molecular brushes in dilute aqueous solution
  DPG-Frühjahrstagung, Berlin, 11 – 16 Mar 2018
- J.-J. Kang, J. Zhao, H. Frielinghaus, L. Barnsley, S. Pispas, C. M. Papadakis
  Morphology of thermoresponsive molecular brushes with copolymer side arms in dilute aqueous solutions
  32th European Colloid and Interface Society Conference, Ljubljana, Slovenia, 2 – 7 Sep 2018
- J.-J. Kang, J. Zhao, H. Frielinghaus, L. Barnsley, S. Pispas, C. M. Papadakis
  Morphology of thermoresponsive molecular brushes with copolymer side arms in dilute aqueous solutions
  4th German SNI Conference, Garching, 17 – 19 Sep 2018
- J.-J. Kang, J. Zhao, H. Frielinghaus, L. Barnsley, S. Pispas, C. M. Papadakis
  Morphology of thermoresponsive molecular brushes with copolymer side arms in dilute aqueous

solutions
12th Hellenic Polymer Society International Conference 2018, Ioannina, Greece, 30 Sep – 3 Oct 2018

- C.-H. Ko, K.-L. Claude, D. Schanzenbach, B.-J. Niebuur, X. Zhang, D. Aravopoulou, A. Kyritsis, H. Frielinghaus, P. Müller-Buschbaum, A. Laschewsky, C. M. Papadakis
  The structural, thermal and dynamic behavior of the thermoresponsive polymer poly(N-isopropylmethacrylamide)
  DPG-Frühjahrstagung, Berlin, 11 – 16 Mar 2018

- C.-H. Ko, K.-L. Claude, D. Schanzenbach, B.-J. Niebuur, F. Jung, J.-J. Kang, H. Frielinghaus, L. Barnsley, V. Pipich, B. Wu, A. Schulte, P. Müller-Buschbaum, A. Laschewsky, C. M. Papadakis
  The structural, thermal and dynamic behavior of the thermoresponsive polymer poly(N-isopropylmethacrylamide)
  14th European Summer School on Scattering Methods Applied to Soft Condensed Matter, Bombannes, 19 – 26 Jun 2018

- C.-H. Ko, K.-L. Claude, D. Schanzenbach, B.-J. Niebuur, F. Jung, J.-J. Kang, H. Frielinghaus, L. Barnsley, V. Pipich, B. Wu, A. Schulte, P. Müller-Buschbaum, A. Laschewsky, C. M. Papadakis
  The structural, thermal and dynamic behavior of the thermoresponsive polymer poly(N-isopropylmethacrylamide)
  32th European Colloid and Interface Society ECIS, Ljubljana, 2 – 9 Sep 2018

- C.-H. Ko, K.-L. Claude, D. Schanzenbach, B.-J. Niebuur, F. Jung, J.-J. Kang, H. Frielinghaus, L. Barnsley, V. Pipich, B. Wu, A. Schulte, P. Müller-Buschbaum, A. Laschewsky, C. M. Papadakis
  The structural, thermal and dynamic behavior of the thermoresponsive polymer poly(N-isopropylmethacrylamide)
  4th German SNI Conference, Garching, 17 – 19 Sep 2018

- V. Körstgens, H. Iglev, R. Kienberger, S.V. Roth, P. Müller-Buschbaum
  Spray deposition of active layers for hybrid solar cells: in situ GISAXS and GIWAXS studies
  DESY user's meeting, Hamburg, 25 – 26 Jan 2018

- V. Körstgens, F. Martin, C. Brett, D. Söderberg, S.V. Roth, P. Müller-Buschbaum
  Cellulose-based conducting nanocomposite films via spray deposition with in situ GISAXS
  8th Colloquium of the Munich School of Engineering, Garching, 19 Jul 2018

- V. Körstgens, F. Martin, C. Brett, D. Söderberg, S.V. Roth, P. Müller-Buschbaum
  Cellulose-based conducting nanocomposite films via spray deposition with in situ GISAXS
  4th German SNI Conference, Garching, 17 – 19 Sep 2018

- V. Körstgens, C. Mayr, G. Santoro, S.V. Roth, H. Iglev, R. Kienberger, P. Müller-Buschbaum
  Hybrid solar cells with laser-ablated titania: in situ investigations of device processing
  7th SolTech Conference: Solar Technologies go Hybrid, Würzburg, 3 – 5 Oct 2018

- L. P. Kreuzer, T. Widmann, N. Hohn, K. Wang, J.-F. Moulin, V. Hildebrand, A. Laschewsky, C. M. Papadakis, P. Müller-Buschbaum
  Water swelling and exchange kinetics in multi-stimuli responsive PNIPAM-based block copolymer thin films
  4th German SNI Conference, Garching, 17 – 19 Sep 2018

- L. P. Kreuzer, T. Widmann, N. Hohn, K. Wang, J.-F. Moulin, V. Hildebrand, A. Laschewsky, C. M. Papadakis, P. Müller-Buschbaum
  Water swelling and exchange kinetics in multi-stimuli responsive PNIPAM-based block copolymer thin films
  ILL & ESS European User Meeting, Grenoble, France, 10 – 12 Oct 2018
- M. Leitner, P. Neibecker, M. Opel, A. Senyshyn, X. Xu, R. Kainuma, W. Petry
  Continuous transition from antiferro- to ferromagnetic state via moment canting in $Ni_{2-x}Co_xMnAl$
  4th German SNI Conference, Garching, 17 – 19 Sep 2018
- M. Leitner
  Electronic structure and phase transitions
  TRR 80 Retreat Meeting, Irsee, 19 – 20 Feb 2018
- N. Li, B. Su, S. Xia, P. Müller-Buschbaum
  Morphology phase diagram of printed titania films derived from block copolymer assisted sol-gel templating
  DPG-Frühjahrstagung, Berlin, 11 – 16 Mar 2018
- N. Li, L. Song, L. Bießmann, S. Xia, W. Ohm, C. Brett, S, V. Roth, P. Müller-Buschbaum
  Morphology phase diagram of printed titania films assisted a sol-gel technique
  8th Colloquium of the Munich School of Engineering, Garching, 19 Jul 2018
- N. Li, L. Song, L. Bießmann, W. Ohm, C. Brett, S, V. Roth, S. Xia, P. Müller-Buschbaum
  Morphology phase diagram of printed titania films derived from block copolymer template assisted a sol-gel technique
  4th German SNI Conference, Garching, 17 – 19 Sep 2018
- N. Li, L. Song, L. Bießmann, S. Xia, W. Ohm, C. Brett, S, V. Roth, P. Müller-Buschbaum
  Morphology phase diagram of printed titania films derived from block copolymer template assisted sol-gel synthesis
  7th SolTech Conference: Solar Technologies go Hybrid, Würzburg, 3 – 5 Oct 2018
- F. Löhrer, C. Senfter, P. Müller-Buschbaum
  Live fast, die young – understanding degradation processes in high-efficiency organic photovoltaicsr
  8th Colloquium of the Munich School of Engineering, Garching, 19 Jul 2018
- F. Löhrer, V. Körstgens, M. Schwartzkopf, A. Hinz, O. Polonskyi, T. Strunskus, F. Faupel, S.V. Roth, P. Müller-Buschbaum
  In-situ investigation of the sputter deposition of metal contacts on polymer thin films
  4th German SNI Conference, Garching, 17 – 19 Sep 2018
- R. Märkl, N. Hohn, P. Müller-Buschbaum
  Next Generation hybrid solar cells based on heavy element containing small molecules and high-performance polymer PTB7-Th
  Polymer Physics Summer School 2018, Obertauern, Austria, 12 – 15 Jun 2018
- R. Märkl, N. Hohn, P. Müller-Buschbaum
  Next Generation hybrid solar cells based on heavy element containing small molecules and high-performance polymer PTB7-Th
  8th Colloquium of the Munich School of Engineering, Garching, 19 Jul 2018

- R. Märkl, N. Hohn, G. Mangiapia, M. Pomm, P. Müller-Buschbaum
  Backfilling of mesoporous titania structures with heavy element containing small molecules and high-efficiency polymer PTB7-Th
  4th German SNI Conference, Garching, 17 – 19 Sep 2018

- B.-J. Niebuur, K.-L. Claude, R. Schweins, V. Pipich, M.-S. Appavou, A. Schulte, C. M. Papadakis
  SANS study on the pressure-dependence of the cononsolvency effect in aqueous PNIPAM solutions
  DPG-Frühjahrstagung, Berlin, 11 – 16 Mar 2018

- B.-J. Niebuur, L. Chiappisi, X. Zhang, F. Jung, A. Schulte, C. M. Papadakis
  Kinetics of mesoglobule formation in aqueous PNIPAM solutions revealed with SANS and fast pressure jumps
  4th German SNI Conference, Garching, 17 – 19 Sep 2018

- S. Pratap, P. Müller-Buschbaum
  Complex morphologies and pattern formation in perovskite thin films
  NIM Summer Retreat, Spitzingsee, 13 – 15 Aug 2018

- S. Pratap, P. Müller-Buschbaum
  Microstructural evolution during thin film growth
  NIM Conference: The Future of Nanoscience, Tutzing, 4 – 6 Sep 2018

- S. Pratap, J. Schlipf, K. John, V. Körstgens, F. Fischer, S. Vema, A. Davydok, C. Krywka, P. Müller-Buschbaum
  An insight into atmospheric degradation processes by mapping local nanoheterogeneities within hybrid polycrystalline perovskite films
  4th German SNI Conference, Garching, 17 – 19 Sep 2018

- S. Pratap, E. Keller, P. Müller-Buschbaum
  On the colloidal behaviour of hybrid perovskite precursor solutions: insights into the nano and mesoscale
  20th CeNS Workshop: Celebrating Nanoscience, Venice, 24 – 28 Sep 2018

- S. Pratap, J. Schlipf, P. Müller-Buschbaum
  On the chemical origins of crystalline preferred orientations in hybrid lead halide perovskite thin films
  ALS Annual User Meeting, Lawrence Berkeley National Laboratory, California, 2 – 4 Oct 2018

- B. Predeschly, S. Grott, P. Müller-Buschbaum
  Printing technology for organic solar cells
  Polymer Physics Summer School Obertauern, Austria, 12 – 15 Jun 2018

- L. Reb, P. Müller-Buschbaum
  Challenging silicon: perovskite based solar cells
  4th German SNI Conference, Garching, 17 – 19 Sep 2018

- N. Saxena, M. Coric, A. Greppmair, J. Wernecke, M. Plüger, M. Krumrey, M. S. Brandt, E. M. Herzig, P. Müller-Buschbaum
  Thermoelectric thin films based on a polymer/nanoparticle nanocomposite
  NIM Conference 'The Future of Nanoscience', Tutzing, 4 – 6 Sep 2018

- N. Saxena, M. Coric, A. Greppmair, J. Wernecke, M. Plüger, M. Krumrey, M. S. Brandt, E. M. Herzig, P. Müller-Buschbaum
  Thermoelectric thin films based on a polymer/nanoparticle nanocomposite
  German Conference for Research with Synchrotron Radiation, Neutrons and Ion Beams at Large-Scale Facilities, Garching, 16 –19 Sep 2018
- S. J. Schaper, F. C. Löhrer, S. Xia, M. Schwartzkopf, P. Pandit, A. Hinz, O. Polonskyi, T. Strunskus, F. Faupel, S. V. Roth, P. Müller-Buschbaum
  in-situ GISAXS during sputter deposition of metal nanolayers on functional polymer thin films for lithium-ion batteries
  4th German SNI Conference, Garching, 17 – 19 Sep 2018
- S. J. Schaper, F. C. Löhrer, S. Xia, M. Schwartzkopf, P. Pandit, A. Hinz, O. Polonskyi, T. Strunskus, F. Faupel, S. V. Roth, P. Müller-Buschbaum
  in-situ GISAXS during sputter deposition of metal nanolayers on functional polymer thin films for lithium-ion batteries
  7th SolTech Conference: Solar Technologies go Hybrid, Würzburg, 3 – 5 Oct 2018
- D. Schwaiger, W. Lohstroh, P. Müller-Buschbaum
  Laser-neutron pump-probe experiment at the neutron time-of-flight spectrometer TOFTOF
  4th German SNI Conference, Garching, 17 – 19 Sep 2018
- K. Shehu, J.-J. Kang, C. Sachse, R. Jordan, C. M. Papadakis
  Morphological study of drug delivery systems based on poly(2-oxazoline) bottle brushes
  DPG-Frühjahrstagung, Berlin, 11 – 16 Mar 2018
- K. Shehu, J.-J.Kang, H. Frielinghaus, L. Barnsley, C. Sachse, R. Jordan, C. M. Papadakis
  Polymeric molecular brushes investigated by scattering methods
  Polymer Physics Summer School Obertauern, Austria, 12 – 15 Jun 2018
- K. Wang, Y. Tong, L. Bießmann, S. V. Roth, P. Müller-Buschbaum
  Morphology control of low temperature synthesized ZnO/P3HT-b-PEO films via spray deposition
  8th Colloquium of the Munich School of Engineering, Garching, 19 Jul 2018
- K. Wang, Y. Tong, L. Bießmann, S. V. Roth, P. Müller-Buschbaum
  Morphology control of low temperature synthesized ZnO/P3HT-b-PEO films via spray deposition
  4th German SNI Conference, Garching, 17 – 19 Sep 2018
- C. Weindl, F. C. Löhrer, P. Müller-Buschbaum
  Investigation of novel material systems for increasing the efficiency of organic solar cells
  DPG-Frühjahrstagung, Berlin, 11 – 16 Mar 2018
- C. Weindl, F. C. Löhrer, P. Müller-Buschbaum
  Investigation of novel material systems for increasing the efficiency of organic solar cells
  Polymer Physics Summer School 2018, Obertauern, Austria, 12 – 15 Jun 2018
- C. Weindl, F. C. Löhrer, P. Müller-Buschbaum
  Investigation of novel material systems for increasing the efficiency of organic solar cells
  8th Colloquium of the Munich School of Engineering, Garching, 19 Jul 2018
- C. Weindl, F. C. Löhrer, P. Müller-Buschbaum
  Investigation of novel material systems for increasing the efficiency of organic solar cells
  4th German SNI Conference, Garching, 17 – 19 Sep 2018

- K. Wienhold, P. Müller-Buschbaum
  Printed films of conjugated polymers and small acceptor molecules
  DPG-Frühjahrstagung, Berlin, 11 – 16 Mar 2018
- K. Wienhold, P. Müller-Buschbaum
  Printed films of conjugated polymers and small acceptor molecules
  8th Colloquium of the Munich School of Engineering, Garching, 19 Jul 2018
- K. Wienhold, P. Müller-Buschbaum
  Printed films of conjugated polymers and small acceptor molecules
  4th German SNI Conference, Garching, 17 – 19 Sep 2018
- S. Yin, L. Song, S. Xia, P. Müller-Buschbaum
  TiO_2 and SnO_2 anode material for lithium ion battery
  DPG-Frühjahrstagung, Berlin, 11 – 16 Mar 2018
- S. Yin, L. Song, S. Xia, P. Müller-Buschbaum
  TiO_2 and SnO_2 anode material for lithium ion battery
  8th Colloquium of the Munich School of Engineering, Garching, 19 Jul 2018
- S. Yin, L. Song, S. Xia, P. Müller-Buschbaum
  TiO_2 and SnO_2 anode material for lithium ion battery
  4th German SNI Conference, Garching, 17 – 19 Sep 2018
- A. Zheng, V. Körstgens, H.-Y. Chiang, E. Herth, S. Xia, P. Müller-Buschbaum
  Conductive dry adhesives for detecting electroencephalography
  DPG-Frühjahrstagung, Berlin, 11 – 16 Mar 2018
- A. Zheng, V. Körstgens, H.-Y. Chiang, E. Herth, S. Xia, P. Müller-Buschbaum
  Conductive dry adhesives for detecting electroencephalography
  Polymer Physics Summer School Obertauern, Austria, 12 – 15 Jun 2018
- U. Zweck, M. Riedl, A. Baum, D. Jost, A. Erb, R. Hackl
  Magnetic and electronic excitations in underdoped YBCO
  RACIRI summer school, Rügen, 25 Aug – 1 Sep 2018

8.4 Invited Talks at the Chair of Functional Materials

- Prof. Dr. Walter Schirmacher, Universität Mainz
  Theory of vibrational anomalies of glasses
  10 Jan 2018

- Prof. Dr. Pieter Glatzel, ESRF Grenoble, France
  Unconventional electronic structure in metal oxide nanoparticles
  17 Jan 2018

- Jingxiang Su, CAU Kiel
  The effect of substrate temperature on the properties of Ag nanoparticle films deposited by gas aggregation source
  24 Jan 2018

- Julian Heger, University of Regensburg
  Process development of clean carbon nanotube device
  31 Jan 2018

- Dominik Schwaiger, Ludwig-Maximilians-University of Munich
  Investigation of impact craters, in order to draw conclusions about eruptive dynamics at Mt. Etna, Italy
  23 Feb 2018

- Prof. Dr. Martina Schwager, Hochschule München
  Effect of interchain interactions on the optical characteristics of polythiophene derivatives
  24 Apr 2018

- Christina Geiger, LMU
  Van-der-Waals layered compounds β-FeSe and hexachalcogeno-hypodiphosphates Mx(P2X6)y (X = S, Se)
  8 May 2018

- Dr. Vladislav Stroganov, Universität Bayreuth
  4D biofabrication using self-folding polymer films
  29 May 2018

- Dr. Leonardo Chiappisi, Institut Laue-Langevin, Grenoble, France
  From shrimp shells to smart materials: shaping polysaccharides into responsive assemblies and coatings
  26 Jun 2018

- Prof. Dr. Annabelle Bertin, German Federal Institute for Materials Research and Testing (BAM) Berlin
  Upper critical solution temperature (UCST)-type thermoresponsive polymers from monomers with hydrogen bonding interactions
  3 Jul 2018

- Prof. Dr. Alfons Schulte, University of Central Florida, USA
  Vibrational spectroscopy and applications in soft matter
  17 Jul 2018

- Anna-Lena Oechsle, Julius-Maximilian-Universität Würzburg
  Analysis of the ion conductive behavior of highly concentrated polymer electrolytes for solid lithium-ion battery cells
  24 Jul 2018

8.5 Funding

Deutsche Forschungsgesellschaft:

- *In-situ Untersuchungen zu Kondensation, Nukleation und Wachstum von Metallfilmen und Nanostrukturen auf organischen Oberflächen während Sputterbeschichtung*
  Grant Number: MU 1487/18-2
  Project Leader: Prof. Dr. Peter Müller-Buschbaum

- *Transport und Morphologie, Einfluss auf nichtgeminale Rekombination in Organischen Solarzellen*
  Grant Number: MU 1487/22-1
  Project Leader: Prof. Dr. Peter Müller-Buschbaum

- *Rheologie und Grenzflächenstrukturen von Protein- und Partikelstabilisierten Schäumen - ein Multiskalenansatz*
  Grant Number: MU 1487/32-1
  Project Leader: Prof. Dr. Peter Müller-Buschbaum

- *Cononsolvency-induzierte Selbstorganisation thermoresponsiver Blockcopolymere in Lösung und im dünnen Film*
  Grant Number: MU 1487/29-1, Project Leader: Prof. Dr. Peter Müller-Buschbaum
  Grant Number: PA 771/20-1, Project Leader: Prof. Dr. Christine Papadakis

- *Kinetik der Aggregation in thermoresponsiven Polymerlösungen bei Drucksprüngen*
  Grant Number: PA 771/22-1, Project Leader: Prof. Dr. Christine Papadakis

- Teilprojekt *Inorganic-organic hybrid photovoltaic solar cells using novel hybrid materials* im GRK 2022: University of Alberta / Technische Universität München Internationale Graduiertenschule für Funktionelle Hybridmaterialien (ATUMS) der DFG
  IRTG-2022
  Project Leader: Prof. Dr. Peter Müller-Buschbaum

- In the framework of the Memorandum of Understanding on Cooperation between DFG and RFBR:
  Mischungen aus Lösungsmitteln und Mischungen aus Blockcopolymeren für die kontrollierte Präparation strukturierter dünner Blockcopolymerfilme
  Grant Number: PA 771/10-2
  Project Leader: Prof. Dr. Christine Papadakis

- *Dünne Filme aus pH und thermoresponsiven Triblockcopolymeren: von der Netzwerkdynamik zum defektfreien Film*
  Grant Number: PA 771/19-1
  Project Leader: Prof. Dr. Christine Papadakis

- In the framework of the Memorandums of Understanding on Scientific Cooperation between DFG and GACR:
  Kugelförmiges Pferd im Vakuum oder anwendbare Mizellen? Verhalten und Form von Nanopartikeln als Wirkstoffträger für Krebsmedikamente in reeller Blutumgebung
  Grant Number: PA 771/17-1
  Project Leader: Prof. Dr. Christine Papadakis

Bundesministerium für Bildung und Forschung:

- *FlexiProb: Flexible Probenumgebungen für die Untersuchung weicher Materie zur Implementierung an der ESS*
  Teilprojekt: 3
  Project Leader: Prof. Dr. Peter Müller-Buschbaum
- *Optische In-situ Methoden für das Flugzeitspektrometer TOFTOF*
  Project Leader: Prof. Dr. Peter Müller-Buschbaum

Bayerisches Staatsministerium für Wissenschaft und Kunst:

- Im Rahmen der Munich School of Engineering (MSE):
  Solar Technologies Go Hybrid (SolTech) - Forschungsnetzwerk TUM.solar
  Project Leader: Prof. Dr. Peter Müller-Buschbaum
- Im Rahmen der Munich School of Engineering (MSE): Netzwerk Regenerative Energien
  Aufbau eines interdisziplinären Netzwerks aus Lehrstühlen der Technischen Universität München und anderen Forschungseinrichtungen zur Förderung der Forschungsaktivitäten im Bereich der regenerativen Energien
  Project Leader: Prof. Dr. Peter Müller-Buschbaum

Technische Universität München:

- Im Rahmen der International Graduate School of Science and Engineering (IGSSE)
  Interface Science for Photovoltaics - a EuroTech GreenTech Initiative
  Project Leader: Prof. Dr. Peter Müller-Buschbaum

Others:

- Im Rahmen des Exzellenzclusters Nanosystems Initiative Munich (NIM)
  Nanosystems for Energy Conversion
  Principal Investigator: Prof. Dr. Peter Müller-Buschbaum

9 The chair

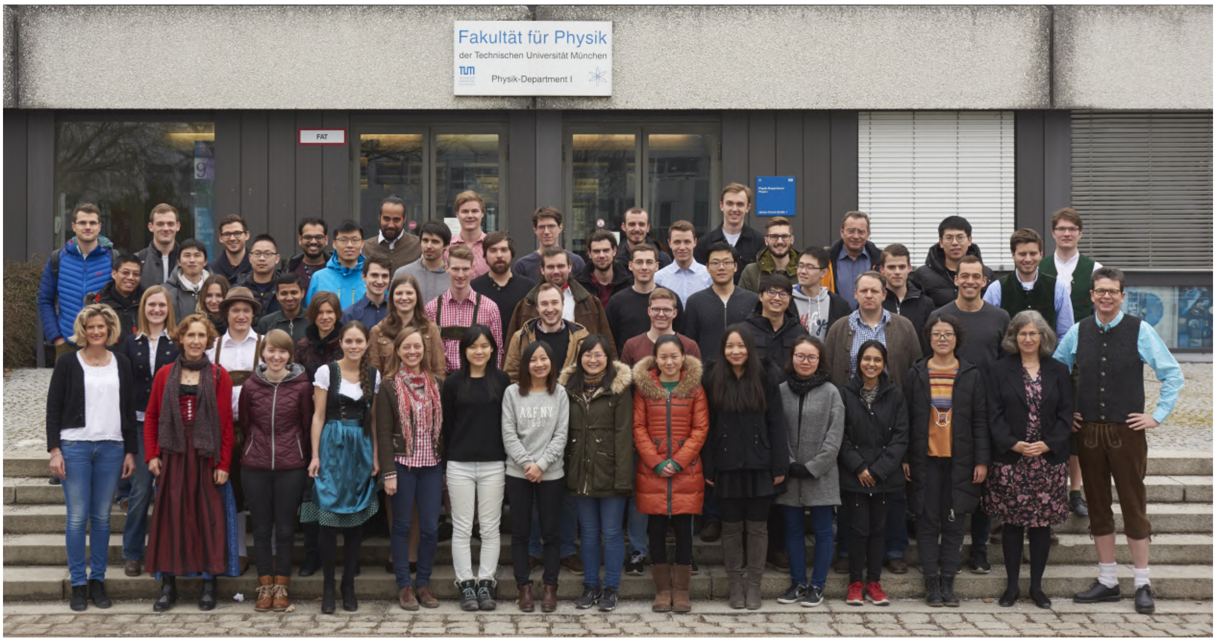

9.1 Staff

Chair:

until March 31, 2018: Prof. Dr. Winfried Petry
as of April 1, 2018: Prof. Dr. Peter Müller-Buschbaum

Professor:

Prof. Dr. Christine M. Papadakis

Fellows:

Dr. Volker Körstgens
Dr. Michael Leitner
Dr. Wiebke Lohstroh
Dr. Jürgen Neuhaus
Dr. Neelima Paul
Dr. Lin Song
Dr. Marcell Wolf

PhD Students:

Bruno Baumeister
Lorenz Bießmann
Wei Cao
Tobias Chemnitz
Wei Chen
Mihael Coriç
Oliver Filonik
Sandra Geara
Christina Geiger
Marc Gensch
Sebastian Grott
Renjun Guo
Julian Heger
Alexander Ewin Heldmann
Nuri Hohn
Xinyu Jiang
Florian Jung
Jia-Jhen Kang
Chia-Hsin Ko
Lukas Karge
Jenny Lebert
Nian Li
Xiaohu Li
Franziska C. Löhrer
Lucas Kreuzer
Pascal Neibecker
Bart-Jan Niebuur
Anna-Lena Oechsle
Shambhavi Pratap
Stephan Pröller
Christian Reiter
Nitin Saxena
Roy Schaffrinna
Simon Schaper
Johannes Schlipf
Dominik Schwaiger
Christian Schwarz
Jingyi Shi
Riane Elizabeth Stene
Christian Steyer
Bo Su
Sandro Szabò
Kun Wang
Rui Wang
Tobias Widmann
Kerstin Wienhold
Senlin Xia
Dan Yang
Shanshan Yin
Xiaohan Zhang
Ulrike Zweck

Master Students:

Seraphin Aeschbach
Nawarah Aldosari
Doaa Ali
Amira Baccari
Christoph Bilko
Kalyan Biswas
Rodrigo Delgado Andres
Johannes Costa
Lautaro Dìaz Piola
Korbinian Faust
Johannes Gallitscher
Jiabin Gui
Goran Ivkovic Ivandekiç
Hongwon Kim
Vladislav Kochetov
Amir Kotobi
Raphael Märkl
Valentin Munteanu
Benjamin Predeschly
Kaltrina Shehu
Cristian Telescu
Christian Weindl
Andreas Zheng

Bachelor Students:

Xaver Simon Brems
André Deyerling
Benedikt Fuchs
Hendrik Hegels
Elisabeth Keller
Raphael Maier
Wolfgang Männer
Elisabeth Meidinger
Michael Mörtl
David Müller
Johannes Pantle
Jonas Schmitt
Benedikt Schoof
Paul Steinacker
Johannes Thalhammer
Lina Maria Todenhagen
Julian Trapp
Patrick Wastian
Veronika Wenger
Simon Wörle
Wolfgang Männer
Michael Ziemba

Students Assistants:

André Deyerling
Hendrik Hegels
Regina Kluge
Moritz Makowski
Jonas Puchmair
Maximilian Schart
Safwan Uddin Ahmed

Internships/Exchange Students:

Florian Fink
Tommaso Riccitelli
Alida Severin
Vema Sundeep
Shaleahk Wilson
Hezhen Xie

Technical/Administrative Staff:

Reinhold Funer
Josef Huber
Josef Kaplonski
Carola Kappauf
Dieter Müller
Thomas Seitzl
Marion Waletzki

9.2 Graduations

- **Accomplished PhD Theses**

  Lukas Karge
  Co-Re alloys for ultra-high temperature applications – investigated by in-situ neutron scattering and complementary methods

  Jenny Lebert
  Polythiophene thin films – structure formation during in situ polymerization

  Xiaohu Li
  Co-Re alloys for ultra-high temperature applications – investigated by in-situ neutron scattering and complementary methods

  Pascal Neibecker
  Atomic order and its influence on functional properties of MiMn based Heusler systems

  Stephan Pröller
  Morphology formation and manipulation in printed organic solar cells

  Joahnnes Schlipf
  The morphology of hybrid perovskite thin films for photovoltaic application

  Bo Su
  Optical design of titania films in dye-sensitized solar cells and perovskite solar cells

  Rui Wang
  Nanostructuring and understanding morphology-property correlation in semiconductor thin films

  Xiaohan Zhang
  Macromolecular pHPMA-based nanoparticles for solid tumor targeting: behavior in protein environment

- **Accomplished Master Theses**

  Christoph Bilko
  Investigation of new materials for high-efficiency polymer solar cells

  Rodrigo Delgado
  Printed fullerene-free organic thin films for photovoltaic applications

  Jiabin Gui
  Films of water-processable polythiophene in energy applications

  Vladislav Kochetov
  Analysis and reconstruction of X-ray and neutron diffraction computed tomography data

  Margerita Pfab
  Methods of determining modified BET parameter for prediction of ternary salt hydrate phase diagrams

  Kaltrina Shehu
  Polymeric molecular brushes investigated by scattering methods

  Andreas Zheng
  Novel dry electrodes for electroencephalography

- **Accomplished Bachelor Theses**

  Xaver Simon Brems
  TISANE: AC coil setup for time resolved kinetic neutron scattering

  André Deyerling
  PNIPAM solutions at high pressure studied with dynamic light scattering - the cononsolvency effect

  Benedikt Fuchs
  Hybrid thermoelectric materials based on a polymer-nanoparticle composite

  Hendrik Hegels
  Non-equililbrium assembly processes in supramolecular materials in dependence on oligomer length

  Elisabeth Keller
  High efficiency perovskite solar cells

  Raphael Maier
  Investigations on polymer electrodes

  Wolfgang Männer
  Morphology and microstructure of organometallic lead halide perovskite thin films

  Elisabeth Meidinger
  Structural analysis of multi-responsive block copolymers with dynamic light scattering

  Michael Mörtl
  Role of molecular interactions for stimuli-responsive polymers of potential use in soft robotics

  David Müller
  Synthesis and characterization of novel, mesoporous Ge thin films for Li-Ion battery applications

  Johannes Pantle
  Role of molecular interactions for stimuli-responsive polymers of potential use in soft robotics

  Jonas Schmitt
  Fundamental characterization of thin films based on a novel heavy element containing small molecule for photovoltaic applications

  Benedikt Schoof
  Analysis of metalnanosgtructure evolution on p9olymer surfaces

  Paul Steinacker
  Effect of an ionic liquid post-treatment on thermoelectric properties of thin PEDOT:PSS films

  Johannes Thalhammer
  Photocromic paper

  Lina Maria Todenhagen
  A comparative investigation on PEDOT:PSS-based anodes in ITO-free organic light-emitting diodes

  Julian Trapp
  Strukturelle Untersuchungen eines multiresponsiven Blockcopolymers mit dynamischer Lichtstreuung

  Patrick Wastian
  Cononsolvency in novel thermoresponsive polymers

  Veronika Wenger
  Investigation of polymer electrodes

Simon Wörle
Conductive paper

Michael Ziemba
The concentration and temperature dependence of the hydrodynamic radius of molecular brushes

9.3 Guests

- Prof. Dr. Walter Schirmacher, Universität Mainz
  10 Jan 2018

- Prof. Dr. Pieter Glatzel, ESRF, Grenoble, France
  17 Jan 2018

- Jingxiang Su, CAU Kiel
  24 Jan 2018

- Julian Heger, University of Regensburg
  31 Jan 2018

- Dominik Schwaiger, Ludwig-Maximilians-University of Munich
  23 Feb 2018

- Prof. Dr. Martina Schwager, Hochschule München
  24 Apr 2018

- Christina Geiger, LMU Munich
  8 May 2018

- Prof. Alfons Schulte, University of Central Florida, USA
  14 May – 20 Jul 2018

- Dr. Vladislav Stroganov, Universiät Bayreuth
  29 May 2018

- Dr. Carolin Sutter-Fella, University of California, Berkeley, USA
  4 Jun 2018

- Dr. Leonardo Chiappisi, Institut Laue-Langevin, Grenoble, France
  26 Jun 2018

- Prof. Dr. Annabelle Bertin, German Federal Institute for Materials Research and Testing (BAM), Berlin
  3 Jul 2018

- Hezhen Xie, University of Alberta, Canada
  Sep 10 – Nov 17, 2018

- Tommaso Riccitelli, University of Florence, Italy
  Sep 17, 2018 – Feb 28, 2019

- Prof. A. Rothschild, Israel Institute of Technology, Haifa, Israel
  5 Nov 2018